Tip-enhanced Raman spectroscopy for the characterization of biological systems : From nanoscale chemical and structural imaging in air to its development in liquid media

Gary Sean Cooney

▶ **To cite this version:**

Gary Sean Cooney. Tip-enhanced Raman spectroscopy for the characterization of biological systems : From nanoscale chemical and structural imaging in air to its development in liquid media. Medicinal Chemistry. Université de Bordeaux, 2024. English. NNT : 2024BORD0267 . tel-04907811

HAL Id: tel-04907811

https://theses.hal.science/tel-04907811v1

Submitted on 23 Jan 2025

HAL is a multi-disciplinary open access archive for the deposit and dissemination of scientific research documents, whether they are published or not. The documents may come from teaching and research institutions in France or abroad, or from public or private research centers.

L'archive ouverte pluridisciplinaire **HAL**, est destinée au dépôt et à la diffusion de documents scientifiques de niveau recherche, publiés ou non, émanant des établissements d'enseignement et de recherche français ou étrangers, des laboratoires publics ou privés.

université de BORDEAUX

THÈSE PRÉSENTÉE

POUR OBTENIR LE GRADE DE

DOCTEUR DE

L'UNIVERSITÉ DE BORDEAUX

ÉCOLE DOCTORALE SCIENCES CHIMIQUES

CHIMIE PHYSIQUE

Par Gary Sean COONEY

Spectroscopie Raman exaltée de pointe pour la caractérisation de systèmes biologiques : De l'imagerie chimique et structurale nanométrique à l'air à son développement en milieu liquide

Tip-enhanced Raman spectroscopy for the characterization of biological systems: From nanoscale chemical and structural imaging in air to its development in liquid media

Sous la direction de : Sébastien BONHOMMEAU

Soutenue le 27 Novembre 2024

Membres du jury :

M. BONHOMMEAU, Sébastien	Maître de Conférences ISM, Université de Bordeaux	Directeur de thèse
Mme. ALVES, Isabel	Directrice de Recherche CNRS CBMN, Université de Bordeaux	Présidente
Mme. ZHANG, Dai	Associate Professeure Universität Tübingen	Rapporteure
M. PIOT, Olivier	Professeur Université de Reims Champagne-Ardenne	Rapporteur

Membres invités :

M. TALAGA, David	Ingénieur de Recherche CNRS ISM, Université de Bordeaux	Invité
Mme. LECOMTE, Sophie	Directrice de Recherche CNRS CBMN, Université de Bordeaux	Invité

Résume

Cette thèse a pour objectif le développement de la spectroscopie Raman exaltée de pointe (TERS) pour des applications en milieux liquides, et plus particulièrement pour l'étude de membranes lipidiques et de protéines amyloïdes qui sont impliquées dans des maladies neurodégénératives comme la maladie d'Alzheimer. La TERS s'affranchit de la limite de diffraction de la spectroscopie Raman conventionnelle en combinant la haute résolution spatiale de la microscopie à sonde locale et la spécificité chimique de la spectroscopie Raman exaltée de surface (SERS). En utilisant une pointe de microscope à sonde locale métallisée et effilée au niveau nanométrique, la TERS génère une exaltation localisée du signal Raman au sommet de la pointe. Ceci permet l'étude de biomolécules optiquement non-résonnantes à l'échelle nanométrique sans marquage moléculaire et de manière non-destructive.

Les défis clés qui sont traités dans ce travail incluent la fabrication de pointes actives en TERS, l'optimisation d'un nouveau système TERS en réflexion totale interne (RTI) pour des utilisations en environnements liquides, et l'exploitation de données complexes obtenues par imagerie TERS hyperspectrale. Des protéines amyloïdes sous forme de fibrilles de protéine Tau ont été étudiées au moyen de notre instrument de RTI-TERS en prenant des fibrilles induites par de l'héparine comme référence pour évaluer la performance du système. Des études TERS de fibrilles Tau induites par de l'ARN ont donné un aperçu des mécanismes de formation sous-jacents des fibrilles amyloïdes. Par ailleurs, ces données ont été utilisées pour explorer le potentiel des méthodes chimiométriques, telles que l'Analyse en Composantes Principales (ACP) et l'Analyse en Cluster Hiérarchique (ACH), pour leur analyse fine. Ces méthodes ont été évaluées dans le contexte des méthodes plus traditionnelles de sélection de pics individuels.

Cette thèse détaille aussi le développement d'un système RTI-TERS compatible avec le milieu liquide et son application à l'étude de bicouches lipidiques supportées en milieux aqueux. Cette avancée permet la caractérisation nanométrique de membranes lipidiques dans des milieux biologiquement pertinents et plus réalistes que l'air. Dans la perspective de futurs travaux examinant les interactions protéines-lipides, ces innovations sont cruciales pour comprendre la formation des fibrilles amyloïdes et leurs effets délétères sur les cellules neuronales.

Au final, cette thèse a amélioré la TERS en tant qu'outil pour étudier les structures biomoléculaires à l'échelle nanométrique dans le contexte des maladies neurodégénératives, et le système RTI-TERS optimisé fournit une plateforme pour de futures recherches dans des applications biologiques et biomédicales.

Abstract

The aims of this thesis are the development of tip-enhanced Raman spectroscopy (TERS) for applications in liquid media, specifically for the study of lipid membranes and amyloid proteins which are implicated in neurodegenerative diseases like Alzheimer's. TERS overcomes the diffraction limit of conventional Raman spectroscopy by combining the high spatial resolution of scanning probe microscopy with the chemical specificity of surface-enhanced Raman spectroscopy (SERS). By employing a metal-coated nano-tapered scanning probe microscopy probe tip, TERS generates a localised enhancement of the Raman signal at the tip apex. This enables the study of optically non-resonant biomolecules at the nanoscale in a label-free and non-destructive manner.

The key challenges that are addressed in this work include the fabrication of TERS-active tips, the optimisation of our novel total-internal reflection (TIR)-TERS system for use in liquid environments, and the handling of the complex data obtained from hyperspectral TERS imaging. Amyloid proteins in the form of Tau fibrils were studied using this TIR-TERS setup with heparin-induced Tau fibrils being a benchmark for evaluating the performance of the system. TERS studies of RNA-induced Tau fibrils provided insight into the underlying formation mechanisms of amyloid fibrils. In addition, these data were used to explore the use of chemometric methods, such as Principal Component Analysis (PCA) and Hierarchical Cluster Analysis (HCA), for their fine analysis. These methods were evaluated in the context of more traditional peak-picking methods.

This thesis also details the development of a liquid-compatible TIR-TERS system and its application to the study of supported lipid bilayers in aqueous media. This advancement enables the nanoscale investigation of lipid membranes in biologically relevant media, which is more representative compared to TERS in air. With the outlook of future works investigating protein-lipid interactions, these innovations are crucial for understanding amyloid fibril formation and their deleterious effects on neuronal cells.

To conclude, this thesis enhances TERS as a tool for studying biomolecular structures in the context of neurodegenerative diseases at the nanoscale, and the optimised TIR-TERS system provides a platform for future research in biological and biomedical applications.

Table of Contents

List of Figures

List of Tables

List of Abbreviations

Aβ	Amyloid-β
AD	Alzheimer's Disease
AFM	Atomic Force Microscopy
Asym	Asymmetrical
ATR	Attenuated Total Reflectance
ATR-FTIR	Attenuated Total Reflectance - Fourier Transform Infrared Spectroscopy
CBMN	Institut de Chimie et Biologie des Membranes et des Nano-objets
CCD	Charge Coupled Device
CE	Counter Electrode
CHEM	Non-resonant Chemical Mechanism
CM	Chemical Mechanism
Cryo-EM	Cryogenic Electron Microscopy
CT	Charge-Transfer
CV	Column Volume
DBS	Double-Strand Break
Def	Deformation vibrational mode
EF	Enhancement Factor
EFM	Electrostatic Force Microscopy
EM	Electronic Mechanism
EM-CCD	Electron-Multiplying CCD
FA	Factor Analysis
FDTD	Finite-Difference Time-Domain
FIB	Focused Ion Beam
GSM	Groupe Spectroscopie Moléculaire
HCA	Hierarchical Clustering Analysis
HS	High-Spin
HSAFM	High-Speed Atomic Force Microscopy
ICMCB	Institut de Chimie de la Matière Condensée de Bordeaux
IR	Infrared
ISM	Institut des Sciences Moléculaires
KPFM	Kelvin Probe Force Microscopy
LS	Low-Spin
LSP	Localised Surface Plasmon
LSPR	Localised Surface Plasmon Resonance
MBD	Microtubule Binding Domain
MCR	Multivariate Curve Resolution
MDA	Multivariate Data Analysis
MFM	Magnetic Force Microscopy
NA	Numerical Aperture
NF	Nominal Force
NP	Nanoparticle
OD600	Optical Density 600 nm light source
PC	Principal Component
PCA	Principal Component Analysis
PC/CAFM	Photoconductive/Conductive Atomic Force Microscopy
PD	Parkinson's Disease
PID	Proportional-Integral-Derivative
PM	Parabolic mirror

PrP	Prion Protein
PVD	Physical Vapour Deposition
ROC	Radius Of Curvature
RE	Reference Electrode
RRE	Resonance Raman Effect
RRS	Resonance Raman Spectroscopy
SAM	Self-Assembled Monolayer
SCM	Scanning Capacitance Microscopy
SEM	Scanning Electron Microscopy
SERS	Surface-Enhanced Raman Spectroscopy
SERRS	Surface-Enhanced Resonance Raman Spectroscopy
SMM	Scanning Microwave Microscopy
SNOM	Scanning Near-Field Optical Microscopy
SOR	Spatial Optical Resolution
SPP	Surface Plasmon Polaritons
SPR	Surface Plasmon Resonance
SPM	Scanning Probe Microscopy
SSRM	Scanning Spreading Resistance Microscopy
SThM	Scanning Thermal Microscopy
STM	Scanning Tunnelling Microscopy
Str	Stretching vibrational mode
SVD	Single Value Decomposition
SVM	Scanning Voltage Microscopy
Sym	Symmetrical
TERS	Tip-Enhanced Raman Spectroscopy
TIR	Total-Internal Reflection
Tw	Twisting vibrational mode
UV	Ultraviolet
UVC	Ultraviolet C
Vis	Visible
WE	Working Electrode
WT	Wild Type

List of Acronyms of Chemical Compounds

A	Adenine
Ag	Silver
Ala	Alanine
APTES	3-aminopropyltriethoxysilane
Ar	Argon
Arg	Arginine
Asn	Asparagine
Asp	Aspartate
Au	Gold
Cyt-c	Cytochrome C
Cys	Cysteine
CNT	Carbon Nanotube
DMSO	Dimethyl Sulfoxide
DNA	Deoxyribonucleic Acid

DOPC	Dipalmitoylphosphatidylcholine
DOPS	1,2-dioleoyl-sn-glycero-3-phospho-L-serine
DTT	Diothiothreitol
EDTA	Ethylenediaminetetraacetic acid
FDTD	Finite-Difference Time-Domain
GDH	Glucose dehydrogenase
Glu	Glutamate
Gln	Glutamine
HaCaT	Human dermal derived keratinocyte
His	Histidine
HEPES	4-(2-hydroxyethyl)-1-piperazineethanesulfonic acid
Ile	Isoleucine
Im	Imidazole
IPTG	Isopropyl β-D-1-thiogalactopyranoside
LB	Lysogeny Broth
Leu	Leucine
Lys	Lysine
MBN	4-mercaptobenzonitrile
Met	Methionine
mRNA	Messenger RNA
MWCNT	Multiwalled Carbon Nanotube
Phe	Phenylalanine
PIP_2	Phosphatidylinositol 4,5-bisphosphate
PMSF	Phenylmethylsulphonyl fluoride
PolyA	Poly-Adenosine
PolyC	Poly-Cytosine
PolyU	Poly-Uracil
POPC	1-palmitoyl-2-oleoylphosphocholine
POPS	1-palmitoyl-2-oleoylphospho-L-serine
Py	Pyranose
RNA	Ribonucleic Acid
rRNA	Ribosomal RNA
SWCNT	Single-Walled Carbon Nanotube
Tris	Trisaminomethane
tRNA	Translational RNA
Tyr	Tyrosine
Val	Valine
4-PBT	4’-(pyridin-4-yl) biphenyl-4-yl)-methanethiol

List of Symbols and Corresponding Units

λ	Wavelength	nm
ω	Raman shift	cm^{-1}
f_0	Resonance Frequency	Hz
r_c	Radius of curvature (TERS tip)	nm
t	Time	s
T	Temperature	K

Acknowledgements

This thesis was conducted within the Groupe Spectroscopie Moléculaire (GSM) which is part of the Institut des Sciences Moléculaires (ISM). Therefore, I would foremost like to thank the director of the institute, **Mr. Éric Fouquet** for welcoming me into the ISM. I also thank **Ms. Sophie Sobanska** as group leader of GSM for her welcome and support.

I am especially grateful to **Ms. Dai Zhang** and **Mr. Olivier Piot** for agreeing to evaluate this manuscript, for their careful reading, and their expert advice, thank you. I want to extend my gratitude to **Mr. Sébastien Bonhommeau**, **Mr. David Talaga**, and **Ms. Sophie Lecomte** for their participation in this jury and their interest demonstrated in this work. A special thank you to **Ms. Isabel Alves** for acting as president of the jury.

I thank **Veronique Jubera** and **Marc Lamy de la Chapelle** for being members of the individual monitoring committee, who have followed and supported the progress the PhD over the past three years.

These past years gave me the opportunity to collaborate closely with the members of the Spectroscopy and Imaging of Active Peptides on Membranes team at Institut de Chimie et Biologie des Membranes et des Nano-objets (CBMN), Bordeaux. I would therefore like to thank **Ms. Sophie Lecomte**, **Mr. Yann Fichou**, **Ms. Cecille Feuillie**, and **Mr. Michael Molinari** for their contributions and fruitful discussions towards the thesis project. I want to express my gratitude to **Ms. Vicky Ury-Thiery** who, in taking the time out of her own PhD endeavours to provide high-quality biological samples for my research, ensured the success of this work. For your patience, understanding, and friendship, I thank you. I want to thank the collaborative works with the Groupe Molécules et Matériaux Commutables at Institut de Chimie de la Matière Condensée de Bordeaux (ICMCB). Specifically, I thank **Mr. Patrick Rosa**, **Mr. Mathieu Gonidec**, **Ms. Margaux Penicaud**, and **Ms. Rebecca Rodrigues de Miranda** for their insight and discussion on thermal evaporation processes, for providing gold substrates, and allowing the use of their facilities for my work on physical vapour deposition. I want to thank the collaborative efforts of **Mr. Sébastien Plissard** and **Mr. Emmanuel Scheid** of the Materials and Processes for Nanoelectronics (MPN) team at The Laboratory for Analysis and Architecture of Systems (LAAS), Toulouse for their efforts in tip fabrication and the resulting discussions to this end.

I would also like thank all those who participated in this thesis work, directly or indirectly. Within GSM, **Mr. David Talaga** deserves the acknowledgement for his commitment to TERS, in the development of the TIR-TERS system, and patience in teaching

and performing experiments alongside me. I thank you. I extend my appreciation and thanks to **Mr. Thierry Buffeteau** for fruitful discussions, to **Mr. Frédéric Adamietz** for his assistance in performing UV measurements, to **Ms. Sophie Sobanska** for her invaluable knowledge and support on multivariate data processing, and to **Mr. Marc Dussauze** for his humour when faced with malfunctioning sputter coaters. I want to thank my peers, the past and current students at GSM; **Ms. Clara Becote**, **Ms. Lara Karam**, and **Ms. Alice Goillot,** I thank you for your warm welcome and friendship in the first years of the PhD. To **Mr. Alexis Maillard**, your kind nature and outlook are qualities that I've fondly appreciated throughout this journey. To **Ms. Yuhan Huang**, we started our PhDs together and both experienced the trials and tribulations of TERS. This is a bond that has been enhanced over the years (no thanks to troublesome tips) and it was a pleasure to share this endeavour together. To my dear friend **Mr. Simon Dubuis**, ever since our first encounter you have showed nothing but kindness and understanding. I am thankful for the time wasted drinking coffees, playing quarto or chess, piecing puzzles together, and other social activities outside the lab; as time wasted in someone's company that you enjoy, is not time wasted at all. I hope I have been even half as supportive to you as you have been to me through challenging times. I wholeheartedly thank you.

To the members of AdoC and later members of the weekly boardgames meetings: **Mr. Loïc Delcourte**, **Mr. Vaclav Krupicka**, **Mr. Nicolas Abouab,** and **Mr. Muhammad Bilal Abdul Shukkoor**, for the competitive and humorous evenings min-maxing that served as an important release from the PhD day-to-day, I thank you.

I want to thank my fellow ASC alumnus **Mr. Diego Fernando Garcia del Rio** for his support and encouragement at a distance over the past three years. I am thankful for our friendship that began over five years ago, which has accumulated in celebrating your marriage with your family in Mexico. I wish you the greatest success in academia and life, mi amigo.

I thank **Ms. Katharina Hoffmann** for always standing by my side and supporting me throughout this endeavour. You embraced my decision to pursue this undertaking, and were the motivation to see it through to the end. I thank you from the bottom of my heart.

To my parents, **Mr. Sean Cooney** and **Ms. Ita Kelly**, who have always encouraged me to continue my academic career. Thank you for your unwavering support throughout the years.

Finally, I thank my mentor **Mr. Sébastien Bonhommeau,** for your steadfast supervision throughout the thesis, and for always making time to answer questions and give advice. Thank you for this opportunity.

Introduction

Understanding biomolecules on the molecular scale is of paramount importance for describing their function and their role within biosystems. This molecular characterisation can then in turn be used to develop targeted medical treatments for ailments and diseases with the outlook of leading to potential cures.

This search for fine characterisation of biomolecules has led to the development of a plethora of chemical and structural analysis techniques over the past century, which can be used to describe conformation, structure, and chemical composition. In life sciences, fluorescence microscopy has gained popularity due to its ability of study living tissue on the cellular level, in addition to its high emission cross section (ca. 10^{-16} cm^2 $molecule^{-1}$). The more recent developments of super-resolved fluorescence microscopy, has allowed fluorescence microscopy to go beyond the diffraction limit of hundreds of nanometres, down to ca. 5 nm.[1] However, despite these advances, fluorescence microscopy is flawed in the lack of molecular structure information and the need for fluorescent labelling. The use of such labels results in photobleaching and phototoxicity, where the fluorescent dyes used become non-fluorescent overtime due to alteration of their molecular structure, and where biomolecules are damaged due to prolonged exposure to excitation light, respectively.

Contrary to fluorescence imaging techniques, vibrational spectroscopies such as infrared (IR) absorption spectroscopy and Raman scattering spectroscopy can provide non-destructive label-free molecular characterisation. These two techniques are seen as complementary, as due to certain selection rules, vibrational modes that may not be observable in IR absorption spectra can often be present in Raman spectra (and *vice-versa*). In the context of studying biomolecules in model or native environments, while IR absorption measurements can provide useful information about molecular structure, interpretation of IR spectra in aqueous media is hindered by the presence of intense H_2O vibrations. Specifically, in the investigation of protein structure, amide I and amide II bands characteristic of the protein backbone secondary structures are masked by the H_2O scissoring vibration between 1500 – 1700 cm^{-1}. This is not the case in Raman spectra, where OH vibrational modes are low in intensity, giving Raman spectroscopy a suitability for studying biomolecules in aqueous media.

Nevertheless, spontaneous Raman spectroscopy is often insufficient for studying weakly scattering biomolecules, and has a spatial optical resolution (SOR) limited by diffraction to half the excitation wavelength, typically. This limit of resolution prevents the use

of conventional vibrational spectroscopies to study biomolecules individually at the nanoscale. To this end, tip-enhanced Raman spectroscopy (TERS) has been developed to provide spectroscopic characterisation beyond the diffraction limit.

TERS is an apertureless scanning near-field optical microscopy (SNOM) technique. It combines the nanoscale topographical imaging of scanning probe microscopies (SPM) with the chemical specificity of surface-enhanced Raman spectroscopy (SERS). SPM techniques include scanning tunnelling microscopy (STM) and atomic force microscopy (AFM) which both use a nano-tapered probe tip to raster scan a surface to build a topographical image. They differ in their z-feedback mechanisms, where tip distance to the sample is controlled via the measured tunnelling current of an applied voltage in STM, and via the deflection of a laser on the probe cantilever in AFM. In SERS, molecules absorbed on nanostructured metal surfaces benefit from an enhanced Raman scattering signal in the region of $10^2 – 10^{10}$. This enhancement is due to the excitation of a localised surface plasmon resonance (LSPR) of a metal nanoparticle in close proximity to the analyte. This LSPR is dependent on the composition, size, and shape of the nanoparticle, as well as the surrounding dielectric medium. Compared to other plasmonic metals such as aluminium, palladium, and platinum, gold (Au) and silver (Ag) are preferentially used in SERS due to the low imaginary part of their dielectric function in the ultraviolet (UV) to near-IR range, which in turn leads to a higher signal enhancement. This enhancement means SERS has a very high molecular sensitivity, and in specific conditions, has single-molecule specificity.[2]

If a SERS-active metal layer is instead coated onto a SPM probe, then the apex of this tip becomes the active enhancing nanostructure i.e. the TERS tip. The TERS signal then originates from the nanoscale “hotspot” at the tip apex when in close contact to the analyte at the surface. By raster scanning this “hotspot” at nanoscale increments, a chemical map can be obtained in tandem with the topographical map from the SPM technique. While SERS and TERS are analogous in many respects, their respective spectra often differ in band intensity due to specific selection rules. Nevertheless, Raman and SERS often have similar band position that they are often used as reference for interpreting TERS spectra of biomolecules.[3]

TERS has already been successfully deployed in the study of nucleic acids, proteins and peptides, and more complex biological systems such as membranes and cells.[4] Amyloid proteins piqued interest in the TERS community due to their deleterious deposits being implicated in various neurodegenerative disorders, such as Alzheimer’s disease (AD) and Parkinson’s disease. These proteins are β-sheet rich fibril assemblies that form via unknown aggregation mechanisms at the surface of neuronal membranes. Their precise structure and

formation in the disease state is still debated. Initially, researchers used TERS to characterise insulin fibrils as a model amyloid system,[5–8] but more recent efforts have focused on AD-relevant proteins such as amyloid-β (Aβ),[9–11] and Tau protein.[12–14]

While TERS has revealed the heterogeneity of amyloid fibrils and uncovered potential aggregation pathways, only a handful of experiments have been performed in liquid media.[10] This is due to both difficulties in optimisation of the illumination configuration and TERS tip stability in aqueous media. The next step in understanding amyloid formation should consider the cellular environment, and TERS in aqueous media is an obvious step. Lipid membranes are of interest to study in liquid TERS not only to study target lipids as a function of membrane composition, but to investigate protein-cell interactions at the nanoscale. To this end, our group has developed a bottom-illumination geometry TERS system in total-internal reflection (TIR) configuration.[12] TIR-TERS has been proven to achieve superior enhancement compared to traditional bottom-illumination configurations.

Accumulating all that has been previously mentioned, the objectives of this thesis are to develop the TERS technique for biological applications in liquid, and, specifically, to study lipid membranes and amyloid proteins with the outlook of better understanding their interaction in the frame of neurodegenerative disease. Several challenges have been faced in this pursuit, notably the fabrication of TERS-active tips via vapour-deposition methods, optimisation of the TIR-TERS system for operation in liquid, and data handling of the hyperspectral TERS images.

This thesis work was carried out in the Groupe Spectroscopie Moleculaire (GSM) as part of the Institut de Spectroscopie Moleculaire (ISM) of the University Bordeaux, Talence. The developments in TERS instrumentation and applications have been pioneered for over 10 years in our laboratory. The main motivation is to develop a TERS platform for the study of biomolecules and biosystems using enhanced Raman techniques.

In this thesis, the first chapter provides a general overview and background context of this study. It provides a concise grounding in Raman spectroscopy and SPM, including their coupling in the form of TERS. A brief history of the use of TERS for characterising biomolecules at the nanoscale will be described, and the advances and future challenges of the technique will be discussed.

The second chapter will be dedicated to the technical aspects of a TERS experiment, notably the optical coupling between the SPM and the Raman spectrometer. In addition to the most typical TERS system configurations, our unique TIR-TERS setup will be described including the coupling and functioning of Dark-Field Scattering Microscopy, notably used to determine LSPR of TERS tips. The considerations for performing TERS experiments in liquid,

including the production of a suitable liquid cell, is detailed. Methods for TERS probe fabrication are evaluated, and the general performance of a TERS experiment will be detailed.

The third chapter will describe the work on amyloids, a group of proteins that aggregate and form fibrillar structures. These proteins are implicated in neurodegenerative diseases, and TERS has given us insights into their formation and function. Specifically, heparin-induced and RNA-induced Tau fibrils are studied using our novel TIR-TERS system. The work on heparin-induced fibrils was published in The Journal of Physical Chemistry B, as "Total Internal Reflection Tip-Enhanced Raman Spectroscopy of Tau Fibrils" by Talaga *et al.* (2022). The work on polyA-induced Tau fibrils was published in Angewandte Chemie International Edition, as "Chemical Imaging of RNA-Tau Amyloid Fibrils at the Nanoscale Using Tip-Enhanced Raman Spectroscopy" by Cooney *et al.* (2023).

The fourth chapter details chemometric investigations of TERS spectra using the Tau fibril datasets of Chapter 3. Principal Component Analysis and Hierarchical Cluster Analysis were both evaluated and compared to traditional peak-picking methods. These investigations were presented as a poster at the 19th European Conference on the Spectroscopy of Biological Molecules, Reims, France (August 29 – September 1 2022).

The fifth and final chapter will detail the investigation of supported lipid bilayers in liquid media using TIR-TERS. The adaption of our system to perform measurements in liquid and the considerations needed for performing a TERS experiment in liquid is given. The nanoscale analysis of model membranes is of great interest for studying protein-lipid interactions. These investigations are not yet published.

References

1. Cremer, C., Birk, U., Perspectives in super-resolved fluorescence microscopy: What comes next?, Front. Phys., 4, 1–9 (2016).
2. Kneipp, J., Kneipp, H., Kneipp, K., SERS—a single-molecule and nanoscale tool for bioanalytics, Chem. Soc. Rev., 37, 1052–1060 (2008).
3. Bonhommeau, S., Lecomte, S., Tip-Enhanced Raman Spectroscopy: A Tool for Nanoscale Chemical and Structural Characterization of Biomolecules., ChemPhys Chem, 19, 8–18 (2018).
4. Bonhommeau, S., Cooney, G. S., Huang, Y., Nanoscale chemical characterization of biomolecules using tip-enhanced Raman spectroscopy, Chem. Soc. Rev., 51, 2416–2430, (2022).
5. Kurouski, D., Deckert-Gaudig, T., Deckert, V., Lednev, I. K., Structure and composition of insulin fibril surfaces probed by TERS., J. Am. Chem. Soc. 134, 13323–13329 (2012).
6. Deckert-Gaudig, T., Kurouski, D., Hedegaard, M. A. B., Singh, P., Lednev, I. K., Deckert, V., Spatially resolved spectroscopic differentiation of hydrophilic and hydrophobic domains on individual insulin amyloid fibrils, Sci. Rep., 6, 33575 (2016).
7. Moretti, M., Proietti Zaccaria, R., Descrovi, E., Das, G., Leoncini, M., Liberale, C., de Angelis, F., Di Fabrizio, E., Reflection-mode TERS on Insulin Amyloid Fibrils with Top-Visual AFM Probes, Plasmonics, 8, 25–33 (2013).
8. Kurouski, D., Deckert-Gaudig, T., Deckert, V., Lednev, I. K., Surface characterization of insulin protofilaments and fibril polymorphs using tip-enhanced Raman spectroscopy (TERS), Biophys., 106, 263–271 (2014).
9. Lipiec, E., Kaderli, J., Kobierski, J., Riek, R., Skirlinska-Nosek, K., Sofinska, K., Szymonski, M., Zenobi, R., Nanoscale Hyperspectral Imaging of Amyloid Secondary Structures in Liquid, Angew. Chem. Int. Ed., 60, 4545-4550 (2021)
10. Paulite, M., Blum, C., Schmid, T., Opilik, L., Eyer, K., Walker, G., Zenobi, R., Full spectroscopic tip-enhanced Raman imaging of single nanotapes formed from β-Amyloid (1-40) peptide fragments, ACS Nano., 7, 911–920 (2013).
11. Lipiec, E., Perez-Guaita, D., Kaderli, J., Wood, B. R., Zenobi, R., Direct Nanospectroscopic Verification of the Amyloid Aggregation Pathway., Angew. Chemie Int. Ed., 130, 8655–8660 (2018).

12. Talaga, D., Cooney, G. S., Ury-Thiery, V., Fichou, Y., Huang, Y., Lecomte, S., Bonhommeau, S., Total Internal Reflection Tip-Enhanced Raman Spectroscopy of Tau Fibrils, J. Phys. Chem. B, 126, 5024–5032 (2022).
13. Talaga, D., Smeralda, W., Lescos, L., Hunel, J., Lepejova-Caudy, N., Cullin, C., Bonhommeau, S., Lecomte, S., PIP 2 Phospholipid-Induced Aggregation of Tau Filaments Probed by Tip-Enhanced Raman Spectroscopy, Angew. Chem. Int. Ed., 130, 15964–15968 (2018).
14. Cooney, G. S., Talaga, D., Ury-Thiery, V., Fichou, Y., Huang, Y., Lecomte, S., Bonhommeau, S., Chemical Imaging of RNA-Tau Amyloid Fibrils at the Nanoscale Using Tip-Enhanced Raman Spectroscopy. Angew. Chem. Int. Ed., 62, 6–11 (2023).

Chapter 1

Theory and State-of-the-art

1.1. Vibrational spectroscopy and Raman Scattering

1.1.1. Introduction to vibrational spectroscopy

On a fundamental level, the individual molecule can be described as a number of atoms connected together by elastic bonds. These analogical rubber bands can stretch and contract with a given periodicity, and this motion is termed a molecular vibration. When all atoms of the molecule are vibrating with the same phase at normal frequency, these motions are termed normal vibrations. In the case of simple linear molecules (e.g. HCN, CO_2, N_2, C_2H_2), the number of normal vibrations is $3n - 5$, where n is the number of atoms. For all other polyatomic molecules of n number of atoms there are $3n - 6$ normal vibrations. In order to observe these vibrational modes, vibrational spectroscopy is required to generate spectra of the investigated molecules. The individual spectrum of a molecule depends on the strength of the chemical bonds (i.e. single, double, triple bonds), the geometrical arrangement of the atoms involved in the vibration mode, and the mass of the atoms.

The most important methods in vibrational spectroscopy are infrared (IR) and Raman spectroscopy. These methods are often viewed as complementary, as a vibration may be active or forbidden in either the IR or Raman spectrum, depending on the nature of a given vibration (more specifically, the molecular symmetry). A plethora of information can be obtained from vibrational spectroscopy, including the elucidation of molecular structure and determination of concentration. IR and Raman spectroscopy are non-destructive analytical methods, which may also be automatized to obtain spectra in-line and in real time. This is complemented by the time needed to record a typical vibrational spectrum to be in the order of seconds to minutes.[1]

The first report on the existence of IR radiation dates back to 1800 when the astronomer Sir William Herschel described that there was a form of light beyond the visible spectrum that generated heat.[2] However, it wasn't until the 1882 work by Abney and Festing[3] that the first spectrum of molecular vibrations was recorded. The groundwork for IR spectroscopy was laid by the physicist William Coblentz who in 1905 published an atlas of IR absorption spectra containing 120 organic compounds. More sophisticated IR spectrometers were propelled by the

technological advancements realised during World War II, with Perkin-Elmer being the first company to produce a commercial IR spectrometer. Further technological improvements in the following decades such as the introduction of Fourier transformation of interferograms into spectra enhanced the sensitivity, resolution, and ultimately the speed of IR measurements. Digital technology has given rise to increased processing power, increased detector sensitivity, and user accessibility of IR spectroscopy. These advancements have enabled the technique to become widely adopted in the modern age for various types of analysis.

The first spectrum of scattered light that contained frequency-shifted lines was published by Sir Chandrasekhara Venkata Raman, an Indian physicist who would go on to win the 1930 Nobel prize in physics for his discovery of the effect which now bears his name.[4,5] While the basic theory of the Raman effect had been described prior to the first experimental publication, it was slow to be adopted due to being a much more difficult technique compared to IR at the time. The importance of the Raman effect for structure determination as well as for qualitative and quantitative analysis was nevertheless realised in the subsequent years[6,7] and was to be viewed in the community as complementary to IR spectroscopy. The most important advancements in the adoption of Raman spectroscopy were due to the invention of the laser, which provided truly monochromatic light and a much higher power compared to the mercury arcs of yesteryear.[8] Further advancements in instrumentation including but not limited to, the introduction of photomultipliers instead of photographic plates, scanning grating spectrometers instead of prism spectrographs, and charged coupled devices (CCDs) have aided the wide adoption of Raman spectroscopy in the scientific community.

1.1.2. Fundamentals of the Raman effect

Rayleigh scattering of light is the elastic scattering process involving molecules that are significantly smaller than the wavelength of incident light. The light power radiated by a molecular scatterer is given by:

$$P_r \propto \frac{1}{\lambda^4} \qquad (1)$$

where λ is the wavelength of incident light. This process can be used to explain natural phenomena such as the colour of sunrises and sunsets, and it is the most probable scattering outcome of the interaction of light and matter. The significantly less probable outcome is that of inelastic scattering, which is termed Raman scattering. Here, the interaction of a quantum of

light with energy $h\nu_0$ with a molecule modifies the energy by the amount of vibrational energy $h\nu_s$, resulting in the emission of quanta with an energy of $h\nu_0 \pm h\nu_s$. As Most molecules are present in their vibrational ground state at room temperature, as Boltzmann's law states that there is a much smaller population that are present in their vibrational excited state. The population of an excited state according to the Boltzmann law is:

$$\frac{N_{n+1}}{N_n} = \exp\left(-\frac{\Delta E}{k_B T}\right) \quad (2)$$

where N_n is the number of molecules in the vibrational state, ΔE is the energy difference between states, k_B is the Boltzmann constant (1.38065 x10^{-23} J K^{-1}), and T is the temperature (K). This starting condition means that the Raman process where energy is transferred to the molecule and the resulting quantum has a lower energy than the incident quantum ($h\nu_0 - h\nu_{vib}$) is significantly more probable than the counter process. The Raman lines that are produced by the more (less) probable process are termed Stokes (anti-Stokes) lines. When recording a Raman spectrum of a molecule, usually only the Stokes lines are recorded as the anti-Stokes lines are less intense. The inelastic scattering processes are visually summarised in **Figure 1.1.**

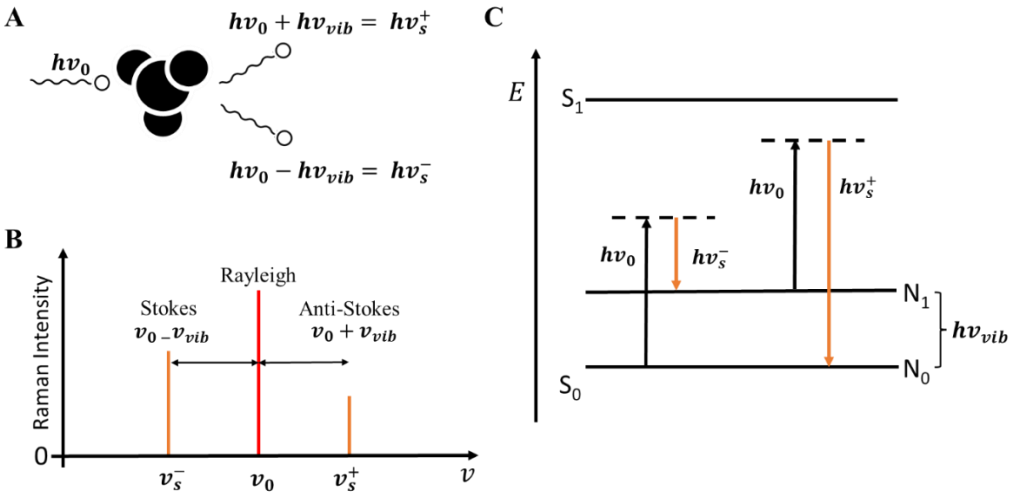

Figure 1.1. *The phenomenon of Raman scattering.* ***[A]*** *A quantum of light $h\nu_0$ hits a molecule where the inelastic scattering results in two possible quanta that have either higher or lower energy than the elastic Rayleigh scattering.* ***[B]*** *The resulting Raman spectrum has two lines that differ by the vibrational energy ν_{vib}; the lower frequency or Stokes line is more intense than the higher frequency anti-Stokes line.* ***[C]*** *The term diagram demonstrates how irradiation of molecules in the vibrational ground state can lead to population of a vibrational excited state where scattered quanta have $h\nu_s^-$ energy. Boltzmann's law states that some molecules are already in the vibrational excited state, and the larger energy quanta $h\nu_s^+$ is also possible.*

The absolute intensity of a Raman line is related to the change in the molecular polarizability of a vibration. If a molecule is placed within an electric field, a dipole moment is induced. This induced dipole moment can be described by the polarizability $\bar{\bar{\alpha}}$, which depends on the mobility of the nuclei and electrons of the molecule. If a fixed Cartesian coordinate system is used, the induced dipole moment $\overrightarrow{\mu'}$ in the electric field with components E_x, E_y, and E_z can be described as:

$$\begin{aligned}\mu'_x &= \alpha_{xx}E_x + \alpha_{xy}E_y + \alpha_{xz}E_z \\ \mu'_y &= \alpha_{yx}E_x + \alpha_{yy}E_y + \alpha_{yz}E_z \\ \mu'_z &= \alpha_{zx}E_x + \alpha_{zy}E_y + \alpha_{zz}E_z\end{aligned} \qquad (3)$$

This can be written in matrix notation as:

$$\begin{bmatrix}\mu'_x \\ \mu'_y \\ \mu'_z\end{bmatrix} = \begin{bmatrix}\alpha_{xx}\alpha_{xy}\alpha_{xz} \\ \alpha_{yx}\alpha_{yy}\alpha_{yz} \\ \alpha_{zx}\alpha_{zy}\alpha_{zz}\end{bmatrix} \cdot \begin{bmatrix}E_x \\ E_y \\ E_z\end{bmatrix}$$

or simply:

$$\overrightarrow{\mu'} = \bar{\bar{\alpha}}\vec{E} \qquad (4)$$

If an oscillating electric field of frequency ν_0 is considered, the induced dipole moment will also oscillate at the frequency ν_0 and emit a quantum of frequency ν_0. This gives rise to Rayleigh scattering. The frequency of internal molecular vibrations ν_{vib} can modulate the induced dipole moment and hence the amplitude of the emitted electromagnetic radiation. This modulation of the emitted radiation at frequency $\nu_0 \pm \nu_{vib}$ results in Raman scattering.

For a molecular vibrational mode to be observable in the Raman spectrum, the following selection rule must be observed:

$$\left(\frac{\delta\bar{\bar{\alpha}}}{\delta q}\right)_0 \neq 0 \qquad (5)$$

that is, there must be a modulation of the molecular polarizability $\bar{\bar{\alpha}}$ by the normal vibration, where q is the normal coordinate describing the atomic motion during the vibration. If this condition is met by symmetry, then the vibrational mode is allowed and said to be Raman active.

In the case where the condition is not met by symmetry, this forbidden mode is Raman inactive. Symmetry is a concept that defines relationships between molecular structures and their associated spectra. In vibrational spectroscopy, the most important take away is the defining of molecular vibrations by their characteristic symmetry species and their activity in IR or Raman spectroscopy. An in-depth description of group theory will not be discussed, and can be found elsewhere in the literature.[9]

If a very high intensity excitation is used, the induced dipole moment (**Eq. (3)**) can show non-negligible high-order terms beyond the linear approximation and, in simplified notations, it can be written as:

$$\mu' = \alpha E + \frac{1}{2}\beta E^2 + \frac{1}{6}\gamma E^3 + \cdots \qquad (6)$$

These non-linear effects result in experimental methods and phenomena such as hyper Raman scattering[10] and Coherent anti-Stokes Raman spectroscopy (CARS).[11]

1.1.3. Enhancement of Raman scattering

Spontaneous Raman scattering which has been described up until this point, produces very weak signals that can be a million times lower than the elastic scattered light, Rayleigh scattering. This limits the application of Raman spectroscopy to good Raman scatterers, and high concentration samples. However, the signal produced by the Raman effect can be successfully and greatly enhanced by two techniques. Resonance Raman spectroscopy (RRS) utilises the electronic absorption of molecules, while surface enhanced Raman spectroscopy (SERS) makes use of plasmonic metal nanoparticles that influence the fundamental process of Raman scattering. The combination of these two techniques is also possible in surface enhance resonance Raman spectroscopy (SERRS). In any case, the instrumentation largely remains the same with regular Raman spectrometers being used to record spectra. The main difference lies in the specialised sample techniques and the excitation conditions.

1.1.4. Resonance Raman Spectroscopy

If the frequency of the incident excitation radiation is similar to that of the dipole-allowed electronic transitions of an investigated molecule, the resonance Raman effect can be observed. Specifically, if the excitation frequency lies within the observable vibrational structure, the rigorous resonance Raman effect (RRE) takes place. On the contrary, the pre-resonance Raman effect (pre-RRE) is observed when the excitation frequency lies on the fringes of the vibrational structure. An intensity enhancement up to 10^6 is possible with RRS due to the strong coupling between the electronic excited state and the totally symmetric vibrational modes of the molecule. The technique permits the investigation of both vibrational and electronic properties of a molecule simultaneously, which is especially useful in the Raman band assignment of biological chromophores. Even at low concentrations (10^{-3} – 10^{-5} M) RRS has been employed to study biological systems tagged with dyes, which eliminated the issue of intermolecular interactions between investigated molecules as seen at higher concentrations. This technique of using resonance Raman labels is useful for the chemical investigation of ligand-active-site interactions, resulting in vibrational spectra of biologically active molecules *in situ*.[12]

Resonant Raman spectra can be conveniently obtained using standard Raman spectrometers, given appropriate excitation lasers are used. The main caveats of RRS are the need of elimination of photodegradation.

1.2. Surface-Enhanced Raman Scattering (SERS)

Conventional Raman spectroscopy struggles to probe thin layers due to the inherent weakness of the Raman effect. However, the reinterpretation of initial experiments[13] of the absorption of pyridine on roughened silver in the 1970s demonstrated the powerful enhancement of the SERS effect. It was realised that compared to the pyridine molecule in pure liquid the Raman scattering cross-section was enhanced by 10^4 – 10^6 per molecule when absorbed on the rough silver electrode.[14] The theoretical understanding of the SERS effect is still incomplete, but surface enhancement has been proven to originate from two main processes: the electromagnetic enhancement mechanism (EM) and the chemical enhancement mechanism (CM).

1.2.1. Electromagnetic field enhancement

In brief, molecules in close proximity to metal particles experience a localized enhanced electromagnetic field compared to that of the incident radiation. For the molecule, this enhancement depends on the distance from the metal as well as its orientation with respect to the normal of the surface. The enhancement factor (EF) due to the EM can be written as:[15]

$$EF_{EM} = |E(\omega)|^2 |E(\omega')|^2 \quad (7)$$

where $E(\omega)$ is the frequency-dependent electric field enhancement at incident frequency ω, and $E(\omega')$ is the frequency-dependent electric field enhancement at the Stokes shifted frequency ω', with the field enhancement being the ratio of localized and incident electric fields. As the Stokes shift is small relative to the laser wavelength, this can be further approximated and simplified to:

$$EF_{EM} = |E(\omega)|^4 \quad (8)$$

The EM is typically the largest contributor in SERS, which results in enhancements between $10^4 - 10^8$.[15] The electronic properties of the metal, its shape and size, in addition to the energy of the incident beam, are also factors influencing the enhancement of the electromagnetic field. Rough surfaces or nanoparticles (NPs) of metals are used in SERS, as the conduction electrons in the metal can be excited by incident laser light to produce a plasmon resonance. This resonance polarises the NP as a dipole causing the interior electromagnetic field to become substantially larger than the applied field. This intense field decays rapidly by following nearly a $1/r^3$ law with the distance from the NP surface, which makes SERS a highly surface-sensitive technique.

Figure 1.2 demonstrates a model SERS substrate as a metallic sphere that is smaller than the incident wavelength. Irradiation of the NP with laser light induces a displacement of the conduction electrons, which in turn generates an oscillating dipole. This dipole produces a secondary electromagnetic field, which along with the incident field, makes up the oscillating field at the NP surface. This collective oscillation of electrons (or plasma oscillation) in phase can be excited at a specific resonance frequency termed localised surface plasmon resonance (LSPR), where plasmons are quasi-particles associated with collective electron oscillations in (nanostructured or bulk) metals. The LSPR is determined by the shape, size, and type of metal,

of which noble metals such as gold and silver resonate in the visible or near-IR spectral region. Light excitation at the LSPR frequency produces a large induced dipole, leading to enhanced secondary electric field at the NP surface. This effect typically occurs in noble metal NPs that are between 10 – 200 nm in diameter. Any analyte nearby the enhanced electric field will thus exhibit an increased Raman signature by SERS effect. It is appropriate to note here that the light excitation of thin but smooth noble metal films can produce propagating plasmons called surface plasmon polaritons (SPP). These propagating plasmons have a large spatial range normal to the plane of propagation (ca. 1000 nm) and have smaller field enhancements compared to their localised counterparts.[16] SPPs are utilised in the surface analysis technique surface plasmon resonance (SPR)[17] and not of direct interest to this body of work, and henceforth any mention of plasmons will be referring to LSPRs.

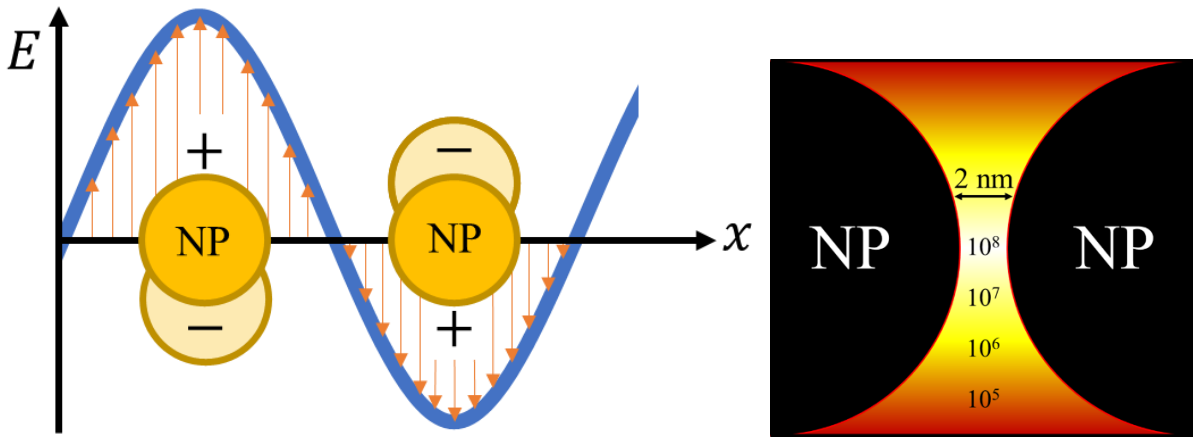

Figure 1.2. (Left) *Electromagnetic enhancement of gold nanoparticles (NP) whose radius is smaller than the wavelength of an oscillating electromagnetic field. Excitation at the plasma resonance frequency generates a high electric field on the surface of the NP.* ***(Right)*** *"Hotspot" where the electromagnetic field confined between two NP in very close proximity giving rise to very high enhancement factors.*

1.2.2. Chemical enhancement mechanism

The second component of the Raman effect that can be enhanced due to the electronic interaction between the metal NP and the analyte is the polarizability $\bar{\bar{\alpha}}$. Charge transfer (CT) from the metal to the analyte can increase the apparent value of $\bar{\bar{\alpha}}$ components via the mechanism detailed in **Figure 1.3**. A molecule with discrete, filled π and empty π* orbitals is displayed on the left next to the continuous levels of the metal conduction band. The conduction band is assumed to have a constant density of states p_0 and ranges between *A* and *B*. These levels are filled up to the Fermi level *F*, where the remaining unfilled levels are depicted by the

dashed lines. The metal-to-molecule charge transfer transition μ_{FK} is allowed by borrowing charge transfer intensity from the allowed transition μ_{IK} via the Herzberg-Teller vibronic coupling h_{IF}. This type of coupling modifies the electronic transition selection rules by including the influence of vibrational modes of the molecule which can allow certain transitions that would otherwise be forbidden by pure electronic selection rules.[18,19] The one-electron charge transfer transitions from the Fermi or lower metal levels to the empty π* orbitals have large oscillator strengths and correspond to photons in the visible range. If the incident light has a frequency that matches the charge transfer band, this increases the polarizability of the molecule at the metal surface and the metal-molecule complex becomes a resonant Raman scatterer. Both CT and resonance Raman scattering (RRS) are accepted as the main contributing factors to the CM, each having enhancements between $10 - 10^7$ and $10^3 - 10^4$ respectively. In addition to the CT and RRS, the non-resonant chemical mechanism (CHEM) results in a small contribution to enhancement, in the order of 10^2 or less.[15] CHEM stems from relaxation of the electronic structure of the molecule in the ground-state as it is initially placed onto the metal surface.

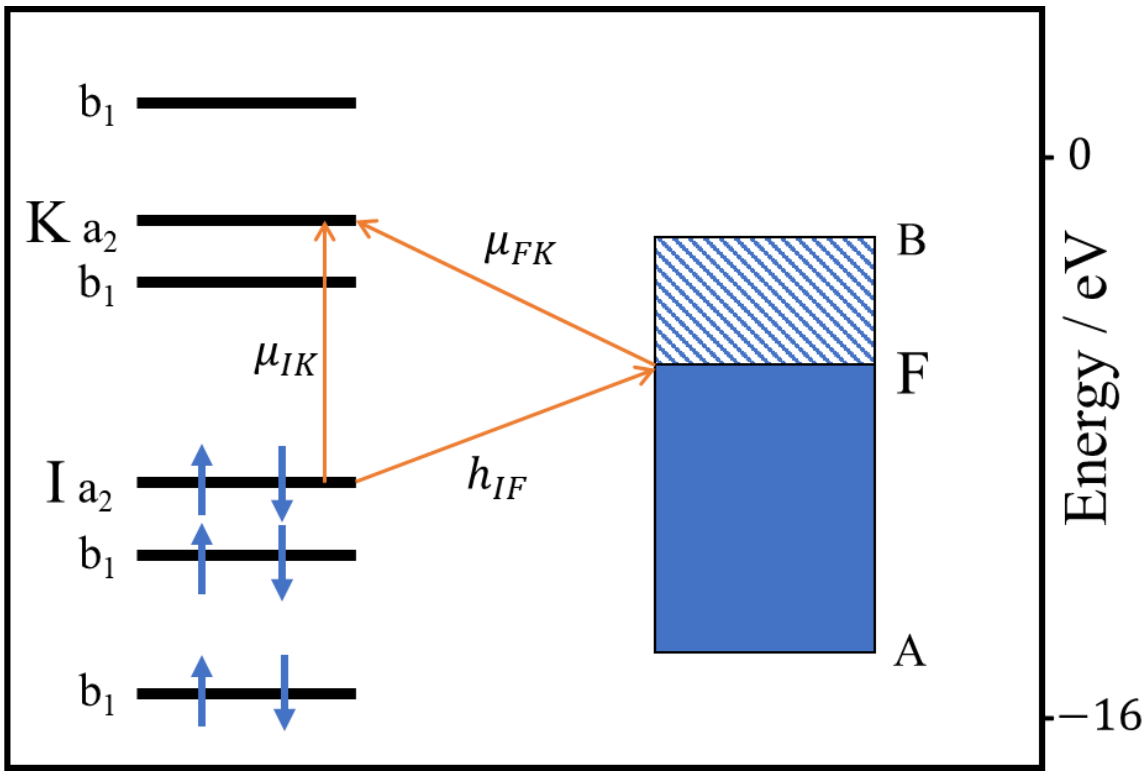

Figure 1.3. *Energy level state diagram for a molecule-metal system. The molecular ground state (I) and excited states (K) have an allowed transition through μ_{IK}. The metal→molecule charge transition from the Fermi state (F) is allowed through μ_{FK}, where the Herzberg-Teller vibronic coupling term h_{IF} connects the states molecular ground state I and the metal Fermi state F. Figure adapted from Lombardi et al. (1986).*[19]

1.3. Tip-Enhanced Raman Spectroscopy (TERS)

The need to characterise materials and molecules with high spatial resolution brought about the invention of scanning near-field optical microscopy (SNOM) in 1984.[20] SNOM is effectively the coupling between an optical system and a scanning probe microscope. Depending on the probe used, SNOM can be further classified as "a-SNOM" or "al-SNOM". A-SNOM (aperture-SNOM) uses a perforated tip with an aperture diameter greater than 50 nm, while al-SNOM (apertureless-SNOM) feature a probe tip without an opening. The coupling of a-SNOM with fluorescence spectroscopy quickly dominated the field, largely due to the high fluorescence emission selection making single molecule detection possible.[21,22] Using a 514.5 nm laser excitation source, a-SNOM was used to detect the SERS signature of rhodamine 6G molecules on silver.[23] However, a-SNOM was proven ineffective at probing non-resonant Raman scatterers as the low laser power at the perforated tip was in the order of nanowatts. On the other hand, the proposed use of al-SNOM for Raman characterisation at the nanoscale lead to the development of tip-enhanced Raman spectroscopy (TERS).

The first proposal of the tip enhancement effect was made in 2000[24–27] and is arguably one of the greatest breakthroughs in the field of Raman spectroscopic analysis. The potential of TERS was quickly realised in the proceeding years, as TERS allows for nanoscale chemical imaging with high enhancement factors. In comparison to SERS, the application of TERS in fields such as electrochemistry, heterogenous catalysis, and biology is not limited by the requirement to perform the experiment on a nanostructured metal surface.[16] This is made possible by incorporating the enhancing unit as an external source allowing for enhanced Raman spectra to be measured on any molecule on any surface. TERS couples Raman spectroscopy with a scanning probe microscopy (SPM) tip that is made from, or has been coated with, a noble metal. Irradiation of the metal SPM tip with an appropriate laser light effectively excites the tip LSPR, producing electromagnetic enhancement at the tip apex, which increases in turn the Raman scattering of any analyte molecules in close proximity to the tip. Such metallised tips of silver or gold were quickly demonstrated to have effective enhancement factors in the order of $10^3 – 10^6$.[28,29]

The coupling of Raman spectroscopy with a metallised SPM tip not only provides high sensitivity and a wealth of chemical information, but nanometre scale spatial optical resolution (SOR) can be achieved thanks to the SPM technique. Optical microscopy is said to be diffraction limited, where the smallest resolvable distance (d) between two objects is limited approximately to half the wavelength (λ) of illumination light used:

$$d \approx \frac{\lambda}{2NA} \quad (9)$$

where $n\ sin\theta$ is the numerical aperture (NA) of the microscope objective. As SPM images are obtained by raster scanning the sample using a physical probe, the lateral spatial resolution is only dependent on the radius of curvature (ROC) of the SPM tip, provided that the pixel size is small enough not to add an additional pixelization effect. The axial resolution is dependent on the resolution of the vertical scanner movement (< 1 Å), the number of data points in the vertical z-direction, and on the AFM noise that arises from mechanical, electronic, and acoustic sources. In TERS, the SOR is directly related to the size of the noble metal structures enhancing and confining the electromagnetic field at the tip apex, thus allowing the diffraction limit to be overcome and SOR down to the angstrom scale to be reached.[31]

1.3.1. Enhancement mechanisms in TERS

In TERS, a strong and localised electromagnetic field is generated at the extremity of a sharp metal tip.[30] In fact, for any tapered metal structure there are three main contributions to this field enhancement. One of these is the "lightning rod" effect, which refers to the spatial confinement of electric charges on a metal surface due to the geometric structure. Essentially in this electrostatic phenomenon, non-resonant incident light that is polarised parallel to the tip axis (*p* component) induces a higher surface charge density at the tip apex. This effect is dependent on the conductivity of the material, which typically increases from the visible to the IR spectral range. As previously discussed for SERS, the shape and dielectric properties of metal particles lead to surface plasmon resonances and give rise to characteristic extinction spectra. Additionally, if the length of the metal structure is a multiple of half an effective wavelength depending on the wavelength of the incident radiation as well as the geometry and the dielectric properties of the structure,[32] the "nano-antenna" effect also contributes. This effect allows for the interconversion of local and propagative electromagnetic fields under resonant light excitation.[31] Both plasmon and nano-antenna resonances are tuneable in the visible spectral range as these two effects have distinct wavelength dependencies.[32] Together, the plasmonic, "lightning-rod", and "nano-antenna" effects result in a nanoscale "hotspot" below the tip, allowing for the detection of the enhanced Raman signal.[30–32]

1.3.2. TERS enhancement in the gap-mode configuration

Like in SERS, in TERS, the intensity of the excitation electromagnetic field decays rapidly with the distance to the tip apex. Furthermore, the enhanced Raman signal of the sample is evanescent, and thus decreases exponentially with the distance.[32] Since the metal tip behaves as a nano-antenna, it can convert this intense near-field signal into a far-field signal able to be detected, when placed at nanoscale distance to the sample. TERS is thus a surface-sensitive technique, ideal to probe analytes of nanoscale thicknesses (typically below 10 nm). However, the TERS signal is also drastically dependent on the Raman scattering cross section of the excited molecules, and the enhancement of the tip alone may not be sufficient to probe molecular monolayers. One method to improve the TERS signal uses a combination of a conductive metal substrate and a TERS-active tip. Many such metals have been tested for this purpose, but noble metal ones, and especially gold, have been found to be the most efficient.[33] If a TERS tip is engaged on a noble metal substrate there is a huge field enhancement within this "gap", and the Raman scattering of any molecule within this space is greatly enhanced.[34] This gap-mode TERS configuration stems from the theoretical basis of simulations of two NPs in close proximity to one another (**Figure 1.2**, right-hand side).[35] When the tip-sample distance falls below 1 – 2 nm typically, charges mirroring those at the tip end accumulate at the surface of the substrate. This creates a dipole image of the one induced at the tip apex by resonant laser light excitation. The degree of gap-mode enhancement also depends on the polarisation of the excitation light, as well as the shape and size of metal nanostructures at the tip apex. Accordingly, the ideal laser excitation wavelength in gap-mode configuration can be different from the optimal wavelength in a non-gap-mode one.

1.3.3. STM-TERS

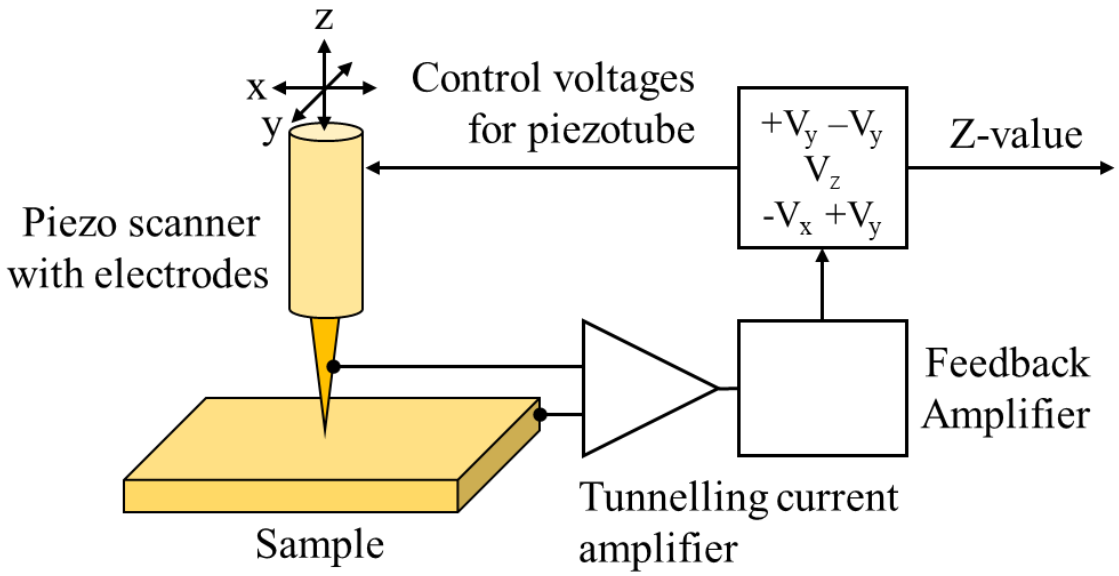

Figure 1.4. *STM feedback schematic. The feedback loop maintains a constant tunnelling current by adjusting the control voltages of the piezotube modulating the tip-sample distance. Adapted from Shah (2019).*[36]

The first scanning probe microscope was the scanning tunnelling microscope (STM) which won Binning and Rohrer the 1986 Nobel prize in physics for its invention.[37] In STM, a very sharp metal tip is brought into close proximity (< 2 nm) to a conducting surface and an applied electrical voltage generates a tunnelling current between the sample and the tip (**Figure 1.4**). The tip is raster scanned over the surface and the tunnelling current maintained by a feedback loop which adjusts the tip-to-sample distance. This tunnelling current is a result of the quantum mechanical effect where electrons can pass through classically impermeable barriers that are sufficiently thin. For STM, this barrier is the gap between the tip and the sample. The electron movement from the sample to the tip (or vice versa depending on the set-up) can be read out as the tunnelling current. STM imaging can be performed in two modes: constant current and constant height mode. In constant current mode, the topography of the sample is measured using constant tunnelling current as the tip-sample distance is adjusted in real time. If the sample is very smooth, then the constant height mode can be applied, where the tip is kept at a constant height from the surface and the tunnelling current is measured at different positions on the surface. The exponential relation between the tunnelling current and the distance of the tip to the sample surface results in a very high spatial resolution down to the single-molecule level. However, as STM requires an electric circuit, the technique is limited by the need for a

conducting sample. Additionally, STM is often performed in a vacuum and therefore its applications to biological samples are narrowed.

The coupling of STM with TERS allows for the study of surface properties and molecular structure with high spatial and spectral resolution. The integration of a Raman spectrometer (and the accompanying laser excitation source) with the STM system allows for the enhancement of Raman signals thanks to the metallic STM tip. While STM-TERS can provide atomic resolution and high enhancements due to the gap-mode effect,[38] the combination and alignment of the two systems is complex. The need for conductive or semi-conductive samples is a major limiting factor for the technique, especially for its application with biomolecules.

1.3.4. AFM-TERS

Building on the principles of STM, Binnig, Quate, and Gerber invented the first atomic force microscope in 1986.[40] Rather than the tunnelling current used in STM, atomic force microscopy (AFM) maintains the tip-sample distance of a silicon cantilever using a feedback system that measures the deflection of an IR laser off of the cantilever on a quadrant photodiode. The typical AFM system consists of the aforementioned feedback system, an optical lever system, a position sensitive photodetector (quadrant photodiode), a piezoelectric scanner, and the AFM tip and cantilever (see **Figure 1.5**).

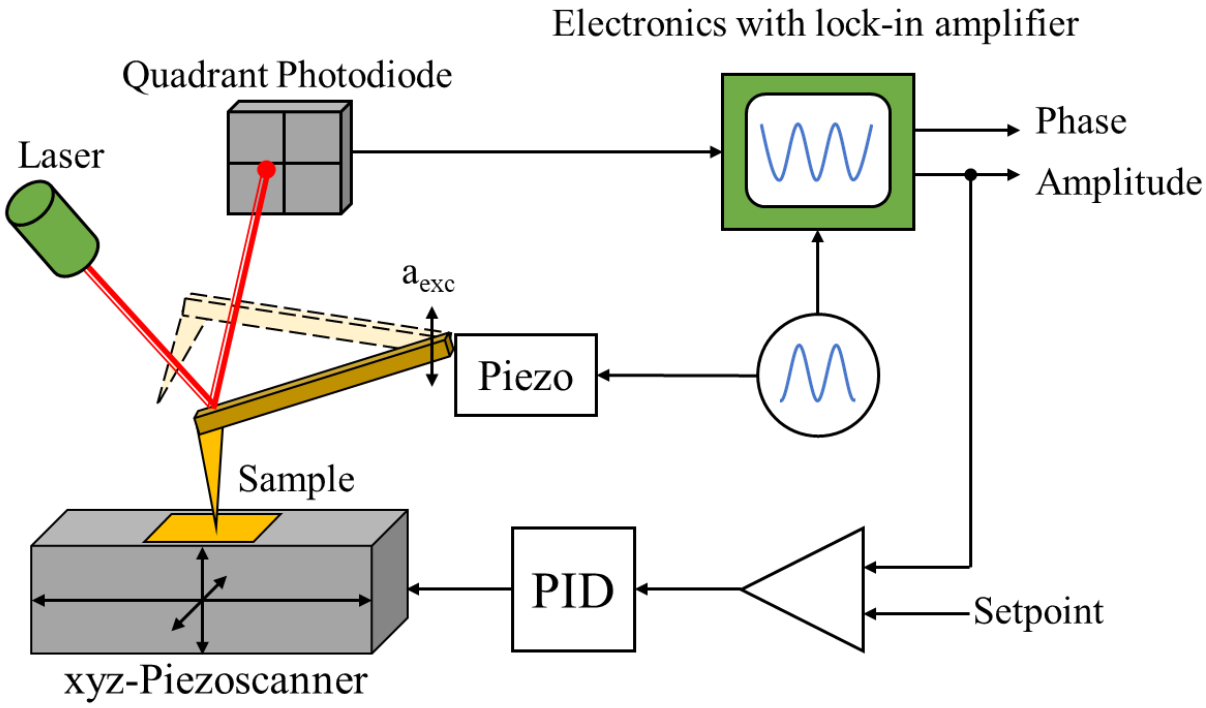

Figure 1.5. *AFM feedback schematic for amplitude modulation (tapping) mode. A quadrant photodiode measures the deflected IR laser from the backside of the cantilever. This signal is sent to a lock-in amplifier that compares the driving frequency supplied by the cantilever excitation piezo with its measured oscillation. The amplitude signal is maintained constant and used in the feedback loop that controls the cantilever-sample distance via the stage xyz-piezoscanner. Adapted from Maghsoudy-Louyeh et al. (2018).*[40]

The interaction between the tip and the sample is fundamental to the AFM operation, and is analogous to the bonding forces between two atoms. Specifically, van der Waals forces make up the attractive forces and electrostatic forces are the repulsive forces, with the sum being the total force the tip exerts on the sample in contact mode operation (10^{-8} – 10^{-6} N).[41] The AFM base support chip, cantilever, and tip are typically made from doped silicon or silicon nitride via nanofabrication methods and can be coated or functionalised with various metals or materials depending on their intended application. For example, reflective gold coatings make the tip conductive and electrical properties of a sample can be mapped.[42] Such gold coatings are also useful to improve the AFM laser reflection and detection, which is necessary when working in liquid environments due to the IR laser absorption by water. AFM cantilevers are flexible beams that are either rectangular (diving board) or triangular and have various spring constants, depending on their length, material, and desired application. For example, AFM indentation measurements require very high forces and range from 100 – 1000 N/m. On the contrary soft specimens, such as biological samples, are often probed with 1 N/m down to 0.01

N/m. The spring constant k (N/m) and the effective mass of the probe m (kg) are related to the probe resonance frequency f_0 (Hz) by the following relationship:

$$f_0 = \frac{1}{2\pi}\sqrt{\frac{k}{m}} \quad (10)$$

As a rule of thumb, a higher spring constant or lower effective mass gives rise to higher resonance frequencies, and *vice versa*. For imaging softer samples such as biomolecules, lower resonant frequency tips typically have low spring constants and/or high effective masses. When considering TERS coupling to AFM systems, the addition of plasmonic metal coatings increases the effective mass of the probe which leads to lower resonant frequencies compared to an uncoated tip.

The monitoring system for the tip deflection involves a focused laser beam onto the end of the cantilever which is reflected and hits a quadrant photodetector. The photodiode can detect differences in the laser spot position reflecting height variations down to the atomic level. It functions by generating a signal from the difference between the two top segments and the two bottom segments which reflects the vertical motion of the tip. The lateral and torsional motion of the tip is measured from the difference between the two left and two right quadrant segments.[39]

The scanner head features all the elements needed for image measurement, and contains the deflection sensor which monitors cantilever deflection via an IR laser. The xyz-scanner controls the cantilever position relative to the sample, and maintains constant deflection by positioning the stage up or down to match the surface topography. The deflection signals sent from the deflection sensor are compared to a reference signal which produces an error signal. With this input a feedback signal is generated and is transferred to the xyz-scanner compensating for the measured error, thus maintaining constant tip force or cantilever deflection depending on the mode of operation. Additional signal processing modules include lock-in amplifiers and phase-locked loops which are necessary for more advanced imaging modes. To ensure good tracking, the proportional-integral-derivative (PID) controller gains need to be optimised during experiments.[42]

The AFM system can be operated in various modes depending on the sample compatibility and desired sample information to be gained. Broadly, there are contact modes and dynamic modes, with the combination of modes being referred to as hybrid modes. In

contact AFM, the tip interacts directly with the sample and the cantilever deflection is measured straight from this tip-sample interaction. Surface roughness can be measured in contact mode via the lateral force applied to the tip during scanning. If a biased sample and a conductive AFM probe are used in contact mode, the sample voltage, current, conductance, capacitance, and resistance can be obtained. The corresponding modes are termed scanning voltage microscopy (SVM), scanning microwave microscopy (SMM), photoconductive/conductive atomic force microscopy (PC/CAFM), scanning capacitance microscopy (SCM), and scanning spreading resistance microscopy (SSRM). If the AFM tip features a temperature-sensitive filament, then the sample temperature can also be measured through scanning thermal microscopy (SThM).[42]

Dynamic mode AFM can be further subdivided into "tapping mode" and "non-contact" modes, which have a subtle difference of whether the tip-sample interaction force is within the repulsive or attractive region of the Lennard-Jones potential.[42] In any case, a piezo acoustically excites the AFM probe resonance frequency which generates a sinusoidal cantilever deflection. Contrast maps are subsequently generated from the regulation of the cantilever amplitude, phase, or frequency. Other non-contact modes include Electrostatic Force Microscopy (EFM), Magnetic Force Microscopy (MFM), and Kelvin Probe Force Microscopy (KPFM), which measure the electrostatic force, magnetic force, or surface potential respectively.

AFM can be seen as more versatile technique than STM as it can be performed on any surface, in high vacuum, ambient air, or even liquid environments including buffer solutions. For these reasons, AFM-TERS is becoming the standard coupling within the TERS community, except for investigations on ultra-high (angstrom-scale) resolution TERS.[31] This is even more prevalent for TERS studies of biomolecules in native environments as well as requiring the use of biocompatible substrates. Nevertheless, AFM is limited in its relatively slow imaging speed due to the line-for-line process of raster scanning the AFM tip across the sample surface. More recently high-speed AFM (HSAFM) imaging has partially alleviated this issue, however at the cost of a smaller imaging area. Especially when imaging fragile biological samples, care is needed in selecting the correct imaging mode (tapping mode) and tuning of parameters to ensure good quality imaging. AFM in its pure state can provide topographical and mechanical information about a sample, but cannot capture spectroscopic information which contains complementary information about the studied system. While sophisticated in nature, electromagnetic wave emission and detection sources have been successfully coupled with AFM systems and have even progressed into commercially available instruments.

1.3.5. Optical Coupling

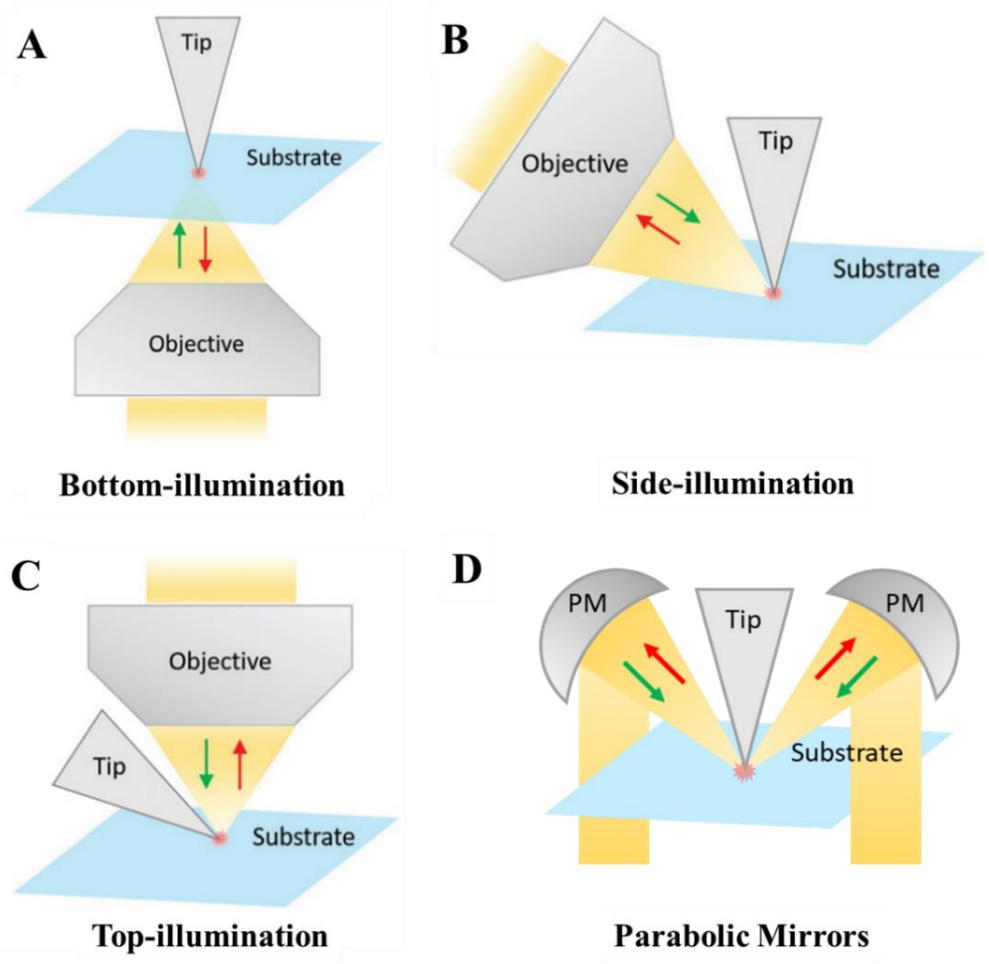

2.

Figure 1.6. *Laser-probe optical coupling configurations for TERS instruments.* ***[A]*** *Bottom-illumination,* ***[B]*** *side-illumination,* ***[C]*** *top-illumination, and* ***[D]*** *top with parabolic mirrors. Green arrows indicate excitation light and red arrows indicate scattered light. Adapted from Bonhommeau et al. (2022).*[31]

There are three main optical configurations used in the laser-probe coupling of SPM with a Raman spectrometer. The main difference between the configurations is the illumination conditions of the TERS tip, but there are also certain limitations depending on the geometry used. One of the most popular geometries is the bottom-illumination configuration shown in **Figure 1.6A**. A high numerical aperture objective (NA ≥ 1.4) is used to tightly focus linearly or radially polarised laser light onto the tip end, with the backscattered light being efficiently collected through the same lens. This configuration provides a high signal-to-noise ratio and convenient for alignment of laser beam with the extremity of the tip apex. As the laser light must penetrate the substrate in order to excite the TERS tip, the bottom-illumination configuration is largely limited to optically transparent samples.[31] Recently, our group has

developed a total-internal reflection (TIR)-TERS system[43,44] which is analogous to the bottom-illumination configuration. This system will be described in detail later in **Chapter 2**.

If optically opaque samples are desired to be studied using TERS, then either the side-illumination or top-illumination configurations should be used. For the case of side-illumination systems (**Figure 1.6B**), a long working-distance objective with relatively low NA (≤ 0.7) is used to focus linearly polarised laser light onto the tip apex. Due to the angle of incidence, the laser spot is enlarged by a few microns and is asymmetric with respect to the tip axis. This results in typically lower laser fluence, which can be offset by increasing the laser power output to a few mW. Care is needed with higher laser powers, especially when investigating delicate biological samples, as these could induce sample degradation. The fine alignment of the laser spot on the TERS tip end is not a trivial task in side-illumination. Ideally, two objective piezo scanners are used to map the scattering of the tip with the maximum scattered signal being the desired "hotspot".[31] Top-illumination configurations (**Figure 1.6C**) attempt to combine the advantages of both bottom- and side-illumination. In comparison with side-illumination, a tighter symmetrical laser focusing can be achieved using intermediate NA objectives ($NA \leq 1.0$). Despite this improvement over side-illumination, the main issue with top-illumination is the "shadowing effect". Essentially, the tip is located between the objective and the laser focal point which reduces the amount of excitation photons as well as the intensity of the collected signal.[31] This effect can be minimised if high NA objectives are used, or alternatively parabolic mirrors (PMs).[45]

PMs are well-suited for applications in confocal microscopy as the sample is imaged point-by-point, ensuring the mirror stays aligned with respect to the incident beam. This reduces aberrations typically seen in other forms of imaging with PMs that arise from deviations from parallelism from the optical axis or the incoming beam.[46] It has been demonstrated that a radially cylindrical laser beam focused with PMs is the optimal configuration for TERS. The incident beam path comes from below and is focused onto the tip at the sample surface via reflection from PMs (**Figure 1.6D**). This set-up results in a significantly stronger z-component of the electric field (parallel with the tip axis) when compared to an objective lens.[46]

2.1. TERS of biomolecules and biomaterials

Spectroscopic techniques including (but not limited to) fluorescence, IR, and Raman, have been widely used to characterise biomolecular structure, conformation, and chemical composition. While fluorescence imaging is a popular technique in biomedical imaging in particular, the need for a fluorescent tag to be attached to the molecule of interest is undesirable when studying native state biomolecules. The advantage of IR and Raman vibrational spectroscopy is their label-free characterisation. However, they are not without their drawbacks. Specifically, the previously discussed selection rules of IR and Raman results in the appearance or lack-of certain vibrational modes in their respective spectra. IR has been traditionally preferred over Raman when investigating biomolecules, but the intense contribution of H_2O modes in IR spectra complicate their interpretation in aqueous media. For example, the amide I (1600 – 1700 cm^{-1}) and amide II (1500 – 1580 cm^{-1}) bands that are important for studying protein secondary and tertiary structure can often be obscured by the H_2O scissoring vibration in the 1500-1700 cm^{-1} spectral region. The quasi-suppression of these H_2O modes in Raman spectra make the technique initially desirable for the study of biomolecules but unfortunately, the Raman scattering cross-section is typically 8 orders of magnitude lower than the IR absorption cross-section. This drawback is even more apparent when studying biosystems on the nanoscale where only weak Raman signals are obtained from irradiation of small sample quantities. For this purpose, near-field optical spectroscopy such as TERS has been developed.

In TERS, the nanoscale imaging capabilities of SPM techniques (AFM or STM) is combined with the chemical sensitivity of SERS.[31,47] The enhanced Raman signal originating from the nanoscale “hotspot” below the tip in a single-point measurement is not reflective of large heterogenous samples. Therefore, TERS imaging can be used to build up the chemical and structural map in nanoscale steps. Both single-point measurements and imaging have been successfully utilised in the characterisation of biomolecules and biosystems such as nucleic acids, proteins and peptides, lipid membranes, and even whole cells such as bacteria and viruses.

2.1.1. Characterisation of DNA and RNA using TERS

The first biopolymers to be investigated using TERS were nucleobases of deoxyribonucleic acid (DNA), specifically adenine due to its high Raman cross-section.[47,48] DNA is the primary genetic macromolecule that is encoded with either pyrimidine (cytosine C, and thymine T) or purine (adenine A and guanine G) bases attached to a deoxyribose-phosphate backbone. Ribonucleic acid (RNA) is the related ribose-phosphate macromolecule that features uracil U instead of thymine in its sequences. RNA has several roles: coding protein synthesis as messenger RNA (mRNA), helping decode mRNA as transfer RNA (tRNA), and non-coding ribosomal RNA (rRNA). Both DNA and RNA can take different structures, such as single-stranded (ss) and double-stranded (ds). Moreover, dsDNA adopts one of three double-helix conformations termed the A-form, B-form, and Z-form. The native right-handed B-form is present at neutral pH and physiological conditions. The A-form is typically thicker than B-form DNA due to the shortened distance between base pairs as a result of dehydration of the macromolecule.[49] Z-form is very different from the other two due to its left-handed double helical structure forming under high-salt conditions.[50] The importance and ubiquity of these macromolecules in living creatures sparked the interest in the TERS community to characterise their conformation and composition with nanoscale resolution.

Using Ag-coated AFM tips, Watanabe *et al.* (2004) successfully assigned vibrational modes in nanocrystals of adenine, where the characteristic in-plane ring breathing mode (ca. 736 cm^{-1}) and in-plane combination vibrations of C-H, N-H, C-N (ca. 1330 cm^{-1}) were the most intense.[28,51] While the TERS bands were shifted with respect to their Raman and SERS counterparts, this discrepancy was explained using density functional theory (DFT) calculations which suggested a tip-induced pressure effect of silver atoms on the adenine molecule.[28] The following 2006 work by Hayazawa *et al.* demonstrated the formation of silver-adenine isomers from the interaction of the silver atoms of the TERS tip, which led to additional vibrational modes in the adenine TERS spectra. This demonstrated the sensitivity of TERS to be atomically site-selective.[52] Continuing their investigation on adenine, Ichimura *et. al* (2007) investigated the temporal fluctuation of the adenine TERS signal. It was noted that both peak frequencies and intensities fluctuated, and reasoned to be due to the changes in the adenine molecular orientation under the TERS tip. Theoretical calculations were used to support the experimental findings that different polarisation conditions i.e. adsorption angles and sites of the adenine molecule alter the frequency and intensity of Raman peaks.[53] This study not only demonstrated the potential for TERS for single-molecule sensitivity, but defined important tip-sample

phenomena that make up a TERS spectrum. Other DNA nucleobases, specifically the pyrimidine bases cytosine and thymine, were subsequently explored in the TERS community. The 2006 study by Rasmussen and Deckert featured the collection and comparison of SERS and TERS spectra of the two pyrimidine nucleobases with conventional Raman. It was argued that TERS can provide high spatial resolution without significantly altering the structure of complex biological molecules such as DNA or their spectral features due to the enhancement mechanism.[54] Picomole quantities of adenine, guanine, thymine, and cytosine adsorbed onto atomically smooth gold surfaces were investigated by Domke, Zhang, and Pettinger (2007) using STM-TERS. Not only was the detection limit of TERS of non-resonant biological species proven, but detailed chemical and topographical information could be obtained. In particular, the STM images of a thymine monolayer showed surface lattice arrangements and specific metal-analyte bonds in the 220-250 cm^{-1} region could be observed in the TERS spectra.[55] This work was followed by the 2010 paper that explored the hydrogen bonding in DNA base pairing using TERS. Specifically, adenine-thymine base pairs had different orientation on the surface and different Raman spectra compared to the individual adenine and thymine molecules. The effect of pH was shown to influence the base pairing, as protonation of thymine and deprotonation of adenine enhanced hydrogen bonding.[56] These studies proved TERS effectiveness in probing DNA molecular interaction and dynamics on surfaces at the nanoscale.

The first notable application of TERS to RNA was to assess the technique's ability to perform direct sequencing of RNA strands. Bailo and Deckert used polycytosine (polyC) RNA, demonstrating the detection of a single cytosine molecules with distinguishable spectral features. The potential for TERS as a future method for sequencing was argued by the acquisition of stable spectra at different positions on the RNA homopolymer strand.[57] This work was followed-up with a similar study on polyadenine (polyA) and polyuracil (polyU), confirming the technique's reproducibility. A noteworthy observation of this study is the effect of the substrate on the immobilisation of the homopolymer. Specifically, there was minimal contribution from the phosphate backbone in TERS spectra on gold surfaces, which indicated that the RNA molecule binds via the backbone structure. This was not the case for mica, in which the investigated calf thymus DNA had spectral variations that suggested different orientations of the nucleobases.[48] Calf thymus DNA Raman signals shared by the nucleobases could be distinguished from specific bands of the deoxyribose units and phosphate backbone of distinct bases.[48,58]

The technique of DNA combing was used by Najjar *et al.* to immobilise and orient dsDNA on a silane-functionalised borosilicate glass slide before being probed using TERS.[59]

An AFM tip covered in an Ag/Au bilayer allowed for the characterisation of OPO groups of the dsDNA backbone which were not observed in ssDNA. This work demonstrated TERS capability to probe DNA structures that are finely organised. Subsequently, TERS was used to compare plasmid-free and plasmid-embedded DNA.[60] Plasmids are physically separate DNA that carry additional genes to the essential genes of chromosomal DNA. TERS was shown to be a useful tool for studying DNA properties in local nanoscale environments, as the plasmid-embedded DNA featured additional Raman bands that originate from the plasmid. Additionally, key vibrational modes of the individual nucleobases, the phosphate backbone, and deoxyribose sugar could be identified with SOR down to 8 nm.[60]

As previously mentioned, DNA can adopt various conformations depending on the environmental conditions such as hydration and pH. TERS was first employed to study short DNA fragments of different conformations in the 2016 paper by Japaridze *et. al*.[61] It was found that DNA deposited on mica with divalent cations (Mg^{2+} or Mn^{2+}) showed partial transition from the B-form to the A-form, with a 20% shorter length. This contrasts with the silane-functionalised mica (APTES) which retained the B-form of the deposited DNA. Interestingly, TERS was able to localise the B-to-A transition as being more likely to occur at the DNA ends. TERS thus helped identify key factors in conformational changes of DNA, which is especially relevant for DNA-based templates and nanostructures. The need for standardisation of TERS sample preparation was emphasized in the group's follow-up paper, which scrutinized the use of carbon nanotubes (CNTs) versus commercial DNA plasmids as potential standards for TERS.[62] The use of multiple TERS tips and several DNA samples demonstrated the reproducibility of the methods outlined. The work highlighted that cation fixation of DNA is preferable for less interaction of the DNA and the substrate, and that in the interest of studying the native DNA structure APTES-fixation is favourable.[61,62]

When DNA is exposed to ultraviolet C (UVC) light, severe DNA lesions termed double-strand breaks (DSBs) can occur. TERS was successfully deployed to visualise and analyse DNA DSBs, and it was found that the 3' and 5'-bond of the deoxyribose units were particularly susceptible to UVC radiation.[63] It was noted that CH_3/CH_2 deformation and POH modes were enhanced in TERS spectra of DNA irradiated with UVC, which implied the presence of terminal hydrogens at the strand break sites. This was supported by the use of hybrid QM/MM calculations which showed agreement of the terminal hydrogen band positions.

The possibility of the use of TERS for label-free DNA sequencing was assessed early on,[57] but sub-nanometre resolution was not achieved until almost a decade later using STM-TERS.[64] Nucleobases have a distance of 0.34 nm between each other in a typical DNA strand,

and so it was suggested that a TERS tip with a nanostructured apex would be a necessity to achieve single molecule detection.[65,66] Additionally, the Raman cross-section varies between the 4 nucleobases,[67] with typical TERS enhancements occurring directly under the tip and lessening further away from it due to the lower electric field.[65] Despite these restraints, single base detection can in principle be achieved via spectral deconvolution of repeat TERS measurements at sub-nanometre steps as individual nucleobases pass through the hotspot.[57] A great demonstration of the capability of TERS as a label-free technique for DNA sequencing was the 2017 paper by Zhang *et al.*[64] A high spatial resolution of 0.9 nm was achieved, which outperformed previous results using other SPM methods. Specifically, the DNA bases adenine and thymine could be distinguished spectroscopically due to their characteristic bands at 680 cm^{-1} and 880 cm^{-1}, respectively. He *et al*. broke this resolution record in their 2019 work, claiming a spatial resolution of 0.5 nm.[68] This spatial resolution allowed individual DNA bases to be resolved, with at least 90% accuracy successful sequencing of M13mp18 ssDNA. Characteristic peaks of adenine, cytosine, guanine, and thymine were used for sequence mapping, which was then validated against known M13mp18 sequences. The work solidified TERS for high-resolution DNA sequencing which could potentially be extended for other biopolymers. This was subsequently proven for RNA strands by the same group in 2021.[69] For this study, the authors used a 4000-base CRISPR-associated protein 9 (Cas9) ssRNA with TERS maps being referenced against known sequences for identification. Similar to their previous work, a spatial resolution of 0.5 nm with 90% sequencing accuracy was claimed. While these works present the significant advancements in TERS as a direct-method for sequencing, the reliability and repeatability of the measurements could still be improved. This is especially true for the fabrication of TERS-active tips, which is an acknowledge choke-point across all applications of TERS.

2.1.2. Characterisation of Proteins using TERS

The first investigation of a protein using the TERS technique wasn't reported until 2008 when Yeo *et al.* investigated cytochrome c (Cyt-c).[70] Cyt-c is a heme protein found in the inner membrane of mitochondria that acts as an electron transport mediator. Due to the importance of porphyrins like heme in biosystems, and for being resonant biomolecules, they have been extensively studied using conventional Raman spectroscopy, RRS, SERS, and SERRS.[71–73] Typical marker bands of the porphyrin molecule appear in the 1300 – 1700 cm^{-1} range, which are sensitive to oxidation state of the iron moiety (Fe^{III}, Fe^{II}), the spin state (low-spin (LS) or

high spin (HS)), and its coordination state (six-coordinated 6c or five-coordinated 5c). In the case of the above mentioned TERS study, Cyt-c was found to be present mainly in the 6cLS configuration with some bands of the 5cHS state observable at 1570 cm^{-1}.[70] The comparative use of SERS in this study highlighted the superior spatial resolution and sensitivity of TERS, which was able to resolve signals that were otherwise obscured by the resonantly enhanced heme bands within SERS spectra. Böhme *et al*. were able to observe Cyt-c using TERS on isolated mitochondria extracted from yeast cells.[74] While Cyt-c was predominantly in the oxidised 6cHS or 5cHS conformational states, HS and LS states could be distinguished based on the Raman modes between 1480 – 1640 cm^{-1}. A 7-10 nm spatial resolution allowed for the precise localisation of Cyt-c within the intermembrane space of the mitochondria.[74] This work was a significant advance in the capability of TERS to study single biomolecules in their native environment.

Other haemoproteins that were studied using TERS include haemoglobin[75] and deoxyhaemoglobin.[76] In the case of the former, TERS was employed to follow the nanoscale oxidation changes on the surface of crystals for haemoglobin. Two bands at 1378 cm^{-1} and 1355 cm^{-1} revealed the occurrence of the Fe^{III} and Fe^{II} states, which were not observable in comparative RRS spectra. The sensitivity of TERS was thus demonstrated to be capable of studying nanoscale oxidation processes and structural changes, and thus has the outlook to potentially monitor other biological dynamic processes such as ligand exchange and protein binding.[75] The latter study on deoxyhaemoglobin investigated the photooxidation process of this molecule using different types of Ag nanoparticles for comparative SERRS and TERS measurements. A high SOR of 10 nm was achieved using TERS, and the technique did not induce molecule oxidation as the Ag particles of the tip were not in direct contact with the sample. This was compared to the unprotected Ag SERS particles which oxidized deoxyhaemoglobin to its oxidised form, methaemoglobin.[76] This work emphasised the importance of avoiding unwanted oxidation reactions during Raman measurements, as well as accentuating the application of TERS to studying oxidation-sensitive biomolecules.

TERS has the major advantage over SERS in that its extreme sensitivity and high spatial resolution allows for the probing of individual amino acid residues that make up peptides and proteins. As a first observation, the TERS spectral intensity of a specific amino acid is dependent on the orientation with respect to the tip axis.[31] This observation was first reported in 2009,[77] in which histidine (His) was analysed on atomically flat silver substrates. The interaction of His with the substrate lead to different molecular orientations, and showed differences in TERS intensity, peak shapes, and peak shifts. The vibrational mode of the

imidazole C=C ring stretch at 1590 cm^{-1} was used to identify an inclined histidine molecule relative to the substrate surface. While this mode is observable for phenylalanine (Phe),[78,79] and tyrosine (Tyr) dipeptides,[79] it is not observed for monolayers of Phe, Tyr, and tryptophan (Trp) adsorbed on gold plates. Theoretical calculations interpreted these observations as being due to the respective parallel orientation of the molecular rings with the substrate via the interaction of carboxyl or amine groups.[80]

In general, aromatic amino acids (Tyr, Phe, Trp, His) give rise to the most intense and sharp bands observed in TERS spectra of peptides and proteins. This high degree of enhancement is twofold: i) aromatic amino acids exhibit high scattering cross sections as a result of the polarizability of their delocalised electrons, and ii) a strong confinement of the electromagnetic field occurs at the TERS tip apex.[81] Tyr can be identified by the characteristic doublet between 819 – 868 cm^{-1}, which is due to Fermi resonance between the ring breathing and the overtone of the out-of-plane ring bending vibrational mode.[47,82] Phe is often identified in protein primary sequences through the two bands at 997 – 1014 cm^{-1} and 1018 – 1056 cm^{-1}, while the NH indole ring stretching mode at 1423 – 1455 cm^{-1} signifies the presence of Trp.[47] His is unlike the other aromatic amino acids in that it does not contain an individual characteristic band, but rather requires multiband identification for its absolute assignment. Therefore, the spectral marker for His is often the combination of three bands centred at 1180, 1330, and 1495 cm^{-1}.[47,83]

In comparison, amino acids that have saturated hydrocarbon chains (i.e. alanine (Ala), valine (Val), leucine (Leu), isoleucine (Ile)) cannot be reliably distinguished using TERS due to their spectral similarities. Apart from the aromatic amino acids, cysteine (Cys) and proline (Pro) have characteristic modes that allow for their clear identification in TERS. The C-S stretching modes of Cys are identifiable in the 650 – 698 cm^{-1} and 745 – 806 cm^{-1} ranges, with the ring stretch of Proline occurring around 900 cm^{-1}.[47] The basic amino acids lysine (Lys) and arginine (Arg) can be identified in TERS by their amino and guanidinium groups, respectively. These amino acids still require two-peak assignments in the 1080 – 1179 cm^{-1} range as the other modes are not individually specific to these amino acids.[47,83] For the amino acids that contain a carboxylic acid side chain, glutamic acid (Glu) and aspartic acid (Asp), the assignment of the COO^- stretching modes at 1385 – 1455 cm^{-1} is generally unspecific to distinguish the two.[47]

2.1.3. Characterisation of Amyloids using TERS

Peptides are typically defined as having less than 50 amino acids in their sequence, while proteins have more than 50 amino acids in their sequences. Additionally, proteins often have more defined structure compared to peptides, having secondary, tertiary, and even quaternary structures. Amyloids are one particular group of peptides and proteins that can assemble into amyloid fibrils, despite sometimes having vastly different primary sequences. These somewhat 50 different proteins and peptides are known to form accumulative deposits of fibrils that make up plaques or inclusions which are associated with human diseases.[84] While these amyloid deposits were first observed nearly 400 years ago, it has only been in the last decades that these fibril structures have been resolved with atomic detail.[85–87] Even so, their pathway of formation and implication especially in neurodegenerative diseases is still yet to be fully unravelled. Amyloid diseases include, but are not limited to, Alzheimer's disease (AD),[88] Parkinson's disease (PD),[89] Huntington disease (HD),[90] and Creutzfeldt-Jakob disease (CJD),[91] involving aggregation of Amyloid β (Aβ) and/or tau protein (in AD), α-synuclein (in PD), huntingtin (in HD), and prion protein (PrP) (in CJD).

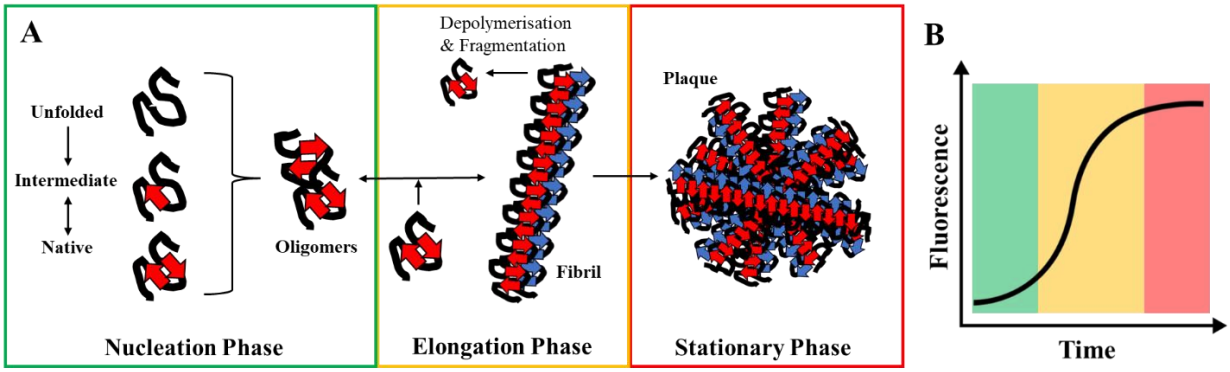

Figure 1.7. [A] *Schematic of amyloid nucleation-growth mechanism. Native, partially-folded, and/or unfolded amyloid proteins initiate fibrilization by first assembling into oligomeric species in the nucleation phase. As oligomers assemble into fibrils, they undergo depolymerisation and fragmentation, which can nucleate additional fibrils. The elongation phase sees exponential growth of fibrillar species up until the stationary phase, where fibrils may further associate with each other forming aggregates like amyloid plaques characteristic of amyloid disease.* ***[B]*** *Typical S-curve of thioflavin T (ThT) assay used to monitor fibril growth in vitro. Green, yellow, and red zones indicate the nucleation, elongation, and stationary phase respectively.*

The formation of amyloid fibrils and plaques is believed to occur via a nucleation-growth mechanism (**Figure 1.7**). Precursor peptide or protein monomers, which may be intrinsically disordered or partially folded, first need to associate with each other to form dynamic oligomers which in turn, can produce higher-order species. There is further evidence that suggests the native protein can also act as a seed for aggregation.[92] During the oligomerisation process, the kinetically most unstable species called the critical nucleus must be formed, which is superseded by the rapid polymerisation into fibrils. These assemblies may continue to form the end amyloid fibril, or alternatively dead-end assemblies that still may be relevant to disease.[84] The transformation of precursors to form β-strand-rich secondary structures is a defining moment of amyloidogenesis. With this characteristic cross-β structure fragments of the original parent fibril can recruit other monomers for fibril formation and elongation, in addition to secondary nucleation processes which effectively catalyse oligomer formation on the surface of pre-existing fibrils.[93,94] To study the kinetic assembly of amyloid fibrils *in vitro*, the dye thioflavin T (ThT) is commonly used. The dye binds to the newly formed β-sheets and the change in the fluorescence emission from 445 nm to 482 nm is dependent on the aggregation state of the amyloid which produces a kinetic curve of fibril formation over time.[95]

Many biophysical and biochemical studies on amyloids have focused on the effects of various fibrils and oligomeric species within the frame of cellular dysfunction. However, it is likely that combinations of active species are present, in addition to precursor mutations, post-translational modifications, and stress all adding up to bring about the disease state. Therefore, there is a need to clarify protein aggregates with atomic scale resolution to be able to better understand this complex network of interactions. The comparison of the molecular interaction of functional and disease-associated amyloid fibrils with cellular components would enable the comprehension of their role in neurodegenerative diseases. At the subunit level, the defining cross-β-sheet structure was first defined using X-ray diffraction and found to have an intermolecular spacing of 4.7 – 4.8 Å.[96] This ubiquitous structure has been since confirmed with several other methods including cryo-EM[97] and FTIR.[98] The β-sheet core strands are stabilised by interlinked hydrophobic side chains that exclude water which are unique to amyloids, termed “steric zippers”.[99] This work featured the structures of fragments of Aβ, tau, α-synuclein, PrP, and insulin, amongst others. Four parallel β-sheet and four antiparallel β-sheet zipper structures were identified, but only five of the eight had been experimentally observed.[99] Following on from the formation of the stable fibril core structure and fibril elongation, inter-fibril interaction results in the plaques and inclusions found in amyloid associated diseases.

Despite the advances in high-resolution structural data on amyloid fibrils, polymorphism, the effects of the cellular environment, and aggregation mechanisms for fibril formation are still poorly documented.

TERS has the capability to characterise individual amyloid fibrils on the nanoscale due to its high lateral SOR. The original model protein insulin was first used to characterise amyloid fibrils using TERS. However, amyloid species including Aβ and tau that are related to AD have more recently been studied with the technique. For the former, TERS has successfully been implemented to study protein secondary structures, amino acid composition, and the correlation between the two. The pioneering work by Kurouski *et. al* in 2012, was the first implementation of TERS for the nanoscale characterisation of bovine insulin fibrils. Structural features such as the left-handed twist of the insulin fibrils were found to be consistent with previous studies using other characterisation methods. The surface of the fibrils was found to be heterogenous, featuring both β-sheet and unordered/random secondary structures. A correlation between secondary structures and specific amino acids were also evaluated, with β-sheet regions being rich in hydrophobic amino acids such as Cys, Phe, and Tyr.[100] The scientific letter that followed this work added to the previous findings in that more precise chemical mapping was achieved for Cys, Phe, Tyr, and Pro. This was in addition to His being identified by distinct marker bands with a lateral resolution below 1.5 nm being achieved.[101] During their investigation of insulin fibrils, the Deckert group hypothesised that amide I band suppression in enhanced Raman techniques is not influenced directly by the aggregation state of the protein. Rather, it was shown that bulky side chains (such as Tyr, Trp) and thus greater distance between nanoparticle and peptide, resulted in missing amide I bands.[102] Specific amino acids that allowed for the differentiation between hydrophilic and hydrophobic domains of insulin fibrils was later demonstrated by the same group. An unprecedented spatial resolution of 0.5 nm was claimed in this study, as individual amino acids (Cys, Tyr, Asp/Glu) were identified. Analysis of the amide III band region demonstrated the structural heterogeneity of the fibril surface with unordered structures being dominant.[103] TERS was also used to study insulin fibrils and protofibrils with twisted and flat topologies. These topologies are hypothesised to arise from either a templating mechanism in the case of twisted, and a side-on association of protofilaments for topologically flat fibrils. There were also notable differences in secondary structure and amino acid composition between the two morphologies, with twisted fibrils having relatively less unordered protein structures, lower quantities of Cys, but higher amounts of Tyr, Pro, and His when compared to flat fibrils. These differences are also notable when compared to the immature protofibrils studied as the high abundance of Phe, Tyr, and carboxyl

groups suggest their likely involvement in the propagation mechanisms.[104] The effect of different fibrillization inhibitors (benzonitrile, quercetin, β-carotene, and dimethyl sulfoxide (DMSO)) on insulin were also probed using AFM-TERS.[83] Specifically, DMSO had concentration-dependence effects on the formation of mature fibrils, where at high concentrations non-amyloidogenic aggregates formed similar to those observed with β-carotene and quercetin. Addition of benzonitrile during fibrilization resulted in the formation of protofilaments. The work demonstrated TERS ability to gain insights into potential therapeutic strategies against amyloid diseases.

The first reported use of TERS to study amyloids directly linked to AD was the 2013 work by Paulite *et al.*, specifically peptide fragments of $A\beta_{1-40}$.[105] In general, Aβ plaques found in patients suffering from AD consist of fibrils, protofibrils, and oligomers of both the 40 and 42 amino acid isomers of Aβ. The self-assembled $A\beta_{1-40}$ nanotapes were characterised with AFM, STM, and FTIR for comparison with the TERS images obtained. While the TERS and STM images correlated globally, the TERS images revealed structural differences that were not visible with STM alone. Such secondary structures like the presence of both antiparallel and parallel β-sheets were confirmed in the FTIR spectrum. The robustness of the TERS imaging was also verified as the spectral fingerprints were consistent with the confocal Raman spectrum of bulk $A\beta_{1-40}$ nanotapes.[105] The year 2017 saw two major studies contribute to Aβ characterisation using TERS. The second by Tabatabaei *et al.*, mapped the chemical composition of $A\beta_{1-42}$ aggregates at mice neuronal spines. After culturing the neurons with Aβ oligomers for several hours, distinct Raman features of Aβ could be detected using TERS. These Aβ could be more easily detected with longer exposure times, however the amide I bands were largely suppressed throughout the measurements. As reported for insulin fibrils, this suppression could arise from shielding amino acid side chains, molecular orientation, or through interaction with the TERS tip.[102,106] This work successfully demonstrated the application of TERS imaging as a probe for molecular interaction and localisation of amyloid species in model AD neurons.

Our group's contribution to the field was the first TERS paper of 2017, which successfully utilised TERS to distinguish more and less toxic forms of $A\beta_{1-42}$.[107] Specifically, the wild-type $A\beta_{1-42}$ fibrils were compared with fibrils of the less-toxic L34T mutant and oligomers of the highly toxic oG37C mutant. These Aβ peptides could not previously be resolved using methods such as FTIR spectroscopy, and so TERS presents a unique potential to distinguish these isoforms with nanoscale resolution. The spatial resolution of the AFM system used could characterise the morphology of the different fibrils as having 10, 7 – 8, and

5 nm diameters, with 50 – 300, 100 – 500, and 20 – 200 nm lengths for the WT, L34T, and oG37C structures respectively. In addition, TERS spectra revealed that the proportions of amide III bands vary between the isoforms, with significant 15-25% differences between WT/L34T fibrils and oG37C oligomers in the spectral regions assigned to parallel and anti-parallel β-sheets. This led to the conclusion that WT and L34T fibrils had mostly parallel β-sheets, whereas oG37C oligomers contained anti-parallel β-sheets. Random coil secondary structures were ubiquitous to all isoforms. TERS was thus shown to distinguish toxic oligomers from amyloid fibrils with nanometre resolution, demonstrating the technique's promise in clinical research and diagnosis for neurodegenerative diseases.[107]

The comprehensive study by Lipiec *et al.* in the following year utilised TERS to characterise the different stages of amyloid fibril aggregation, providing direct experimental observations to the chemical changes of the aggregation pathway.[108] The $A\beta_{1-42}$ peptides were characterised as three major forms: oligomers, protofibrils, and fibrils, who appeared smoother and more densely packed. The TERS amide III bands were noted to change from random coils to more β-sheet structures as the fibril matured signifying conformational transitions. The high sensitivity of TERS allowed for the spatial distribution of β-sheet structures to be mapped in the different stages of aggregation. This verified the Aβ aggregation pathway to begin with monomers, form metastable oligomers, and then through structural rearrangement form oligomers or protofibrils with ordered β-sheet cores. Three potential pathways were described by the authors. The first "blue" pathway involved the transition of disordered oligomers into ordered protofibrils and mature fibrils. The second "red" pathway differed from the blue pathway in that structural reorganisation takes precedence from the disordered oligomer to the ordered oligomer stage. The third "green" pathway does not suggest an intermediate disordered stage, but rather direct monomer conversion into ordered β-sheet structures. Out of the three pathways, TERS maps provided evidence for the blue pathway as disordered β-sheets in oligomers and protofibrils were detected.[108] This work is significant as for TERS as a method to gain insight into conformational dynamics of amyloids. The same authors later published one of the first works of studying amyloids in a liquid environment using TERS.[109] Liquid TERS was argued to have better spectral resolution and reproducibility when compared to TERS in air, which is a pertinent step towards future TERS studies under physiological conditions. Similar to their previous entry, the TERS signatures of individual Aβ aggregates distinguished oligomers from mature fibrils. Specifically, during aggregation it was noted that β-sheet orientation transitions from antiparallel to parallel over the course of fibril maturation.

The microtubule-associated protein tau, has also been linked to AD. In its native state, tau is an intrinsically disordered protein that acts by binding and stabilising microtubules. Tau is positively charged at physiological pH and depending on the isoform, has between 352 and 441 amino acids in its primary sequence. The pathological form of the protein dissociates from microtubules and aggregates, forming insoluble neurofibrillary tangles in neuronal cells.[110] These neurofibrillary deposits are typically made up of either paired helical filaments (PHF) or straight filaments (SF), which in turn consists of hyperphosphorylated tau.[111–113] Several types of polyanionic cofactors have been demonstrated to induce tau fibrilization *in vitro,* including sulphated glycosaminoglycans such as heparin,[111,113,114] RNA,[86,112,115–118] and lipids.[119,120] It has been demonstrated that upon removal of these cofactors, rapid spontaneous depolymerisation occurs signifying cofactors as critical to fibril integrity.[121,122]

Despite its relevance to neurodegenerative diseases, tau protein has received less attention than other amyloid species like insulin and Aβ. Our group achieved in 2018 the first TERS characterization of tau fibril fragments with a SOR lower than 10 nm.[120] The K18 tau fragment used contained only the amino acids that form the core β-sheet when fibrillated, allowing for the easy study of the fibril organisation without the impeding fuzzy coat. These K18 tau fragments were incubated with heparin sulphate, phosphatidylcholine (POPC), or POPC with phosphatidylinositol 4,5-biphosphate (PIP_2), where K18 alone or with POPC alone did not form fibrils. PIP_2 as a cofactor is interesting to study as it is typically found in the inner cytoplasmic membrane, which could have implications in the neurodegenerative action of amyloids. Heparin-induced fibrils had the fastest aggregation which forms fibrils of 4 – 8 nm diameter, while PIP_2-induced fibrils had diameters of 3 – 7 nm. Based on the analysis of the amide I and amide III bands, it was noted that PIP_2-induced fibrils had a lower β-sheet and higher random coil content when compared with the heparin-induced fibrils. This finding suggests PIP_2 alters the secondary structure as the active aggregation cofactor. This is opposed to POPC, which did not form fibrils when incubated alone with K18. Most significantly though, was the identification of specific C=O ester vibrations in the PIP_2-induced fibrils. This indicated the definite association of PIP_2 phospholipids within the K18 fibrils.[120] This work gave nanoscale insights into the aggregation of tau protein with lipids with implications in the future investigations of tau-related neurodegenerative disease.

Most recently, Sofinska *et al*. published their work on the structural rearrangements of tau protein aggregates during fibril growth.[123] AFM-TERS was used to track morphological changes of tau aggregates during different phases of aggregation while observing the secondary

structure marker bands. Specifically, TERS spectra of protofibrils and "young" fibrils were dominated by anti-parallel β-sheets and parallel β-sheets respectively.

2.1.4. Characterisation of Lipid Membranes and Cells using TERS

In order to better understand the processes that occur inside biological cells, it is necessary to develop model systems that can mimic the cellular environment in addition to characterising real cellular systems. For these reasons, it was identified early on that TERS can provide nanoscale characterisation of lipids and other cellular components. The first application of TERS to a complex biological sample was the 2006 paper by Neugebauer *et al*. in which *S. epidermidis* cells on glass were investigated using AFM-TERS. [124] AFM was used to generate topographical images of the round bacterial cells with TERS spectra being recorded at various positions on the cell surface. A high enhancement factor was reported ($10^4 – 10^5$), with bands associated with peptides (e.g. amide I, Phe, Tyr), polysaccharides, and lipids being reported. The same group continued their work on *S. epidermidis*, this time utilising IR, micro-Raman, and UV-RRS in addition to TERS to characterise the cells.[125] The heterogeneity of the cell surface was demonstrated using TERS, especially when compared with micro-Raman spectra. Surface proteins, extracellular teichoic acids, and polysaccharides including the subunit N-acetylglucosamine were identified.[125] Demonstrating the reproducibility of their experiments, a final study on *S. epidermidis* revealed prominent TERS bands corresponding to amide III of peptides/proteins, and the presence of carbonyls, CH_2, and C-C modes of membrane lipids.[126]

The first use of TERS to investigate model membranes was the 2009 paper by Böhme *et al.*[127] Specifically, lipid bilayers of 1-palmitoyl-2-oleoyl-glycero-3-phosphocholine (POPC) / 1,2-dioleoyl-sn-glycero-3-phospho-L-serine (DOPS) were used as a model for investigating composition of human dermal derived keratinocyte (HaCaT) cells at the nanoscale. Characteristic lipid bands were identified in the DOPS/POPC bilayers, such as O-P-O stretching modes of the phosphate head group, and C-H modes of the aliphatic tails. The confirmation of these modes in the spectra of the cultured cells indicated the presence of lipid structures at the cell surface. Additionally, contributions from proteins (Phe, Tyr) and oligosaccharides were also detected on the cells surface. Thus, TERS shown to be a valuable label-free alternative for studying biological membranes, with further potential in biomedical research. Continuing their research on model lipid membranes, lipid films consisting of dipalmitoylphosphatidylcholine (DOPC), 1-palmitoyl-2-oleoylphospho-L-serine (POPS), and Biotin-PS were investigated using TERS after streptavidin labelling.[128] Again, specific marker bands associated with lipids

(phosphate) and proteins (amide bands) could be discerned in the TERS spectra. These were then used to map distinct lipid-dominated, protein-dominated, and mixed domains on the membrane surface.[128] The investigation of lipid domains is of interest to study the concept of lipid rafts, in which protein sorting and signalling processes are theorised to be mediated by lipid phase separation.[129] Opilik *et al.* utilised TERS to study binary lipid mixtures of DPPC and DOPC on gold substrates in order to study membrane compartmentalisation. The substitution of DPPC with the deuterated form DPPC-d62 allowed for the clear differentiation of lipid species based on the C-D stretching modes present at ca. 2100 cm^{-1}.[130]

TERS was used by Richter *et al.* to investigate the distribution of protein and lipid domains on membranes derived from HT29 human colon cancer cells.[131] Chemical maps depicting the distribution of lipid domains were generated. Marker bands from cholesterol and fatty acids signified the presence of lipid domains, while typical amide bands indicated membrane proteins.[131] Cyt-c within whole mitochondria was probed by TERS in the 2011 study by Böhme *et al*.[74] The oxidation states of the heme moiety were identified by the bands at 1360 and 1373 cm^{-1} indicating the Fe^{II} reduced state and the Fe^{III} oxidised state, respectively. Similarly, the spin state was deduced from specific bands in the 1480 – 1640 cm^{-1} range. The Raman modes associated with the lipid matrix were identified as originating from the phosphate residue (790 – 800 cm^{-1}, 1080 cm^{-1}) and C-H deformation at 1310 cm^{-1} and 1440 cm^{-1}. Despite the reported 7 – 10 nm SOR,[74] the distribution of oxidation states could be adequately resolved, demonstrating TERS ability to perform single-molecule characterisation within lipid systems.

The structural organisation of membrane patches of *Halobacterium salinarum* was investigated using TERS by Deckert-Gaudig *et al.*[132] More specifically, purple membrane patches containing bacteriorhodopsin could be distinctly assigned as retinal-containing and retinal-free domains based on specific marker bands. The retinal-free domains showed lipid phosphate modes without specific bacteriorhodopsin bands, such as C=C and C=N stretching modes, and C-H and N-H deformation modes. Maps of specific domains on the membrane surface could be visualised, providing insights into the arrangement of cell surface components. Micrometre-scale TERS (m-TERS) was utilised by Naumenko *et al*. to study biological transformations in living cells.[133] The m-TERS technique uses a larger tip radius to propagate surface plasmon resonance enabling subsurface process monitoring near or within the cell wall. The enriched glucose dehydrogenase protein (GDH) could be successfully identified within the genetically modified yeast cells using this technique despite its low contribution to the total protein set, demonstrating its effectiveness in monitoring protein accumulation within the cell.[133]

Prior to the 2013 paper by Nakata *et al.*, TERS measurements of lipid systems were exclusively performed in air.[134] Unique alumina- and silver-coated tungsten TERS tips were used which gave apparent reliable stability and performance for extended periods in liquid. Time-lapse measurements of DOPC bilayers showed dynamic fluctuations of the lipid molecules in close proximity to the tip, suggesting fluidity of the liquid phase lipids. This was in contrast to the gel-phase DPPC bilayers that showed minimal time-dependence.[134] While this study stands out as a significant advancement in TERS for the study of dynamic lipid bilayers in aqueous media, the research group did not publish any further studies with this TERS and tip set-up, instilling ambiguity in the reported results.

Watkins-Mariani *et al.* utilised TERS to investigate lipid aggregates, specifically caveolar bulbs (bulb-shaped plasma membrane invaginations) during the wound healing process.[135] For this purpose, real-time reverse transcription quantitative polymerase chain reaction (RT-qPCR) monitored gene expression levels as human-derived epidermal keratinocyte cells (HaCaT) were used as the *in vitro* wound healing model. The caveolar bulbs were simultaneously visualised and characterised using TERS, with lipid structures and associated caveolin proteins identified by choline and amide bands, respectively. This study highlighted TERS potential for future non-invasive studies as it maintained the native state of cellular components without the need for digestion or detergent treatment compared to traditional biochemical methods.[135] In the 2014 paper by Rusciano *et al.*,[136] TERS was used to image *Bacillus subtilis* spores which are unique in their multilayered coat that makes them resilient to harsh environmental conditions. Point-to-point variation in chemical composition highlighted the heterogeneity of the spore surface. Specifically, the spore ridges displayed a denser arrangement of protein (amide) and carbohydrate (glycosidic ring breathing modes) spectral signatures.[136] Kumar *et al.* 2017 paper demonstrated the application of TERS to map newly-synthesized phospholipid molecules in mouse pre-adipocyte cells.[137] The use of deuterated sodium stearate enabled the visualisation new phospholipid incorporation by detecting the C-D bands. TERS results were compared with confocal Raman results, with the former achieving SOR below 20 nm. Notably, chain-like structures of phospholipids corresponding to the smooth endoplasmic reticulum were observed,[137] which showcased the potential of TERS for label-free mapping of biomolecules within cells. The same continued their work with phospholipids and published in 2021 a study of DPPC monolayers on crystalline gold surfaces (Au (111)).[138] The key findings in this work were the identification of nanometre-sized holes within the DPPC monolayer in addition to differences in molecular packing.[138]

Mrdenovic *et al.* published two works on lipid membranes in 2022[139] and 2023.[140] The former study used TERS to map molecular distribution of membrane molecules in pancreatic cancer cell membranes (BxPC-3). Confocal Raman imaging was also employed to give an overview of the chemical composition on the cell surface prior to TERS which gave significantly higher resolution and sensitivity. Bands corresponding to Phe, Trp, amide I, and CH_2 bending were identified with confocal Raman measurements, but TERS was able to map domains rich in cholesterol, protein, and amino acids with a spatial resolution of 2.5 nm.[140] The latter work used TERS to investigate the C-H spectral region of DPPC bilayers and then compared this with human pancreatic cancer cell membranes. The noteworthy point of this work was the observation of uniquely shaped C-H bands compared to those observed in far-field Raman. This shape was deconvoluted and it was found to primarily arise from the CH_3 groups of the choline headgroups, suggesting a high sensitivity of enhancement with respect to the molecular orientation and proximity to the TERS tip.[140] While these works present compelling evidence for TERS analysis of lipid membranes with high sensitivity and spatial resolution, they were performed in ambient conditions which is not representative of the native cellular environment. There is therefore a need for future works concerning lipid and cellular characterisation using TERS to be performed in aqueous media, as factors such as the degree of hydration and pH could affect these systems' function and behaviour.

2.1.5. Practical issues with TERS of biomolecules

Care is needed when studying biomolecules in TERS as these samples are often fragile being prone to both mechanical degradation from the SPM tip, and laser-induced degradation from the excitation source. For the latter case, laser-induced heating during a TERS experiment can be problematic due to the highly confined electromagnetic field at the sample surface. This can result in denaturation of the investigated biomolecule, where structure is lost when exposed to excessive heat, typically above 50 °C. In the extreme case, high laser intensities can lead to carbonisation which appear in the TERS spectrum as intense broad carbon bands.[141] These heating effects can be estimated by increasing the laser fluence until noticeable changes are observed in the TERS spectrum, thus determining an upper limit. Single TERS spectra can have acquisition times from a few seconds to a few minutes depending on the efficiency of the TERS tip. While these are relatively short exposure times, a large portion of the sample area is nonetheless irradiated continuously over the course of a TERS spectrum acquisition. This is

evermore true in the case of TERS imaging where sample durability to long exposures of laser light should be evaluated, as sample heating by energy accumulation can degrade the sample.

The extreme sensitivity of TERS often complicates interpretation, as minute quantities of contaminants can be detected. A common issue with TERS, that is not limited only to the study of biomolecules, is contamination of the TERS tip. Generally speaking, there are three types of tip contamination: carbon, metal oxides and sulphides, and analyte.[31,142] As mentioned previously, carbon contamination of a TERS tip can arise from the decomposition of the analysed sample under high laser powers. When care is taken and the appropriate laser power is used, the only other source of carbon contamination is from the fabrication method of the TERS tip. This is especially true for physical vapour deposition (PVD) techniques when metal deposition is performed under imperfect conditions. In any case, the carbon contamination appears superimposed on the sample spectrum, typically featuring the broad so-called G and D bands that are centred around 1580 cm^{-1} and 1350 cm^{-1} respectively. This is an obvious issue for studying biomolecules, where useful bands such as Amide II (1510 – 1580 cm^{-1}) and Amide III (1200 – 1340 cm^{-1}) can be significantly obscured. Metals typically used for TERS tips are Au, Ag, Cu, and Al, with Au and Ag being the metals of choice for most TERS experiments of biomolecules. The formation of metal oxides and metal sulphides from exposure to ambient condition can not only reduce the effectivity of the TERS tips, but can manifest as parasitic bands in the acquired spectra. Fortunately, the Ag-O, Ag-S, and Au-S bands appears below 270 cm^{-1},[143] which is a region of little interest when studying biomolecules. The last type of tip contamination is when contaminants in the ambient air or liquid environment adsorb onto the metal that acts as a SERS substrate. These analyte contaminants can have intense spectra that closely resemble the true TERS spectrum. The TERS intensity can fluctuate over time if the contaminant is somewhat mobile, but equally can give relatively stable spectra that can recur in a continuous line of a TERS image. If such a contamination is suspected, then the TERS tip in question must be measured after retraction from the sample surface and the far-field signal scrutinized. If a signal is obtained with a retracted tip, then the tip must be replaced and the sample remeasured to ensure measurement integrity.

The implementation of TERS in liquid media to study biomolecules brings about additional difficulties compared to measurements in air or under vacuum. Keeping with the theme of the TERS tip, in liquid environments TERS tips are more prone to delamination. This is especially true for most common type of TERS tips made via PVD methods without an additional annealing step, which would increase the metal coating ductility. A common work around for this issue is to first either treat the silicon of the AFM tip, or to add a primary

adhesion layer that improves the binding of the deposited plasmonic noble metal. Common adhesion layers usually consist of Al, Ti,[109] Cr, or Ag, but care is needed as these metals can alter the plasmonic properties of the TERS tip. Additionally, a capping layer can be added on top of the plasmonic layer to either prevent oxidation (Ag rapidly oxidises in liquid environments) or to reduce tip contamination. To this end, Au is useful due to its inherent inertness while still maintaining plasmonic activity. Insulating layers such as aluminium or silicon oxides are effective at reducing tip contamination, albeit at the cost of some tip efficiency as a function of layer thickness.[144]

The next difficulty lies is the optimisation of photon excitation and collection to account for the change in refractive index between the different media. For side- and top-illumination TERS set-ups, a liquid cell that allows for the focalisation of the laser onto the tip end is required. Immersion objectives are not plausible in this case, and the objective lens also needs to account for the change in refractive index as the laser light passes from air to liquid. Bottom-illumination TERS set-ups are capable of using oil immersion objectives, but are nevertheless limited to a transparent substrate. This can be an issue when studying biomolecules as the AFM substrate of choice is muscovite mica, a hydrated phyllosilicate mineral known for its perfect basal cleavage which produces atomically flat surfaces.

2.1.6. Chemometric methods in TERS

Data processing of TERS spectra has largely followed the trends of other vibrational spectroscopic techniques. The simplest and most traditional method of data analysis in spectroscopy is “peak picking”. The position (wavenumber) and intensity of marker bands of interest are compared with reference data in the literature for interpretation. Interpretation of TERS data is more complex compared to Raman and SERS due to the influence of different selection rules[18,19] (See **Chapter 1.2.2**), and the nanoscale spatial resolution of the TERS technique. Nevertheless, TERS spectra are commonly compared with their SERS and Raman counterparts for assignment purposes. Spectral imaging brings about additional dimensionality to the data which is ever more complicated when investigating complex biological systems. The “peak picking” approach to this type of dataset can be very time consuming due to the large number of spectra collected per TERS map. Additionally, restricting interpretation to only specific vibrational modes can lead to potential information omission.[31] For this purpose, chemometric methods are deployed.

Chemometrics uses mathematical and statistical models to help extract relevant chemical information from complex datasets, such as TERS maps of biological samples. Several groups have already used chemometric methods based on unsupervised learning methods such as principal component analysis (PCA),[62,63,108,123,136,145] hierarchical cluster analysis (HCA),[108,109,145] multivariate curve resolution (MCR),[46,146] amongst others.[83,131,136,147] PCA is mainly used to reduce the dimensionality of TERS data, which helps identify the most significant patterns within the data. This method simplifies data interpretation and allows the visualisation of chemical distribution via scores and loadings plots. The fundamentals of PCA will be further described in **Chapter 4**. HCA has been used to group TERS spectra into clusters based on their similarity. This aids in identifying regions of similar chemical composition, revealing spatial distributions. Further discussion on HCA is given in **Chapter 4**. MCR attempts to decompose TERS spectra into pure component spectra, which is useful especially when there are overlapping signals. While this method does not require prior knowledge of the number or nature of components, it is sensitive to the initial estimates of spectra that need to be provided.

The 2011 study by Richter *et al.* was the first reported use of chemometric methods applied to a TERS dataset of biomolecules. This work used PCA and N-FINDR to investigate lipid and protein distributions on the surface of HT29 human colon cancer cells. The N-FINDR algorithm was used to identify spectral signatures within TERS maps by identifying the purest pixel in the dataset resulting in endmembers of pure spectral components. PCA identified 6 principal components (PCs) which accounted for 99.5% of the spectral variance. These PC's were then used as the minimum number of expected endmembers. The identified endmembers were employed to reconstruct the input spectra and visualise the distribution of lipids and proteins.[131] Rusciano *et al.* used PCA in their TERS investigation of *Bascillus subtilis* spores. PCA was employed to simplify the complex and heterogenous spectral data, with PCA-generated chemical maps being strongly correlated with AFM phase images. This led the authors to conclude that certain morphological features correspond to specific chemical compositions.[136] Lipiec *et al.* have focused on using PCA and HCA methods to answer different questions on various biological systems.[62,63,108,109,123] Specifically, PCA has been used to assess the inter- and intra-variation of TERS spectra of dsDNA, with different TERS tips having distinct but clustered spectral profiles.[63] PCA was also demonstrated to be able to distinguish TERS of DNA samples with Mg^{2+} ions versus DNA with APTES.[62] When investigating amyloid species, HCA was the method of choice with PCA being used for comparison. In the investigation of the aggregation pathway of Aβ, HCA clustered TERS maps into four groups,

two associated with the fibril structure and two associated with the background. The HCA average spectrum could then be used as a reference when assigning other TERS maps of the same species.[108] A similar HCA approach to reduce data dimensionality and establish relationship between variables was employed the study of Aβ in liquid. HCA classified TERS spectra into one of three groups attributed to either oligomers, protofibrils, or fibrils. A correct classification of 87% was reported for this method.[109] Most recently, HCA and PCA gave similar outputs when applied to TERS maps of tau fibrils during growth. PCA effectively separated the data into protofibrils and fibrils after 24 h and 72 h of incubation, respectively. HCA average spectra suggest different spatial arrangement of secondary structure across the two groups.[123]

The high variability of TERS band intensities as a function of the metal nanostructure at the TERS tip apex and as a function of the molecular orientation make the implementation of multivariate analysis in TERS challenging. The inconvenience of certain chemometric methods for TERS explains the variety of methods that have been tested on biomolecular TERS datasets. There is a need for the development of more sophisticated algorithms that are tailored to TERS datasets, which consider the variation in TERS intensity and band wavenumber to be able to better describe structure and composition of biomolecules.

2.2. TERS in liquid

The best part of all TERS studies to date have been performed in dry conditions. These have served to set the groundwork for the development and fundamental understanding of the technique, giving proof-of-concept and preliminary insights into relevant biological species. The main goal of developing TERS in liquid media for biological investigations is to provide an environment that more closely resembles the native state of the system, as opposed to measurements in air. The characterisation of single biomolecules with TERS in dry conditions is simply not sufficient to probe biological activity. Moreover, certain systems are limited to their hydration state and ensuring this quality would allow for the study of molecular processes such as protein-cell interactions with nanoscale spatial resolution.[31] Of particular interest is the thorough characterisation of lipids, in the form of model membranes or whole cells. This could take the form of the determination and localisation of target lipids within membranes, or the elucidation of lipid microdomains in the form of lipid rafts. Additionally, amyloid fibrils involved in neurodegenerative disease could be investigated as complex systems to better understand the process of amyloidogenesis. The use of model membranes that resemble the

composition of neuronal cells could give fascinating insights into the amyloid-induced neurodegeneration process.

In recent years, several research groups have made efforts to bring TERS in liquid into routine analysis. These developments are prevalent in the electrochemical TERS (EC-TERS) community, who aim to study catalytical processes with high sensitivity and nanoscale resolution. The biological TERS community has been following suit, with both communities adapting TERS for liquid and solving issues such as tip delamination by using additional adhesion and/or capping layers to produce robust TERS tips.[47,109,144] Similar to TERS in air, the main illumination geometries for TERS in liquid are bottom-, side-, and top-illumination with each having their corresponding disadvantages as previously described in **Chapter 1.3.5.** Compared to the other geometries, measurement in liquid using bottom-illumination has the advantage that the laser light only needs to pass through a relatively thin layer of liquid before exciting the tip.[148] There is also no interface between the solution and the external air, therefore no correction collar objective is needed to compensate for the change in refractive index.[149] Both STM and AFM feedback mechanisms have been used for TERS measurements in liquid. STM was proven to be the more successful method for detecting molecules in general as presented by Blum *et al.*[150] The fully metallic tip of STM gives high enhancement factors, especially considering the fine adjustments of tip-substrate distance possible via the modification of the current and bias voltage. Such tips are commonly manufactured by the chemical etching of an Au or Ag wire, which results in a nanotaper giving the tip a high spatial resolution. The major drawback of STM remains in the fact that the sample must be conductive and therefore its applications, especially within biology, are limited. In aqueous environments, the Faraday current needs to be reduced using protective layers on the STM tip and the electrochemical window confined depending on the oxidation potential of either the Au or Ag tip used.[150] In contrast to STM, AFM does not require such insulation layers to be able to perform TERS measurements in liquid (even if capping layers may be used to better preserve the tip from contamination). AFM is also the more versatile technique, being able to perform on virtually any substrate or sample.

1.5.1. TERS of biomolecules in liquid

The first study describing AFM-TERS in liquids was reported by Schmid *et al.* in 2009.[151] The authors used a bottom-illumination TERS system to characterize a self-assembled monolayers (SAM) of brilliant cresyl blue dye and thiophenol deposited on a gold-coated substrate. As the desired plasmonic metal to use for the tip was Ag, the authors conducted stability tests for Ag tips coated with an insulating layer of either AlF_3 or SiO_x (where $0 < x < 2$). The AlF_3/Ag-coated tips were deemed unsuitable for liquid applications as evident peeling of the outer layer occurred with soaking. On the contrary, SiO_x/Ag-coated tips demonstrated stability and retained their TERS enhancement. A further monolayer of ethanethiol was proven to prevent tip contamination in the liquid environment. However, this came at a cost of a reduced enhancement factor.[151] This work demonstrated the potential to perform TERS in aqueous environments, all the while addressing some of the most pertinent issues with the technique. The first reporting of liquid TERS on biomolecules was the 2013 paper by Nakata *et al.* The authors used alumina/Ag-coated tungsten tips to investigate supported lipid bilayers (SLBs) of DPPC/DOPC in water in a time-resolved manner.[134] The results of this work can be criticised however, as the demonstrated enhancement is low, no TERS images was presented, and the authors have not continued to publish using their "robust" tips.

Lipiec *et al.* published their findings on the secondary structure of amyloid fibrils in liquid in 2021.[109] Using a Ti/Au-coated tip, the authors distinguished oligomers from mature fibrils based on the evolution of β-sheet structure (from antiparallel to parallel). The AFM-TERS spectra acquired in liquid gave an apparent better signal-to-noise ratio (SNR) and better reproducibility compared to measurement in air. The most notable difference was the presence of the amide I band which is often absent in measurements in air possibly due to plasmon-induced dissociation.[102] As confirmed by DFT calculations, the authors concluded that this phenomenon was a direct result of the greater heat dissipation of water and thus increased the stability of the enhanced Raman signal. This is an important motivation to perform TERS in liquid environments when studying sensitive samples such as biomolecules.[109]

1.5.2. Technical advances of TERS in liquid

There is a significant gap between the first and second reporting of TERS in liquid environments for the investigation of biosystems. This demonstrates the difficulty in performing such experiments and the need for technological improvements such as robust tips.

In the 2018 paper by Kumar *et al*., the authors sought to develop robust, plasmonic-active TERS probes suitable for measurements in liquid using multilayer metal coatings.[152] Using a bottom-illumination AFM-TERS system, pure Ag-, Cr/Ag-, and Cr/Au/Ag-coated probes were tested on polystyrene thin films, biphenyl thiol SAMs, and single-wall carbon nanotubes (SWCNTs). The Cr/Au/Ag-coated probes were found to have the highest stability against delamination after 1 hour in water. Possibly the more meaningful demonstration from this work was the comparative measurements, which showed a reduced plasmonic enhancement in water compared to in air. This was corroborated by numerical simulations that indicated a negative correlation between the refractive index of the medium and the field enhancement.[152] Also using a bottom-illumination system, Bhattarai *et al.* in 2019 acquired exceptionally fast (0.25 s/pixel) AFM-TERS maps of 4-mercaptobenzonitrile (MBN) on monocrystalline gold triangles immersed in water. The enhanced optical fields at the edges and corners of the gold triangles could be successfully mapped using Au-coated tips, with finite-difference time-domain (FDTD) simulations corroborating the results.[153] These works demonstrate the potential of future TERS in liquid with fast and reliable measurements.

1.5.3. EC-TERS in liquid

EC-TERS in liquid was independently developed by both Van Duyne[154] and Ren[155] groups in 2015, and offers *in situ* measurements in real time with nanoscale spatial resolution. In a bottom-illumination set-up, Van Duyne *et al.* investigated the redox behaviour of Nile blue at the nanoscale.[154] Ren *et al*. used a side-illumination set-up to monitor changes in the molecular configuration of (4'-(pyridin-4-yl) biphenyl-4-yl)-methanethiol (4-PBT) with respect to changes in potential.[155] In a general EC-STM TERS set-up, both the tip and sample act as independent working electrodes (WE), in addition to a reference electrode (RE) and a counter electrode (CE). In addition to the tunnelling current between the tip and the sample, the electrochemical current flows between the sample and the CE with a bi-potentiostat controlling the chemical potentials of the sample and the tip separately against the RE.[148]

EC-TERS can also be performed using AFM systems, as demonstrated in the examination of redox behaviour of Nile blue[154,156] and polycrystalline indium tin oxide.[157] EC-AFM-TERS has the benefit over EC-STM systems in that no protection against the Faradaic current is required.[158] The photocatalytic oxidation of *p*-aminothiophenol into *p,p'*-dimercaptoazobenzene (DMAB) on a heterogenous metal surface was mapped *in-situ* by Kumar *et al*.[158] A ZrO_2-coated tip improved the lifetime and the LSPR of the tip, which

monitored the relative formation of DMAB by the average ratio of 1473 and 1071 cm^{-1} bands. This was the first reported instance of mapping chemical transformation using EC-TERS.[158] El-Khoury *et al.* used EC-TERS to image chemical reactions at solid-liquid interfaces of plasmonic hotspot in 2019.[159] The plasmon-enhanced chemical transformation (dimerization) of *p*-nitro-thiophenol to DMAB was monitored using their bottom-illumination set-up. Many aspects still need to be explored, however EC-TERS experiments are currently focusing on the study of model systems and the fabrication of TERS tips, which is still tedious for STM and AFM coupled systems.[158]

Conclusions

TERS applied to the study of biomolecules has come a long way since the technique's inception in the early 2000s. Key classes of molecules, including DNA and RNA, proteins, and lipids have been investigated with nanoscale spatial resolution proving the technique's analytical capability. TERS is well-suited for the study of disordered proteins in particular, and insights into structure and aggregation of amyloids such as Aβ and tau have already been proven. The lack of current studies on tau protein (when compared to Aβ) was identified and the investigations on this Alzheimer's-related amyloid are detailed in **Chapter 3**. An assessment of popular chemometric methods on this dataset is subject of **Chapter 4**. With the outlook of future works studying protein-membrane interactions, SLBs were used to test our first investigations into TERS in liquid. These trials and tribulations are subject of **Chapter 5**.

As for TERS in liquid environments, there are several challenges that still hinder the application of the technique. These come in the form of the tip quality, the laser focusing and signal collection, and the diode reflection of AFM feedback. For tips, the key issues are mechanical degradation, contamination, or laser heating damage. There is a clear need for high quality and robust tips that are performative in liquid environments. Regarding the laser focusing and signal collection, the distortion of the optical path due to the different refractive indices when measuring in liquid is the main challenge. This distortion can be reduced using correction collar objectives when in side-illumination, and water- or oil-immersion objectives achieve better light direction and collection. Bottom-illumination configurations can surmount this issue, but forgo the ability to perform measurements on non-transparent samples. An AFM system operating in liquid environments needs a reflective backside of the probe cantilever to effectively reflect the feedback diode laser. This layer (usually Au) plus the plasmonic layer on the tip modifies the tip resonance frequency. This is in addition to the liquid resistance against the cantilever. These factors can influence the tip stability and therefore the reliable operation and measurement. Our AFM-TERS systems in side-illumination and a one-of-a-kind total-internal reflection configuration will be detailed in the following **Chapter 2.**

References

1. Schrader, B., Infrared and Raman Spectroscopy: Methods and Applications, John Wiley & Sons, (2008).
2. William Herschel, S. B., Experiments on the Refrangibility of the Invisible Rays of the Sun, (1800).
3. Abney, W. & Festing, E., On the influence of the atomic grouping in the molecules of organic bodies on their absorption in the infra-red region of the spectrum, Phil. Trans. R. Soc., 172, 887–918 (1881).
4. Raman, C. V., Plate, F. R. S., A New Radiation, Indian J. Phys., 2 (1928).
5. Raman, C. V., Krishnan, K. S., A New Type of Secondary Radiation, Nature, 121, 501–502 (1928).
6. Kohlrausch, K. W. F., Der Smekal-Raman-Effekt, Springer Berlin, Heidelberg (1931).
7. Dadieu, A., Kohlrausch, K. W. F., Hollaender, A., The Raman Effect in organic substances and its use in chemical problems, J. Opt. Soc. Am., 21, 286-322 (1931).
8. Maiman, T. H., Stimulated Optical Radiation in Ruby, Nature, 187, 493–494 (1960).
9. Atkins, P., de Paula, J., Physical Chemistry, Oxford University Press, New York, (2010).
10. Kelley, A. M., Hyper-Raman scattering by molecular vibrations, Annu. Rev. Phys. Chem., 61, 41–61 (2010).
11. Evans, C. L., Xie, X. S., Coherent anti-Stokes Raman scattering microscopy: Chemical imaging for biology and medicine., Annu. Rev. Anal. Chem., 1, 883–909 (2008).
12. Carey, P. R., Resonance Raman spectroscopy in biochemistry and biology, Q. Rev. Biophys., 11, 309–370 (1978).
13. Fleischmann, M., Hendra, P. J., McQuillan, A. J., Raman spectra of pyridine adsorbed at a silver electrode, Chem. Phys. Lett., 26, 163–166 (1974).
14. Albrecht, M., Creighton, J., Anomalously intense Raman spectra of pyridine at a silver electrode, J. Am. Chem. Soc., 99, 5215–5217 (1977).
15. Morton, S. M., Silverstein, D. W., Jensen, L., Theoretical studies of plasmonics using electronic structure methods, Chem. Rev., 111, 3962–3994 (2011).
16. Young, M. A., Dieringer, J. A., Van Duyne, R. P., Chapter 1 Plasmonic materials for surface-enhanced and tip-enhanced Raman spectroscopy, 1–39 (2006).
17. J. Homola., Surface plasmon resonance sensors for detection of chemical and biological species, Chem. Rev., 108, 462-493 (2008).
18. Lombardi, J. R., Birke, R. L., A unified approach to surface-enhanced Raman spectroscopy, J. Phys. Chem. C, 112, 5605–5617 (2008).

19. Lombardi, J. R., Birke, R. L., Lu, T., Xu, J., Charge-transfer theory of surface enhanced Raman spectroscopy: Herzberg-Teller contributions, J. Chem. Phys., 84, 4174–4180 (1986).

20. Pohl, D. W., Fischer, U. C., Durig, U. T., Scanning near-field optical microscopy (SNOM), J. Microsc. Oxf., 152, 853–861 (1988).

21. Dunn, R. C., Near-field scanning optical microscopy, Chem. Rev., 99, 2891–2927 (1999).

22. Bian, R. X., Dunn, R. C., Xie, X. S., Leung, P. T., Single molecular emission characteristics in near-field microscopy, Phys. Rev. Lett., 75, 4772–4775 (1995).

23. Emory, S. R. & Nie, S. M., Near-field surface-enhanced Raman spectroscopy on single nanoparticles, Anal. Chem., 69, 2631–2635 (1997).

24. Anderson, M. S., Locally enhanced Raman spectroscopy with an atomic force microscope, Appl. Phys. Lett., 76, 3130–3132 (2000).

25. Stöckle, R. M., Suh, Y. D., Deckert, V., Zenobi, R., Nanoscale chemical analysis by tip-enhanced Raman spectroscopy, Chem. Phys. Lett., 318, 131–136 (2000).

26. Hayazawa, N., Inouye, Y., Sekkat, Z., Kawata, S., Metallized tip amplification of near-field Raman scattering, Opt. Comm., 183, 333–336 (2000).

27. Pettinger, B., Picardi, G., Schuster, R., Ertl, G., Surface Enhanced Raman Spectroscopy: Towards Single Molecule Spectroscopy, Electrochemistry, 68, 942–949 (2000).

28. Watanabe, H., Ishida, Y., Hayazawa, N., Inouye, Y., Kawata, S., Tip-enhanced near-field Raman analysis of tip-pressurized adenine molecule, Phys. Rev. B, Condens. Matter Matter Phys., 69, (2004).

29. Pettinger, B., Ren, B., Picardi, G., Schuster, R. Ertl, G., Nanoscale probing of adsorbed species by tip-enhanced Raman spectroscopy, Phys. Rev. Lett., 92, (2004).

30. Schmid, T., Yeo, B.-S., Zhang, W., Zenobi, R., Chapter 4 Use of tip-enhanced vibrational spectroscopy for analytical applications in chemistry, biology, and materials science, 115–155 (2006).

31. Bonhommeau, S., Cooney, G. S., Huang, Y., Nanoscale chemical characterization of biomolecules using tip-enhanced Raman spectroscopy., Chem. Soc. Rev., 51, 2416–2430 (2022).

32. Hartschuh, A., Tip-enhanced near-field optical microscopy, Angew. Chem. Int. Ed., 47, 8178–8191 (2008).

33. Stadler, J., Oswald, B., Schmid, T., Zenobi, R., Characterizing unusual metal substrates for gap-mode tip-enhanced Raman spectroscopy, J. Raman Spec., 44, 227–233 (2013).

34. Inouye, Y., Verma, P., Ichimura, T., Kawata, S., Chapter 3 Near-field effects in tip-enhanced Raman scattering, 87–113 (2006).

35. Futamata, M., Maruyama, Y., Ishikawa, M., Local electric field and scattering cross section of Ag nanoparticles under surface plasmon resonance by finite difference time domain method, J. Phys. Chem. B, 107, 7607–7617 (2003).

36. Shah, J., Atomic and electronic structures of two-dimensional layers on noble metals, Linköping University (2019).

37. Nobel Media AB, The Nobel Prize in Physics 1986 - Press Release, (1986).

38. Jiang, S., Subnanometer-resolved chemical imaging via multivariate analysis of tip-enhanced Raman maps, Light Sci. Appl., 6 (2017).

39. Maghsoudy-Louyeh, S., Kropf, M., Tittmann, B. R., Review of Progress in Atomic Force Microscopy, Open Neuroimag. J., 17, 86–104 (2018).

40. Binnig, G., Quate, C. F., Gerber, C., Atomic Force Microscope, Phys. Rev. Lett., 56, 930–933 (1986).

41. Kinney, J. H., Balooch, M., Marshall, S. J., Marshall, G. W. J., Weihs, T. P., Atomic force microscope measurements of the hardness and elasticity of peritubular and intertubular human dentin, J. Biomech. Eng., 118, 133–135 (1996).

42. Xia, F., Youcef-Toumi, K., Review: Advanced Atomic Force Microscopy Modes for Biomedical Research, Biosensors, 12 (2022).

43. Talaga, D., Bremner, A., Buffeteau, T., Vallée, R. A. L., Lecomte, S., Bonhommeau, S., Total Internal Reflection Tip-Enhanced Raman Spectroscopy of Cytochrome c, J. Phys. Chem. Lett., 11, 3835–3840 (2020).

44. Talaga, D., Cooney, G. S., Ury-Thiery, V., Fichou, Y., Huang, Y., Lecomte, S., Bonhommeau, S., Total Internal Reflection Tip-Enhanced Raman Spectroscopy of Tau Fibrils, J. Phys. Chem. B, 126, 5024–5032 (2022).

45. Steidtner, J., Pettinger, B., High-resolution microscope for tip-enhanced optical processes in ultrahigh vacuum, Rev. Sci. Instr., 78, (2007).

46. Braun, K., Zhang, D., Wang, X., Mihaljevic, J., Meixner, A. J., Novel Parabolic Mirror Microscope Illuminated with Cylindrical Vector Beams for Confocal and Tip Enhanced Super Resolution Imaging, Springer Berlin Heidelberg, Berlin, Heidelberg, 791–796 (2014).

47. Bonhommeau, S., Lecomte, S., Tip-Enhanced Raman Spectroscopy: A Tool for Nanoscale Chemical and Structural Characterization of Biomolecules, Chem. Phys. Chem., 19, 8–18 (2018).

48. Treffer, R., Lin, X., Bailo, E., Deckert-Gaudig, T., Deckert, V., Distinction of nucleobases - A tip-enhanced Raman approach, Beilstein J. Nanotech., 2, 628–637 (2011).

49. Whelan, D. R. Bambery, K. R., Heraud, P., Tobin, M. J., Diem, M., McNaughton, D., Wood, B. R., Monitoring the reversible B to A-like transition of DNA in eukaryotic cells using Fourier transform infrared spectroscopy, Nucleic Acids Res., 39, 5439–5448 (2011).

50. Rich, A., Nordheim, A., Wang, A. H.-J., The chemistry and biology of left-handed z-DNA, Annu. Rev. Biochem., 53, 791–846 (1984).

51. Hayazawa, N., Yano, T., Watanabe, H., Inouye, Y., Kawata, S., Detection of an individual single-wall carbon nanotube by tip-enhanced near-field Raman spectroscopy., Chem. Phys. Lett., 376, 174–180 (2003).

52. Hayazawa, N., Watanabe, H., Saito, Y., Kawata, S., Towards atomic site-selective sensitivity in tip-enhanced Raman spectroscopy., J. Chem. Phys., 125, (2006).

53. Ichimura, T., Watanabe, H., Morita, Y., Verma, P., Kawata, S., Inouye, Y., Temporal fluctuation of tip-enhanced Raman spectra of adenine molecules, J. Phys. Chem. C, 111, 9460–9464 (2007).

54. Rasmussen, A., Deckert, V., Surface- and tip-enhanced Raman scattering of DNA components, J. Raman Spec., 37, 311–317 (2006).

55. Domke, K. F., Zhang, D., Pettinger, B., Tip-enhanced Raman spectra of picomole quantities of DNA nucleobases at Au (111), J. Am. Chem. Soc., 129, 6708–6709 (2007).

56. Zhang, D., Domke, K. F., Pettinger, B., Tip-enhanced Raman spectroscopic studies of the hydrogen bonding between adenine and thymine adsorbed on Au (111), Chem. Phys. Chem., 11, 1662–1665 (2010).

57. Bailo, E., Deckert, V., Tip-enhanced Raman spectroscopy of single RNA strands: Towards a novel direct-sequencing method, Angew. Chem. Int. Ed., 47, 1658–1661 (2008).

58. Hennemann, L. E., Meixner, A. J., Zhang, D., Surface- and tip-enhanced Raman spectroscopy of DNA, Spectroscopy, 24, 119–124 (2010).

59. Najjar, S., Talaga, D., Schué, L., Coffinier, Y., Szunerits, S., Boukherroub, Servant, L., Rodriguez, V., Bonhommeau, S., Tip-enhanced Raman spectroscopy of combed double-stranded DNA bundles, J. Phys. Chem. C, 118, 1174–1181 (2014).

60. Pashaee, F., Tabatabaei, M., Caetano, F. A., Ferguson, S. S. G., Lagugné-Labarthet, F., Tip-enhanced Raman spectroscopy: Plasmid-free: vs. plasmid-embedded DNA, Analyst, 141, 3251–3258 (2016).

61. Japaridze, A., Vobornik, D., Lipiec, E., Cerreta, A., Szczerbinski, J., Zenobi, R., Dietler, G., Toward an Effective Control of DNA's Submolecular Conformation on a Surface, Macromolecules, 49, 643–652 (2016).

62. Lipiec, E., Japaridze, A., Szczerbiński, J., Dietler, G., Zenobi, R., Preparation of Well-Defined DNA Samples for Reproducible Nanospectroscopic Measurements, Small, 12, 4821–4829 (2016).

63. Lipiec, E., Sekine, R., Bielecki, J., Kwiatek, W. M., Wood, B. R., Molecular Characterization of DNA Double Strand Breaks with Tip-Enhanced Raman Scattering, Angew. Chem. Int. Ed., 126, 173–176 (2014).

64. Zhang, R., Zhang, X., Wang, H., Zhang, Y., Jiang, S., Hu, C., Zhang, Y., Luo, Y., Dong, Z., Distinguishing Individual DNA Bases in a Network by Non-Resonant Tip-Enhanced Raman Scattering, Angew. Chem. Int. Ed., 129, 5653–5656 (2017).

65. Yeo, B. S., Stadler, J., Schmid, T., Zenobi, R., Zhang, W. Tip-enhanced Raman Spectroscopy - Its status, challenges and future directions, Chem. Phys. Lett., 472, 1–13 (2009).

66. Trautmann, S., Aizpurua, J., Goetz, I., Undisz, A., Dellith, J.m Schneidewind, H., Rettenmayr, M., Deckert, V., A classical description of subnanometer resolution by atomic features in metallic structures, Nanoscale, 9, 391–401 (2017).

67. Green, M., Liu, F. M., Cohen, L., Köllensperger, P., Cass, T., SERS platforms for high density DNA arrays, Faraday Discussions, 132, 269–280 (2006).

68. He, Z., Han, Z., Kizer, M., Linhardt, R. J., Wang, X., Sinyukov, A. M., Wang, J., Deckert, V., Sokolov, A. V., Hu, J., Scully, M. O., Tip-Enhanced Raman Imaging of Single-Stranded DNA with Single Base Resolution, J. Am. Chem. Soc., 141, 753–757 (2019).

69. He, Z., Qiu, W., Kizer, M. E., Wang, J., Chen, W., Sokolov, A. V., Wang, X., Hu, J., Scully, M. O., Resolving the Sequence of RNA Strands by Tip-Enhanced Raman Spectroscopy, ACS Photonics, 8, 424–430 (2021).

70. Yeo, B. S., Mädler, S., Schmid, T., Zhang, W., Zenobi, R., Tip-enhanced Raman spectroscopy can see more: The case of cytochrome c, J. Phys. Chem. C, 112, 4867–4873 (2008).

71. Parthasarathi, N., Hansen, C., Yamaguchi, S., Spiro, T. G., Metalloporphyrin core size resonance Raman marker bands revisited: implications for the interpretation of hemoglobin photoproduct Raman frequencies, J. Am. Chem. Soc., 109, 3865–3871 (1987).

72. Hildebrandt, P., Polyanion binding to cytochrome c probed by resonance Raman spectroscopy, Biochimica et Biophysica Acta, 1040, 175–186 (1990).

73. Keating, C. D., Kovaleski, K. K., Natan, M. J., Heightened electromagnetic fields between metal nanoparticles: Surface enhanced Raman scattering from metal - Cytochrome c-metal sandwiches, J. Phys. Chem. B, 102, 9414–9425 (1998).

74. Böhme, R., Mkandawire, M., Krause-Buchholz, U., Roesch, P., Roedel, G., Popp, J., Deckert, V., Characterizing cytochrome c states - TERS studies of whole mitochondria, Chem. Commun., 47, 11453–11455 (2011).

75. Wood, B. R., Asghari-Khiavi, M., Bailo, E., McNaughton, D., Deckert, V., Detection of nano-oxidation sites on the surface of hemoglobin crystals using tip-enhanced Raman scattering, Nano Lett., 12, 1555–1560 (2012).

76. Tanabe, I., Egashira, M., Suzuki, T., Goto, T., Ozaki, Y., Prevention of photooxidation of deoxymyoglobin and reduced cytochrome c during enhanced Raman measurements: SERRS with thiol-protected Ag nanoparticles and a TERS technique, J. Phys. Chem. C, 118, 10329–10334 (2014).

77. Deckert-Gaudig, T., Deckert, V., Tip-enhanced Raman scattering studies of histidine on novel silver substrates, J. Raman Spec., 40, 1446–1451 (2009).

78. Sinjab, F., Lekprasert, B., Woolley, R. A. J., Roberts, C. J., Tendler, S. J. B., Notingher, I., Near-Field Raman Spectroscopy of Biological Nanomaterials by in Situ Laser-Induced Synthesis of Tip-Enhanced Raman Spectroscopy Tips, Optics Letters, 37 (2012).

79. Blum, C., Schmid, T., Opilik, L., Weidmann, S., Fagerer, S. R., Zenobi, R., Understanding tip-enhanced Raman spectra of biological molecules: A combined Raman, SERS and TERS study, J. Raman Spec., 43, 1895–1904 (2012).

80. Deckert-Gaudig, T., Rauls, E., Deckert, V., Aromatic amino acid monolayers sandwiched between gold and silver: A combined tip-enhanced Raman and theoretical approach, J. Phys. Chem. C, 114, 7412–7420 (2010).

81. Hermann, P., Fabian, H., Naumann, D., Hermelink, A., Comparative study of far-field and near-field Raman spectra from silicon-based samples and biological nanostructures, J. Phys. Chem. C, 115, 24512–24520 (2011).

82. Siamwiza, M. N., Lord, R. C., Chen, M. C., Takamatsu, T., Harada, I., Matsuura, H., Shimanouchi, T., Interpretation of the Doublet at 850 and 830 cm^{-1} in the Raman Spectra of Tyrosyl Residues in Proteins and Certain Model Compounds, Biochem., 14, 22, 4870-4876 (1975).

83. Deckert-Gaudig, T., Deckert, V., High resolution spectroscopy reveals fibrillation inhibition pathways of insulin., Sci. Rep., 6, 33575 (2016).

84. Iadanza, M. G., Jackson, M. P., Hewitt, E. W., Ranson, N. A., Radford, S. E., A new era for understanding amyloid structures and disease., Nature Rev. Mol. Cell Bio., 19 755–773 (2018).

85. Fitzpatrick, A. W. P., Falcon, B., He, S., Murzin, A. G., Murshudov, Garringer, H. J., Crowther, R. A., Ghetti, B., Goedert, M., Scheres, S. H. W., Cryo-EM structures of tau filaments from Alzheimer's disease, Nature, 547, 185–190 (2017).

86. Abskharon, R., Sawaya, M. R., Boyer, D. R., Cao, Q., Nguyen, B. A., Cascio, D., Eisenberg, D. S., Cryo-EM structure of RNA-induced tau fibrils reveals a small C-terminal core that may nucleate fibril formation. PNAS, 119, (2022).

87. Tuttle, M. D., Comellas, G., Nieuwkoop, A. J., Covell, D. J., Berthold, D. A., Kloepper, K. D., Courtnery, J. M., Kim, J. K., Barcley, A. M., Kendall, A., Wan, W., Stubbs, G., Schwieters, C. D., Lee, V. M. Y., George, J. M., Rienstra, C. M., Solid-state NMR structure of a pathogenic fibril of full-length human α-synuclein, Nat. Struct. Mol. Biol., 23, 409–415 (2016).

88. Goedert, M., Wischik, C. M., Crowther, R. A., Walker, J. E., Klug, A., Cloning and Sequencing of the CDNA Encoding a Core Protein of the Paired Helical Filament of Alzheimer Disease: Identification as the Microtubule-Associated Protein Tau., Proc. Nati. Acad. Sci. USA, 85 (1988).

89. Chartier-Harlin, M.-C., Kachergus, J., Roumier, C., Mouroux, V., Douay, X., Lincoln, S., Levecque, C., Larvor, L., Andrieux, J., Hulihan, M., Waucquier, N., Defebvre, L., Amouyel, P., Farrer, M., Destée, A., Alpha-synuclein locus duplication as a cause of familial Parkinson's disease, The Lancet, 364, 1167–1169 (2004).

90. Warby, S. C., Montpetit, A., Hayden, A. R., Carroll, J. B., Butland, S. L., Visscher, H., Collins, J. A., Semaka, A., Hudson, T. J., Hayden, M. R., CAG Expansion in the Huntington Disease Gene Is Associated with a Specific and Targetable Predisposing Haplogroup, Am. J. Hum. Genet., 84, 351–366 (2009).

91. Prusiner, S. B., Prusiner, S. B., Mckinley, M. P., Bowman, K. A., Bolton, D. C., Bendheim, P. E., Groth, D. F., Glenner, G. G., Scrapie Prions Aggregate to Form Amyloid-like Birefringent Rods, Cell, 35, 349-358 (1983).

92. Sicorello, A., Torrassa, S., Soldi, G., Gianni, S., Travaglini-Allocatelli, C., Taddei, N., Relini, A., Chiti, F., Agitation and High Ionic Strength Induce Amyloidogenesis of a Folded PDZ Domain in Native Conditions, Biophys. J., 96, 2289–2298 (2009).

93. Linse, S., Monomer-dependent secondary nucleation in amyloid formation. Biophys. Rev., 9, 329–338 (2017).

94. Meisl, G., Kirkegaard, J. B., Arosio, P., Michaels, T. C. T., Vendruscolo, M., Dobson, C. M., Linse, S., Knowles, T. P. J., Molecular mechanisms of protein aggregation from global fitting of kinetic models, Nat. Protoc., 11, 252–272 (2016).

95. Levine, H., Thioflavine T interaction with synthetic Alzheimer's disease β-amyloid peptides: Detection of amyloid aggregation in solution, Protein Science, 2, 404–410 (1993).

96. Bonar, L., Cohen, A. S., Skinner, M. M., Characterization of the Amyloid Fibril as a Cross-β Protein, Proceedings of the Society for Experimental Biology and Medicine, 131, 1373–1375 (1969).

97. Serpell, L. C., Smith, J. M., Direct visualisation of the β-sheet structure of synthetic Alzheimer's amyloid, J. Mol. Biol., 299, 225–231 (2000).

98. Jahn, T. R., Tennent, G. A., Radford, S. E., A common β-sheet architecture underlies in vitro and in vivo β2-microglobulin amyloid fibrils., J. Biol. Chem., 283, 17279–17286 (2008).

99. Sawaya, M. R., Sambashivan, S., Nelson, R., Ivanova, M. I., Sievers, S. A., Apostol, M. I., Thompson, M. J., Balbirnie, M., Wiltzius, J. J. W., McFarlane, H. T., Madsen, A., Riekel, C., Eisenberg, D., Atomic structures of amyloid cross-β spines reveal varied steric zippers, Nature, 447, 453–457 (2007).

100. Kurouski, D., Deckert-Gaudig, T., Deckert, V., Lednev, I. K., Structure and composition of insulin fibril surfaces probed by TERS, J. Am. Chem. Soc., 134, 13323–13329 (2012).

101. Deckert-Gaudig, T., Kämmer, E., Deckert, V., Tracking of nanoscale structural variations on a single amyloid fibril with tip-enhanced Raman scattering, J. Biophotonics, 5, 215–219 (2012).

102. Kurouski, D., Postiglione, T., Deckert-Gaudig, T., Deckert, V., Lednev, I. K., Amide i vibrational mode suppression in surface (SERS) and tip (TERS) enhanced Raman spectra of protein specimens, Analyst, 138, 1665–1673 (2013).

103. Deckert-Gaudig, T., Kurouski, D., Hedegaard, M. A. B., Singh, P., Lednev, I. K., Deckert, V., Spatially resolved spectroscopic differentiation of hydrophilic and hydrophobic domains on individual insulin amyloid fibrils, Sci. Rep., 6, (2016).

104. Kurouski, D., Deckert-Gaudig, T., Deckert, V., Lednev, I. K., Surface characterization of insulin protofilaments and fibril polymorphs using tip-enhanced Raman spectroscopy (TERS), Biophys. J., 106, 263–271 (2014).

105. Paulite, M., Blum, C., Schmid, T., Opilik, L., Eyer, K., Walker, G. C., Zenobi, R., Full spectroscopic tip-enhanced Raman imaging of single nanotapes formed from β-Amyloid (1-40) peptide fragments, ACS Nano, 7, 911–920 (2013).

106. Tabatabaei, M., Caetano, F. A., Pashee, F., Ferguson, S. S. G., Lagugné-Labarthet, F. Tip-enhanced Raman spectroscopy of amyloid β at neuronal spines, Analyst, 142, 4415–4421 (2017).

107. Bonhommeau, S., Talaga, D., Hunel, J., Cullin, C., Lecomte, S., Tip-Enhanced Raman Spectroscopy to Distinguish Toxic Oligomers from Aβ 1 – 42 Fibrils at the Nanometer Scale, Angew. Chem. Int. Ed., 129, 1797–1800 (2017).

108. Lipiec, E., Perez-Guaita, D., Kaderli, J., Wood, B. R. Zenobi, R., Direct Nanospectroscopic Verification of the Amyloid Aggregation Pathway, Angew. Chem. Int. Ed., 130, 8655–8660 (2018).

109. Lipiec, E., Kaderli, J., Kobierski, J., Riek, R., Skirlinska-Nosek, K., Sofinska, K., Szymonski, M., Zenobi, R., Nanoscale Hyperspectral Imaging of Amyloid Secondary Structures in Liquid, Angew. Chem. Int. Ed., 60, 4545-4550 (2021).

110. Pavlova, A., Cheng, C. Y., Kinnebrew, M., Lew, J., Dahlquist, F. W., Han, S., Protein structural and surface water rearrangement constitute major events in the earliest aggregation stages of tau, Proc. Natl. Acad. Sci. USA, 113, 127–136 (2016).

111. Hasegawa, M., Crowther, R. A., Jakes, R., Goedert, M., Alzheimer-like changes in microtubule-associated protein tau induced by sulfated glycosaminoglycans. Inhibition of microtubule binding stimulation of phosphorylation filament assembly depend on the degree of sulfation, J. Biol. Chem., 272, 33118–33124 (1997).

112. Kampers, T., Friedhoff, P., Biernat, J., Mandelkow, E.-M., Mandelkow, E., RNA Stimulates Aggregation of Microtubule-Associated Protein Tau into Alzheimer-like Paired Helical Filaments, FEBS Lett., 399 (1996).

113. Goedert, M., Jakes, R., Spillantini, M. G., Hasegawa, M., Smith, M. J., Crowther, R. A., Assembly of microtubule-associated protein tau into Alzheimer-like filaments induced by sulphated glycosaminoglycans, Proc. Natl Acad. Sci. USA, 15, 15125–15129 (1996).

114. Zhang, W., Falcon, B., Murzin, A. G., Fan, J., Anthony-Crowther, R., Goedert, M., Scheres, S. H. W., Heparin-induced tau filaments are polymorphic and differ from those in Alzheimer's and Pick's diseases, eLife (2019).

115. Cooney, G. S., Talaga, D., Ury-Thiery, V., Fichou, Y., Huang, Y., Lecomte, S., Bonhommeau, S., Chemical Imaging of RNA-Tau Amyloid Fibrils at the Nanoscale Using Tip-Enhanced Raman Spectroscopy, Angew. Chem. Int. Ed., 62, 6–11 (2023).

116. Zwierzchowski-Zarate, A. N., Mendoza-Oliva, A., Kashmer, O. M., Collazo-Lopez, J. E., White, C. L., Diamond, M. I., RNA induces unique tau strains and stabilizes Alzheimer's disease seeds, J. Biol. Chem., 298, (2022).

117. Ginsberg, S. D., Crino, P. B., Lee, V. M. Y., Eberwine, J. H., Trojanowski, J. Q. Sequestration of RNA in Alzheimer's disease neurofibrillary tangles and senile plaques, Ann. Neurol., 41, 200–209 (1997).

118. Dinkel, P. D., Holden, M. R., Matin, N., Margittai, M., RNA Binds to Tau Fibrils and Sustains Template-Assisted Growth, Biochemistry, 54, 4731–4740 (2015).

119. Wilson, D. M., Bindert, L., Free Fatty Acids Stimulate the Polymerization of Tau and Amyloid Peptides In Vitro Evidence for a Common Effector of Pathogenesis in Alzheimer's Disease, Am. J. Path., 150, (1997).

120. Talaga, D., Smeralda, W., Lescos, L., Hunel, J., Lepejova-Caudy, N., Cullin, C., Bonhommeau, S., Lecomte, S., PIP 2 Phospholipid-Induced Aggregation of Tau Filaments Probed by Tip-Enhanced Raman Spectroscopy. Angew. Chem. Int. Ed., 130, 15964–15968 (2018).

121. Fichou, Y., Lin, Y., Rauch, J. N., Vigers, M., Zeng, Z., Srivastava, M., Keller, T. J., Freed, J. H., Kosik, K. S., Han, S., Cofactors are essential constituents of stable and seeding-active tau fibrils, Proc. Natl. Acad. Sci. USA, 115, 13234–13239 (2018).

122. Fichou, Y., Oberholtzer, Z. R., Ngo, H., Cheng, C. Y., Keller, T. J., Eschmann, N. A., Han, S., Tau-Cofactor Complexes as Building Blocks of Tau Fibrils, Front. Neurosci., 13, (2019).

123. Sofińska, K., Seweryn, S., Skirlińska-Nosek, K., Barbasz, J., Lipiec, E., Tip-enhanced Raman spectroscopy reveals the structural rearrangements of tau protein aggregates at the growth phase, Nanoscale, 16, 5294–5301 (2024).

124. Neugebauer, U., Rösch, P., Schmitt, M., Popp, J., Julien, C., Rasmussen, A., Budich, C., Deckert, V., On the way to nanometer-sized information of the bacterial surface by tip-enhanced Raman spectroscopy, ChemPhysChem, 7, 1428–1430 (2006).

125. Neugebauer, U., Schmid, U., Baumann, K., Ziebuhr, W., Kozitskaya, S., Deckert, V., Schmitt, M., Popp, J., Towards a detailed understanding of bacterial metabolism - Spectroscopic characterization of Stophylococcus epidermidis, ChemPhysChem, 8, 124–137 (2007).

126. Budich, C., Neugebauer, U., Popp, J., Deckert, V., Cell wall investigations utilizing tip-enhanced Raman scattering, J. Microsc., 229, 533–539 (2008).

127. Böhme, R., Richter, M., Cialla, D., Rösch, P., Deckert, V., Popp, J., Towards a specific characterisation of components on a cell surface - combined TERS-investigations of lipids and human cells, J. Raman Spec., 40, 1452–1457 (2009).

128. Böhme, R., Cialla, D., Richter, M., Rösch, P., Popp, J., Deckert, V., Biochemical imaging below the diffraction limit - probing cellular membrane related structures by tip-enhanced Raman spectroscopy (TERS), J. Biophotonics, 3, 455–461 (2010).

129. Lajoie, P., Kojic, L. D., Nim, S., Li, L., Dennis, J. W., Nabi, I. R., Caveolin-1 regulation of dynamin-dependent, raft-mediated endocytosis of cholera toxin–B sub-unit occurs independently of caveolae, J. Cell. Mol. Med., 13, 3218–3225 (2009).

130. Opilik, L., Bauer, T., Schmid, T., Stadler, J., Zenobi, R., Nanoscale chemical imaging of segregated lipid domains using tip-enhanced Raman spectroscopy, Phys. Chem. Chem. Phys., 13, 9978–9981 (2011).

131. Richter, M., Hedegaard, M., Deckert-Gaudig, T., Lampen, P., Deckert, V., Laterally resolved and direct spectroscopic evidence of nanometer-sized lipid and protein domains on a single cell, Small, 7, 209–214 (2011).

132. Deckert-Gaudig, T., Böhme, R., Freier, E., Sebesta, A., Merkendorf, T., Popp, J., Gerwert, K., Deckert, V., Nanoscale distinction of membrane patches - a TERS study of Halobacterium salinarum, J. Biophotonics, 5, 582–591 (2012).

133. Naumenko, D., Snitka, V., Serviene, E., Bruzaite, I., Snopok, B., In vivo characterization of protein uptake by yeast cell envelope: Single cell AFM imaging and μ-tip-enhanced Raman scattering study, Analyst, 138, 5371–5383 (2013).

134. Nakatam A., Nomoto, T., Toyota, T., Fujinami, M., Tip-enhanced Raman Spectroscopy of Lipid Bilayers in Water with an Alumina- and Silver-coated Tungsten Tip, Anal. Sci., 29, 865–869 (2013).

135. Watkins-Mariani, M., Deckert-Gaudig, T., Deckert, V., Label-free in vitro visualization and characterization of caveolar bulbs during stimulated re-epithelialization, Anal. Bioanal. Chem., 406, 6993–7002 (2014).

136. Rusciano, G., Zito, G., Isticato, R., Sirec, T., Ricca, E., Bailo, E., Sasso, A., Nanoscale chemical imaging of bacillus subtilis spores by combining tip-enhanced Raman scattering and advanced statistical tools, ACS Nano, 8, 12300–12309 (2014).

137. Kumar, N., Drozdz, M. M., Jiang, H., Santos, D. M., Vaux, D. J., Nanoscale mapping of newly-synthesised phospholipid molecules in a biological cell using tip-enhanced Raman spectroscopy, Chem. Commun., 53, 2451–2454 (2017).

138. Pandey, Y., Kumar, N., Goubert, G., Zenobi, R., Nanoscale Chemical Imaging of Supported Lipid Monolayers using Tip-Enhanced Raman Spectroscopy, Angew. Chemie Int. Ed., 60, 19041–19046 (2021).

139. Mrđenović, D., Ge, W., Kumar, N., Zenobi, R., Nanoscale Chemical Imaging of Human Cell Membranes Using Tip-Enhanced Raman Spectroscopy, Angew. Chem. Int. Ed., 134, (2022).

140. Mrđenović, D., Tang, Z. X., Pandey, Y., Su, W., Zhang, Y., Kumar, N., Zenobi, R., Regioselective Tip-Enhanced Raman Spectroscopy of Lipid Membranes with Sub-Nanometer Axial Resolution, Nano Lett., 23, 3939–3946 (2023).

141. Szczerbiński, J., Metternich, J. B., Goubert, G., Zenobi, R., How Peptides Dissociate in Plasmonic Hot Spots, Small, 16, (2020).

142. Schmid, T., Opilik, L., Blum, C., Zenobi, R., Nanoscale chemical imaging using tip-enhanced raman spectroscopy: A critical review, Angew. Chem. Int. Ed., 52, 5940–5954, (2013).

143. Nyamekye, C. K. A., Weibel, S. C., Smith, E. A., Directional Raman scattering spectra of metal–sulfur bonds at smooth gold and silver substrates, J. Raman Spec., 52, 1246–1255 (2021).

144. Huang, Y.-P., Huang, S.-C., Wang, X.-J., Bodappa, N. Li, C.-Y., Yin, H., Su, H.-S., Meng, M., Zhang, H., Ren, B., Yang, Z.-L., Zenobi, R., Tian, Z.-Q., Li, J.-F., Shell-Isolated Tip-Enhanced Raman and Fluorescence Spectroscopy, Angew. Chem. Int. Ed., 57, 7523–7527 (2018).

145. Xiao, L., Bailey, K. A., Wang, H., Schultz, Z. D., Probing Membrane Receptor-Ligand Specificity with Surface- and Tip- Enhanced Raman Scattering, Anal. Chem., 89, 9091–9099 (2017).

146. Xiao, L., Wang, H., Schultz, Z. D., Selective Detection of RGD-Integrin Binding in Cancer Cells Using Tip Enhanced Raman Scattering Microscopy, Anal. Chem., 88, 6547–6553 (2016).

147. Olschewski, K., Kämmer, E., Stöckel, S., Bocklitz, T., Deckert-Gaudig, T., Zell, R., Cialla-May, D., Weber, K., Deckert, V., Popp, J., A manual and an automatic TERS based virus discrimination, Nanoscale, 7, 4545–4552 (2015).

148. Britz-Grell, A. B., Saumer, M., Tarasov, A., Challenges and Opportunities of Tip-Enhanced Raman Spectroscopy in Liquids, J. Phys. Chem. C, 125, 21321–21340 (2021).

149. Wang, X., Huang, S. C., Huang, T. X., Su, H. S., Zhong, J. H., Zeng, Z. C., Li, M. H., Ren, B., Tip-enhanced Raman spectroscopy for surfaces and interfaces, Chem. Soc. Rev., 46, 4020–4041 (2017).

150. Blum, C., Opilik, L., Atkin, J. M., Braun, K., Kämmer, S. B., Kravtsov, V., Kumar, N., Lemeshko, S., Li, J. F., Luszcz, K., Maleki, T., Meixner, A. J., Minne, S., Raschke, M. B., Ren, B., Rogalski, J., Roy, D., Stephanidis, B., Wang, X., Zhang, D., Zhong, J. H., Zenobi, R., Tip-enhanced Raman spectroscopy - An interlaboratory reproducibility and comparison study, J. Raman Spec., 45, 22–31 (2014).

151. Schmid, T., Yeo, B. S., Leong, G., Stadler, J., Zenobi, R., Performing tip-enhanced Raman spectroscopy in liquids, J. Raman Spec., 40, 1392–1399 (2009).

152. Kumar, N., Su, W., Veselý, M., Weckhuysen, B. M., Pollard, A. J., Wain, A. J., Nanoscale chemical imaging of solid-liquid interfaces using tip-enhanced Raman spectroscopy, Nanoscale, 10, 1815–1824 (2018).

153. Bhattarai, A., Joly, A. G., Krayev, A., El-Khoury, P. Z., Taking the Plunge: Nanoscale Chemical Imaging of Functionalized Gold Triangles in H2O via TERS, J. Phys. Chem. C, 123, 7376–7380 (2019).

154. Kurouski, D., Mattei, M., Van Duyne, R. P., Probing Redox Reactions at the Nanoscale with Electrochemical Tip-Enhanced Raman Spectroscopy, Nano Lett., 15, 7956–7962 (2015).

155. Zeng, Z. C., Huang, S. C., Wu, D. Y., Meng, L. Y., Li, M. H., Huang, T. X., Zhong, J. H., Wang, X., Yang, Z. L., Ren, B., Electrochemical Tip-Enhanced Raman Spectroscopy, J. Am. Chem. Soc., 137, 11928–11931 (2015).

156. Mattei, M., Kang, G., Goubert, G., Chulhai, D. V., Schatz, G. C., Jensen, L., Van Duyne, R. P., Tip-Enhanced Raman Voltammetry: Coverage Dependence and Quantitative Modeling, Nano Lett., 17, 590–596 (2017).

157. Kang, G., Yang, M., Mattei, M. S., Schatz, G. C., Van Duyne, R. P., In Situ Nanoscale Redox Mapping Using Tip-Enhanced Raman Spectroscopy, Nano Lett. 19, 2106–2113 (2019).

158. Bao, Y. F., Cao, M. F., Wu, S. S., Huang, T. X., Zeng, Z. C., Li, M. H., Wang, X., Ren, B., Atomic Force Microscopy Based Top-Illumination Electrochemical Tip-Enhanced Raman Spectroscopy, Anal. Chem., 92, 12548–12555 (2020).

159. Kumar, N., Wondergem, C. S., Wain, A. J., Weckhuysen, B. M., In Situ Nanoscale Investigation of Catalytic Reactions in the Liquid Phase Using Zirconia-Protected Tip-Enhanced Raman Spectroscopy Probes, J. Phys. Chem. Lett., 10, 1669–1675 (2019).

160. Bhattarai, A., El-Khoury, P. Z., Nanoscale Chemical Reaction Imaging at the Solid Liquid Interface via TERS, J. Phys. Chem. Lett., 10, 2817–2822 (2019).

Chapter 2

Instrumentation and Experimental Developments

Introduction

TERS can achieve fine chemical characterization with nanoscale spatial resolution thanks to the efficient coupling of Raman spectroscopy with SPM. Since its inception in the early 2000's, TERS instrumentation has developed at a steady pace. The evolution of the technique has been driven by advancements in both Raman spectroscopy and SPM technologies. Specifically, improvements in the fabrication of TERS-active tips, optimisation of the optical set-up, and incorporation of advanced microscopy techniques have led to significant enhancements in spatial resolution and sensitivity. Additionally, the commercialisation of TERS instrumentation in the last decade has broadened the userbase, making the technique more accessible to the wider scientific community.

The first experimental demonstrations of TERS used STM as the SPM system, with gold or silver acting as the plasmonic metal enabling the Raman enhancement at the tip apex. While this system coupling is still valid to this day, the combination of TERS with AFM as the SPM system is the greatest development with regards to advanced microscopy techniques. STM can operate in vacuum, under inert gas, ambient air, or liquid but requires a conductive sample surface for the tunnelling effect to occur. AFM is more versatile as an SPM technique comparatively as there is no environment or substrate conditions. AFM-TERS has allowed for non-conductive materials, polymers, and biological samples to be effectively studied. Additionally, improvements in the AFM instrument directly contributed to the development of TERS systems that are more user-friendly and performant than the first AFM-TERS set-ups. For example, the development of AFM for operation in liquids has directly inspired the development of TERS in liquids. TERS in liquid media is of interest to both the electrochemical and the biological TERS communities. The efforts to optimise our AFM-TERS system for use in liquid media is subject of **Chapter 5**. Technological advancements such as high-speed AFM (HS-AFM)[1] begs the question of the future application of TERS in similar high-speed set-ups for near real-time mapping of biological processes, as already demonstrated in the HS-AFM literature.

Improvements in the Raman spectrometer has also helped the development of TERS. In particular, high-sensitivity detection systems such as charged-coupled device (CCD) detectors have improved the signal-to-noise ratio. Optimisation of optical set-ups including side-, top-, and bottom-illumination geometries has led to better laser focus on the tip-sample junction allowing for more efficient tip enhancement in addition to Raman signal collection. Inspired by the developments of the Kawata group,[2] our group has developed a one-of-a-kind total-internal reflection TERS (TIR-TERS) which is described in detail in **Chapter 2.1.2**. This TIR system combines the efficient TERS tip excitation of bottom-illumination geometries with the low laser fluence of the evanescent field excitation and has been demonstrated to give 8 times more enhancement over direct illumination conditions.[3] The TIR-TERS system allows for not only conventional Raman and SERS measurements to be performed, but TIR-based dark-field scattering microscopy (DFSM) enables the visualisation and characterisation of nano-objects including measuring the LSPR band of TERS tips. See **Chapter 2.1.3** for details.

Chapter 2.2 discusses some of the available physical vapour deposition methods at GSM for the fabrication of TERS probes. Their characterisation and suitability for our desired TERS applications are discussed.

2.1. Description of TERS instrumental set-ups

If a sample is irradiated with coherent or non-coherent monochromatic radiation in the UV, visible, or near-IR range, a Raman spectrum can be obtained via the process described in **Chapter 1.1.3**. The emitted radiation is usually non-coherent, where the weak Raman lines are shifted from the excitation frequency and the strong Rayleigh line by definite quantities. To measure this scattered light, a Raman spectrometer is required.

A typical Raman spectrometer combines several key components: a radiation source, sample arrangement, spectral dispersion or selection devices, a CCD detector, and recording and evaluation facilities which are served by computers nowadays. The laser source produces monochromatic light to excite the sample and typically come in the form of diodes and noble gas ion lasers. Microscope stages are typically used as sample holders as they can provide precise positioning of the objective lens which is focused onto the sample. Depending on the desired experiment, extra units can be used with the sample stage such as heating or cooling elements that can be attached to study samples with temperature dependence. For TERS experiments, the special coupling to an SPM system has to be considered, with the sample having to conform to the restrictions of the given SPM type.

The optical system housed inside the spectrometer consists of the mirrors, lenses, filters, and beam splitters that direct and focus the laser light onto the sample. This is in addition to collecting the scattered light and directing it towards the detecting elements. To maximise signal intensity and resolution great care is needed in the alignment of the system optics, which is extended in TERS to the focus and alignment of the laser beam with the SPM tip. After the sample light is backscattered, a filter (notch or edge filter) isolates the significantly weaker Raman signal from the intense elastic Rayleigh scattering. Before reaching the detector, the collected Raman scattered light is dispersed by a spectrograph into its component wavelengths giving rise to the measurement spectrum. The spectrograph is most typically taking the form of concave mirrors or lenses and diffraction grating with a set number of grooves per mm determining the spectral resolution and conversely the spectrum measurement window. Finally, the detector captures the dispersed Raman signal which is converted into an electrical signal output that is converted into the readable spectrum. Photomultiplier tubes, avalanche photodiodes, and charged-coupled devices are typical detectors used in Raman spectrometers. The details of the specific Raman spectrometers and their coupling with AFM systems used in this work are outlined in the subsequent sections.

2.1.1. Side-illumination geometry

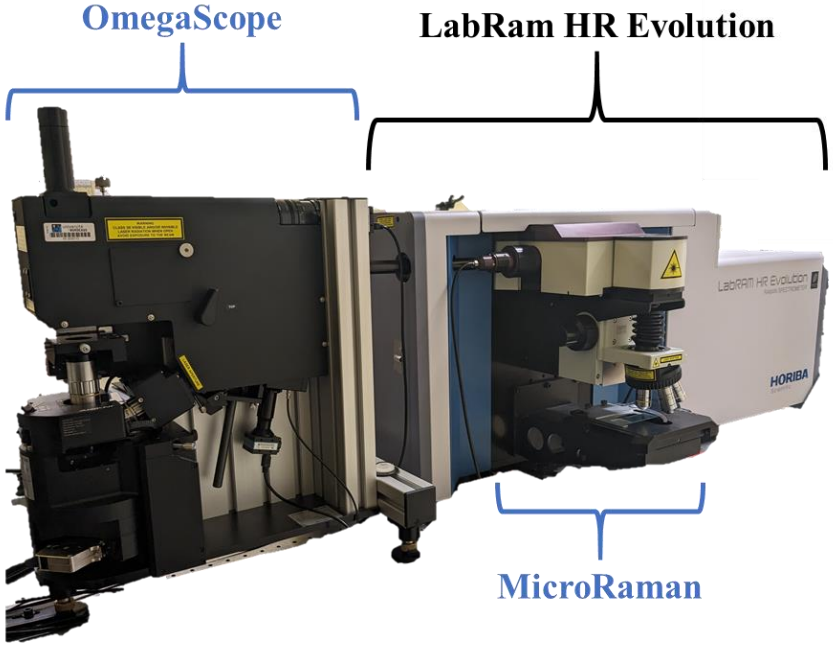

Figure 2.1. *Side-illumination TERS system consisting of the piezo-controlled OmegaScope optical platform coupled to the SmartSPM system, and a LabRam HR Evolution Raman spectrometer. The LabRam system is also coupled to a MicroRaman platform.*

The first of the two TERS instruments available at GSM is the side-illumination geometry instrument shown in **Figure 2.1**, which consists of the coupling between an OmegaScope scanning probe microscope (AIST-NT), and a LabRam HR Evolution Raman spectrometer (HORIBA Scientific). Our LabRam HR Evolution spectrometer is fitted with the two laser lines 532 nm and 633 nm, which typically match well with the plasmon bands of Ag- and Au-coated TERS tips respectively. For detection, an electron multiplier CCD (Synapse EM, HORIBA) is used for its high sensitivity and fast spectral acquisition capability. The optical path of the spectrometer is illustrated in **Figure 2.1**, and has two modes of operation. The MicroRaman optical microscope protrudes from the side of the spectrometer, allowing for general purpose Raman measurements and spectrometer calibration using silicon wafers. The system can be configured towards the OmegaScope, located to the left side of the spectrometer. This optical coupling system features the scanning probe microscope (Smart SPM, AIST-NT) and the optical microscope equipped with top and side piezo-mounted objectives. The top objective is mainly used for tip-sample alignment and visual inspection, while the side objective aids laser-tip alignment including hotspot localisation, focalisation of the incident laser light, and collection of the back-scattered light.

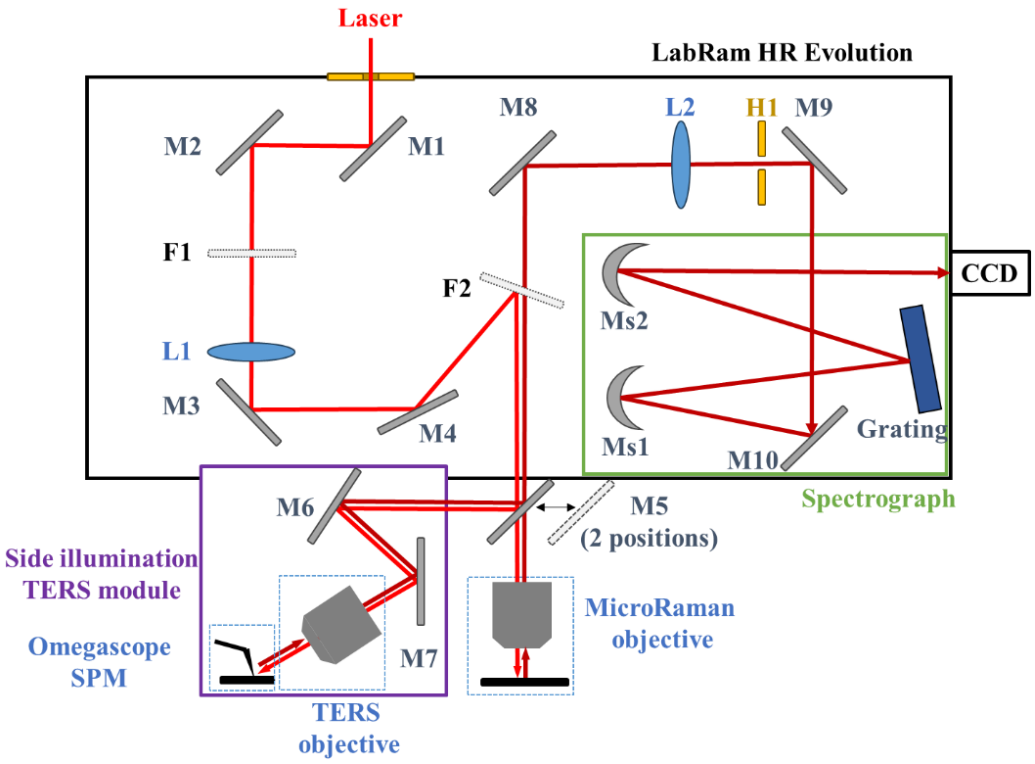

***Figure 2.2**. LabRAM HR Evolution schematic of the laser optical path and its optical coupling with the MicroRaman optical microscope and side illumination TERS module equipped with the OmegaScope SPM system (Top objective omitted for clarity). M = mirror, F = filter, L = lens, H = hole, Ms = spherical mirror.*

Prior to entering the Raman spectrometer, a flip-mounted mirror enables the selection of either the 532 nm diode laser (Huebner Photonics) or the 633 nm HeNe laser (LASOS Lasertechnik GmbH) for the optical path (not pictured). When the 633 nm HeNe laser is used, an additional narrow bandpass filter is implemented to supress non-lasing lines arising from secondary emissions and background plasma. As depicted in **Figure 2.2**, the laser light subsequently enters the spectrometer and is directed by mirrors M1 and M2 along the main path. The beam passes through the filter wheel F1 to control the laser fluence at the sample. This laser intensity attenuation filter wheel has 8 different neutral density (ND) filters, resulting in optical densities of 100%, 50%, 25%, 10%, 5%, 1%, 0.1%, and 0.01%. This unit is controlled via the LabSpec 6 (HORIBA Scientific) software, and enables the tuning of the laser power depending on measurement requirements and sample sensitivity. The beam expander lens L1 increases the laser beam diameter (in order to fill the entrance pupil of the 100X TERS objective) and is directed to the laser rejection filter set F2 with mirrors M3 and M4. This filter set features pass-band edge filters for both the 532 and 633 nm lasers, which can be selected via the LabSpec 6 software. This filter also acts as a mirror to send the laser light towards a following retractable mirror M5, that selects the optical path of either the MicroRaman microscope head (fitted with various objective lenses), or the reflection TERS module equipped with the OmegoScope SPM. There is a manually-operated retractable camera before the TERS objective that allows for the real time visualisation and facilitates the coarse laser-tip alignment (not pictured in **Figure 2.2**). The back-scattered sample signal, either from the MicroRaman or TERS module, is collected through the same objective and passes back through filter set F2 and the L2 lens to focus the Raman signal on the H1 adjustable pinhole aperture which controls the confocal nature of the microscope and serves as the entrance slit of the spectrometer. For TERS, a better focus on the tip apex results in more intense near-field signal and a good confocal system reduces far-field background contribution. After H1, a shutter enables discrete spectral acquisition times. Mirror M9 directs the beam into a Czerny-Turner monochromator, which consists of two concave mirrors Ms1 and Ms2, and one planar diffraction grating. Depending on the desired resolution for the acquired spectra, either a 300 or 600 grooves per mm grating can be selected. This is because when the groove density of the diffraction grating increases (or when the excitation wavelength or exit focal length increases) the spectral separation decreases (i.e. the spectral resolution increases). The photodetector, the Synapse EM-CCD, consists of an array of 1600 x 200 pixels with 16 x 16 µm pixel size.

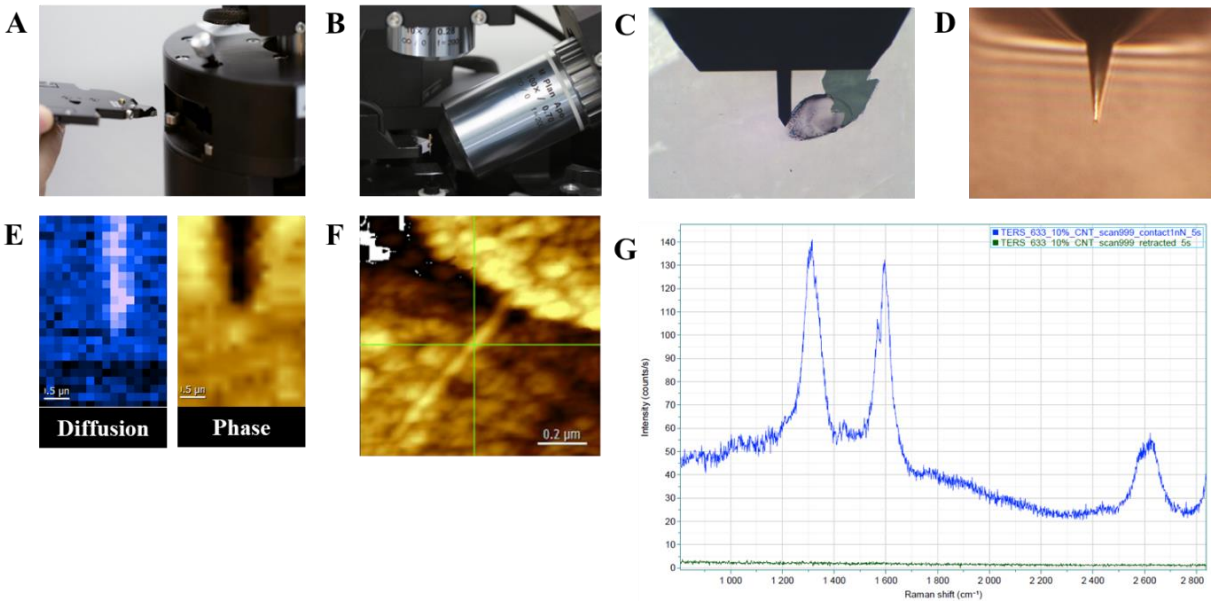

***Figure 2.3**. Steps of TERS measurement using the side-illumination configuration. **[A]** Mounting the AFM chip holder into the SmartSPM head. **[B]** View of the top 10X / 0.28 NA objective, and the side 100X / 0.70 NA objective. **[C]** Top camera view of an ACCESS-FM cantilever positioned close to the sample surface. **[D]** Side camera view of an ACCESS-FM tip with illuminated apex. **[E]** Diffusion and phase images of the tip from D recorded using the SWIFT™ scan mode. **[F]** AFM image of a carbon nanotube (CNT) on gold. **[G]** TERS point spectra at 633 nm of CNT (green cross) when the tip is in contact with the sample (blue spectrum) or retracted (green). The TERS spectrum features the characteristic D- (1300 cm^{-1}), G- (1580 cm^{-1}), and G'-bands (2600 cm^{-1}).*

The AFM system features two sample stages (a motorized motors stage for long range travel and a piezo stage for short range travel and AFM scanning) that can move in X, Y, and Z directions with a fixed tip. The protocol for TERS measurements on such a system follows several steps. Initially, correct calibration of the Raman spectrometer should be verified using the wavenumber and intensity of a Si reference sample. After the preparation of a convenient sample, the prepared TERS tip is mounted on the AFM probe holder which is subsequently inserted into the AFM head (**Figure 2.3A**). As with any tapping-mode AFM measurement, the first step is the cantilever alignment with the AFM infrared laser. The AFM probe holder is moved via stepping motors so as to scan the cantilever in the XY-plane relative to the IR laser. The cantilever is located by the reflection of the IR laser on the backside of the cantilever, and the laser spot is positioned at 25% of the cantilever length from the tip end (for diving board cantilevers). The position can be manually adjusted to an area of greater reflection if desired. This is often the case for inhomogeneous backside coatings from deposition methods, or in liquid environments where the cantilever diffusion is reduced. Once the laser position has been

adjusted, the laser diode focus is then set to give an accurate magnitude read-out of the tip oscillation. After setting adjusting the laser diode, the tip resonance is set. This is done by sweeping between a set low and high frequency (55 – 550 kHz, for example) and identifying the maximum magnitude frequency (ca. 70 kHz for ACCESS-FM AFM tips). For AFM measurements in liquid, the resonance frequency is typically halved, and may not appear as the strongest or sharpest peak. Therefore, extra care is needed to verify the actual resonance frequency when performing measurements in liquid environments. Next, the positioning of the AFM cantilever with respect to the objective lenses and excitation laser need to be aligned (**Figure 2.3B**). Three screws, two on either side of the SmartSPM and one on the bottom, allow for the coarse adjustment, which can be visualised by the use of the top-mounted optical camera (to position the tip relative to the sample centre), and by the side-mounted camera (to position the laser onto the tip apex) (**Figure 2.3C** and **D**). The excitation laser spot is visualised on the end of the AFM probe using the 0.01% filter before using the side camera and preparing to localise the TERS hotspot. This is achieved via objective piezo scanners by scanning the laser over the tip and generating a diffusion image using a low laser power (1 – 3.2% filter). The SWIFT^{TM} mode is used here, which allows for optimised detector-stage coordination and for the fast (sub-second) spectral acquisition. Diffusion and phase images are recorded in the XY plane (relative to the Z incident beam) and the highest diffusing pixel is determined as the hotspot (**Figure 2.3E**). This is repeated in the XZ and the XY plane again to guarantee laser focalisation onto the tip end in three dimensions. With the tip-laser alignment complete, the tip can be approached to the sample and the resonance frequency of the tip double-checked, as thermalisation of the tip during the alignment may alter the frequency. The landing procedure is performed, and a preliminary AFM height image of the sample is recorded (**Figure 2.3F**). When a convenient area of sample is located, the TERS signal should be identified using a point measurement (**Figure 2.3G**). If obtained, then TERS imaging can be attempted. If not, the hotspot positioning might need fine adjustment using the previously measured tip diffusion images. A continued lack of signal may require realignment of the laser on the tip apex, or total replacement of the tip given TERS inactivity.

2.1.2. Total-Internal Reflection geometry

The second TERS instrument available at GSM is the bottom-illumination geometry total-internal reflection (TIR) system shown in **Figure 2.4**. This instrument consists of the coupling between an inverted optical microscope (Olympus IX 71), Combiscope AFM instrument (AIST-NT, HORIBA Scientific), and a LabRam HR Raman spectrometer (HORIBA Scientific). It includes an oil-immersion high NA (1.49) 60X TIR objective. The system is fitted with four laser lines 532 nm, 561 nm, 633 nm, and most recently 660 nm. The additional lasers lines with respect to the side-illumination TERS system help with more closely matching LSPR bands of TERS tips, which can also be measured by this system through the use of dark-field scattering microscopy (DFSM). DFSM is further detailed in **Chapter 2.1.3**. The optical path of the TIR-TERS system is illustrated in **Figure 2.5**. The retractable AFM head enables the measurement of conventional Raman, SERS, and TERS in direct bottom or TIR configurations in addition to standard AFM and DFSM measurements. An accompanying video camera and backlight can be used via a retractable beam splitter to visualise the sample surface and help adjust laser focus on the sample.

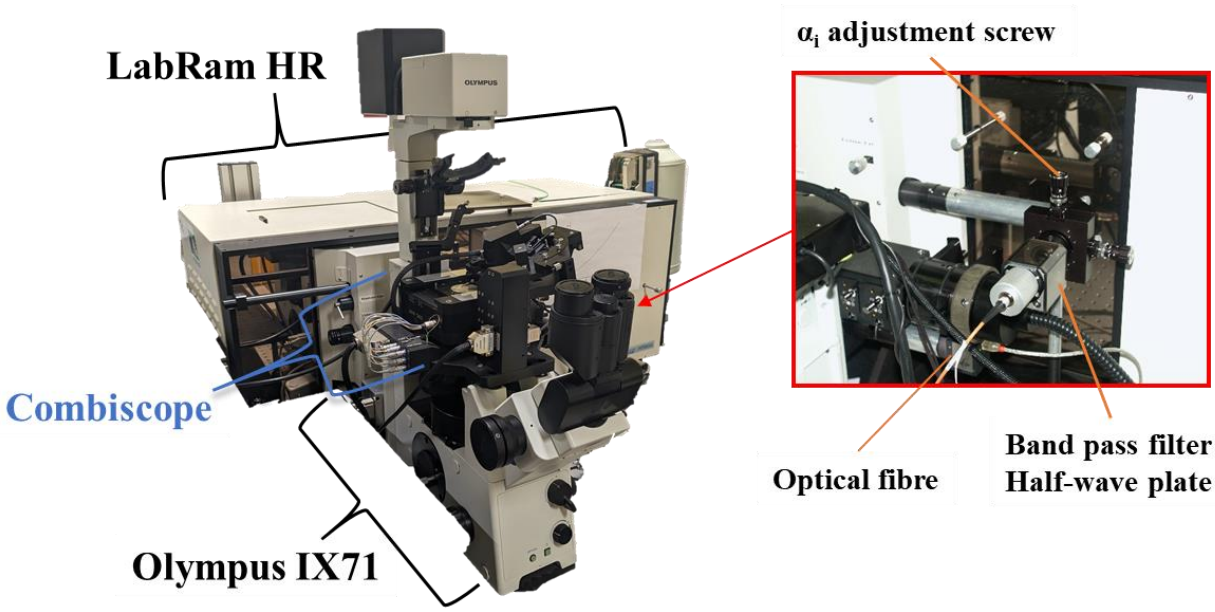

Figure 2.4. *TIR-TERS system consisting of the Combiscope AFM mounted on an inverted microscope Olympus IX71 coupled to a LabRam HR Raman spectrometer. The red insert shows the input of the laser optical fibre into the TIR optical unit that allows for the adjustment of light polarisation and incidence angle, α_i.*

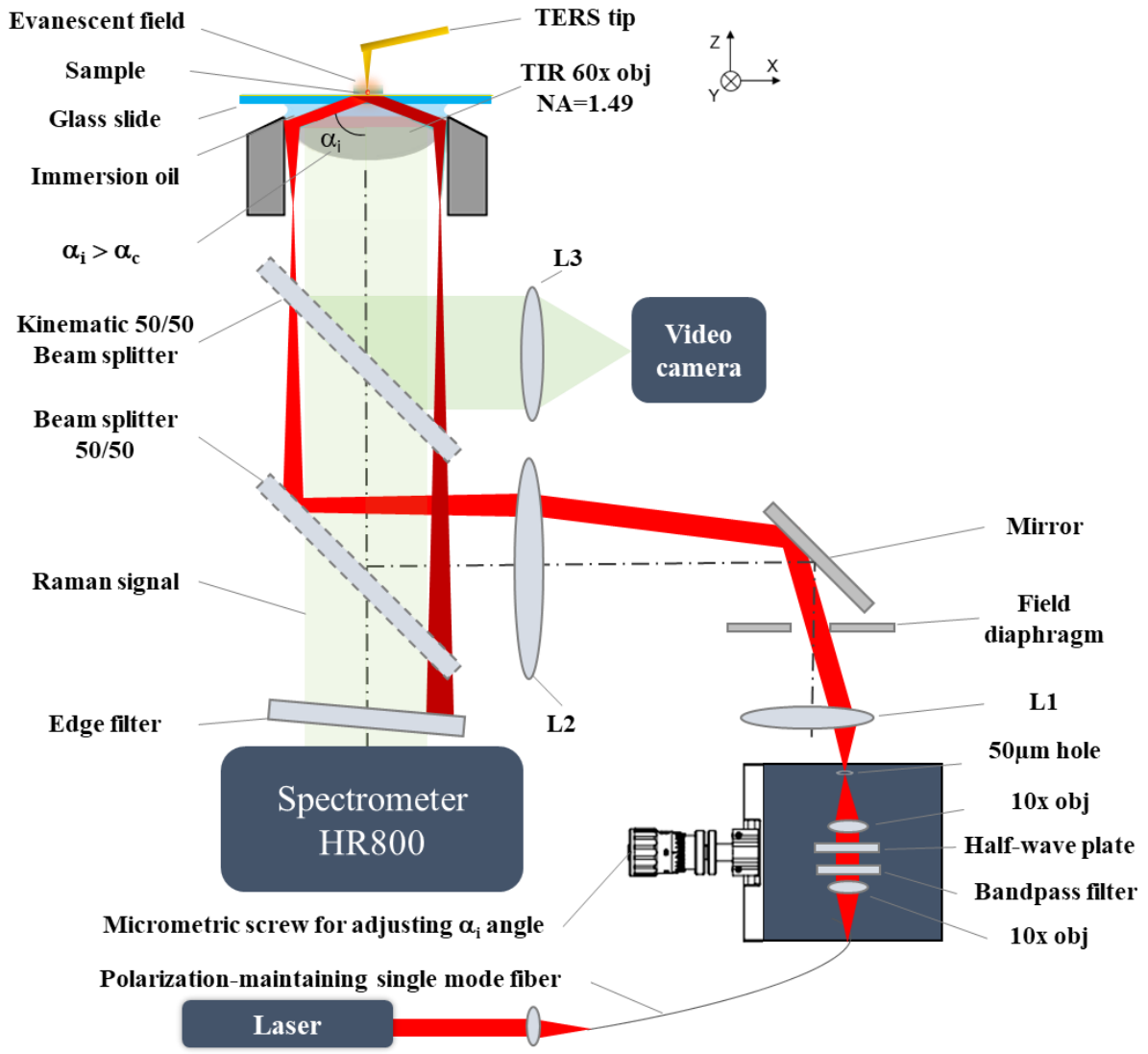

Figure 2.5. *Schematic of Total-Internal Reflection (TIR)-TERS optical path and its coupling between the Combiscope AFM and the LabRAM HR spectrometer. L = Lens. Adapted from Talaga et al. 2020.*[4]

The TIR-TERS system illustrated in **Figure 2.4** features an inverted Olympus IX71 optical microscope, Combiscope AFM (HORIBA Scientific), and the LabRam HR800 spectrometer (HORIBA Scientific). The spectrometer features a 300 grooves per mm grating along with a nitrogen-cooled CCD detector for spectral acquisition. The laser beam is focused into a polarisation-maintaining single mode optical fibre which is connected to a 10X objective for the beam collimation. A second 10X objective focus the light into a 50 µm-diameter pinhole. A band-pass filter and half-wave plate introduced between the two objective lenses allow the filtration of the Raman signal generated in the optical fibre and for the determination of polarisation at the TIR objective entrance (*p* or *s* polarisation). The positioning of the set (10X objectives, bandpass filter, halfwave plate, pinhole) is controlled by a micrometric screw that

allows for the control of the laser incidence angle at the sample. The incident light is directed via lenses L1 and L2 towards the 50/50 beam splitter, and subsequently onto one side of the back focal plane of the 60X oil-immersion TIR objective (NA = 1.49). The field diaphragm can be adjusted to modulate the spatial extension (5 – 80 µm) of the evanescent wave in the object focal plane. The reflected beam and the scattered light from the sample surface is collected through the same TIR objective, with the elastic scattered light being filtered out by an edge filter before entering the spectrometer.

Similar to the side-illumination TERS system, the first step before performing an experiment is the calibration of the Raman spectrometer. This is achieved by setting the Rayleigh line of the scattered radiation to 0 cm^{-1}. This calibration can be also verified using the 520.5 cm^{-1} Si signature from the AFM probe. A convenient sample for studying in TIR geometry must be optically transparent while allowing for correct focalisation on the sample surface. To this end, glass or quartz glass coverslips with a thickness of 0.13 – 0.17 mm are most suited for TIR-TERS measurements. A smooth film of Au can be sputtered up to a thickness of 10 nm onto the glass or quartz coverslip to give gap-mode enhancement while still remaining largely optically transparent. Muscovite mica, which is commonly used in AFM imaging of biomolecules, is not compatible with the system in its pure form. As detailed in **Chapter 5**, a glass substrate with a thin layer of mica can be fabricated to try and achieve a compromise in surface biocompatibility and substrate structural integrity. The prepared TERS tips are loaded into the AFM holder. An alignment with the AFM IR laser follows as previously discussed for the side-illumination geometry (see **Chapter 2.1.1**). The adjustment of the AFM laser diode is followed by setting the tip resonance, as per **Chapter 2.1.1**. The positioning of the AFM cantilever with respect to the objective lenses and excitation laser differs significantly from side-illumination. Initially, the oil-immersion objective needs to be engaged with the substrate and focused onto the top of the sample at the glass-air interface. This is achieved by visualising the TIR laser spot (or broadband white light when operating in DFSM) using the optical camera and carefully adjusting the fine focus of the lens. With the surface in focus, the TERS tip should be next engaged onto the sample surface. The tip is often visible by its relatively bright diffusion, but can also be localised using the projected shadow of the cantilever when backlit. Stepping motors of the TIR sample stage enable the adjustment of the sample over the TIR objective, while a motorized system controls the fine positioning of the TERS tip relative to the TIR objective. As illustrated in **Figure 2.6**, TIR-geometry in *p*-polarization and close to the critical angle (42°) guarantee the optimal excitation of the TERS tip apex (electric field oriented only along the Z direction), which is a major time-save of the technique compared

to side-illumination or direct illumination in bottom configuration. Moreover, the large size of the laser beam in TIR illumination (5 – 80 µm), avoids laser tip misalignment regularly observed during direct illumination setup. With the TERS tip aligned with the centre of the TIR laser spot, the tip resonance frequency and sample focus should be double-checked before proceeding to landing. AFM imaging of the sample is performed and when a convenient sample area is located, TERS point measurements and later mapping can be performed. As true for all TERS measurements, a lack of TERS signal should be investigated by changing the sample area, refocusing and realigning the laser, and changing the sample and/or tip.

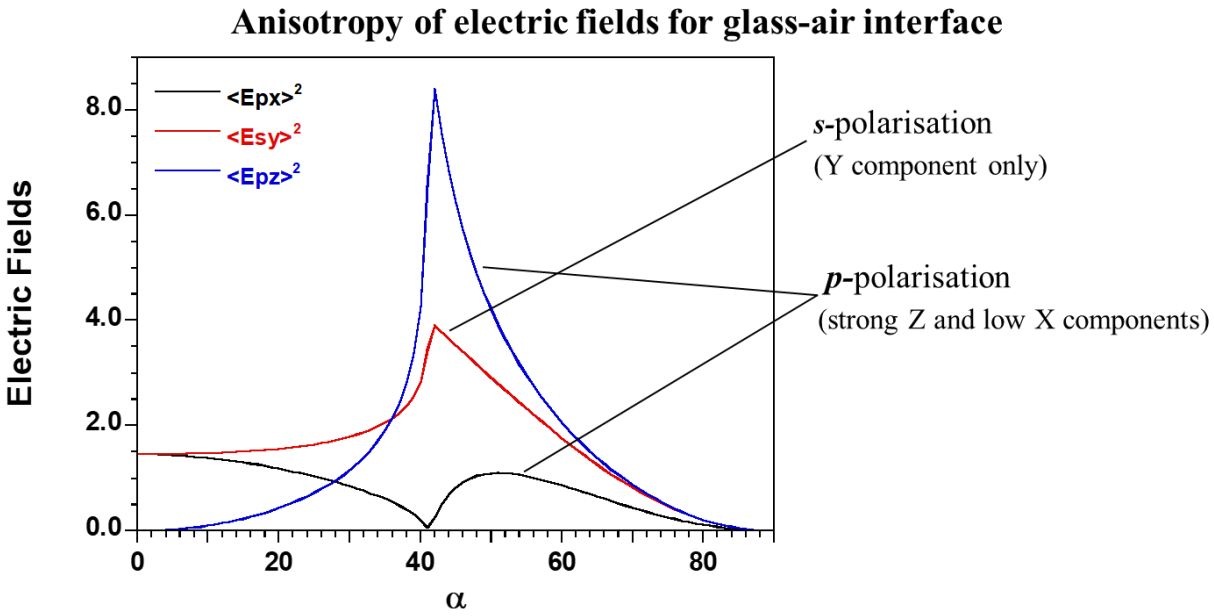

Figure 2.6. *Anisotropy of electric fields for a glass-air interface as the square of electric field versus angle of incidence, α (degrees). Light that is s-polarised is unsuitable for TERS tip excitation as the electric field is orientated only along Y, which is off-axis. Light that is p-polarised is highly suited for TERS tip excitation as, at the critical angle (42°), the electric field is orientated parallel to the tip axis along Z.*

2.1.3. Dark-field Scattering Microscopy

Dark-field scattering microscopy (DFSM) is an interesting technique in that it has been proven to be a powerful tool to examine LSPR responses of nanoparticles, and thus by extension the LSPR response of TERS tips. DFSM surpasses conventional bright field microscopy in analysing nanoparticles as only light scattered by the sample is collected with the direct illumination being blocked, creating an image of bright spots on a dark background, with improved optical contrast. Traditional DFSM uses a high-angle excitation light with scattered

photons being collected with a low NA objective. DFSM can be coupled with TIR by using the correct optics and a light source that creates an evanescent wave at the sample-substrate interface. The TIR illumination only excites particles within a very thin layer near the surface, giving high-contrast images with high surface specificity. Better yet, DFSM can also be combined with AFM to determine nanoparticle morphology and orientation.[5]

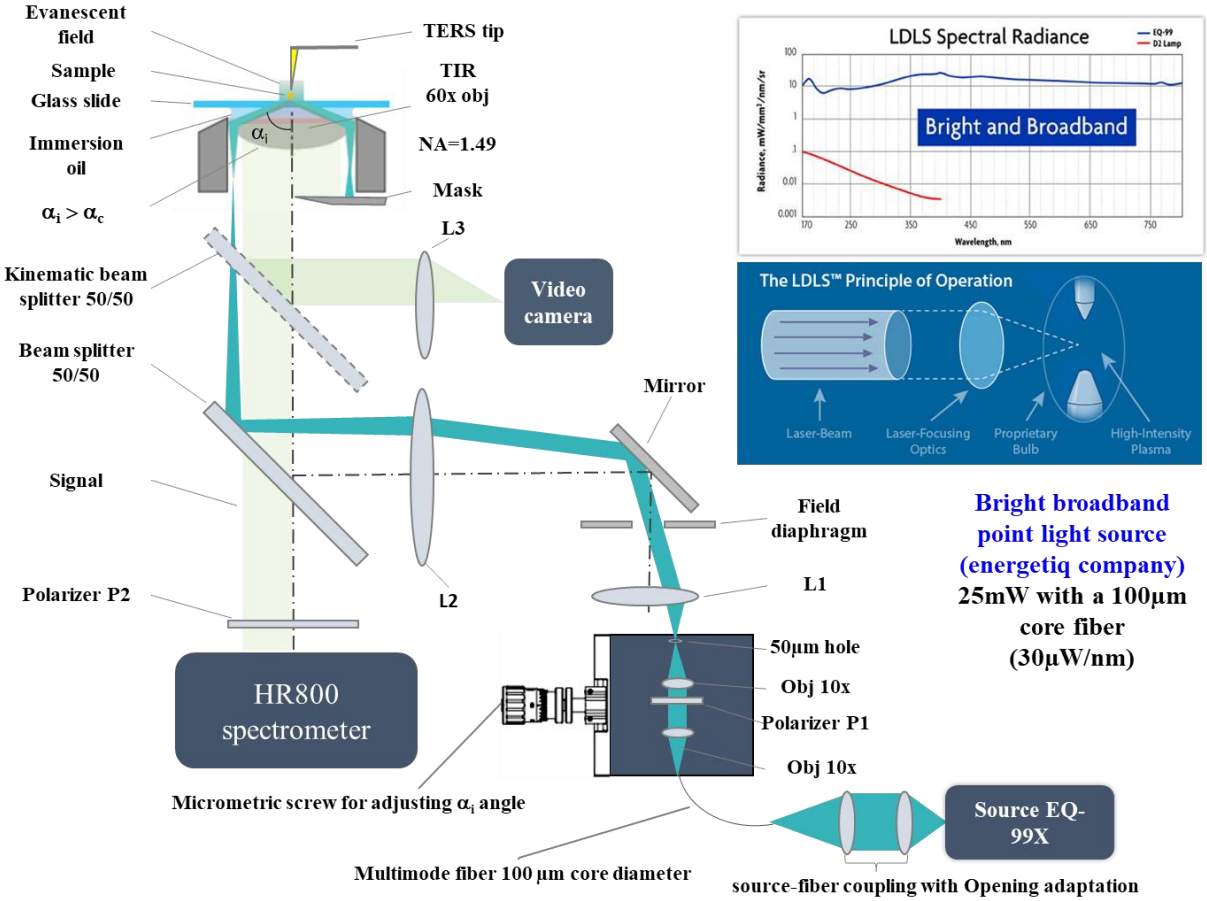

Figure 2.7. *Schematic of the optical path for dark-field scattering microscopy operation. The light source is a bright broadband source that gives high spectral radiance from the UV to the near-IR.*

The DFSM system is illustrated in **Figure 2.7**. The inverted Olympus IX71 optical microscope is integrated with the Combiscope AFM (HORIBA Scientific) allowing for nanoscale imaging and TERS. This is coupled with the LabRam HR800 spectrometer that features a nitrogen-cooled CCD detector and a 300 grooves per mm grating (not pictured). Instead of the laser light used in TERS, for DFSM measurements a compact LDLS EQ-99X Energetiq broadband unpolarised white light source is implemented (see insert). A 100 µm core multimodal optical fibre transfers the emerging light onto a 50 µm-diameter pinhole via two

coupled 10X microscope objectives. The polarizer P1 allows for the modulation of the linearly polarised light from *s*- to *p*-polarisation. The lenses L1 and L2 along with the 50/50 beam splitter reflect the light onto one side of the back focal plane of the oil-immersion TIR objective (60X, NA = 1.49). A tuneable iris (field diaphragm) allows the control of the spatial extension of the evanescent wave in the object focal plane. The incidence angle of the resulting TIR illumination can be finely adjusted by moving the point source out of the L1 optical axis using a micrometre screw. The reflected TIR beam is physically blocked by a mask at the objective exit creating the dark field. The remaining half of the scattered light collected by the TIR objective is focused onto the confocal hole and later onto the entrance slit (not shown) of the spectrometer allowing for spectroscopic measurements. The lens L3 and the kinematic beam splitter allows for video imaging of the sample. A DFSM image of a TERS tip engaged on a glass coverslip and retracted from the surface is shown in **Figure 2.8A** and **B**, respectively.

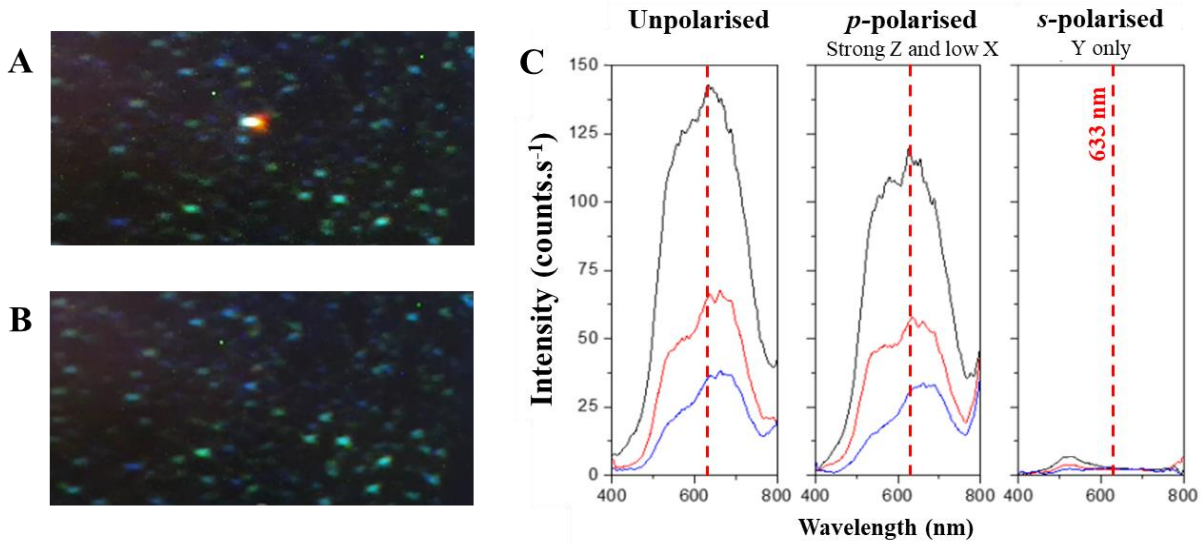

***Figure 2.8**. Characterization of a gold-coated AFM TERS tip by DFSM in air. **[A]** TERS tip engaged on a glass substrate with dust particles visible. **[B]** Retracted TERS tip apex no longer visible. **[C]** DFSM spectra of TERS tip for a tip in contact (black line), 50 nm retracted tip (red-line), and 100 nm retracted tip (blue line). Unpolarised light gives the highest scattering intensity as it is the sum of the p-polarised (strong Z-component, low X-component), and s-polarised light (Y-component only). A 633nm laser conveniently excites the LSPR centred around 641 nm. Adapted from Talaga et. al (2018).*

It has been previously calculated that in air with an incidence angle of 42°, a 250 nm-long portion of the TERS tip apex is excited.[4] For an incidence angle of 48°, this is reduced to 85 nm. A stronger lightning rod effect is expected when a greater proportion of the tip is illuminated, which in turn leads to a greater electromagnetic enhancement. Therefore, the

optimal incidence angle is 42° for any given TERS probe. The LSPR of the TERS probe depends on the metal type and shape, and needs to be paired with an optimal laser source. To achieve this, DFSM can be utilised to study the plasmonic response (i.e. the LSPR) of the metal nanostructure at the TERS tip end. The unpolarised broadband light source effectively excites the LSPR in the visible range as seen in **Figure 2.8C**. The unpolarised light is composed of contributions of all three XYZ components, which can be broken down using a polarisation filter. *P*-polarisation contains a strong Z-component (parallel to the tip axis) and a low X-component, which is well suited for the excitation of the LSPR of the TERS tip. This contrasts with *s*-polarised light, which consists only of the Y-contribution (see **Figure 2.6**). The low intensity of the LSPR using *s*-polarised light compared to using p-polarisation demonstrates the importance of appropriate polarisation when performing TIR-TERS measurements. By measuring the TERS tip LSPR band using DFSM, the appropriate excitation laser can be selected. In the example of **Figure 2.8**, the gold-coated TERS tip produces an LSPR that matches well with the 633 nm excitation laser.

2.2. Physical Vapour Deposition methods for TERS-active probes

The TERS tip is the core element of a TERS experiment, as it is the source of both the high spatial resolution and the Raman signal enhancement that define the technique. The fabrication of TERS tips is primarily based on noble metal (Au and Ag) deposition techniques, nanoparticle coating, or electrochemical etching.[6] The metallisation of commercial AFM probes or the electrochemical etching of noble metal wires for use in STM-TERS, remains the preferred method for the study of biomolecules. While these probes have a high tip-to-tip performance variability, they are cheaper, faster, and easier to prepare than more sophisticated methods. Au tips while being more chemically stable than Ag tips, have a lower electromagnetic enhancement in the visible range due to the higher imaginary part of the dielectric function of gold. Despite the short lifetime of unprotected Ag tips due to oxidation, these are often preferred for the study of weak Raman scatterers such as biological molecules. The lifetime of Ag tips can be improved by the deposition of a thin (1 – 2 nm) protective capping layer of Au, SiO_2, or Al_2O_3 for example. However, this creates an insulating gap between the metal and the analyte, which reduces the TERS enhancement.

2.2.1. Sputtering

Physical vapour deposition (PVD) methods are the prevailing methods for preparation of AFM-TERS tips. While being a cheap and relatively straightforward method for TERS tip preparation, sputtering has been reported for the fabrication of tips with varying morphology, mechanical stability, and enhancement.[6]

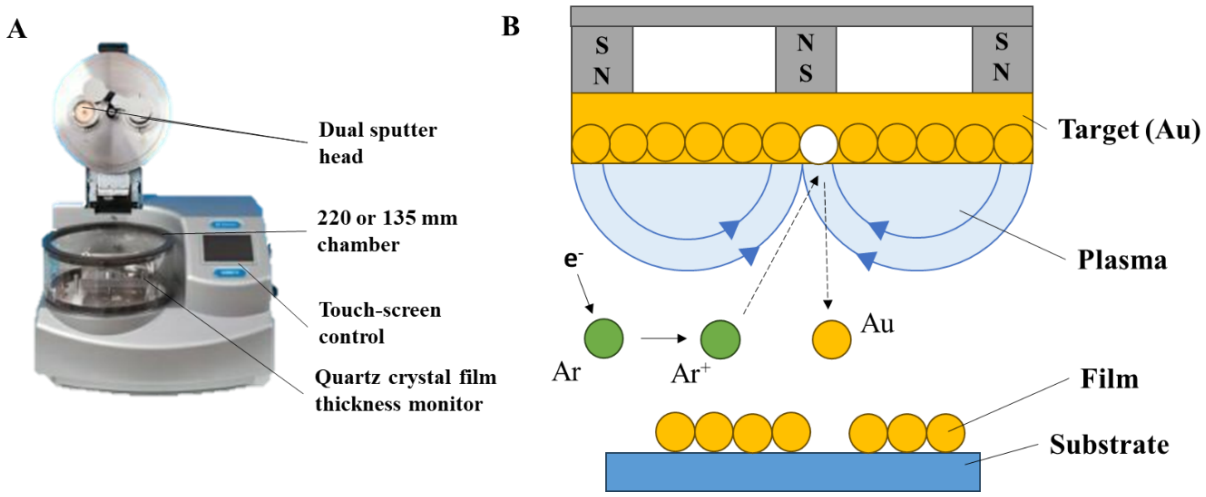

Figure 2.9. [A] *Quorum Q300T D (Quorum Technologies) magneton sputter coater and* ***[B]*** *schematic of the deposition of a thin gold layer using a magneton sputter coater and argon gas. North and south poles are notated as N and S, respectively.*

Figure 2.9 shows a typical sputtering set-up and an illustration of the principle of sputtering. In brief, the ejection of atoms from a solid metal target in a low-pressure environment form nanometric films on substrates. This is achieved by generating a plasma in a vacuum chamber using a small amount of Ar gas along with applying a high voltage between two electrodes. The produced electric field accelerates electrons which collide with the Ar atoms, ionising them forming the plasma. The target is negatively biased, and so the positive Ar^+ atoms are accelerated and collide with the target, transferring their high-kinetic energy to the target atoms. This results in the ejection or "sputtering" of atoms from the surface of the target, which travel through the vacuum and condense on the substrate placed opposite the target. Overtime, a thin layer of the target material is formed on the substrate as atoms accumulate.

There are several factors and parameters that influence the sputtering processes, and thus the quality and characteristics of the sputtered film. The gas pressure within the chamber affects the mean free path of both the sputtered atoms and the plasma ions. High Ar gas pressures result in more collisions and thermalisation of sputtered atoms, while low pressures

have fewer collisions and thus higher energy atoms. Both the film morphology and deposition speed are negatively affected by use of higher sputtering pressures. Another way to increase sputtering rate is to increase the applied electric power to the target. The voltage remains constant, therefore the current (mA) supplied to the target is modified. Higher power density increases the energy and number of ions that bombard the sputtering target, but may heat the substrate which affects the film formation. Specifically, the adhesion, density, and crystallinity of the film is increased at higher substrate temperatures. Our Quorum Q300T D sputter coater does not have the capability of modifying the substrate temperature specifically, and was therefore not considered in TERS tip manufacturing. For sputtering using magnetrons (which confines electrons near the target surface using a magnetic field), the magnetic field needs to be optimised to ensure high deposition rates and uniform film deposition.

The main advantage of sputtering for the fabrication of TERS tips is its versatility in deposited metals. Plasmonic metals such as Au and Ag, can be easily interchanged and deposited individually or as multilayers. This has the potential to enable the user to tune the plasmonic properties of the TERS tip for optimal Raman enhancement. While sputtered metal films have generally good adhesion to silicon probes, the mechanical stability of the probes can be increased by adding an initial adhesion layer to the probe. Typical metals used to achieve good adhesion of the plasmonic metal layer are Ti and Cr. However, this interlayer can affect the LSPR of the noble metal layer.

In contrast, one of the major drawbacks of the method is the poor control over the tip structure which can become double-tipped or rounded at the apex. Even though the uniform coating of the tip is desirable, tip sharpness is important as a first approximation for confining the LSPR and generating a high enhancement. This is in addition to the reduced AFM spatial resolution from the larger apex size. However, the spatial resolution of TERS measurements using rough sputter coatings has been found to be more related to the dimensions of the noble metal protrusion at the tip apex.[3,7] The diameter of the tip apex is not always a good indicator to estimate the expected spatial resolution in TERS. Contaminations originating from the sputtering target or chamber can affect the optical properties and enhancement of the TERS tip fabricated using sputtering. Carbonaceous materials on the tip are enhanced by the SERS-active nanoparticulate surface of the tip, often appearing as a relatively broad background of the tip signal. If such contamination is specifically present at the tip apex (which is not the most likely scenario), the TERS tip becomes inadequate to probe samples by TERS, due to the physical insulating barrier between the tip metal and the sample. In addition, unwanted oxides may also

appear on the tip and contribute in TERS spectra as low-wavenumber Raman bands (**Chapter 1.4.5**).

Table 2.1. *ACCESS-FM sputter-coated tip composition, diffusion, and TERS activity on heparin-induced Tau fibrils using side-illumination geometry. The glass height of the sputter chamber was 220 mm. Sputter currents of 20, 20, 75, and 120 mA were used for the deposition of Au, Ag, Ti, and Cr respectively. The bleed vacuum was set to 0.01 mbar for all depositions.*

	Composition			Tip Diffusion			TERS Activity	Substrate
#	Adhesion Layer	Plasmonic Layer	Capping Layer	Acq. Time (s)	Laser Power (%)	Image Contrast	633/532	Material
1	Ti (5 nm)	Au (25 nm)	-	0.3	3.2	High	No/No	Mica
2	Ti (5 nm)	Au (25 nm)	Au (25 nm)	0.3	3.2	High	No/No	Mica
3	Ti (10 nm)	Ag (50 nm)	Au (5 nm)	0.3	3.2	High	**Tapping**/No	Mica
4	Ti (10 nm)	Ag (50 nm)	Au (15 nm)	0.3	3.2	Medium	No/No	Mica
5	Ti (5 nm)	Ag (50 nm)	Au (5 nm)	0.6	1	Low	**Tapping**/No	Mica
6	Ti (5 nm)	Ag (60 nm)	Au (5 nm)	0.3	3.2	High	**Tapping/Contact**	Mica
7	Ti (5 nm)	Ag (70 nm)	Au (5 nm)	0.3	3.2	High	**Tapping**/No	Mica
8	Cr (5 nm)	Ag (50 nm)	-	0.3	3.2	High	No/No	Mica
9	Cr (10 nm)	Ag (100 nm)	-	0.3	3.2	High	**Tapping/Tapping**	Mica
10	Ag (20 nm)	Au (60 nm)	-	0.3	3.2	High	**Tapping**	Mica
11	-	Ag (50 nm)	-	0.3	1	Med.	**Tapping**	Mica
12	-	Ag (40 nm)	-	0.3	1	High	**Tapping**	Mica
13	-	Ag (60 nm)	-	0.3	1	High	**Tapping**	Glass+Au
14	-	Ag (200 nm)	-	0.3	3.2	Medium	**Tapping**	Au
15	-	Ag (30 nm)	-	0.3	3.2	High	**Tapping**	Au

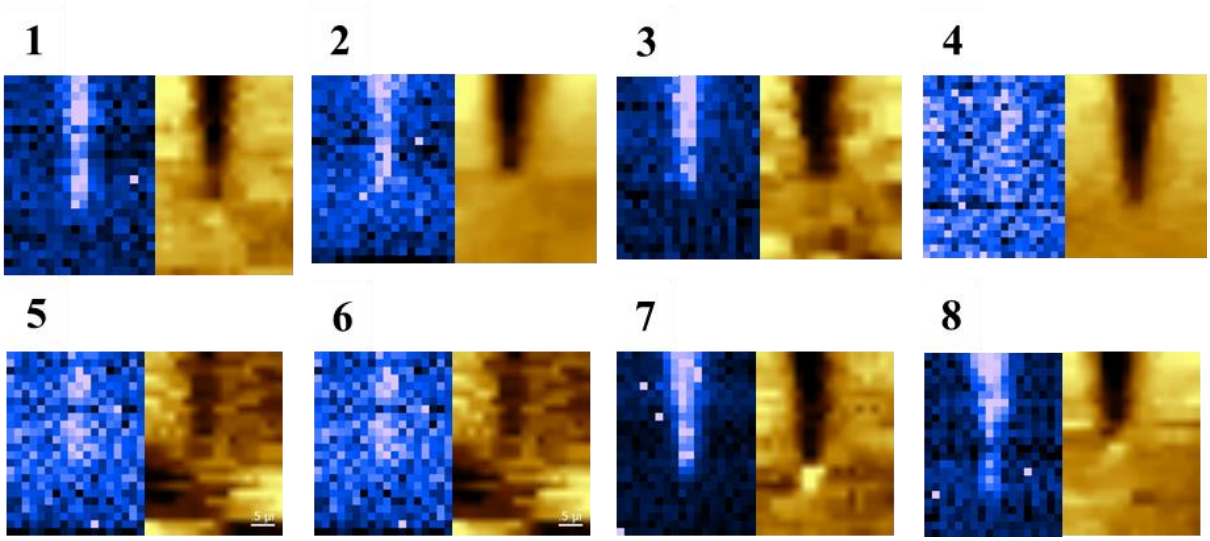

Figure 2.10. *Diffusion (left), and phase (right) images of 8 ACCESS-FM TERS tips fabricated using sputtering. The numbering and deposition composition are outlined in Table 2.1.*

The TERS tip is arguably the key element in the success of a TERS experiment, with great efforts being made by the TERS community to achieve robust, reliable probes. Using the Quorum Q300T D (Quorum Technologies) sputter coater (**Figure 2.9**) several combinations of

metal types and thicknesses were evaluated for their TERS activity using ACCESS-FM Si AFM tips as a base SPM probe. **Table 2.1** summarises the tested sputtered metal film composition, thickness, and activity when tested on heparin-induced Tau fibrils. The fabricated tips were initially tested using a graphene oxide (GO) / carbon nanotube (CNT) sample, as this type of sample is almost a standard in the TERS community currently. However, a more interesting application of such tips is for the study of non-resonant biomolecules such as Tau fibrils which is the topic of **Chapter 3**. The fabricated TERS tips were analysed using the side-illumination TERS system described in **Chapter 2.1.1**.

When performing a TERS experiment in side-illumination geometry, the diffusion of the laser light and phase images are recorded to align the laser with the hotspot of the TERS tip. **Figure 2.10** shows the diffusion and phase images for the tips 1 – 8 with compositions as per **Table 2.1**. The diffusion of the tip could be taken as an initial characterisation of the potential tip activity if looking at tip 3 and tip 7 that have good image contrast as well as being TERS active. However, for low diffusing tips such as tips 4 – 6, two out of three are seen to be TERS active. The tip diffusion is dependent on the properties and quality of the metal film deposited, but a TERS-active tip may have some active nanostructure at the tip apex that leads to the observed enhancement. Nevertheless, a good quality sputtered metal coating allows for easier tip-laser alignment when in side-illumination geometry. There is no evident correlation between sputtered metal and the quality of the obtained diffusion image, but the additional gold capping layers above 5 nm may be associated with poor diffusion. For example, see the diffusion of tip 4 (15 nm Au) versus that of tip 8 (0 nm Au). **Figure 2.11** shows both scanning electron microscopy (SEM) image and electron dispersive x-ray (EDX) spectrum obtained for sputtered tip 3. This tip has a composition of 10 nm Ti, 50 nm Ag, and 5 nm Au. From the SEM image **Figure 2.11A** a homogenous and macroscopically smooth metal film is shown on the tip and part of the cantilever. The insert in the red box shows an enhanced contrast image of the apex showing evident roughness with some blemishes. The SEM system has a coupled EDX spectrometer which allows for the elemental analysis of the imaged tip. A typical EDX spectrum of a sputtered TERS tip is featured in **Figure 2.11B**. The spectrum shows the clear strong contribution of the base Si of the AFM tip, with the Au and Ag sputtered layers being identified. The Ti layer was not identified by the EDX software, which is expected at K_{alpha} = 4.508 keV, K_{β} 4.931 keV, and L_{alpha} = 0.452 keV. The analysis also reveals carbon and oxide species present on the tip, likely arising either from contaminants of the sputtering target or chamber, or from the ambient air after sputtering. However, it is known that for low Z elements (Z < 11) EDX often fails to accurately detect these elements. This can be due to several factors

such as sample thickness and the absorption of generated x-rays due to the sample (low energy x-rays being more absorbed than high energy ones), absorption by the detector window, and the K-shell electrons being involved in bonding. Therefore, the positions and shapes of the peak may change with different compounds,[8,9] and it is not possible to quantify the amount of contaminant present on the tip. After this confirmation of contaminant when sputtering a stricter regime of tip fabrication was implemented, which included the regular cleaning of the sputtering chamber walls in addition to sonicating the target in isopropanol for 10 minutes prior to use. This reduces the contribution of such contaminants in TERS measurements but carbonaceous ones are nevertheless present.

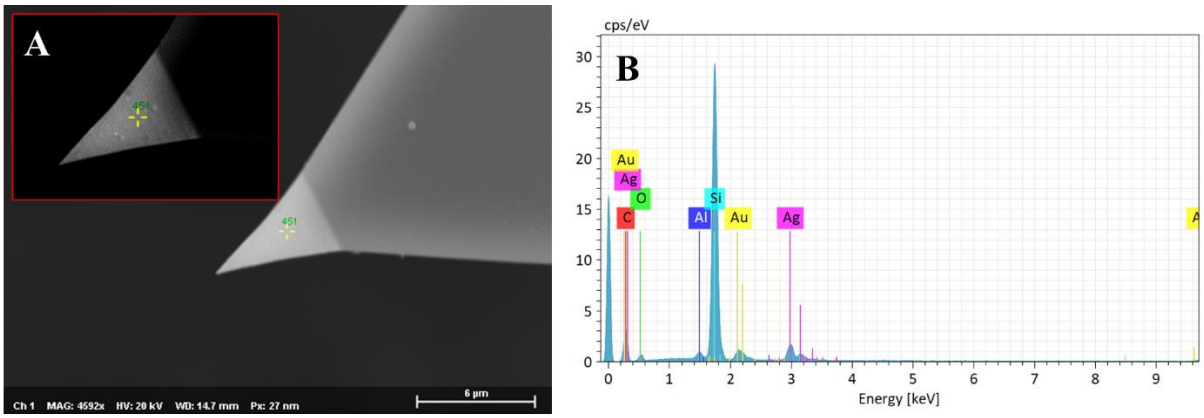

Figure 2.11. [A] *SEM image of sputtered tip 3 (Ti/Ag/Au) with enhanced image of the apex as insert.* ***[B]*** *EDX spectrum with potential assignments taken at yellow cross marker in A.*

From the analysis and characterisation of several tip compositions with varying metal thicknesses and adhesion/plasmonic/capping layers, it was found that simpler is better for our needs of studying non-resonant biomolecules. As evident from **Table 2.1**, pure Ag tips (tips 11 – 15) performed the best when tested on the heparin-induced Tau fibril sample. The optimal thickness of the plasmonic layer of Ag was found to be 60 nm, which was a balance between consistent tip coverage and TERS enhancement. Such tips were used to successfully characterise Tau fibrils in air, which is the subject of **Chapter 3**. Despite the higher enhancement compared to Au-coated tips, the major drawback of pure Ag tips is the tip lifetime. Ag tips must be freshly prepared prior to each experiment due to the rapid oxidation limiting tip activity to a few hours. This is inconvenient for TERS mapping which can take a relatively long time to prepare, let alone the time needed to acquire the map. Often several tips were needed per Tau sample and batch production of Ag tips was not feasible with the rapid oxidation immediately after preparation. With the outlook of performing TERS in aqueous environments,

pure Ag tips are even less suited. There was inconsistent and not convincing enhancement observed for Ag tips with protective Au capping layers. Such capping layers, when increased above 5 nm Au thickness, had little enhancement in air, likely due to insulation of the plasmonic-active Ag layer. Additionally, the tip LSPR is likely red-shifted due to the influence of the plasmon band of the deposited Au particles, which potentially matches poorly with the 532 and 633 nm excitation laser resulting in a lack of enhancement. The tips with 5 nm Au capping layers still showed loss of signal overtime, which indicates inhomogeneity or permeability in the protective layer allowing for the oxidation of the Ag layer. As the brute-force method of using unprotected Ag tips would not be feasible for TERS studies in liquid environments, our group focused on developing electrochemical-based TERS tip fabrication. These electrochemically-fabricated tips are described in the literature[10] and were used for the liquid studies described in **Chapter 5**.

2.2.2. Thermal Evaporation

Thermal evaporation is the most popular PVD technique. The metal to be deposited is heated in a metal crucible under vacuum (typically below 10^{-4} Torr), and the resulting vapour flux rises upward towards the inverted sample where the vapour condenses onto the substrate. Preliminary tests of two Ag TERS tips were conducted involving a collaborator at the Institut de Chimie de la Matière Condensée de Bordeaux (ICMCB). For direct comparison with sputtered tips, two ACCESS-FM AFM Si probes were used without any pre-treatment.

In the measurement of the diffusion image of the tips, a prominent contaminant was discovered which was concentrated towards the cantilever end of the tip (**Figure 2.12**). The contaminant source was found to be likely due to the organic molecules or complexes, such as iron phenanthroline ($Fe(phen)_3^{2+}$) or cobalt bipyrazine ($Co(bpz)_3$) compounds, which have also been evaporated in the chamber prior to tip deposition as confirmed by our collaborators.

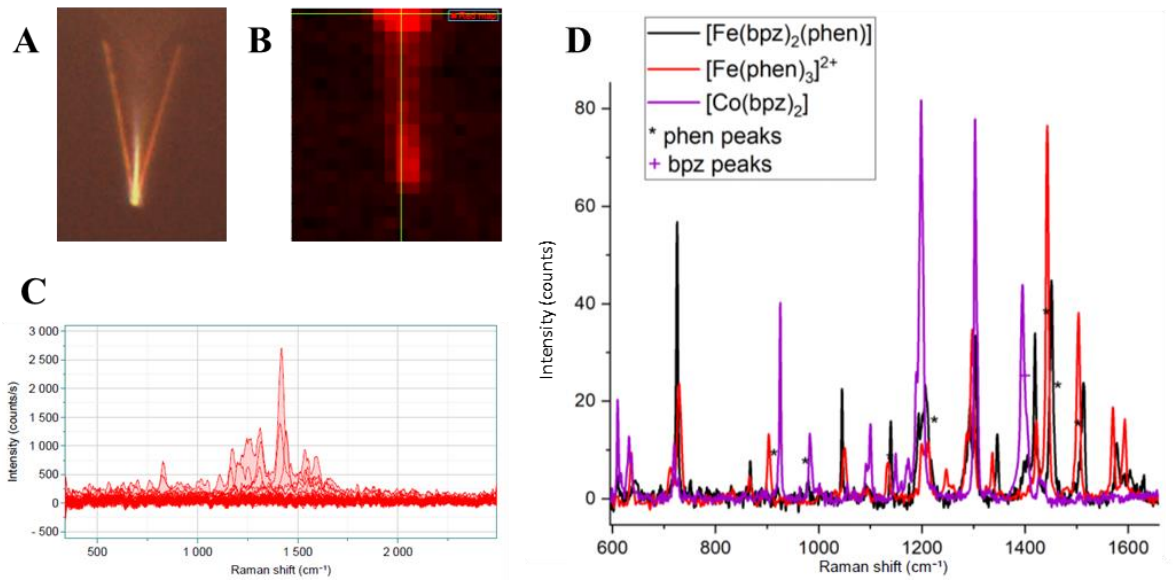

Figure 2.12. *ACCESS-FM TERS tip prepared by thermal evaporation at ICMCB, Bordeaux.* ***[A]*** *Side objective camera image of tip.* ***[B]*** *Diffusion image of tip apex.* ***[C]*** *Raman spectra of diffusion image showing contaminant peaks.* ***[D]*** *Raman spectra of organometallic compounds commonly used in the thermal evaporation chamber.*

TERS tips prepared by thermal evaporation have not been further investigated due to: 1) their morphological similarity to in-house sputtering, 2) high risk of contamination due to non-specific use of the evaporation system, 3) longer fabrication time and need for storage prior to measurement. The thermal evaporation was however useful for producing template-stripped Au substrates for gap-mode TERS using side-illumination geometry. **Figure 2.13** shows a comparison of substrate roughness for an Au-sputter coated glass slide versus the template-stripped gold substrates. For a sputter thickness of 70 nm, a surface roughness of 2.54 nm is demonstrated for **Figure 2.13A**. In contrast, the 200 nm (prior to cleavage) template-stripped Au substrate of **Figure 2.13B** has a surface roughness of 0.56 nm. This atomic flatness is desirable for AFM and gap-mode TERS studies. Theoretically, similar substrates could be easily prepared using the in-house sputtering system available.

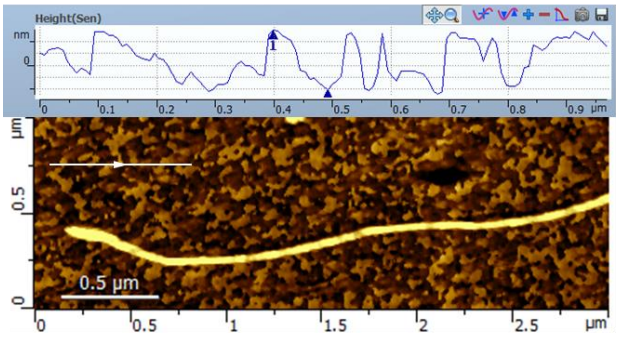

B

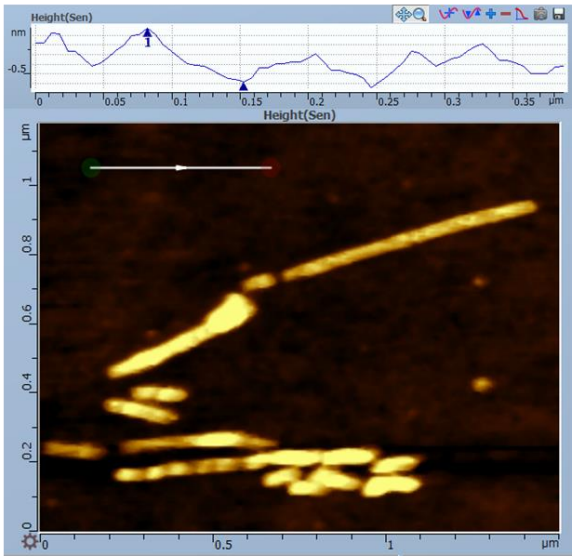

	A. Sputtering Au	B. Template-Stripped Au
Thickness	70 nm	200 nm
dX	94 nm	70 nm
dZ	2.54 nm	**0.56 nm**

Figure 2.13. *Comparison of surface roughness of Au-coated glass using* ***[A]*** *direct sputtering deposition and* ***[B]*** *template stripping after thermal evaporation.*

2.2.3. Commercial TERS-active probes

Companies that are involved in the production of AFM, Raman, and/or TERS instruments often sell complementary TERS tips to provide the user with the "whole package". In addition, independent companies and start-ups are also prevalent on the TERS market, claiming to provide efficient and long-lifetime TERS tips with innovative technologies. Despite these claims, commercial TERS tips have the drawbacks of being expensive, having to undergo transport for delivery (which could damage tips), and needing to be stored under inert gas. The supporting data to the company claims is often limited, with efficiency proved on the resonant standard of carbon nanotubes, as opposed to non-resonant biological molecules. Several commercial tips have been tested using the side-illumination TERS system on Tau fibrils. The results are summarised in **Table 2.2** below. Several gold and silver coated commercial tips were tested, but performed poorly especially when compared to sputtered tips which are significantly cheaper to produce. TERS activity was only observed on the GO/CNT sample, and even then, it was only observed with four of the tips. No tip could achieve a TERS signal while operating in tapping mode. For our desired application on biomolecules, the lack of TERS signal when investigating the non-resonant biomolecule Tau proves commercial tips impractical and ineffective.

Table 2.2. *Tip composition, diffusion, and TERS activity of commercially-available tips tested on GO/CNT and heparin-induced Tau fibrils using side-illumination geometry.*

		Composition		Tip Diffusion			TERS Activity	
Name (No. tips)	**Company**	Plasmonic Layer	Capping Layer	Acq. Time (s)	Laser Power (%)	Image Contrast	GO/CNT	Tau fibrils
OMNI-TERS-SNC-Au (4)	Horiba	Au	-	0.3	3.2	Low	No	No
OMNI-TERS-FM-Ag (4)	Horiba	Ag	Au	0.3	3.2	Low	**Contact**	No
ACCESS-FM-GG (2)	AppNano	Au	-	0.6	1	Low	No	No
ACCESS-FM-GG (2)	AppNano	Au	Ag (30 nm)	0.6	1	Medium	No	No
ACCESS-FM-GG (2)	AppNano	Au	Au (30 nm)	0.3	3.2	Medium	No	No
NT-TERS-E85-Ag (7)	NextTip	Ag	Au	0.3	3.2	High	**Contact**	No
NT-TERS-E85-Au (2)	NextTip	Au	-	0.3	3.2	High	**Contact**	No
NT-EASY-TERS-70Ag (5)	NextTip	Ag	Au	0.3	3.2	High	**Contact**	No

Commercial tips have found to be too expensive for their lack of enhancement of our biomolecules of interest. Tips tested as "active" in our set-ups were found to be only active in contact mode (probably due to the protective capping layer creating a greater distance to the active plasmonic layer), which in turn led to visible damage of fibrils after measurement. **Figure 2.14** showcases this with two commercial tips provided by the company NextTip. Both the NextTip EASY-TERS (**Figure 2.14A**) and TERS-E (**Figure 2.14B**) were tested using our side-illumination set-up on GO and Tau fibrils. The NT EASY-TERS has a pyramidal tip shape and the NT TERS-E features an elephant trunk tip shape. Both are coated in a unique non-disclosed nanostructured metal layer, with the TERS-E claiming higher imaging resolution compared to the EASY-TERS. Both tips seem to have uniform coating as seen in **Figure 2.14C** (side optical camera) and **Figure 2.14D** (SEM images). While these tips could produce an enhanced signal of GO flakes **Figure 2.14E**, no spectrum could be observed in tapping-mode TERS. The tip was required to be in direct contact with the GO sample to get its TERS fingerprint. Unfortunately, as is the case for all commercial tips tested, the need to perform TERS in contact mode makes them unsuitable for biological applications. Mechanical damage to heparin-induced Tau fibrils from attempting TERS in contact mode is evident as seen in **Figure 2.14F**. The damaged areas are marked by the red arrows.

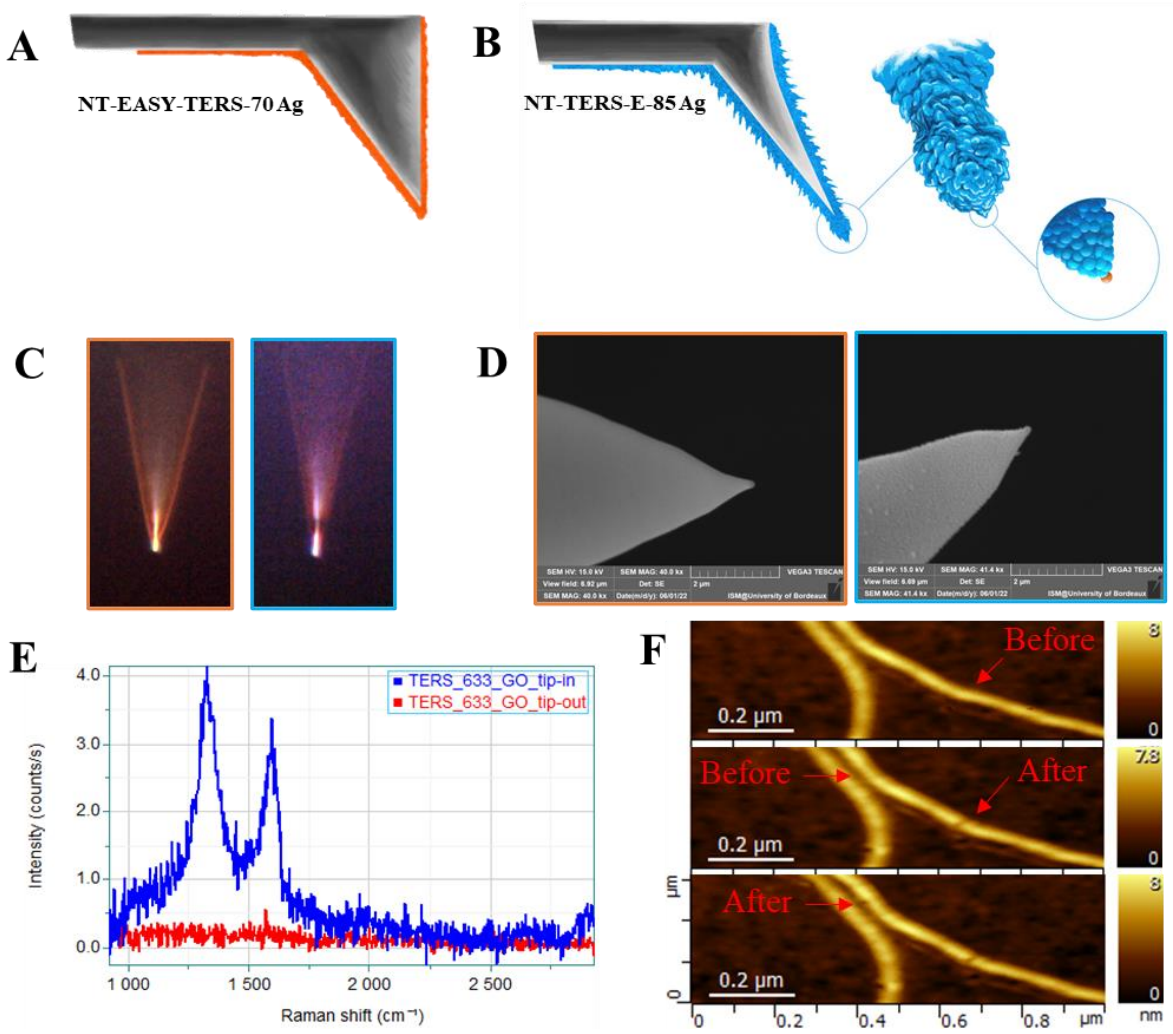

Figure 2.14. ***[A]*** *NextTip "Easy TERS 70 Ag" and* ***[B]*** *"TERS-E-85 Ag" tip morphologies.* ***[C]*** *Tips visualised through the side-illumination camera.* ***[D]*** *SEM images of tips showing nano-tapering of the apex.* ***[E]*** *TERS spectrum of GO with the tip in contact (blue) and retracted (red).* ***[F]*** *Contact mode results in visible damage to Tau fibrils, marked by red arrows.*

Five OMNI-TERS tips fresh from the box are shown in **Figure 2.15A**, which have wildly different tip morphologies. While these tips were refunded, it demonstrates another unreliable quality from such expensive commercial TERS tips. **Figure 2.15B**, shows the mechanical damage to a Tau fibril sample when using one of these tips. Additionally, the clarity of the AFM imaging is poor, with noticeable image doubling observable in the height images. Given the cost-benefit analysis of such tips, commercial TERS tips were not used for further biological investigations.

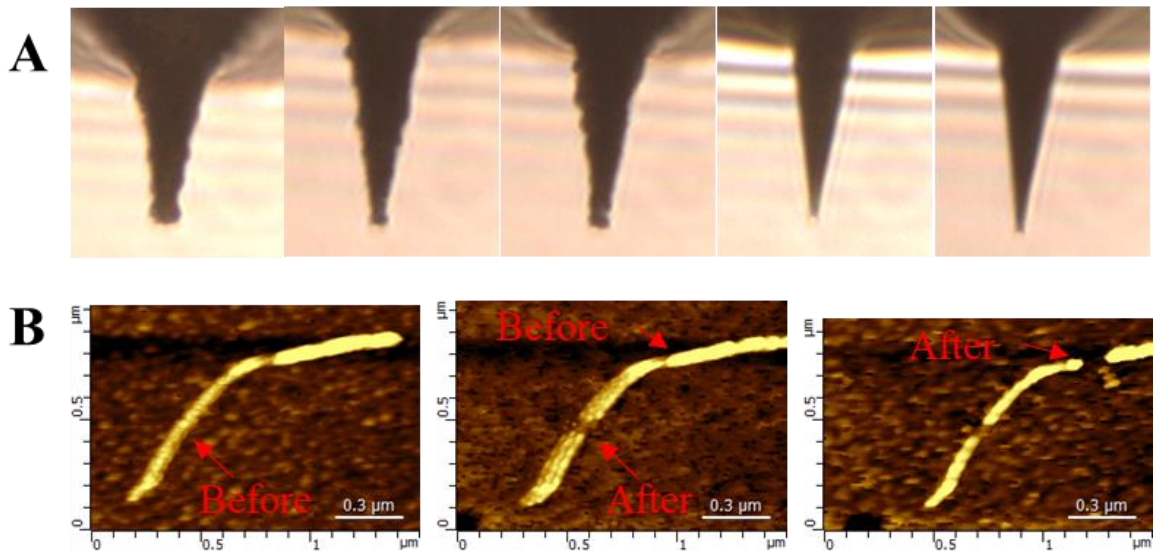

Figure 2.15. [A] *5 new OMNI-TERS FM Ag tips with wildly varied morphologies.* ***[B]*** *Contact mode results in visible damage to Tau fibrils, marked by red arrows.*

Conclusion

There is no doubt that the commercialisation of TERS instrumentation has made the technique more accessible to a wider scientific community. The implementation of commercially available TERS systems, such as the side-illumination geometry LabRAM HR-OmegaScope coupled system described in **Chapter 2.1.1**, enables new users to contribute to the field without the need to construct one's own instrument. These instruments are well suited for routine analyses in air, including (but not limited to) testing the activity of fabricated TERS tips using standard GO-CNT samples. As described in **Chapter 2.2**, the aforementioned side-illumination system enables the visualisation of fabricated TERS tips and the characterisation of their TERS enhancement. For the purpose of studying non-resonant biomolecules, TERS tips consisting of an Ag sputter-coating of at least 60 nm were determined the most effective for TERS studies of Tau fibrils. These Tau studies are described in further detail in **Chapter 3** and their corresponding publications from which they are derived.[3,7] While commercial TERS instrumentation is thriving, the same cannot be said for commercial TERS probes. **Chapter 2.2.3** has outlined the lacklustre results obtained from several commercial probes which, in the author's opinion, are not worthy of their hefty price tag. Specifically, there remains a need for TERS probes that are specifically designed with sensitive soft biological matter in mind. This should take the form of TERS probes that do not mechanically damage the sample and give high enhancement factors (i.e. Ag-based soft tapping-mode tips). For now, the average TERS user is still required to invest into a vapour deposition method for convenient fabrication of

TERS-active probes, although tip manufacturing is less reproducible with this technique than with expensive micro- and nano-fabrication methods.

Having complimented the available commercialisation of TERS instrumentation, there are still useful developments to be made and implemented. The TIR-TERS configuration of **Chapter 2.1.2** and the integrated DFSM of **Chapter 2.1.3** are the major innovations led by our group. This system enables the characterisation of the LSPR of TERS probes using DFSM, subsequently enabling the best pairing of the available laser light sources. DFSM measurements demonstrate that *p*-polarised incident light is best suited for TERS tip excitation in TIR configuration due to the large contribution of the Z-component (close to the critical angle α, ~42° in air). The major benefits of the TIR configuration are the ease of tip-alignment and efficient hotspot excitation, and the low laser power density of the evanescent field. The latter point is significant for working in tapping mode on biological samples, as potential sample degradation is significantly reduced. The efficacy of the TIR-TERS system for the study of biological samples is further detailed in **Chapter 3**.

References

1. Ando, T., Uchihashi, T., Kodera, N., High-speed AFM and applications to biomolecular systems, Annu. Rev. Biophys., 42, 393–414 (2013).
2. Yu, J., Saito, Y., Ichimura, T., Kawata, S., Verma, P., Far-field free tapping-mode tip-enhanced Raman microscopy, Appl. Phys. Lett., 102, (2013).
3. Talaga, D., Cooney, G. S., Ury-Thiery, V., Fichou, Y., Huang, Y., Lecomte, S., Bonhommeau, S., Total Internal Reflection Tip-Enhanced Raman Spectroscopy of Tau Fibrils, J. Phys. Chem. B, 126, 5024–5032 (2022).
4. Talaga, D., Bremner, A., Buffeteau, T., Vallée, R. A. L., Lecomte, S., Bonhommeau, S., Total Internal Reflection Tip-Enhanced Raman Spectroscopy of Cytochrome c, J. Phys. Chem. Lett., 11, 3835–3840 (2020).
5. Talaga, D., Comesaña-Hermo, M., Ravaine, S., Vallée, R. A. L., Bonhommeau, S., Colocalized dark-field scattering, atomic force and surface-enhanced Raman scattering microscopic imaging of single gold nanoparticles, J. Optics,17, (2015).
6. Huang, T. X., Huang, S. C., Li, M. H., Zeng, Z. C., Wang, X., Ren, B., Tip-enhanced Raman spectroscopy: Tip-related issues., Anal. Bioanal. Chem., 407, 8177–8195 (2015).
7. Cooney, G. S., Talaga, D., Ury-Thiery, V., Fichou, Y., Huang, Y., Lecomte, S., Bonhommeau, S., Chemical Imaging of RNA-Tau Amyloid Fibrils at the Nanoscale Using Tip-Enhanced Raman Spectroscopy, Angew. Chem. Int. Ed., 62, 6–11 (2023).
8. Salge, T., Falke, M., Goran, D., Recent Advances in EDS and EBSD Technology: Revolutionizing the Chemical Analysis of Chondritic Meteorites at the Micro and Nanometer Scale, 2nd Lunar and Planetary Science Conference (2011).
9. Malac, M., Egerton, R. F., Calibration Specimens for Determining Energy-Dispersive X-ray k-Factors of Boron, Nitrogen, Oxygen, and Fluorine, Microsc. Microanal., 5, 29–38 (1999).
10. Huang, Y., Talaga, D., Garrigue, P., Salinas, G., Cooney, G. S., Reculusa, S., Kuhn, A., Bouffier, L., Bonhommeau, S., Nanostructured gold-coated AFM tips generated by potentiostatic electrodeposition for tip-enhanced Raman spectroscopy, Chem. Phys. Lett. 832, (2023).
11. Otto, M., What is Chemometrics? Chapter 1, 1–13 (2016).
12. Guo, S., Popp, J., Bocklitz, T., Chemometric analysis in Raman spectroscopy from experimental design to machine learning–based modeling., Nat. Protoc., 16, 5426–5459 (2021).

13. Ryabchykov, O., Guo, S., Bocklitz, T., Analyzing Raman spectroscopic data, Phys. Sci. Rev., 4, (2019).
14. McLaughlin, G., Fikiet, M. A., Ando, M., Hamaguchi, H. O., Lednev, I. K., Universal detection of body fluid traces in situ with Raman hyperspectroscopy for forensic purposes: Evaluation of a new detection algorithm (HAMAND) using semen samples. J. Raman Spec., 50, 1147–1153 (2019).
15. Savitzky, A., E, M. J., Smoothing and Differentiation of Data by Simplified Least Squares Procedures., Physiol. Chem., 40 (1964).
16. Brown, C. D., Wentzell, P. D., Hazards of digital smoothing filters as a preprocessing tool in multivariate calibration, J. Chemom., 13, 133–152 (1999).
17. Varmuza, K., Filzmoser, P., Introduction to Multivariate Statistical Analysis in Chemometrics, (2016).
18. Bonhommeau, S., Cooney, G. S., Huang, Y., Nanoscale chemical characterization of biomolecules using tip-enhanced Raman spectroscopy, Chem. Soc. Rev., 51, 2416–2430 (2022).
19. Lipiec, E., Perez-Guaita, D., Kaderli, J., Wood, B. R., Zenobi, R., Direct Nanospectroscopic Verification of the Amyloid Aggregation Pathway, Angew. Chemie Int. Ed., 130, 8655–8660 (2018).
20. Richter, M., Hedegaard, M., Deckert-Gaudig, T., Lampen, P., Deckert, V., Laterally resolved and direct spectroscopic evidence of nanometer-sized lipid and protein domains on a single cell, Small, 7, 209–214 (2011).
21. Rusciano, G., Zito, G., Isticato, R., Sirec, T., Ricca, E., Bailo, E., Sasso, A., Nanoscale chemical imaging of bacillus subtilis spores by combining tip-enhanced Raman scattering and advanced statistical tools, ACS Nano, 8, 12300–12309 (2014).
22. Lipiec, E., Sekine, R., Bielecki, J., Kwiatek, W. M., Wood, B. R., Molecular Characterization of DNA Double Strand Breaks with Tip-Enhanced Raman Scattering, Angew. Chem. Int. Ed., 126, 173–176 (2014).
23. Lipiec, E., Japaridze, A., Szczerbiński, J., Dietler, G., Zenobi, R., Preparation of Well-Defined DNA Samples for Reproducible Nanospectroscopic Measurements, Small, 12, 4821–4829 (2016).
24. Xiao, L., Bailey, K. A., Wang, H. & Schultz, Z. D., Probing Membrane Receptor-Ligand Specificity with Surface- and Tip- Enhanced Raman Scattering., Anal. Chem., 89, 9091–9099 (2017).

25. Bonhommeau, S., Lecomte, S., Tip-Enhanced Raman Spectroscopy: A Tool for Nanoscale Chemical and Structural Characterization of Biomolecules, Chem. Phys. Chem., 19, 8–18 (2018).

Chapter 3

Tip-Enhanced Raman Spectroscopy of Tau protein

Introduction

This chapter will showcase the experimental advances and results of our group's work with non-resonant biomolecules, specifically focusing on amyloid proteins including tubulin-associated unit (Tau) protein. As extensively detailed in **Chapter 1**, amyloids are protein assemblies that typically form deleterious deposits which are characteristic markers in various neurodegenerative disorders, including, but not limited to, Alzheimer's disease (AD). Even though amyloids are known to feature cross-β structures, the study of their molecular structure and aggregation mechanisms are still largely unclear. Initially in the TERS community, insulin was studied as a model amyloid protein, with amyloid-β (Aβ) gaining large interest in recent years due to its relevance in AD where it is often found as amyloid plaques. Readers are advised to consult **Chapter 1** for the detailed description of the key studies of TERS regarding amyloid proteins.

Initial work in our group on amyloids has focused on characterising Aβ using TERS. The 2017 communication in Angewandte Chemie International Edition utilised TERS to distinguish three toxic Aβ oligomers: the full-length 42-amino acid wild type (WT), and two mutants L34T and oG37C.[1] The synthetic mutants form less toxic amyloid fibrils and highly toxic oligomers respectively, when compared to the WT protein fibrils. This neurotoxicity is defined by the production of reactive oxygen species and the peptides deleterious effects on cell membranes.[2] Compared to previous ATR-FTIR spectroscopy studies which were performed on crystals of mixed monomers, oligomers, and fibrils,[2,3] our group showed that TERS is well suited for fingerprinting oligomers and fibrils at the individual and nanometre scale. AFM-TERS was performed using a previous iteration of our bottom-illumination set-up at 633 nm, using Ag/Au TERS probes, and in gap-mode configuration on 10 nm gold-coated glass coverslips. TERS point measurements of WT and L34T fibrils were used to distinguish them from toxic oG37C oligomers by studying the TERS amide I and amide III bands present, which in turn correlated with the percentage of parallel and antiparallel β-sheet secondary structures present in these samples. In this work, the vibrational modes of amino acids could not be used

for toxicity discrimination due to their weak intensities observed and the contribution of multiple residues in similar spectral regions. Nevertheless, the identification of cysteine (Cys) or methionine (Met), phenylalanine (Phe), and histidine (His) residues demonstrates the sensitivity of our TERS system to detect scarce amino acids (only 3 Phe and 3 His residues are present in these peptides, for example).

Subsequent work on Aβ(1-42) fibrils was published in Chemical Physical Letters in 2021,[4] which rounded out TERS literature on Aβ. Not only were TERS bands of aromatic amino acids and secondary structures such as parallel β-sheets and random coils quantified and qualified in this study, but the fibril twist and hydrophobicity were investigated. Compared to the 2017 study, a side-illumination TERS-AFM instrument (**Chapter 2**) with a 532 nm laser excitation of Ag-coated tips was used. The technological advancement of the TERS instrumentation allowed for mapping to be performed of small portions of fibrils, as opposed to previous limitations only allowing point TERS measurements. From these maps, the lateral spatial optical resolution of the system could be estimated to be ~16 nm, despite the radius of curvature being approximated to 70 nm. Regarding the proportion of assigned random coils, parallel, and anti-parallel β-sheets, this work showed results consistent with our previous work, and therefore to the ATR-FTIR measurements too. It is to be noted, that due to the similar proportions of TERS spectra observed with either core β-sheet or surficial random coil structures, it was concluded that a probe depth of minimum 3 nm was achieved and highlighted TERS' ability to probe both the core and surface of such amyloid fibrils at the nanoscale. Hydrophobic and hydrophilic fibril regions were corroborated by spectral signatures of aromatic amino acids such as His, Phe, and Tyrosine (Tyr), and found to be correlated with parallel β-sheet and random coils respectively. These hydrophobic and hydrophilic domains were estimated to be 10-20 nm in size, and the twisted nature of Aβ(1-42) fibrils reasoned by the abundance of surface His residues. This description of local secondary structures and amino acid spatial distribution paved the way for the probing of other amyloids using TERS.

While Aβ peptides are responsible for the presence of senile plaques in AD, neurofibrillary tangles of Tau are often found alongside. These tangles are believed to be formed after abnormal phosphorylation of Tau leading to a decreased capacity of the protein to bind tubulin, yet the precise aggregation mechanism and structure of Tau fibrils is still poorly understood. Tau has been shown *in vitro* to form fibrils with polyanionic cofactors such as heparin, RNA, fatty acids, and negatively charged lipids. Our group's 2018 communication in Angewante Chemie International Edition characterised the morphology and aggregate structure of the truncated Tau (K18) with heparin sodium (HS) and the phospholipid phosphatidylinositol

4,5-bisphosphate (PIP_2) cofactors using TERS. PIP_2 was used due to its medical relevance as being present in the inner cytoplasmic membrane of neurons. K18 features only the four microtubule-binding domains of Tau, which have been shown to form the cross-β structures observed in amyloids. Not only was PIP_2 demonstrated to induce Tau K18 aggregation, but TERS localised this phospholipid to be present inside the resulting fibril structure for the first time. The occurrence of the ester C=O vibrational mode definitively distinguished the presence of PIP_2 in the K18 fibrils, which was absent in the TERS spectra of K18-heparin fibrils. Indeed, this work is an important step in better understanding the deleterious mechanisms of tauopathies, but the use of the truncated Tau protein is not adequate to fully describe the morphology or homology of tau fibrils with different aggregating cofactors.

Prior to this work, cryo-EM structures of paired helical and straight tau fibrils extracted from the brains of AD patients, revealed some key differences between molecular conformers of tau aggregates,[5] and notably that filaments of K18 or K19 proteins cannot represent the complete core structure. Great care is therefore needed when extrapolating experimental results using such truncated forms. Therefore, it was identified that a new TERS study which included chemical imaging of full-length tau fibrils was needed. This investigation is the content of **Chapter 3.2** below, which was published as an article in J. Phys Chem. B in 2022.[6] This served as a suitable proof-of-concept for our latest TIR-TERS system configuration. Wanting to continue our research on Tau fibrils formed from different cofactors, TERS of polyadenosine (polyA)-induced fibrils was recognised as a prime follow-up investigation due to the high Raman cross-section of the adenine nucleobase. In 2022, the cryo-EM community gave more valuable insight into Tau fibril structure, where full-length Tau-RNA fibrils were shown to have a unique C-terminal fibril core bound to RNA which ran parallel to the fibril axis. TERS is well-suited to corroborate this finding, and this can be found in **Chapter 3.3** which was the basis of my 2023 communication in Angewandte Chemie International Edition.[7]

To summarise, the following sections will detail the most recent TIR-TERS investigations on the amyloid protein Tau. That is firstly, the proof of concept of our latest TIR-TERS system to be applied to the study of non-resonant biomolecules, as well as the exploration of the chemical and structural heterogeneity of such Tau-heparin fibrils. The second study focuses on TIR-TERS of Tau-RNA fibrils. This work demonstrates the chemical mapping and therefore localisation of the model RNA molecule, polyA, as a fibrillating cofactor inside distinct Tau fibrils. The information gained has directly contributed to the study and understanding of amyloid fibrilization and supports current hypotheses of tau fibril structure.

3.1. Description and chemical structures of investigated molecules

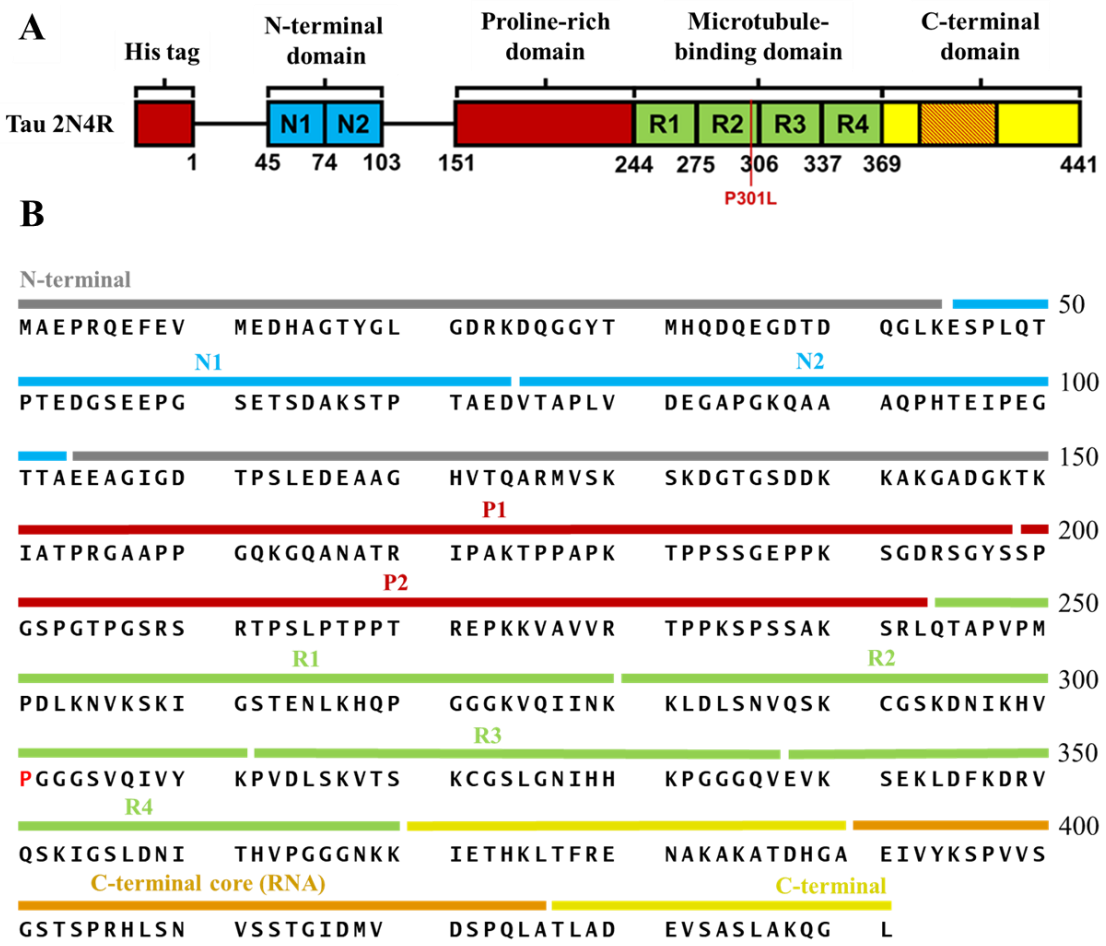

Figure 3.1. [A] *Full-length Tau 2N4R (residues 1 – 441) featuring two alternatively spliced N-terminal domains (N1 and N2), the proline-rich domain (residue 151 – 244), four microtubule-binding domains (R1 – R4), and the C-terminal domain (residues 369 – 441). The N-terminus contains a poly-histidine tag used in the production and purification of the molecule. The shaded region in the C-terminal domain is an RNA binding site proposed by Abskharon et. al.*[8] *The point mutation P301L is located within the R2 domain.* ***[B]*** *Detailed primary sequence of Tau 2N4R.*

In its physiological native form, Tau is an intrinsically disordered cytoplasmic protein that works in binding to and stabilizing microtubules (MT), which facilitates axonal transport within the cell. The 4 repeat domains (R1 – R4, **Figure 3.1A**) are responsible for MT binding and stabilisation. Under pathological conditions, the tubulin binding capacity decreases leading to MT disorganisation and the formation of deleterious neurofibrillary tangles, which are a hallmark of neurodegenerative diseases such as AD. A cross β-sheet core is formed within the repeat domains of Tau giving rise to aggregation into fibrils. The C-terminal, proline-rich, and N-terminal domains make up the disordered fuzzy coat that envelops the fibril β-sheet core.

Figure 3.1B shows the primary amino acid sequence of Tau. Noteworthy amino acid residues that are discernible by TERS include: Cys (2), Phe (3), Tyr (5), His (12), Asn (11), Gln (20), Lys (44), Arg (14), Asp (28), Glu (27), Pro (43), where the number of amino acids in the primary sequence is indicated inside the brackets.

In vitro, an anionic cofactor such as heparin, RNA, or negatively charged lipids are required for fibrilization of Tau. Heparin (**Figure 3.2A**) is produced in mammalian mast cells and is known for its anticoagulant properties in medicine. It is a naturally-occurring sulphated disaccharide consisting of D-glucuronate-2-sulphate and N-sulphoglucosamine-6-sulphate unit. It has been widely used in mechanistic studies of Tau fibrilization, studies on mutated filament assembly, and the identification of aggregation inhibitors of Tau. The sulphated nature of the disaccharide contributes to its negative charge which is believed to stabilise Tau fibrils *in vitro* by neutralisation of positive charge.[9] The negatively-charged phosphate backbone of RNA is believed to interact with Tau in a similar manner to other cofactors. RNA has been shown to colocalise with Tau fibrils in AD[10] and can induce pathogenic Tau fibrils.[11–13] However, it has been far less studied to date using TERS. RNA is likely to give a more accurate representation of possible Tau fibrils generated *in vivo* than heparin as it is much more likely to find free RNA in neuronal cells than heparin. PolyA (**Figure 3.2B**) is a useful RNA mimic in TERS studies due to the higher Raman cross-section of the adenine molecule compared to the other nucleobases.[14] The atom numbering in **Figure 3.2A** and **B** is used throughout the text for the discussion and assignment of Raman, SERS, and TERS bands.

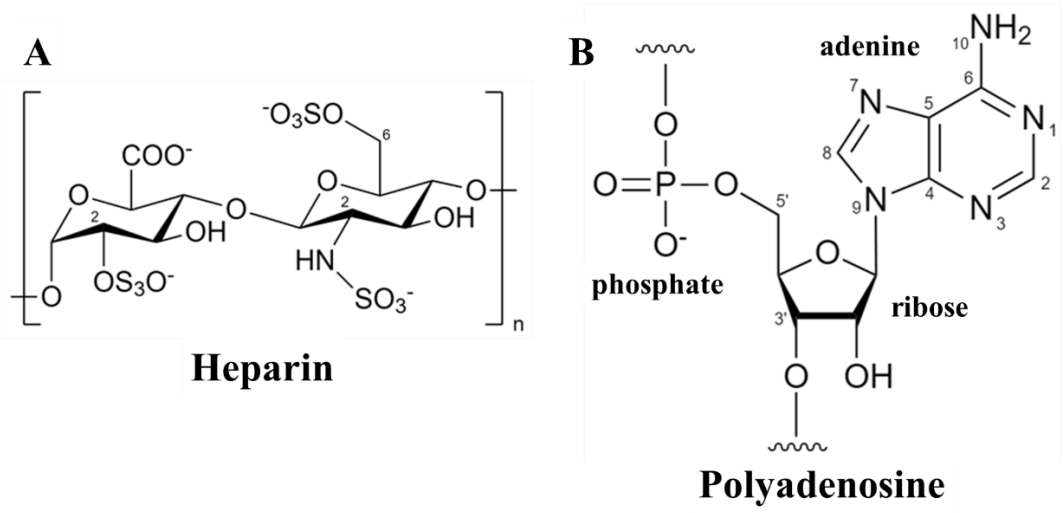

Figure 3.2. [A] *Chemical structure of the heparin disaccharide unit consisting of D-glucuronate-2-sulphate and N-sulphoglucosamine-6-sulphate.* ***[B]*** *Chemical structure of polyadenosine (polyA) unit, consisting of an adenine nucleobase attached to a phosphate-ribose backbone.*

3.2. TIR-TERS of Tau Fibrils

3.2.1. Experimental Procedures

Full-length Tau 2N4R P301L was expressed and purified by PhD candidate Vicky Ury-Thiery at CBMN under a previously established protocol.[13] This protocol is described in detail in **Annex 1**.

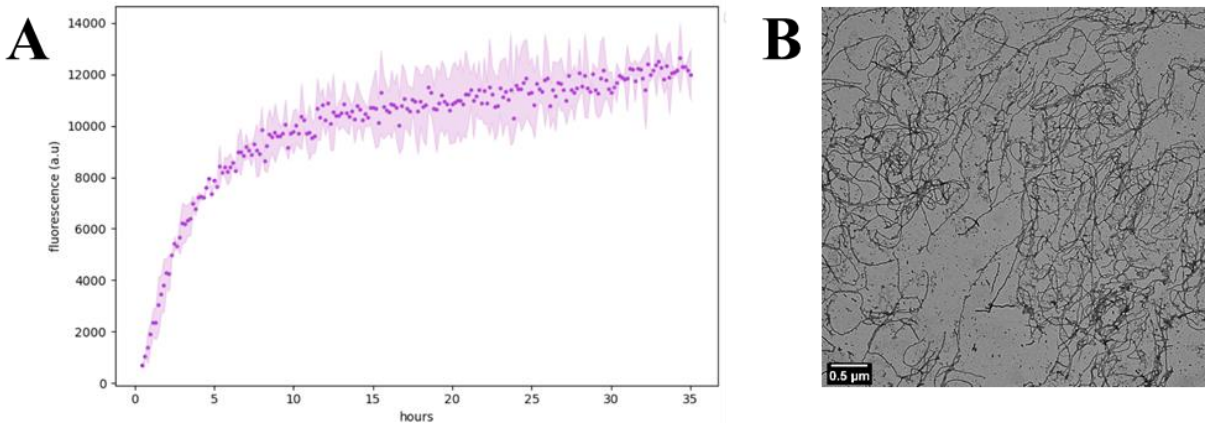

Figure 3.3. [A] *Thioflavin T fluorescence assay which monitors the fibril formation by the intensity of fluorescence over time. Fibrils were grown using Tau protein (20 µM) in HEPES buffer (20 mM, pH 7) with heparin sodium (5 µM).* ***[B]*** *TEM of the formed Tau fibrils.*

To form amyloid fibrils from the Tau solution, 20 µM of Tau was incubated for 3 days at 37 °C in buffer (HEPES 20 mM pH 7, DTT 5 mM) along with the cofactor heparin sodium (Sigma-Aldrich, H62795, from porcine intestinal mucosa, 5 µM). The fibrilization was monitored using a thioflavin T (ThT) fluorescence assay and confirmed using transmission electron microscopy (TEM), as shown in **Figure 3.3**. ThT is a benzothiazole dye that binds to the cross-β-sheet quaternary structure of amyloid fibrils. This bonding induces strong fluorescence at 490 nm when a 440 nm excitation wavelength is used. The formation of amyloid-ThT complexes is stochiometric and therefore accurate quantification of fibril number and length is possible using the so-called ThT assay.[15] A typical ThT binding curve follows three distinct phases: the lag phase, elongation phase, and plateau. These phases correspond to an initial low concentration of β-sheet structures and therefore lack of ThT binding, a rapid increase in aggregation and fibrilization mirrored in increasing fluorescence signal, and ceasing of fibrilization due to consumption of monomeric precursors, respectively.

3.2.2. Experimental Measurements

The TIR-TERS system described in **Chapter 2** was used to perform TERS measurements. TERS tips were fabricated by sputtering (Q300T D, Quorum Technologies) 50 – 60 nm silver onto commercial AFM n-doped silicon tips (ACCESS-FM, APPNano, 36 – 98 kHz nominal resonance frequency). The mass thickness of silver sputtered onto the tip was controlled by a microbalance. To reduce any carbon contamination on the silver-coated AFM tip, the silver sputtering target (99.99 % purity) was sonicated for 20 minutes in an isopropanol bath (VWR Chemicals) and dried under nitrogen flow. The ACCESS-FM tips feature an elephant trunk tip shape which is convenient for AFM-TERS imaging in tapping mode. To achieve this, a tip oscillation amplitude of 20 nm and amplitude set-point of 85 % was used for AFM imaging. Soft-tapping mode has the benefits of avoiding mechanical degradation of the delicate biological sample and the tip coating. Moreover, TERS signals measured in contact mode had similar or lower intensities than in soft-tapping mode.[16] The silver-coated TERS tips were irradiated with 561 nm laser light where the laser fluence was minimised to avoid sample damage. Different light polarisations including linear, radial, and TIR *p*-polarisation were applied to different silver-coated tips (see **Figure 3.4** below). The laser directly delivered the linear polarisation, while a half-wave plate and a liquid crystal polarisation convertor produced the TIR *p*-polarisation and radial polarisation respectively[17–19]. The angle of incidence of laser light in TIR configuration can be adjusted between 40 – 70°, allowing for the optimal adjustment of the critical angle depending on the substrate (here, glass and gold-coated glass coverslips).

3.2.3. TIR-TERS Enhancement

The first goal of this work is to establish quantitative data that proves the benefits of TIR-TERS over more traditional bottom-illumination TERS configurations, which have become popular in the investigation of biomolecules.[1,17,19–25] In the literature, a previous study estimated the TERS enhancement of an ATR system to be over 20 times greater compared to a side-illumination configuration.[26]As for bottom-illumination configurations, our group's 2020 letter[17] in the Journal of Physical Chemistry Letters featured finite-difference time-domain (FDTD) calculations that demonstrated the maximum electromagnetic field enhancement of samples on gold-coated glass coverslips is achieved with *p*-polarised laser light at a 42° angle of incidence in the TIR configuration. Following this work, we set out to compare the Raman

enhancement of TIR-TERS under different light polarisations studying the advantages of TIR for TERS.

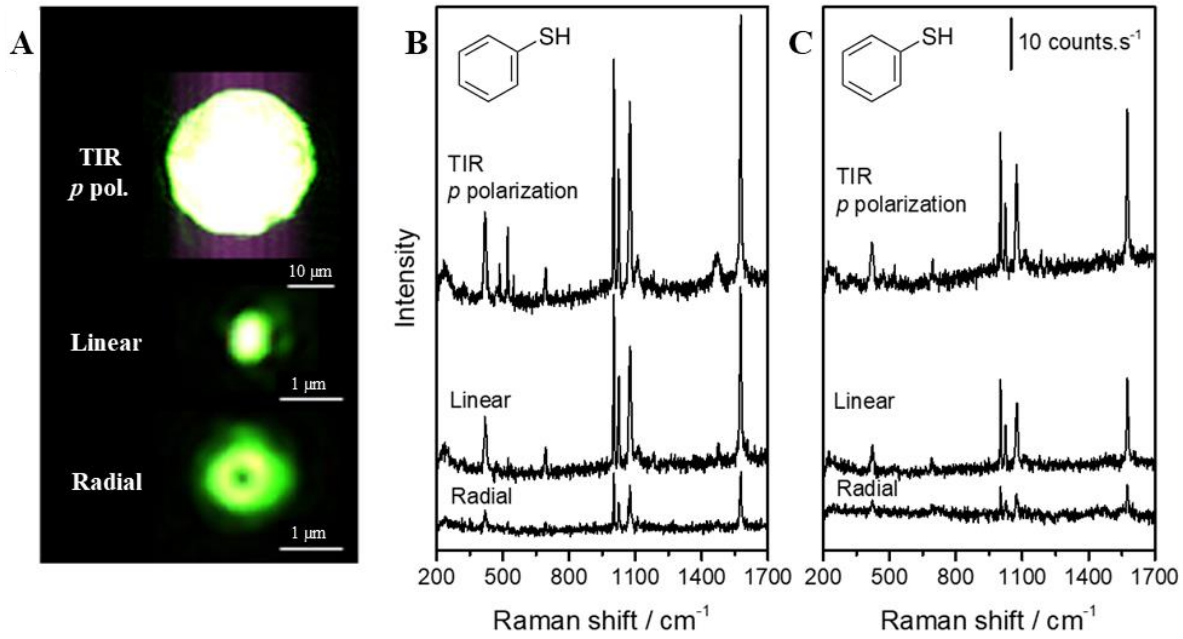

Figure 3.4. *Light polarisation and TERS response of thiophenol-coated silver TERS tips on glass coverslips.* ***[A]*** *Excitation laser spots for TIR p-polarised (top), linearly polarised (middle), and radially polarised (bottom) light.* ***[B]*** *Thiophenol enhanced Raman spectra with engaged TERS tip on borosilicate glass coverslip of TIR p-polarised (top), linearly polarised (middle), and radially polarised (bottom) light.* ***[C]*** *Thiophenol enhanced Raman spectra with engaged TERS tip on gold-coated borosilicate glass coverslip of TIR p-polarised (top), linearly polarised (middle), and radially polarised (bottom) light.*

As shown below in **Figure 3.4**, three light excitations were studied: TIR *p*-polarised (42° angle of incidence), linearly polarised, and radially polarised. To assess these light excitations, three silver-coated AFM tips were functionalised with thiophenol by incubating the tips overnight in small chamber which also contained thiophenol vapour. No noticeable oxidation or contamination of the silver TERS tips was observed, which can be reasoned to be due to the dense molecular packing and rapid functionalisation directly after fresh metallisation of the AFM tips. This method is also preferred compared to the functionalisation of an ultra-flat gold-coated glass substrate with thiophenol and its subsequent TERS characterization using a silver-coated tip, as the time needed to perform the systematic optical adjustments and laser-tip realignments in between changing to different light polarisations would lead to substantial silver oxidation. This in turn, would reduce TERS enhancement and skew interpretation of the effect of light polarisation on enhancement. As demonstrated in **Figure 3.4B** and **C**, signature

Raman bands of thiophenol are observed on both bare borosilicate glass and gold-coated borosilicate glass. The C-S bending and C-S stretching vibrations are observed at 420 and 694 cm^{-1}, respectively. Ring vibrations are seen at 1001, 1023, and 1074 cm^{-1}, along with ring C=C stretching observed at 1575 cm^{-1}.

The TERS intensities in **Figure 3.4** are expressed in counts.s^{-1}, and are relative to the laser power density of the applied polarised light. Therefore, a normalisation to the laser fluence (P_{laser}, µW.µm^{-2}) was firstly performed using the intensity integration (I_{max}, counts.s^{-1}) of the 1575 cm^{-1} band as an estimator for the TERS efficiencies. The calculations for the three TERS tips are presented in

Table 3.1. below for both a bare borosilicate glass coverslip and a gold-coated glass coverslip. From this table it is found that for the glass substrate, the TERS enhancements over the linear polarisation I_{TIR}/I_L are 23.9, 17.5, and 32.9, which averages to 24.7 times higher for TIR geometry. For radial polarisation I_{TIR}/I_R, the enhancements were calculated to be 7.5, 7.5, and 8.5, averaging to be 7.8 times higher for TIR geometry. As for the gold-coated substrates, the TERS enhancements over the linear polarisation I_{TIR}/I_L are 38.4, 15.1, and 40.0, which results in an average of 31.2 times higher enhancement for TIR geometry. Radial polarisation I_{TIR}/I_R enhancements were calculated to be 11.1, 4.4, and 9.7 with an average of 8.4 times higher for TIR geometry. These results show that TIR geometry TERS provides a stronger Raman enhancement when compared to other bottom-illumination configurations that use linearly or radially polarised light. Despite the low laser power density used to excite the TERS tips, TIR-TERS demonstrates efficient excitation of the tip LSPR which in turn leads to intense TERS signatures. This has been previously demonstrated by our group on resonant biomolecules such as cytochrome c.[17] Presented below in **Chapter 3.3** is the first work using TIR TERS to probe non-resonant biomolecules, namely heparin-induced Tau (Tau-heparin) fibrils.

Table 3.1. *TERS intensity of thiophenol for TIR p-polarised (I_{TIR}), linearly polarised (I_L), and radially polarised (I_R) light. The laser power density (P_{laser}) is used to normalise the TERS intensities (I_{max}) and calculate ratio for three thiophenol-coated silver AFM tips.*

Tip 1	Glass Substrate			Glass + Au Substrate		
	TIR	**Linear**	**Radial**	**TIR**	**Linear**	**Radial**
$\mathbf{P_{laser}}$ ($\mu W.\mu m^{-2}$)	1.1	22.2	70.3	2.1	22.2	7.0
$\mathbf{I_{max}}$ ($counts.s^{-1}$)	46.6	39.9	403.0	44.6	12.3	13.5
$\mathbf{I_{max}/P_{laser}}$ ($counts.\mu m^2.s^{-1}.\mu W^{-1}$)	42.8	1.8	5.7	21.1	0.6	1.9
$\mathbf{I_{TIR}/I_X}$ (X=L or R)	-	**23.9**	**7.5**	-	**38.4**	**11.1**
Tip 2	Glass Substrate			Glass + Au Substrate		
	TIR	**Linear**	**Radial**	**TIR**	**Linear**	**Radial**
$\mathbf{P_{laser}}$ ($\mu W.\mu m^{-2}$)	2.4	51.2	4.2	2.4	51.2	4.2
$\mathbf{I_{max}}$ ($counts.s^{-1}$)	44.5	55.5	10.6	13.2	19.3	5.3
$\mathbf{I_{max}/P_{laser}}$ ($counts.\mu m^2.s^{-1}.\mu W^{-1}$)	18.9	1.1	2.5	5.6	0.4	1.3
I_{TIR}/I_X (X=L or R)	-	**17.5**	**7.5**	-	**15.1**	**4.4**
Tip 3	Glass Substrate			Glass + Au Substrate		
	TIR	**Linear**	**Radial**	**TIR**	**Linear**	**Radial**
$\mathbf{P_{laser}}$ ($\mu W.\mu m^{-2}$)	2.4	51.2	4.2	2.4	51.2	4.2
$\mathbf{I_{max}}$ ($counts.s^{-1}$)	53.6	35.3	11.2	31.3	17.3	5.7
$\mathbf{I_{max}/P_{laser}}$ ($counts.\mu m^2.s^{-1}.\mu W^{-1}$)	22.7	0.7	2.7	13.2	0.3	1.4
$\mathbf{I_{TIR}/I_X}$ (X=L or R)	-	**32.9**	**8.5**	-	**40.0**	**9.7**
Average	Glass Substrate			Glass + Au Substrate		
	TIR	**Linear**	**Radial**	**TIR**	**Linear**	**Radial**
$\mathbf{P_{laser}}$ ($\mu W.\mu m^{-2}$)	1.9	41.5	26.2	2.3	41.5	5.1
$\mathbf{I_{max}}$ ($counts.s^{-1}$)	48.2	43.6	141.6	29.7	16.3	8.2
$\mathbf{I_{max}/P_{laser}}$ ($counts.\mu m^2.s^{-1}.\mu W^{-1}$)	27.8	1.2	3.6	13.3	0.42	1.5
$\mathbf{I_{TIR}/I_X}$ (X=L or R)	-	**24.7**	**7.8**	-	31.2	8.4

3.2.4. TIR-TERS spatial optical resolution

An important factor to consider when conducting any form of imaging is the ability of the system to resolve details in the measured object. This spatial optical resolution (SOR) is noteworthy to estimate in TERS imaging, as the metallised tips usually have a higher radius of curvature (ROC) than the nano-tapered standard AFM tips they are based on. While this might decrease the resolution of the AFM imaging, the presence of singular TERS hotspots at the apex of the tip often leads to a SOR lower than that expected for the given ROC of the TERS tip apex, owing to the presence of nanoscale protrusion at the tip apex.[27]

Tapping-mode AFM imaging of Tau-heparin fibrils on gold-coated glass was performed using silver TERS probes (**Figure 3.5**). The height of the Tau-heparin fibrils presented in **Figure 3.5G – I** were found to be typically 5 – 10 nm, which is in agreement with SOR values below 20 nm often reported in the literature.[4,19,24,28] The topographic line section L_D of the fibril in **Figure 3.5B** is presented in **Figure 3.5G**. This section was excited by 561 nm laser light with a scanning step size of 10 nm and an integration time of 10 s. The resulting TERS spectra are presented in **Figure 3.5D**. For points 1, 2, and 3, no TERS enhancement is visible which can be expected as these spectra were taken off of the Tau-heparin fibril. Point 4 could be considered a border region, which gave a slightly weaker TERS signal compared to points 5 and 6 which are definitely located on the fibril structure. This initial measurement suggests the lateral SOR to be at least 10 nm, given the scanning step size of this line section.

The two next line sections, L_E and L_F (**Figure 3.5C**), were taken using a scanning step size of 5 nm and with an integration time of 1 s. The height profile of line L_E and associated TERS spectra are presented in **Figure 3.5H** and **E** respectively. Points 1, 5, 6, 7, and 8 are on the fibril structure, while points 3 and 4 are inside a hole. Point 2 is taken at the fibril border, which is confirmed by the decreased TERS intensity when compared to point 1 especially. This would initially suggest a lateral SOR of 5 nm or less. However, for the off-fibril points 3 and 4, a low TERS signature can still be observed. For the line L_F, the points 1 – 5 and 8 in **Figure 3.5F** are on the fibril structure with points 6 and 7 being located inside a hole. In contrast to line L_E, the border point 5 of line L_F has no TERS signature and therefore the lateral SOR can be assumed to be ca. 5 nm. This lack of a TERS spectrum at point 5 could be related to the greater SOR of the TERS-active tip. This SOR is much higher than the AFM lateral resolution expected for such an AFM tip, which was coated with 60 nm of silver. A SOR of 5 nm cannot be explained by the expected radius of curvature (ROC) of this size of tip, even if AFM spatial resolution is typically better than such a ROC. This may suggest that point 5 is in fact also

located inside a hole, which isn't resolved in the AFM height image. In summary, a lateral SOR of 5 – 10 nm has been demonstrated on Tau-heparin fibrils using our TIR-TERS system. This SOR value is in good agreement with the literature for amyloids fibril and oligomers, being within the 1 – 30 nm range.[1,17,19,22–24]

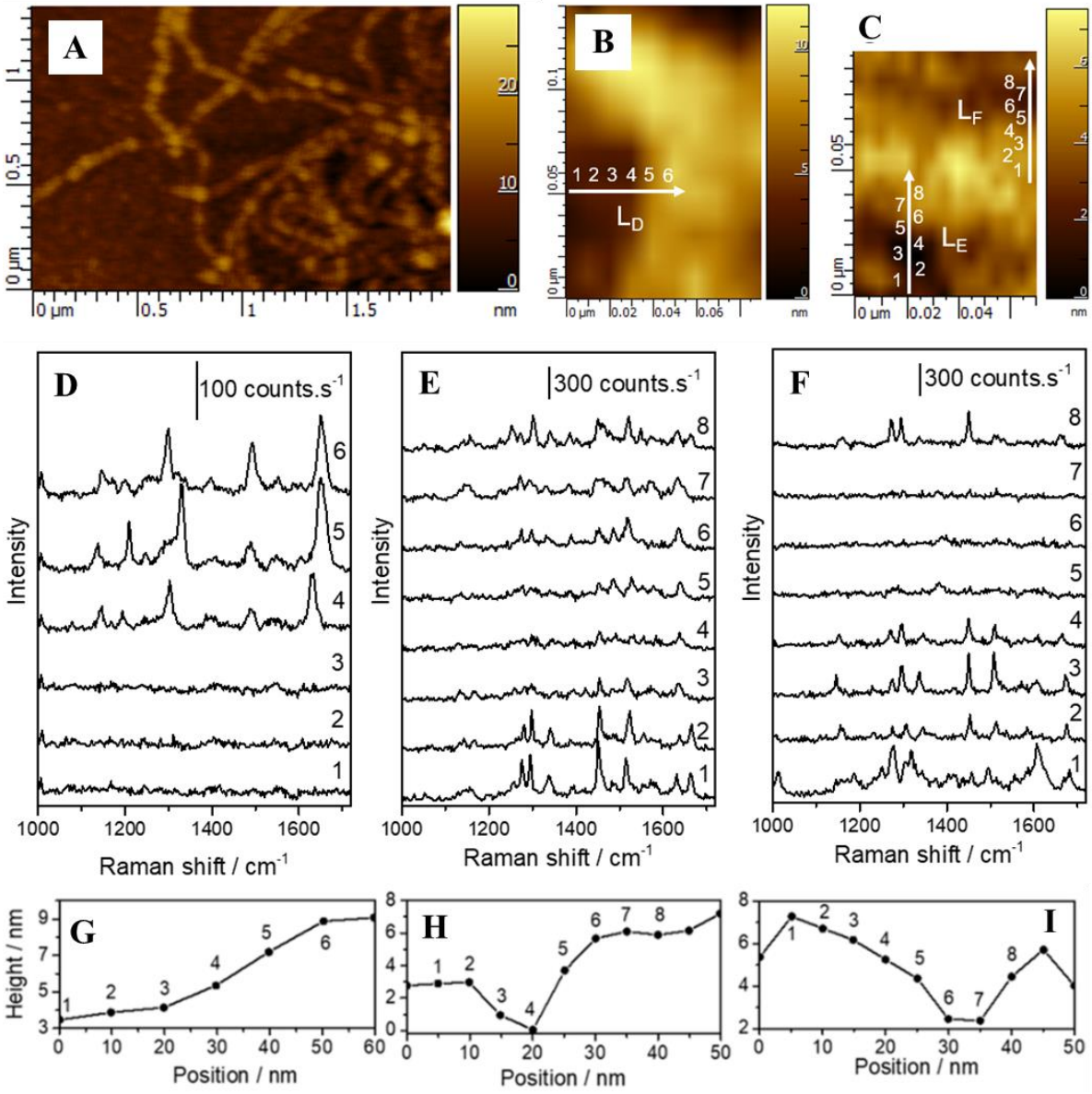

Figure 3.5. *[A] AFM height image of Tau-heparin fibrils and* ***[B, C]*** *enhanced regions on individual fibrils.* ***[D]*** *The associated six TERS spectra of lines L_D (integration time: 10 s, scanning step size: 10 nm).* ***[E-F]*** *Eight TERS spectra corresponding to lines L_E and L_F respectively (integration time: 1 s, scanning step size: 5 nm).* ***[G-I]*** *Measured AFM height profiles of fibrils along lines L_D, L_E, and L_F respectively in B and C. Incident laser: 561 nm.*

While typical AFM imaging gives purely superficial information, TERS has an associated probe depth within the range of a few nanometres typically. The line profiles of **Figure 3.5** can also give information about the aforementioned probe depth. Along line L_D (**Figure 3.5B** and **D**), the TERS spectra corresponding to points 4, 5, and 6 have a consistent intensity despite being acquired in fibril regions of 5.3, 7.1, and 8.9 nm height respectively. A probe depth as low as 1 – 2 nm could be reasoned, given the fact that no TERS signal is observed in the 4.1 nm high region of point 3. A similar trend is seen along line L_E, where the thick fibril regions of 6 nm height (points 6 – 8) have only a slightly increased TERS signal compared to the 3.6 nm high region of point 5. The gap-mode effect of the gold substrate cannot be the reason behind the intense TERS spectra of points 1 and 2, since it is unlikely as such enhancements are expected for very small tip-sample separations of 1 – 2 nm.[20] Maybe the molecular orientation of probed vibrational modes is more aligned with the enhanced electric field polarisation in this region.[16] **Figure 3.6** shows a different set of fibrils, where a line profile was taken along the fibril, rather than across the fibrils in **Figure 3.5**. The 15 points taken from the fibril in **Figure 3.6B**, are displayed as AFM height (**Figure 3.6C**), and their associated TERS signals (**Figure 3.6D**). From the AFM height profile, the fibril varies from 3.4 to 9.6 nm thick over a 90 nm distance along the fibril. Despite the previous discussion on the probe depth analysis, the TERS spectra associated with this fibril is relatively constant with a less obvious dependence on fibril thickness. All in all, the nanoscale surface sensitivity of TERS is believed to be in the 1 – 4 nm range.

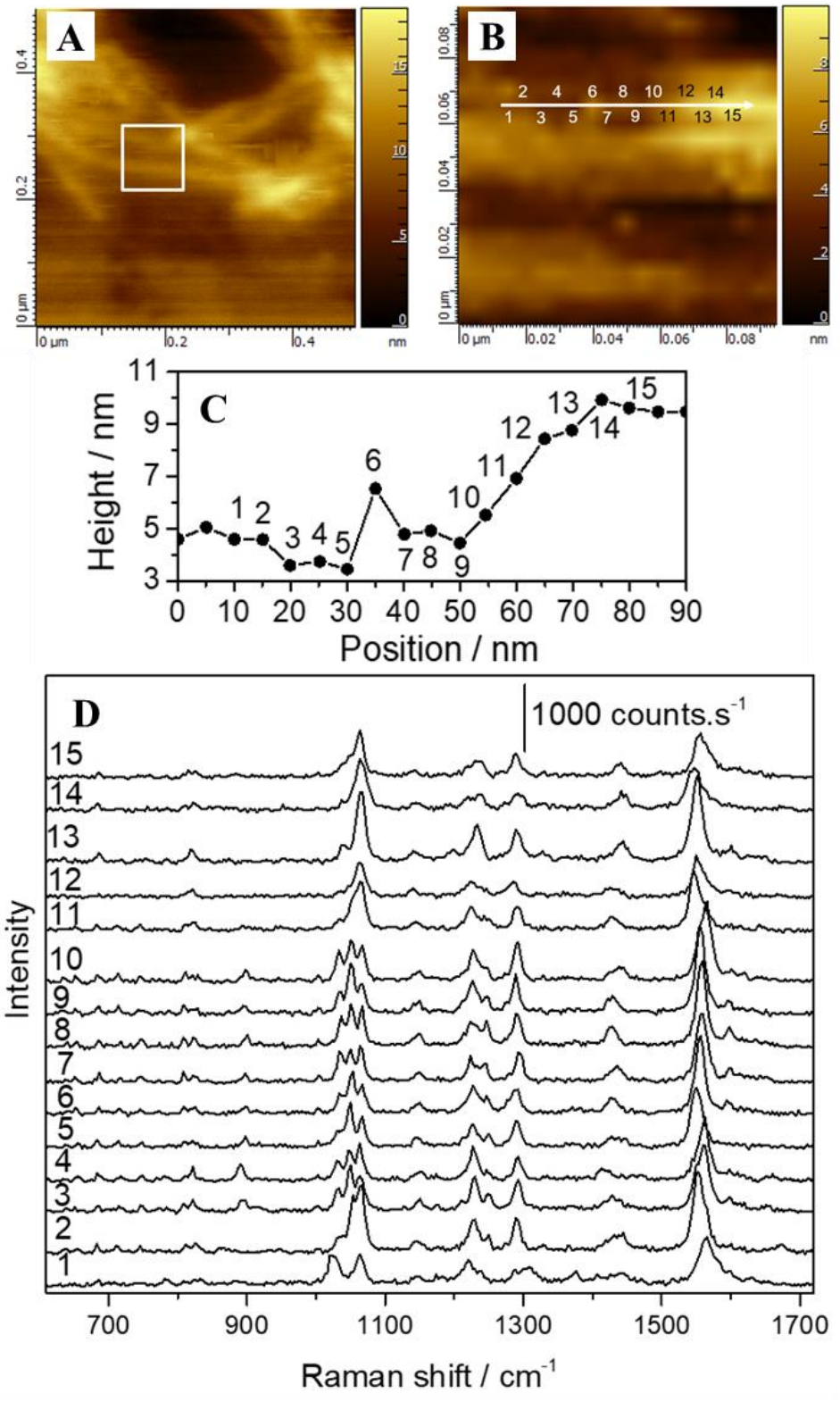

Figure 3.6. [A] *AFM topographic image of Tau-heparin fibrils on gold-coated glass coverslip (0.5 x 0.5 µm, 256 pixels).* ***[B]*** *TERS-AFM topographic image of individual Tau-heparin fibrils indicated by white rectangle in A (0.1 x 0.1 µm, 1s integration time, 5 nm step size).* ***[C]*** *Line height profile shown in B.* ***[D]*** *Representative TERS spectra of 15 points along line of height profile in C. Incident laser: 561 nm.*

3.2.5. Chemical maps of Tau-heparin fibrils using TIR-TERS

Similar to the line profiles taken in **Chapter 3.2.4** above, a step size of 5 – 10 nm was used for generating chemical maps of Tau-heparin fibrils with our TIR-TERS configuration. These chemical maps were generated by the classical peak-picking method, where the integration of specific marker bands in the obtained TERS spectra leads to monochromatic intensity maps. These TERS maps of Tau-heparin thus visualise specific amino acid content, protein secondary structure, and heparin cofactor localisation within the imaged fibrils.

Aromatic amino acids have a higher Raman scattering cross-section[20] which makes them more easily detectable in TERS compared to nonaromatic residues. Tau protein does not contain any tryptophan (Trp), but tyrosine (Tyr), histidine (His), and Phenylalanine (Phe) can all be assigned using specific bands. For Phe, the ring-breathing mode at 1000 – 1015 cm^{-1} allows for the unambiguous assignment of this residue, which is visualised in **Figure 3.7D**. For His, a multi-band assignment approach is needed due to the overlap of multiple bands in a given spectral region.[25] His assignment requires the cooccurrence of at least three bands from the following: NH deformation, C=C asymmetric stretch (1486 – 1519 cm^{-1}), CN stretch (1328 – 1337 cm^{-1}), CN stretch, CH deformation (1112 – 1143 cm^{-1}), and CN stretch, ring deformation (948 – 996 cm^{-1}). For Tyr, two bands from the C=C stretch (1591 – 1619 cm^{-1}), side chain (1172 – 1217 cm^{-1}), ring breathing (813 – 883 cm^{-1}), and the ring deformation (612 – 641 cm^{-1}) are often considered for a definitive assignment. However, the band assigned to the ring breathing (Fermi doublet) can be sufficient for assignment of Tyr.[22]

Our TIR-TERS system allows for the probing of several non-aromatic amino acids including cysteine (Cys) via the C-S stretching vibrations at 655 – 689 cm^{-1} and 740 – 802 cm^{-1} (**Figure 3.7C**), in addition to the disulphide bridges of cystine (i.e. cysteine dimer) S-S vibrations present at 500 – 550 cm^{-1} (**Figure 3.7I**). While individual 4R Tau proteins only contain two Cys residues, the C322 amino acid is located in the microtubule binding domain (MBD) which is the region associated with the core cross β-sheet structure of mature fibrils. The addition of DTT as a mild reducing agent (**Annex 1**) definitely reduces cysteine thiol groups of monomeric Tau to their SH form,[29] which in turn has been shown to aid fibril formation *in vitro* by disrupting the intramolecular monomeric bond.[30] Disulphide bond formation has been proposed to be important for seeding and fibril formation, generating structural polymorphism as seen in different isoforms of Tau. Nevertheless, the presence of such S-S bonds in mature fibrils has not been easily realised even using cryo-EM methods as a regular density pattern of the C322 residue was absent.[5] As is evident from **Figure 3.7A** and **I**,

the studied Tau-heparin fibril indeed contains disulphide bonds amongst its Cys residues that run along the fibrillar axis. This finding suggests that mature Tau 2N4R fibrils seeded with heparin as cofactor do form Cys intermolecular bonds and can be visualised using TIR-TERS.

Other amino acids of interest in the study of hydrophobicity/hydrophilicity of Tau appear in the 1115 – 1171 cm^{-1} range in the form of $=NH_2^+$ or NH_3^+ deformation modes. These modes belong to arginine (Arg), lysine (Lys), asparagine (Asn), and glutamine (Gln), and were treated here as part of a single spectral region due to the fact that the vibrational modes arise from the polar head of their side chains. The aforementioned positively-charged amino acids are also of interest in the study of interactions with the negatively charged cofactors such as heparin here, as they are likely to be involved in charge balancing at binding sites. **Figure 3.5F** shows the distribution of positively charged amino acids, and it can be concurred that they are present along the fibril axis. The overlay of Cys, Phe, and Arg/Lys/Asn/Gln (**Figure 3.7C, D,** and **F**) is presented in **Figure 3.7G**. The green pixels in the middle of this TERS map demonstrate how the Arg/Lys/Asn/Gln are dominant over the less frequently occurring Cys and Phe. While Phe residues are observable in a similar region (blue pixels), intense Phe bands appear where there is a relatively low contribution of Arg/Lys/Asn/Gln (Point 3, **Figure 3.7A** and **B**). On the contrary, areas of intense Arg/Lys/Asn/Gln (Point 5, **Figure 3.5A** and **B**) often don't have a discernible contribution from Phe. These observations can be explained by the presence of nanoscale hydrophilic domains, which have a strong contribution from Arg, Lys, Asn, and Gln, as well as mixed hydrophilic/hydrophobic domains where the contribution from Phe residues is also observed. The amino acid sequence of Tau only contains three Phe residues (F8, F246, F378) and the previous findings imply that it is present at the fibril surface, which agrees with observations of Phe-rich fibril surfaces in mature insulin amyloid fibrils.[24,25] The literature for insulin and $A\beta_{1\text{-}42}$ fibrils[4,25] also reports the presence of heterogenous hydrophilic and mixed domains which is consistent with the observations presented here. Similarly, to the hydrophilic Arg, Lys, Asn, and Gln, Cys is observed primarily in the lower portion of the TERS image (Points 1 – 6, **Figure 3.7A** and **B**). As previously discussed, 4R Tau contains two Cys residues: C291 and C322. The latter is implied in the formation of the core β-sheet structure and intermolecular S-S disulphide bonds were able to be detected using TERS. The former residue is located in the fuzzy coat region, and it is unclear whether this residue reliably forms intermolecular disulphide bridges. The occurrence of both S-S bonds and free SH Cys would explain the intensity differences between the maps presented in **Figure 3.7C** and **I**. Such bridges make Cys hydrophobic, and their presence on the fibril surface also confirms mixed hydrophilic/hydrophobic domains.

The most defining vibrational modes observable in TERS of heparin are located in the 1021 – 1040 cm^{-1} and 1046 – 1069 cm^{-1} spectral region and are related to the N-SO_3 and O-SO_3 moieties, respectively. Heparin as a cofactor is expected to be incorporated into the molecular structure of Tau fibrils,[11] however the exact nature of this incorporation is still poorly understood. **Figure 3.7E** presents the discernible heparin bands in the 1035 – 1065 cm^{-1} region. Unfortunately, these bands are centred in either the border region to Phe and the border region to Asn and Gln, making their absolute assignment uncertain. In addition, the 1035 – 1065 cm^{-1} spectral region in many spectra (see **Figure 3.7B**, **Figure 3.5G – I**) is void of any discernible heparin marker band. This scarcity of spectral features may suggest that heparin is unenhanced by TERS tips as it is buried in the fibril core, being outside of the axial resolution of 1 – 4 nm. Nevertheless, **Figure 3.6D** shows some spectral contribution in this heparin region, which could be reasoned possible due to the relative thinness of the fibril region examined (3.5 – 6 nm).

Amide I and amide III bands are most commonly used for the investigation of secondary structure in TERS.[1,4,17,19–25,28,31,32] The amide I region is between 1600 – 1700 cm^{-1} and is decomposed into parallel β-sheets (1620 – 1629 cm^{-1}), random coils (1630 – 1655 cm^{-1}), and antiparallel β-sheets and fibril core β-sheets (1660 – 1682 cm^{-1}). In a similar fashion, the amide III region is divided into β-sheets (1218 – 1250 cm^{-1}) and random coils (1251 – 1273 cm^{-1}). The amide III β-sheet region can be further subdivided into parallel β-sheets (1218 – 1228 cm^{-1}) and antiparallel β-sheets (1233 – 1242 cm^{-1}). The amide II region (1520 – 1590 cm^{-1}) sometimes mentioned in TERS literature is low in intensity in Raman spectra in addition to overlapping with other amino acid residues. It is therefore not considered further in this analysis.

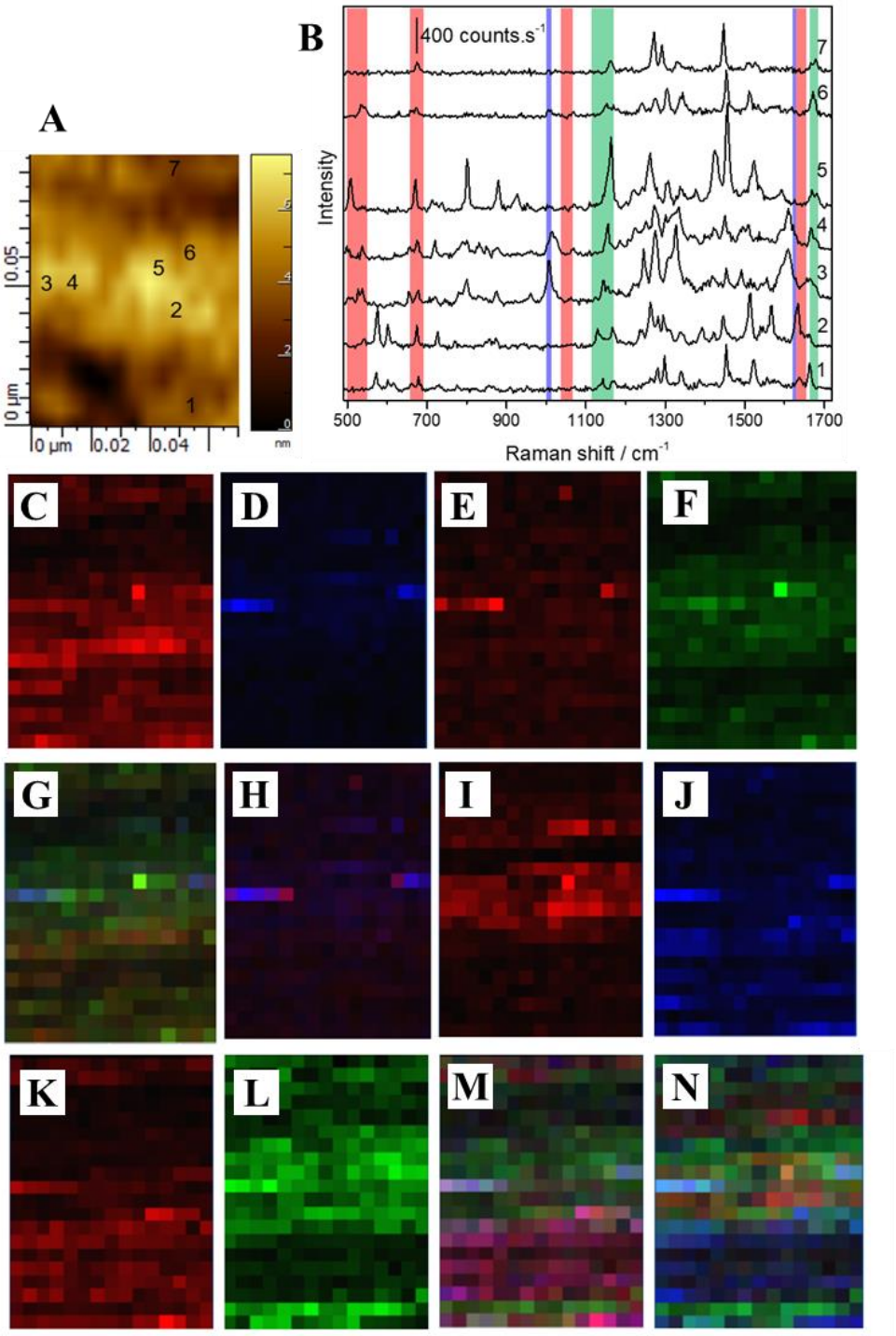

Figure 3.7. ***[A]*** *AFM height image of Tau-heparin fibril, with location of points 1 – 7 that correspond to the TERS spectra in B (75 x 100 nm, scanning step size: 5 nm, integration time: 1s).* ***[B]*** *Seven TERS spectra corresponding to points 1 – 7 on fibril presented in A. Spectral regions used in band integration for generating chemical maps are as follows from left to right: Cys S-S stretching (red), Cys C-S stretching (red), Phe ring breathing (blue), Heparin N-SO stretching (red), Lys/Arg/Asn/Gln N-modes (green), Amide I band of parallel β-sheets (blue), Amide I band of random coils (red), Amide I band of antiparallel/core β-sheets (green).* ***[C-N]*** *Chemical maps corresponding to integration of bands described in B:* ***[C]*** *Cysteine,* ***[D]*** *Phe,* ***[E]*** *Heparin,* ***[F]*** *Lys/Arg/Asn/Gln,* ***[G]*** *Overlay of C+D+F,* ***[H]*** *Overlay of D+E,* ***[I]*** *Cystine S-S, Amide I* ***[J]*** *Parallel β-sheets,* ***[K]*** *Random Coils,* ***[L]*** *Antiparallel/core β-sheets,* ***[M]*** *Overlay of J+K+L,* ***[N]*** *Overlay of I+J+L. Incident laser: 561 nm.*

The peptide backbone bonds are possibly cleaved in TERS experiments under high laser fluences due to the creation of hot carriers in the plasmonic hotspot beneath the TERS tip.[33] This can lead to the absence of amide I bands in TERS spectra. Another possibility is that bulky side chains of amino acids such as Phe, Tyr, and His, can reduce the TERS enhancement due to a greater distance from the plasmonic tip apex. Additionally, the lack of amide I bands for β-sheets could be due to their specific sensitivity with respect to molecular orientation and light polarisation. In **Figure 3.6D**, the absence of amide I bands could be reasoned to be due to the two latter causes, especially since the bulky Phe, Tyr, and Pro spectral bands are observable. Moreover, laser fluences used in our experiment were lower than those for which a photo-induced cleavage of peptide bonds has been demonstrated. The distribution of amide I bands is visualised in **Figure 3.7J** for parallel β-sheets, **Figure 3.7K** for random coils, and **Figure 3.7L** for antiparallel β-sheets and fibril core β-sheets. The amide I bands of multiple secondary structures are sometimes visible in a given pixel, as is the case for **Figure 3.7A** and **B** (points 1 – 3). On the contrary, singular intense peaks associated with only one amide I secondary structure is visible for points 4 – 7 in the same image. **Figure 3.7M** clearly showcases a separation between antiparallel β-sheets or core β-sheets regions (green) and the area of random coils (red) with partial overlap. Taking the height profile of **Figure 3.7A**, the thinner fibril areas are therefore associated with random coils and it can be concluded that the surface fuzzy coat dominates the TERS signal acquired in these regions. Parallel β-sheets can be detected in similar regions, likely being located towards the surface of the fibrils. In thicker fibril regions, antiparallel β-sheets and fibril core β-sheets TERS bands are dominant which is in line with the localisation of the β-sheet rich core of the fibril. Tau-heparin fibrils have a twisted shape about their primary axis, which is concurrent with the dependence observation of fibril thickness on fibril secondary structure. The instances of bands from both random coils of the fuzzy coat and the β-sheet core being observable are likely due to the simultaneous probing of both the surface and β-sheet rich core.

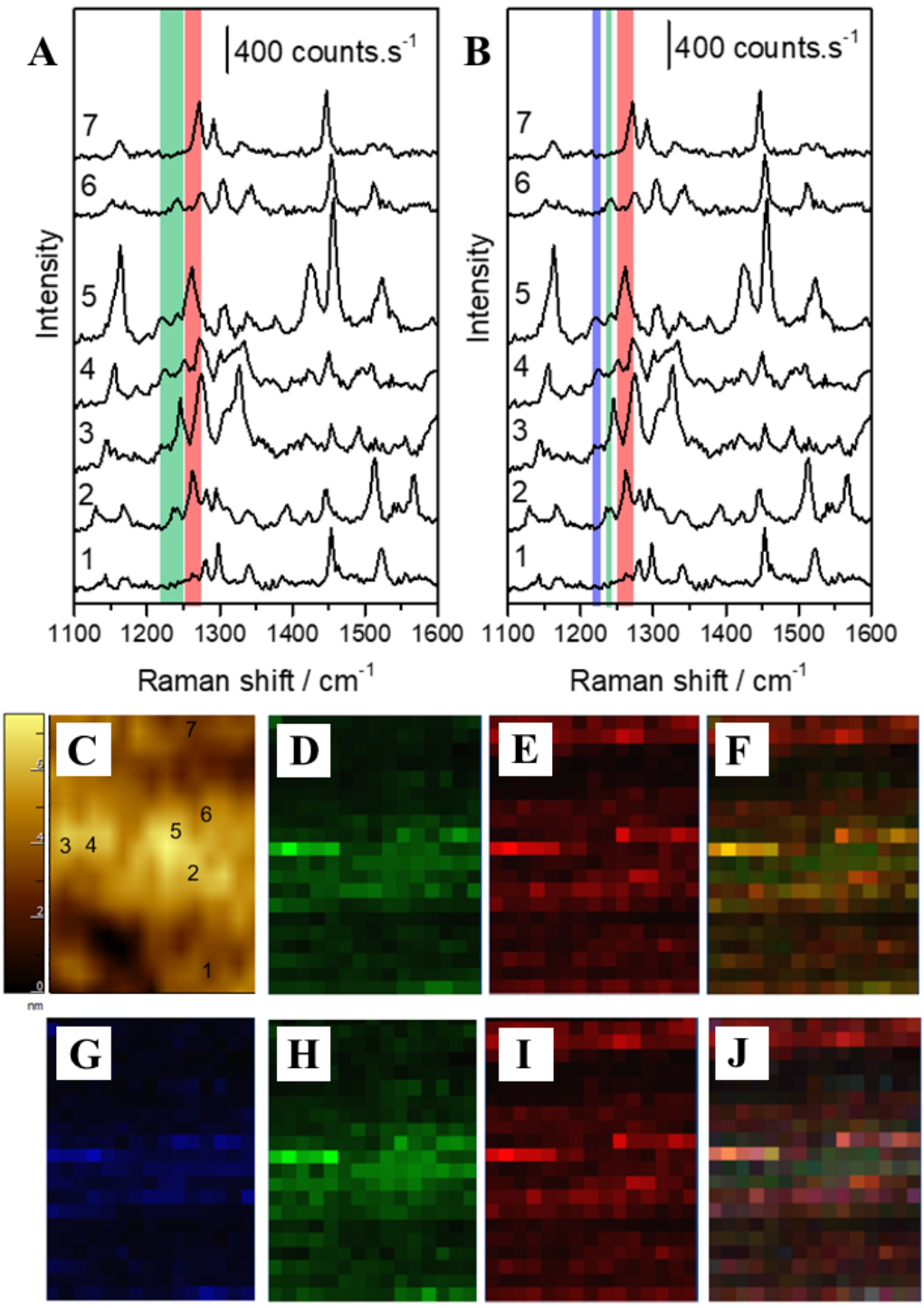

Figure 3.8. [A, B] *TERS spectra associated with points 1 – 7 taken from C. Spectral regions used in band integration for generating chemical maps are as follows from left to right: amide III bands of β-sheets (green) and random coils (red) in A. In B, they are amide III bands of parallel β-sheets (blue), antiparallel β-sheets (green), and random coils (red).* ***[C]*** *AFM height image of Tau-heparin fibril.* ***[D-J]*** *Intensity integration TERS maps of spectral regions as per A and B. Amide III band distribution corresponding to* ***[D]*** *β-sheets,* ***[E]*** *random coils,* ***[F]*** *Overlay of D+E,* ***[G]*** *parallel β-sheets,* ***[H]*** *antiparallel β-sheets,* ***[I]*** *random coils, and* ***[J]*** *Overlay of G+H+I. Incident laser: 561 nm.*

Figure 3.8 shows the spatial distribution of amide III bands that are associated with random coils, parallel β-sheets, and antiparallel and fibril core β-sheets. Compared to amide I bands previously discussed; all three structures are seemingly evenly distributed with the top part of the fibril structure having a greater presence of random coils. Despite this discrepancy, the amide I analysis above can be said to be of greater weight due to the overlap of amide III bands with other vibrational modes in this spectral region. The nonspecific bending vibrations of CH_2 and CH_3 amino acid side chains contribute in this spectral range,[1,19,25,34] and therefore amide III band assignment cannot be absolutely certain without cooccurrence of amide I bands. TERS maps of antiparallel β-sheet distribution using the intensity integration of amide I (**Figure 3.7L**) and amide III (**Figure 3.8H**) bands are very comparable, meaning that they are congruent and unaffected by any potential overlapping band. It is to be noted, that the overall intensity of observed amide III bands is lower than that of amide I bands, which could also contribute to their discrepancy in the case of spatial distribution of random coils along the fibril. This is evident in the comparison of **Figure 3.7K** and **Figure 3.8E**. Undoubtedly, this means there are contributions from uncorrelated bands in the amide III region and this observation has already been reported in our group's previous work with Tau K18 fibrils.[19] Concluding the above analysis, it is preferable to analyse secondary structure of amyloids using amide I bands over amide III where available.

The polar amino acids Arg/Lys/Asn/Gln (**Figure 3.7F**) correlate with regions of antiparallel β-sheets and core β-sheets (**Figure 3.7L**), which demonstrates the presence of these amino acid residues at the fibril core. This in turn could signify the importance of such residues in the binding or incorporation of cofactors in the fibrillization of Tau. Phe is also present in such regions, as well as Cys in the form of S-S disulphide bonds (**Figure 3.7I, L, N**). It is noteworthy that regions of random coils do not feature a strong contribution from these disulphide bonds (**Figure 3.7I, J, N**). It is suggested that there is a dependence on the presence of S-S bonds and Tau-heparin fibril secondary structure,[35] and that therefore disulphide bonds of C322 might stabilize antiparallel β-sheets of the fibril core. Considering that the native Tau protein does not contain disulphide bonds, this demonstrates the ability of TERS to help characterise potential formation mechanisms of amyloids.

3.3. TERS imaging of RNA-Tau Amyloid Fibrils

3.3.1. Experimental Procedures

Full-length Tau 2N4R P301L was expressed and purified by PhD candidate Vicky Ury-Thiery at CBMN under a previously established protocol.[13] In brief, *E. coli* BL21 (DE3) was used to express the full-length Tau protein and purified using nickel affinity chromatography.[36] The mutation P301L was added via site-directed mutagenesis.

The purified P301L Tau was subsequently incubated with heparin sodium (Sigma-Aldrich, H6279, from porcine intestinal mucosa) or polyadenosine (polyA, Sigma-Aldrich, T3516) and suspended in HEPES buffer. To follow fibril formation, a thioflavin T (ThT, Sigma-Aldrich, T3516) fluorescence assay was used. Fibrils were pelleted using an ultracentrifuge and resuspended in Milli-Q water. In what follows, polyA-induced and heparin-induced Tau fibrils will be termed Tau-polyA and Tau-heparin, respectively. Tau-heparin fibrils were produced as described in **Annex 1.**

3.3.2. Tau fibril formation and morphological characterisation

Fibril growth of Tau-heparin and Tau-polyA fibrils was monitored using a ThT fluorescence assay (**Figure 3.9A – C**). The increase in fluorescence intensity over time indicates the formation of β-sheet assemblies of amyloid-like fibrils. **Figure 3.9A** demonstrates that after 15 hours of incubation the plateau is reached for Tau fibrils seeded with heparin. For Tau with polyA, the plateau is only reached after 40 hours. The binding of heparin to Tau has been well documented,[37,38] but the same cannot be said about polyA specifically, as a unique example of RNA binding has been reported.[8] **Figure 3.9B** and **C** show measured TEM images of micrometre-long filaments of Tau-heparin and Tau-polyA, respectively. The fibril structures of Tau-polyA were examined using AFM (**Figure 3.9D**) and were found to have a typical height between 8 – 13 nm, and a helix of 100 – 130 nm pitch. These fibrils are in contrast to heparin fibrils which have reportedly 4 – 10 nm height and 25 – 65 nm pitch.[9]

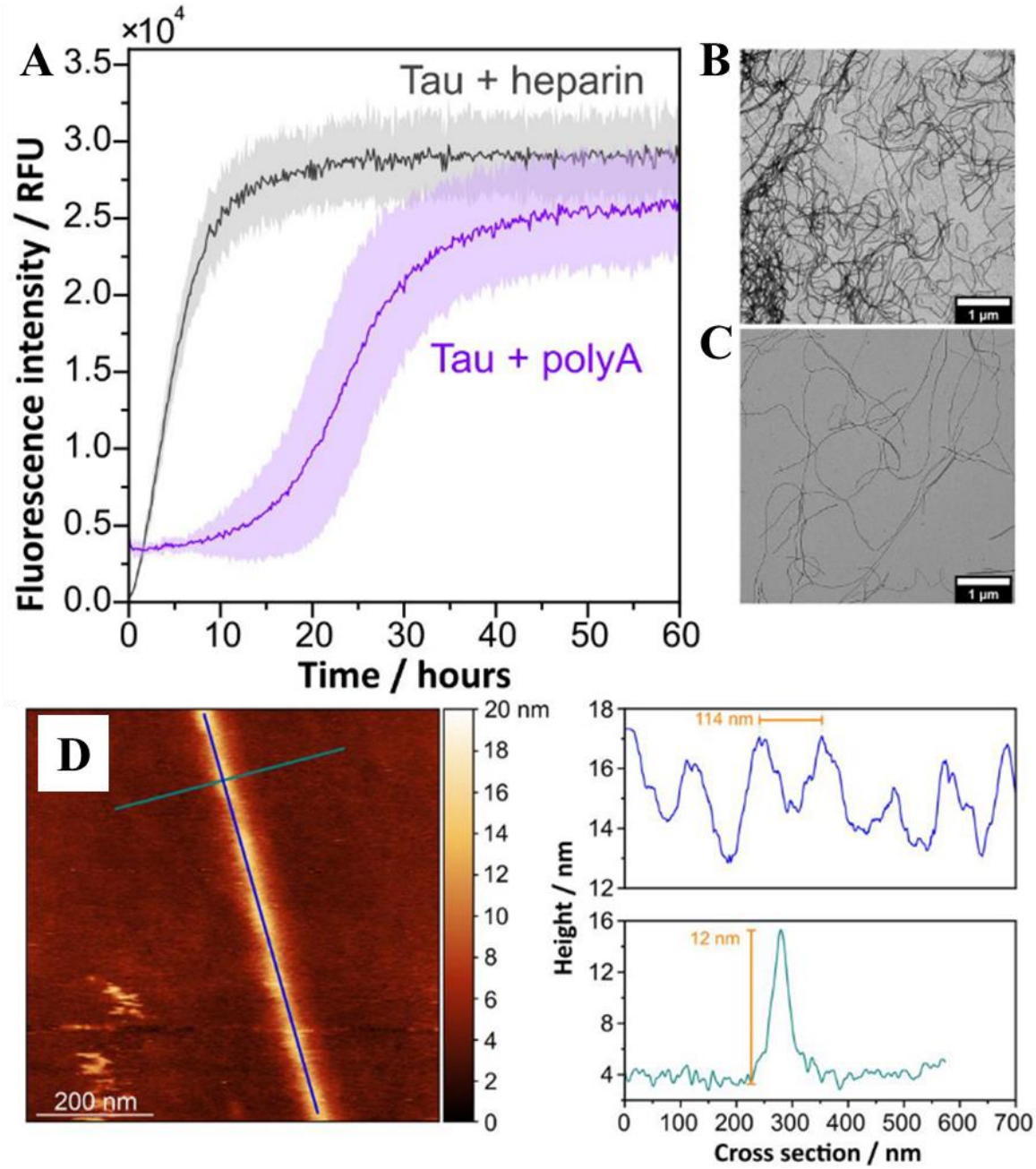

Figure 3.9. ***[A]*** *ThT fluorescence assay of Tau 2N4R P301L incubated with polyA cofactor (purple) and heparin cofactor (grey).* ***[B]*** *TEM image of Tau-heparin fibrils after assay.* ***[C]*** *TEM image of Tau-polyA fibrils after assay.* ***[D]*** *AFM height image of Tau-polyA fibril on freshly cleaved mica. The blue line insert shows the fibril helicity to be ca. 114 nm, with the green line insert showing the maximum measured fibril height of 12 nm.*

3.3.3. Raman and SERS of Tau-polyA fibrils

Compared to unenhanced Raman, the intensity of TERS signatures of biomolecules generally show similar wavenumbers but can differ considerably in intensity.[20,21] Surface-enhanced Raman scattering (SERS) utilises the same phenomenon as TERS of resonant optical excitation of plasmonic noble metal nanoparticles at nanometric distance from probed molecules. This means SERS can often have similar band intensities close to those observed in TERS. Differences can nonetheless occur.[17,34] The larger sample areas of many hotspots in SERS often contributes to an averaged signal,[20] while TERS is capable of single molecule detection, and is more sensitive to changes in molecular orientation. In the assignment of TERS vibrational bands, performing Raman and SERS of the same species is useful as a benchmark, especially for protein primary and secondary structures. The unenhanced Raman and SERS spectra of Tau fibrils including their isolated cofactor has been used here to help chemically and structurally characterise these biomolecules using TERS.

The analysed sample area in TIR configuration is 900 times larger than direct light excitation, with 8.5 µm radius instead of 280 nm, respectively. At the critical angle, the depth probed in TIR is 4 – 5 times lower than direct illumination which leads to a probed volume that is ca. 200 times larger in TIR-Raman and TIR-SERS experiments than in conventional Raman and SERS experiments. Therefore, our TIR system is less sensitive to positional variation of irradiation than conventional micro-Raman spectrometers. Nevertheless, our sample is still expected to show spectral variation as the polyA strands, Tau-polyA, and Tau-heparin fibrils can be several hundred micrometres in length. This is demonstrated in the averaged TIR-Raman and TIR-SERS spectra in **Figure 3.10**. It is noteworthy that while there are some fluctuations in the Raman and SERS intensities depending on the excited sample area, there is little shift in the associated wavenumbers of bands, as shown by calculated standard deviations in Raman and SERS spectra of Tau-heparin, Tau-polyA and pure polyA samples (**Figure 3.11**).

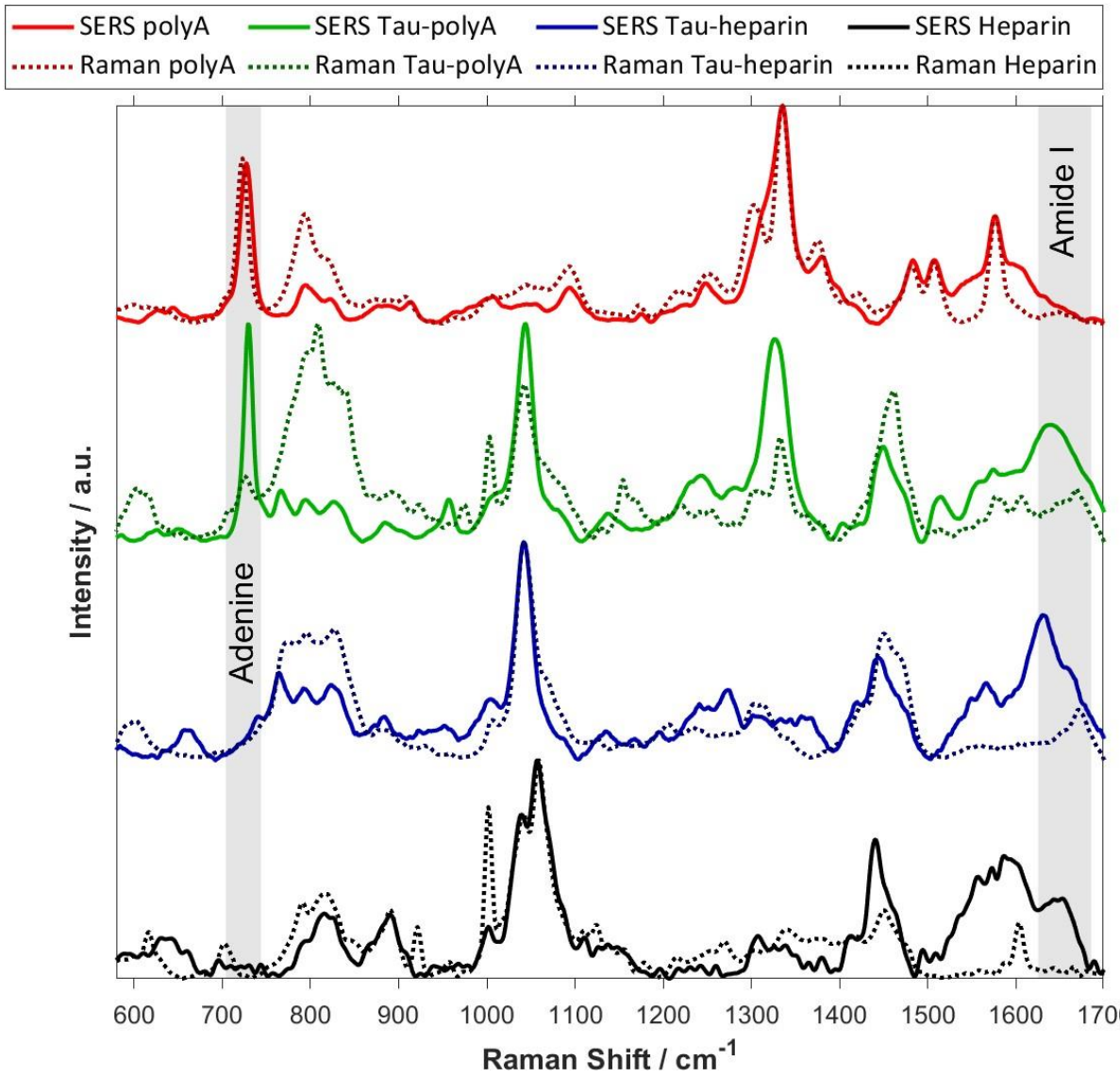

Figure 3.10. *Raman and SERS spectra of pure polyA (red), Tau-polyA fibrils (green), Tau-heparin fibrils (blue), and pure Heparin (black) on glass and silver-coated glass substrates respectively. The amide I region and characteristic adenine ring breathing mode are highlighted as grey bars. Incidence laser: 561 nm.*

Figure 3.10 presents the Raman and SERS spectra obtained on glass and silver-coated glass respectively for pure polyA, Tau-polyA fibrils, and Tau-heparin fibrils. The full band assignments for all Raman and SERS spectra can be found in **Table 3.3** for heparin and Tau-heparin fibrils and **Table 3.2** for polyA and Tau-polyA fibrils. The nucleoside bases of nucleic acids are known to interact and adsorb on noble metal surfaces, rather than the phosphate backbone.[39] This is observed in the Raman band assigned to the backbone O-P-O stretching modes (790 – 831 cm^{-1}) of polyA having a greater intensity than the corresponding SERS band of the same mode. This lack of enhancement is likely due to the distance between this chemical moiety and the SERS-active nanoparticle surface.[40] The strong decrease in the electromagnetic

field and loss of any potential "first layer" chemical enhancement effect with increased sample-metal nanoparticle distance is the reason for this observed distance dependence of SERS enhancement.[41,42] It is suggested that polyA adsorbs onto the silver SERS substrate primarily via the adenine molecule with a greater distance between the surface and phosphate backbone.

Table 3.2. *Band assignments of polyA and Tau-polyA Raman, SERS, and TERS spectra. Raman shifts are given in cm^{-1}. Abbreviations are as follows: def = deformation, str = stretching, bend = bending, asym = asymmetric, sym = symmetric, sci = scissoring, breath = breathing, rk = rocking, py = pyrimidine, im = imidazole.*

Band Assignment 11,15,19-26		PolyA (this work)		Tau-polyA (this work)		
		Raman	SERS	Raman	SERS	TERS
Amide I	Core β-sheet	-	-	1669	1674	1682-1660
Amide I	Random coils	-	-	1646	1635	1655-1630
Adenine	NH_2 sci	1654	1651	-	-	-
Phe, Tyr	C=C str	-	-	-	-	1616-1590
Adenine	NH_2 def	-	1608	1606	1602	1609-1591
Amide II	Random coils	-	-	1577	1572	1590-1570
Amide II	Core β-sheet	-	-	1559	1548	1569-1534
Adenine	Ring str (py)	1580	1576	1559	1548	1583-1538
His	NH def, C=C asym str	-	-	1513	1510	1517-1482
Adenine	Ring	1511	1509	1513	1510	1527-1507
Adenine	C=N str (py), C_2H_2	1485	1483	1457	1476	1486-1461
	CH_3, CH_2 sci	1453	1443	1457	1476	1486-1461
Adenine	NH def, CH def, CN str	1424	1422	1416	1451	
Glu, Asp	COO^- sym	-	-	-	1404	1400-1370
Adenine	C-N str (py)	1379	1337	1379	1374	1378-1359
Adenine	Ring, C-N str (im)	1339	1336	-	-	-
His	C-N str	-	-	1334	1327	1337-1327
	CH_2 bend	-	-	1334	1327	1337-1327
Amide III	Random coils	-	-	1245	1239	1273-1251
Amide III	β-sheet	-	-	1218	-	1250-1218
Phosphate	O-P-O asym str	1255	1248	-	-	1249-1218
Phosphate	PO_2^- asym str	1219	1219	1218	-	1249-1218
Tyr	Side chain	-	-	1218	-	1272-1217
His	NCN str, NH def	-	-	1177	1187	1194-1150
Ribose	C-C str	1178	1174	1170	-	1180-1150
Arg	$=NH_2^+$ def	-	-	1170	-	1171-1156
Lys	NH_3^+ def	-	-	1154	1135	1155-1136
Adenine	CN str, NH def	1142	-	-	-	-
Asn, Gln	NH_3^+ def	-	-	1129	1135	1135-1115
Phosphate	P-O-C sym strm, O-P-O sym str	1097	1096	1070	1088	1104-1072
Arg	$=NH_2^+$ def	-	-	1085	1088	1094-1088
Lys	NH_3^+ def	-	-	1075	1073	1080-1070
Asn, Gln, Phe	NH_3^+ def, CH ring def	-	-	1064, 1041	1044	1069-1046
Ribose	N-sugar str, sugar (CO str)	1051	1050	-	-	-
Phe	Ring breath	-	-	1004	1008	993-1015
His	CN str, ring def	-	-	975	956	965-948
Adenine	NH_2 rk	911	912	-	-	-
Pro	Ring str	-	-	891	889	919-890
Tyr	Ring breath	-	-	829	828	886-813
Phosphate	O-P-O str	797	796	797	794	890-790
Cys	C-S str	-	-	797	794	817-740
Adenine	Ring breath	726	726	725	730	709-739
Cys	C-S str	-	-	-	650	689-655
Cys	S-S str	-	-			550-500

Table 3.3. *Band assignments of heparin and Tau-heparin Raman, SERS, and TERS spectra. Raman shifts are given in cm^{-1}. Abbreviations are as follows: def = deformation, str = stretching, bend = bending, asym = asymmetric, sym = symmetric, sci = scissoring, breath = breathing.*

Band Assignment		Heparin (this work)		Tau-heparin (this work)		
		Raman	SERS	Raman	SERS	TERS
Amide I	Core β-sheet	-	-	1675	1677	1682-1660
Amide I	Random coils	-	-	1655	1637	1655-1630
Heparin	NH def	1606	1649	-	-	-
Phe, Tyr	C=C str	-	-	1606	1597	1616-1590
Heparin	NH def	-	1596	-	1597	-
Amide II	Random coils	-	-	1588	-	1590-1570
Amide II	Core β-sheet	-	-	1553	1560	1569-1534
His	NH def, C=C asym str	-	-	1469	1471	1517-1482
	CH_3, CH_2 sci	1453	1443	1448	1448	1486-1461
Glu, Asp	COO^- sym	-	-	1344	1368	1400-1370
His	C-N str	-	-	1318	1340	1337-1327
	CH_2 bend	1322	1309	1301	1303	1337-1327
Amide III	Random coils	-	-	1272	1276	1273-1251
Amide III	β-sheet	-	-	1235	1254	1250-1218
Tyr	Side chain	-	-	1207	1232	1272-1217
His	NCN str, NH def	-	-	1194	1187	1194-1150
Arg	$=NH_2^+$ def	-	-	1155	1167	1171-1156
Lys	NH_3^+ def	-	-	1132	1141	1155-1136
Asn, Gln	NH_3^+ def	-	-	-	1141	1135-1115
Arg	$=NH_2^+$ def	-	-	1082	1082	1094-1088
Lys	NH_3^+ def	-	-	1070	1071	1080-1070
Heparin	6-OSO_3, 3-OSO_3	1062	1059	1064	1044	1065-1050
Asn, Gln, Phe	NH_3^+ def, CH ring def	-	-	1043	1044	1069-1046
Heparin	N-SO_3	1044	1041	1043	1044	1050-1035
Heparin	C-N str	1004	1005	1004	1005	-
Phe	Ring breath	-	-	1004	1005	993-1015
His	CN str, ring def	-	-	956	954	965-948
Heparin	C-O-C str	893	891	-	-	-
Pro	Ring str	-	-	882	884	919-890
Tyr	Ring breath	-	-	828	829	886-813
Heparin	C-O-C str	818	817	815	-	-
Cys	C-S str	-	-	791	796	817-740
Cys	C-S str	-	-	670	662	689-655
Cys	S-S str	-	-			550-500

Table 3.4. *Band assignments of 4-(2-hydroxyehtyl)-1-piperazineethanesulfonic acid (HEPES) buffer Raman and SERS spectra. Raman shifts are given in cm^{-1}.*

Band Assignment		Raman (this work)	Raman	SERS
HEPES	CH_2 sci	1449	1475 – 1450	1388
	SO_3 asym str	1335	1380	1359 – 1356
	CH_2 tw	1314	1310 – 1260	1295
	CN sym str	1212	1280 – 1180	1258 – 1256
	SO_3 sym str	1059	1046 – 1053	1022
	SO sym str	931	958	915

For the unambiguous detection of the presence of polyA within the Tau-polyA fibrils, the characteristic ring breathing mode of adenine is used (709 – 739 cm^{-1}). This mode is used as this spectral region is void of any vibrational modes associated with the protein itself.[21] In **Figure 3.10,** This mode appears relatively intense in both the unenhanced Raman and SERS spectra of pure polyA which can be expected given the higher Raman cross section of aromatic groups and the aforementioned SERS surface adsorption preference. For Tau-polyA fibrils, the adenine ring breathing mode is exclusively enhanced in SERS with only a small contribution in the Raman spectrum. This observation shows that the adenine group is accessible to the silver nanoparticle enhancement and suggests that the polyA cofactor is bound to the fibril surface. A contribution in the spectral region 1526 – 1561 cm^{-1} in the SERS spectrum of Tau-polyA and pure polyA is assigned to the NH-Ag^{+} mode.[43] The lack of this mode in the corresponding unenhanced Raman spectrum corroborates the previous conclusion of the adenine molecule being exposed to the SERS Ag nanoparticles. The ring breathing mode of adenine is understandably absent in the Tau-heparin spectra. The contribution of heparin can be seen in the 1032 – 1065 cm^{-1} region associated with the N-sulphate/6-O-sulphate/2-O-sulphate chemical groups.

Heparin can be distinguished in both Raman and SERS by a single marker band of the sulphate groups centred around the 1035 – 1065 cm^{-1} region (see **Figure 3.10**). Other notable Raman bands include the NH deformation of the -SO_2-NH- moiety at 1606 cm^{-1}. This band is significantly broader in the corresponding SERS spectrum ranging from 1500 – 1660 cm^{-1}. This broadening could be due to the interaction of the silver substrate with heparin, similar to the previous reasoning in the polyA spectra (see **Figure 3.10**). Full spectral assignment of heparin bands is given in **Table 3.3**.

The secondary structure of protein backbone is indicated in the amide I band region (C=O stretching, 1600 – 1700 cm^{-1}). This band is preferred for the assignment of secondary structures over the amide III band (1200 – 1340 cm^{-1}) as this latter region contains many contributions from other amino acids, in addition to being sensitive to the dihedral (J) peptide bond angle. As seen in **Figure 3.11**, the unenhanced Raman amide I bands of both Tau-polyA and Tau-heparin have maxima at 1667 cm^{-1}, which correlates well with the β-sheet structure of literature Tau P301L in HEPES buffer of 1671 cm^{-1}.[44] The corresponding SERS spectra reveal non-regular/random coil amide I maxima situated at 1634 and 1636 cm^{-1} for Tau-polyA and Tau-heparin fibrils, respectively. This observation shows that the highest intensity amide I band is not centred at the same position for both Raman and SERS spectra. It is thus believed that the disordered "fuzzy coat" is probed to a greater extent than the core β-sheet structure in SERS.

This is due to these structures being closer in proximity to the SERS-active silver nanoparticles, considering the decrease in SERS enhancement with increasing substrate-sample distance. It is noted that this specific enhancement does not occur for the disordered secondary structures in the given unenhanced Raman spectra.

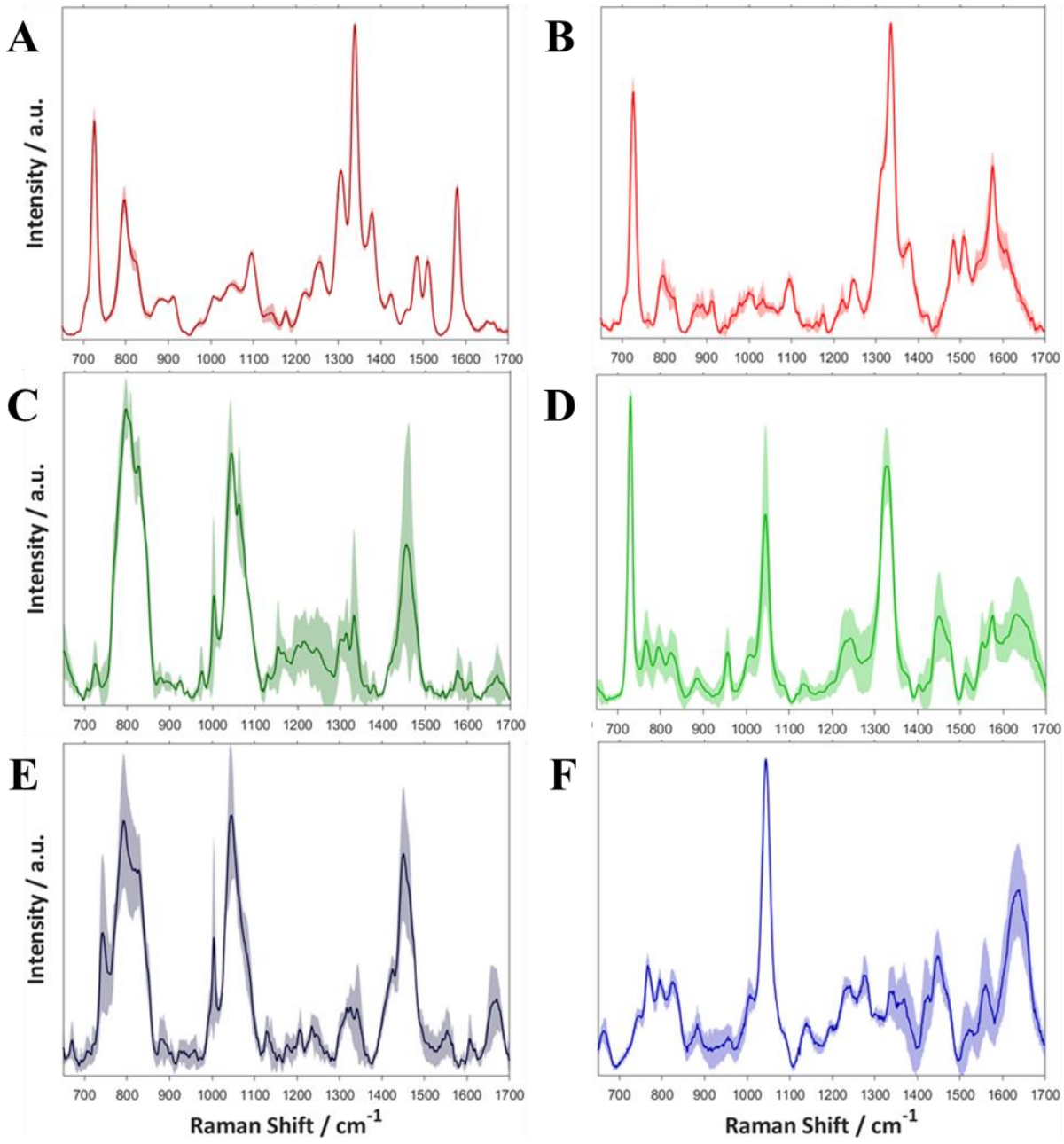

Figure 3.11. *Raman* ***[A, C, E]*** *and SERS* ***[B, D, F]*** *of pure polyA* ***[A and B]****, Tau-polyA fibrils* ***[C and D]****, and Tau-heparin fibrils* ***[E and F]****. The solid lines indicate mean spectra (arithmetic average of 3 – 7-point spectra) with shaded areas indicating standard deviations from the mean. Prior to normalisation, the maximum intensity of Raman spectra ranged from 3 – 22 counts.s^{-1} while the maxima for SERS spectra was between 4 – 75 counts.s^{-1}. Incident laser: 561 nm.*

3.3.4. TERS maps of fibrils

3.3.4.1. TERS maps of integrated regions

In SERS, the resulting spectrum measured is that of many Tau fibrils averaged over the 8.5 µm-diameter sample area. By contrast, TERS enables information to be collected at the single fibril level with nanoscale spatial resolution. This results in the accurate correlation between protein primary/secondary structure and the absence/presence of polyA cofactor. Specifically, the amide I band secondary structures (β-sheet, 1660 – 1682 cm^{-1}; random coils, 1630 – 1655 cm^{-1}) and the ring breathing mode of adenine (709 – 739 cm^{-1}) were investigated in acquired TERS maps. Distinct portions of individual Tau-polyA fibrils were explored, resulting in 10 TERS maps. All raw spectra were first treated by manual removal of spikes caused by cosmic ray emissions. Baseline subtraction of 5^{th} order polynomial was used on collected Raman and SERS spectra before applying a 7-point 2^{nd} order polynomial Savitzky-Golay smoothing. TERS spectra were pre-treated by first subtracting the background contribution of the TERS tip by using the average spectrum over a large region void of sample signal before baseline subtraction and a slight smoothing as previously described for Raman and SERS data. A threshold of peak intensity of at least 3 times higher than the standard deviation of the noise was used to qualify TERS signals. Intensity integration of specific spectral regions was used to generate TERS maps. Binary TERS maps were generated by setting intensities above the threshold of 3 times the standard deviation of the noise to 1, while intensities below this calculated value were set to 0. All spectra were pre-processed using LabSpec 6 (HORIBA, Scientific), and processed using custom MATLAB scripts (R2022a, MathWorks Inc.), and PLS-toolbox (Eigenvector Research Inc.).

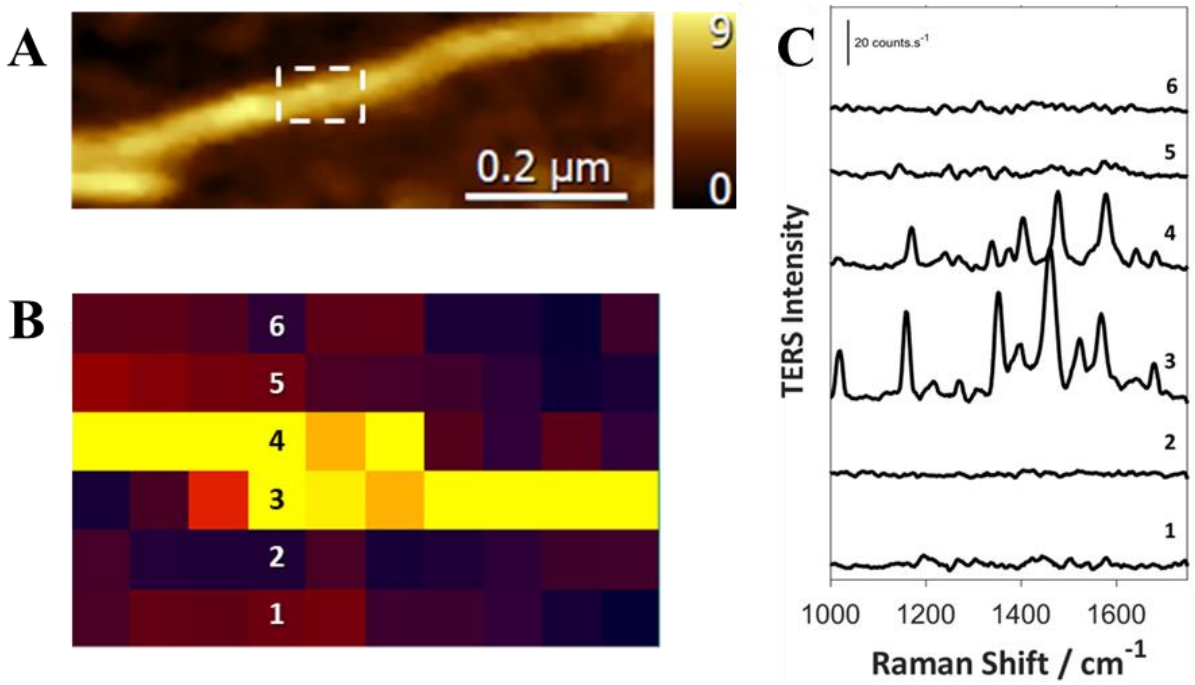

Figure 3.12. [A] *AFM height image of Tau-polyA fibril where dashed box shows the probed region in B.* ***[B]*** *The average TERS spectrum intensity is presented as a heat map.* ***[C]*** *TERS spectra of cross-section of 6 points from TERS map presented in B (integration time 5 s, scanning step size 10 nm, scale bar 20 counts.s^{-1}). Laser influence: 561 nm.*

10 TERS maps with a scanning step size of 5 – 10 nm were obtained from distinct fibril portions of several individual Tau-polyA fibrils. **Figure 3.12** showcases the determination of the lateral SOR for these TERS experiments. From the integration of TERS intensities in the 1000 – 1700 cm^{-1} spectral range, a TERS map of a Tau-polyA fibril portion can be obtained. A cross-section of this fibril suggests a lateral SOR below 20 nm, which is consistent with the 5 – 10 nm resolution of the previous study on Tau-heparin fibrils under the same experimental conditions (**Chapter 3.2.4**). These results are very comparable as the same TIR-TERS system is used, TERS tips were prepared similarly, and the sample substrate were identical. It can be reasoned that a 5 – 10 nm lateral SOR can also be reached for the Tau-polyA study. Differences in the silver tip apex can explain the observed variation in SOR which apparently varies from 10 nm (**Figure 3.12**, **Figure 3.13A** and **B**) to 20 nm (**Figure 3.13E**, **F** and **G**). Note also that the diameter of Tau-polyA fibrils falls in the 8 – 13 nm range, which is greater than that of Tau-heparin fibrils observed to be 5 – 10 nm.

In **Figure 3.13**, for the 10 TERS maps, the ring breathing mode of adenine (709 – 739 cm^{-1}) is presented in blue, amide I bands assigned to core β-sheets (1660 – 1682 cm^{-1}) are presented in green, and random coils (1630 – 1655 cm^{-1}) are presented in red. For the most part, the intensity of TERS bands is sufficient to visualise the outline of the fibril in all three

integrated regions (**Figure 3.13A**, **B**, **C**, **E**, **F**, **G** and **H**). However, the absence of either amide I bands or adenine due to low or even sporadic enhancement results in less clear outlines of fibrils (**D**, **I** and **J**). This is likely due to the tip-to-tip variability between the 5 Ag-coated TERS tips used for measurements. Generally, it is observed that adenine is present in regions of β-sheets (green) which tend to run along the direction of the length of the fibril (eg. **A**, **B**, **C**, **F** and **G**). Random coils (red) can be seen throughout the fibril, likely arising from the "fuzzy coat" which envelops the fibril core. Some maps show a greater intensity of random coils along the fibril length similar to β-sheets (**A**, **B** and **E**), but this could arise from probing a thicker fibril region and hence, probing a greater portion of the "fuzzy coat". An insight to note is that portions of certain probed fibrils contain low amide I intensities (e.g. **B** and **G**). This lack of signal could arise from the absence of these structures, or the insufficient probing of this region, likely due to the helical twist expected within the fibrils. This twist could result in a suboptimal orientation with respect to the probe tip axis, leading to a decreased observed enhancement. The twist of Tau-polyA fibrils was demonstrated to be typically 114 nm in its periodicity (**Figure 3.9**), which doesn't sufficiently explain the above observations, as these gaps appear to be in the 30 – 60 nm range given the 10 nm step size of the TERS maps.

The TERS intensity of these spectral regions can vary significantly along the fibril. Such variations arise from fibril composition and local molecular orientation which is efficiently probed in TERS. The specificity of TERS is indeed a major advantage of the technique. However, for complex biological species, lower intensity vibrational modes and contributions can be masked by more intense TERS bands. As the goal of the study was to investigate the colocalization of the cofactor polyA within the Tau fibril secondary structure, binarization of the spectral data was implemented. This results in a more qualitative interpretation of the TERS maps, which allows for easier visualisation of fibril-cofactor colocalization.

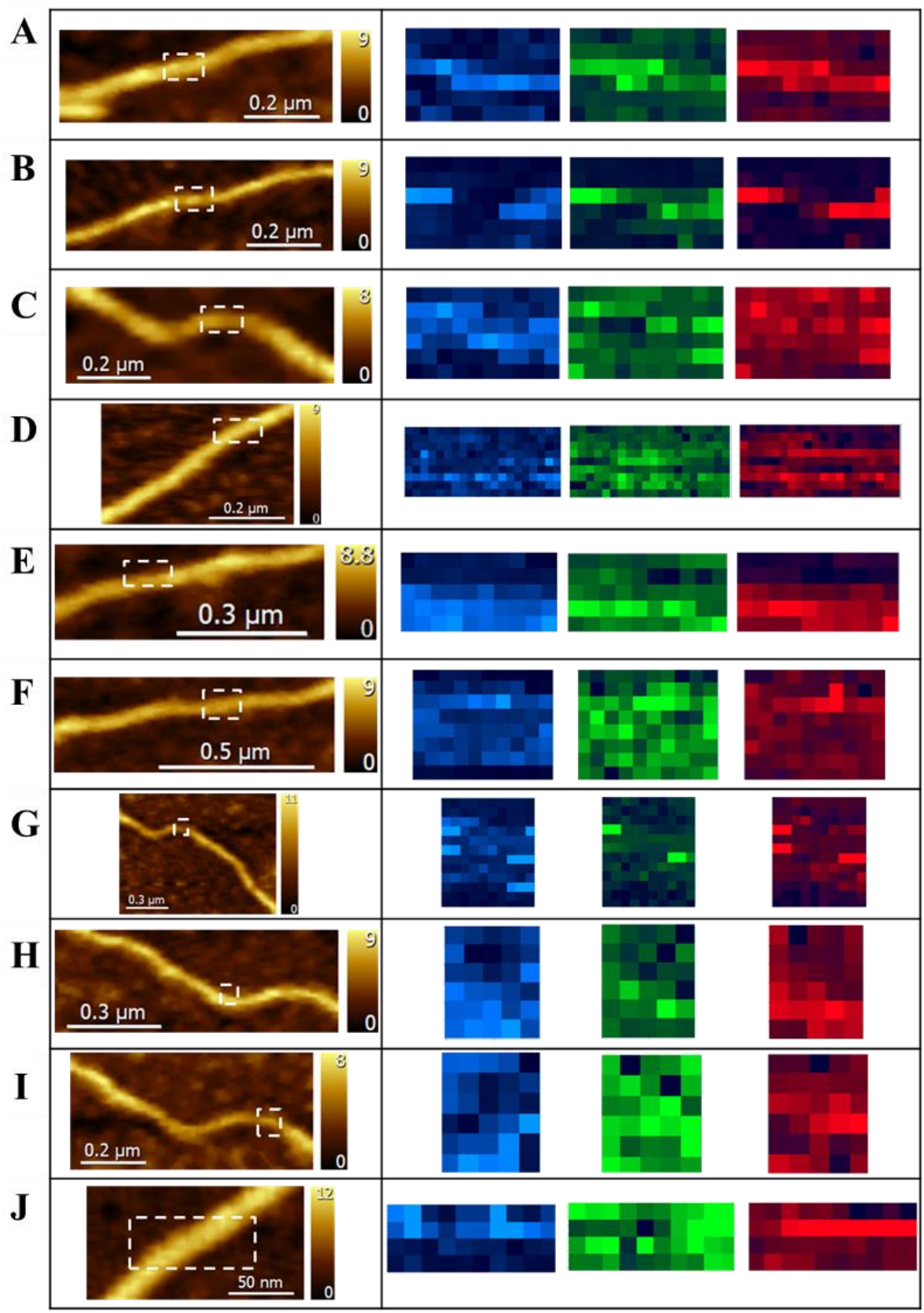

Figure 3.13. *AFM height images of 10 portions of Tau-polyA fibrils* ***[A-J]****. Dashed boxes indicate regions of TERS mapping given on the right. TERS intensity maps of adenine (709 – 739 cm^{-1}, blue), core β-sheets (1660 – 1682cm^{-1}, green), and random coils (1630 – 1655 cm^{-1}, red). Incident laser: 561 nm.*

3.3.4.2. Binary maps

In order to aid visualisation of the colocalization of Tau fibril secondary structure with polyA, a binarization method was implemented on the TERS dataset (**Figure 3.14**). This binarization is based on setting a peak intensity threshold, in which a peak is defined as three times the standard deviation of the background noise.[6] The benefit of this binarization method over intensity integration is that the band intensity dependence based on favourable molecular orientations or number of probed molecular groups is removed. While information is removed from the dataset, the important qualitative information of band cooccurrence remains and is better visualised and interpreted.

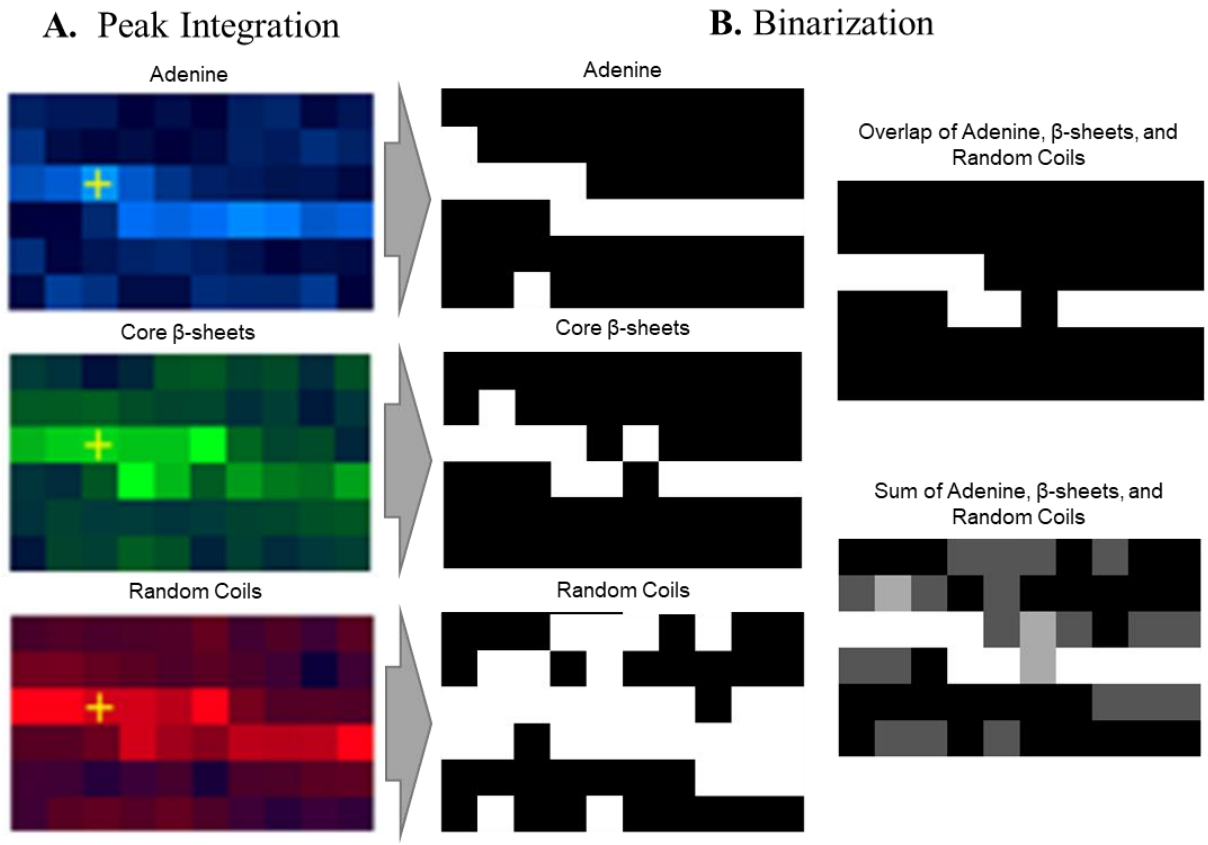

Figure 3.14. *Principle of the binarization procedure.* ***[A]*** *TERS maps of Tau-polyA fibril using peak integration of corresponding bands of adenine, core β-sheets, and random coils.* ***[B]*** *TERS maps of Tau-polyA fibril using binarization of data for adenine, core β-sheets, and random coils. The dot-product of the three binary maps is visualised as the binary overlap image, and the sum of the three maps is visualised in the grayscale sum image, where white = 3, light grey = 2, and dark grey = 1.*

To begin, the adenine ring breathing mode (709 – 739 cm^{-1}) and amide I bands of core β-sheets (1660 – 1682 cm^{-1}) and of random coils (1630 – 1655 cm^{-1}) were selected for study. The resulting binary images of the 10 TERS maps can be found in **Figure 3.15**. The binary images were also combined in an additive manner resulting in areas of overlap between adenine and β-sheets, as well as adenine and random coils. From these images, it is evident that PolyA runs along the length of the fibril and is colocalised with the core β-sheet of fibrils. Random coils are found throughout the images, colocalising with both adenine and core β-sheets. The presence of random coils in neighbouring pixels showcases the "fuzzy coat" extending from the core fibril structure.

In particular, the images corresponding to **Figure 3.15A**, **B**, **C**, **D**, **E**, **F**, **G**, and **J**, show good colocalization of adenine with core β-sheets and random coil structures. The TERS signal of random coils is more prominent in these maps compared to core β-sheets, which is reasonable considering TERS is more sensitive to molecular groups at the fibril surface i.e. the disordered "fuzzy coat". This also explains why random coils are detected whenever core β-sheets are, as seen in several pixels of **Figure 3.15A**, **B**, **C**, **D**, **E**, **F**, and **G**. There are also instances where core β-sheets are identified without contribution from random coils. Such occurrences can be explained by the TERS tip probing a region of the fibril that is locally devoid of random coiled secondary structures. This possibility is likely in a twisted region of the fibril, but in any case, is not a frequent occurrence and will not be discussed in detail further.

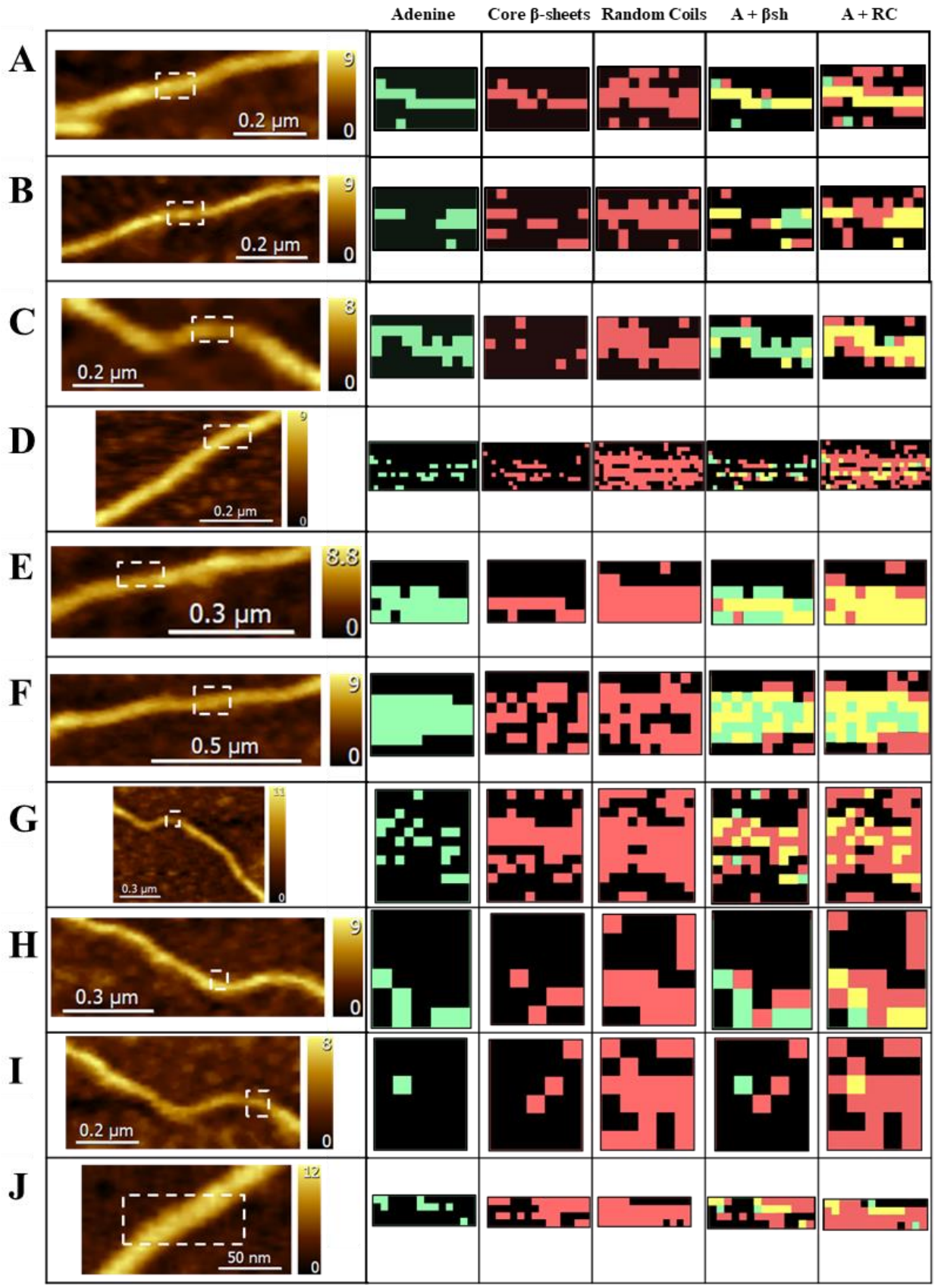

Figure 3.15. *Binary maps of TERS data reflecting presence of adenine (green, 709 – 739 cm^{-1}), core β-sheets (red, 1660 – 1682 cm^{-1}), and random coils (red, 1630 – 1655 cm^{-1}), colocalization of adenine and core β-sheets (yellow, "A+βsh") and adenine with random coils (yellow, "A+RC"). Incident laser: 561 nm.*

Given the proposed binding of anionic cofactors to Tau via positively charged amino acids, binary maps of arginine (Arg: 1088 – 1094, 1156 – 1171 cm^{-1}), lysine (Lys: 1070 – 1080, 1136 – 1155 cm^{-1}), and histidine (His: 1171 – 1194, 1327 – 1337, 1482 – 1517 cm^{-1}) were generated for TERS maps. The band overlap of proteins and the complexity of TERS spectra made it necessary to analyse the selected amino acids using a multiband assignment.

For example, histidine can be acceptably identified using a combination of three bands centred at 1180, 1330, and 1495 cm^{-1}.[25] **Figure 3.16** shows the multiband binary maps of the aforementioned amino acids running along the fibrillar axis. It is to be noted that while many amino acids can be observed, they are not discerned in equal proportions in the TERS maps for various reasons. In the case of histidine, it is one of the most frequently detected amino acids as it is most abundant in the disordered fuzzy coat of Tau fibrils. Even though quantitative analysis is not possible, there are nevertheless 12 histidine moieties in the native Tau protein, with 7 being localised in the fuzzy coat (3 in the C-terminus and 4 in the N-terminus), and the remaining 5 being localised in the R1-R4 binding domains.

Additionally, histidine's aromaticity leads to a relatively high Raman cross section compared to other non-aromatic amino acids. In **Figure 3.16** it is shown that histidine is colocalised with adenine, specifically in regions where both β-sheets and random coils dominate. The sensitivity of TERS can be seen here where both core and fuzzy coat histidine residues are simultaneously detected.

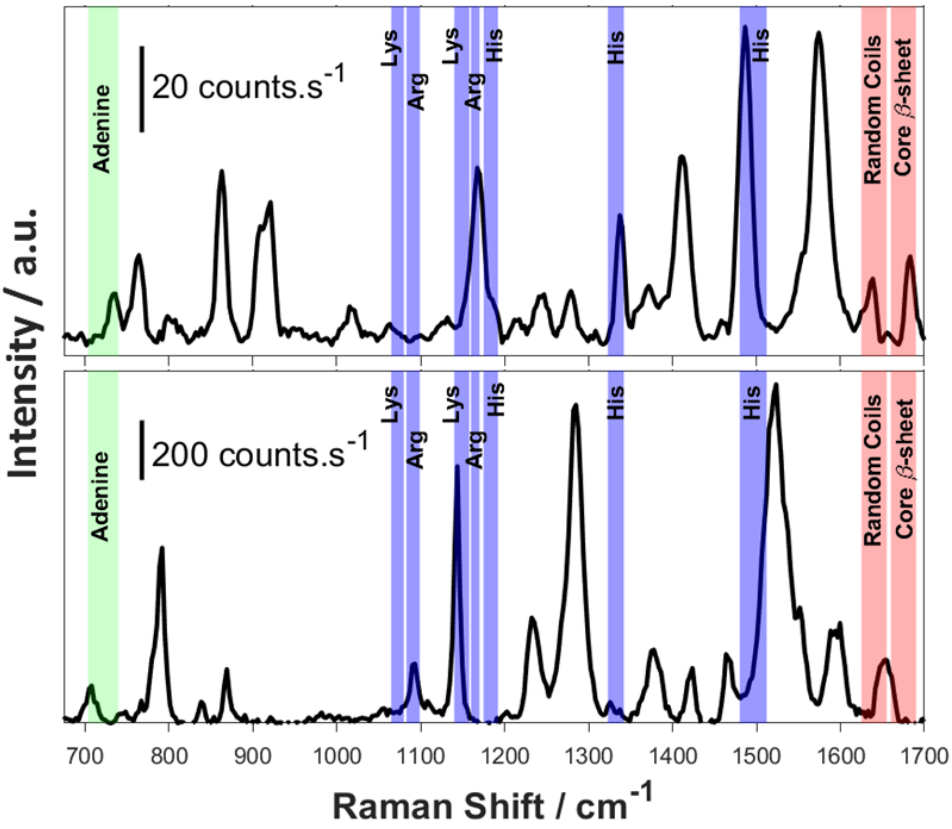

Figure 3.16. *TERS point spectra taken from fibril A and B respectively (see Figure 3.15). His can be identified with relatively low enhancement (top, >20 counts.s^{-1}), while Lys and Arg are more common with high enhancement (bottom, >200 counts.s^{-1}). Adenine (709 – 739 cm^{-1}), core β-sheets (1660 – 1682 cm^{-1}), and random coils (1630 – 1655 cm^{-1}), are noted in green, red, and red respectively. Incident laser: 561 nm.*

Other amino acids studied include Lys and Arg, which are not aromatic and hence are more difficult to observe using Raman spectroscopy. These amino acids also require two bands for their definite assignment, further reducing their observation. The terminal ammonium and guanidinium groups are used for the two-band assignment of these residues respectively. Lys is the most abundant amino acid in Tau that is discernible by TERS, with 44 moieties being distributed throughout the protein sequence. In comparison, Arg has only 14 moieties with most of them being located in the so-called proline rich domains P1 and P2 and in the N-terminal region. There is only 1 Arg residue in the C-terminal domain and 1 in the R4 domain. In **Figure 3.16**, regions that are rich in both β-sheet and random coils also contain Lys and Arg in abundance. It can also be said, that adenine is often found in regions primarily where all 3 amino acids are identified, and in regions with 2 out-of-the 3 amino acids along the fibril core but to a lesser extent. These observations support the hypothesis that positively charged residues in Tau are associated with anionic cofactor binding.

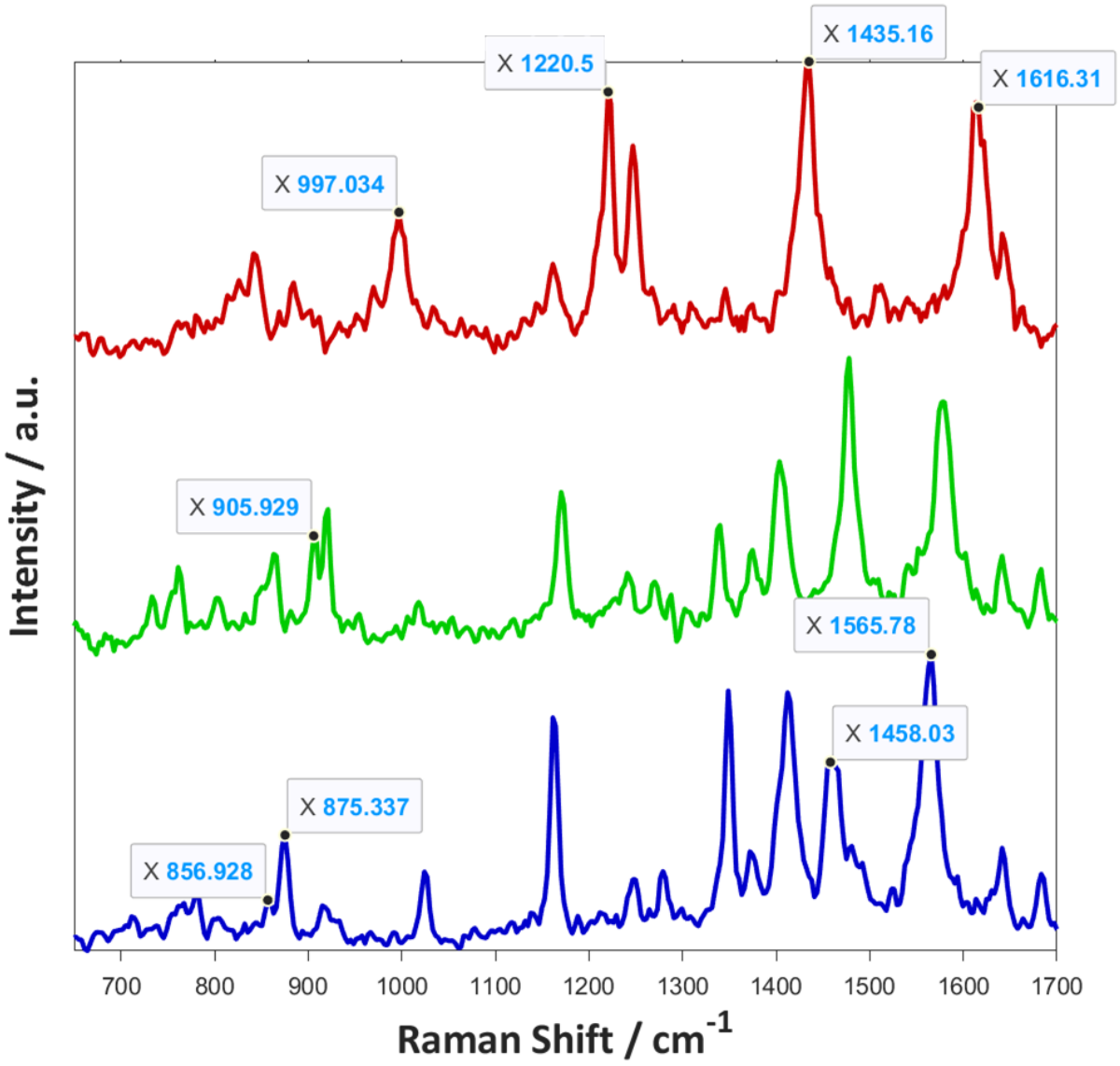

Figure 3.17. *Selected TERS spectra of Tau-polyA fibrils that clearly show the amino acids Phe (red), Pro (green), and Tyr (blue). Phe is identified by the modes C=C str (1616 cm^{-1}), CH_2 sci (1435 cm^{-1}), CC ring (1221 cm^{-1}), and ring breath (997 cm^{-1}). Pro is identified by the ring str mode (906 cm^{-1}). Tyr is identified by the modes C=C str (1566 cm^{-1}), CH_2 sci (1458 cm^{-1}) and, ring breath Fermi doublet (875 and 857 cm^{-1}). Incident laser: 561 nm.*

Tryptophan (Trp), tyrosine (Tyr), and phenylalanine (Phe) are all aromatic, but they are either absent or only present in low quantities in Tau (0 Trp, 2 Phe, 4 Tyr). These residues are also of limited interest in the study of fibril-cofactor binding. Cysteine (Cys) suffers from being present in low proportion and being localised in the core structure (2 Cys). All the while, the cofactor polyA contributes in regions where marker bands of amino acids are also expected (see **Table 3.2**). Admittingly, the efficiency of our TERS tips is the greatest contributor to the non-systematic appearance of Phe, Pro, Tyr, Cys, Lys, and Arg amino acids in the TERS spectra.

This is demonstrated in **Figure 3.16** where Phe, Pro, and Tyr can be identified, and **Figure 3.16** for Lys and Arg, which are mainly detected when TERS intensities are high.

Figure 3.18 shows two fibril portions with His in abundance and colocalised with the adenine-rich fibril regions. Arg and Lys are not very evident in the first image, but are possible to discern in the second. This is especially true for Arg which is colocalised with His, random coils, and β-sheet secondary structures. For the eight other Tau-polyA fibrils, unfortunately, Arg and Lys are not detected.

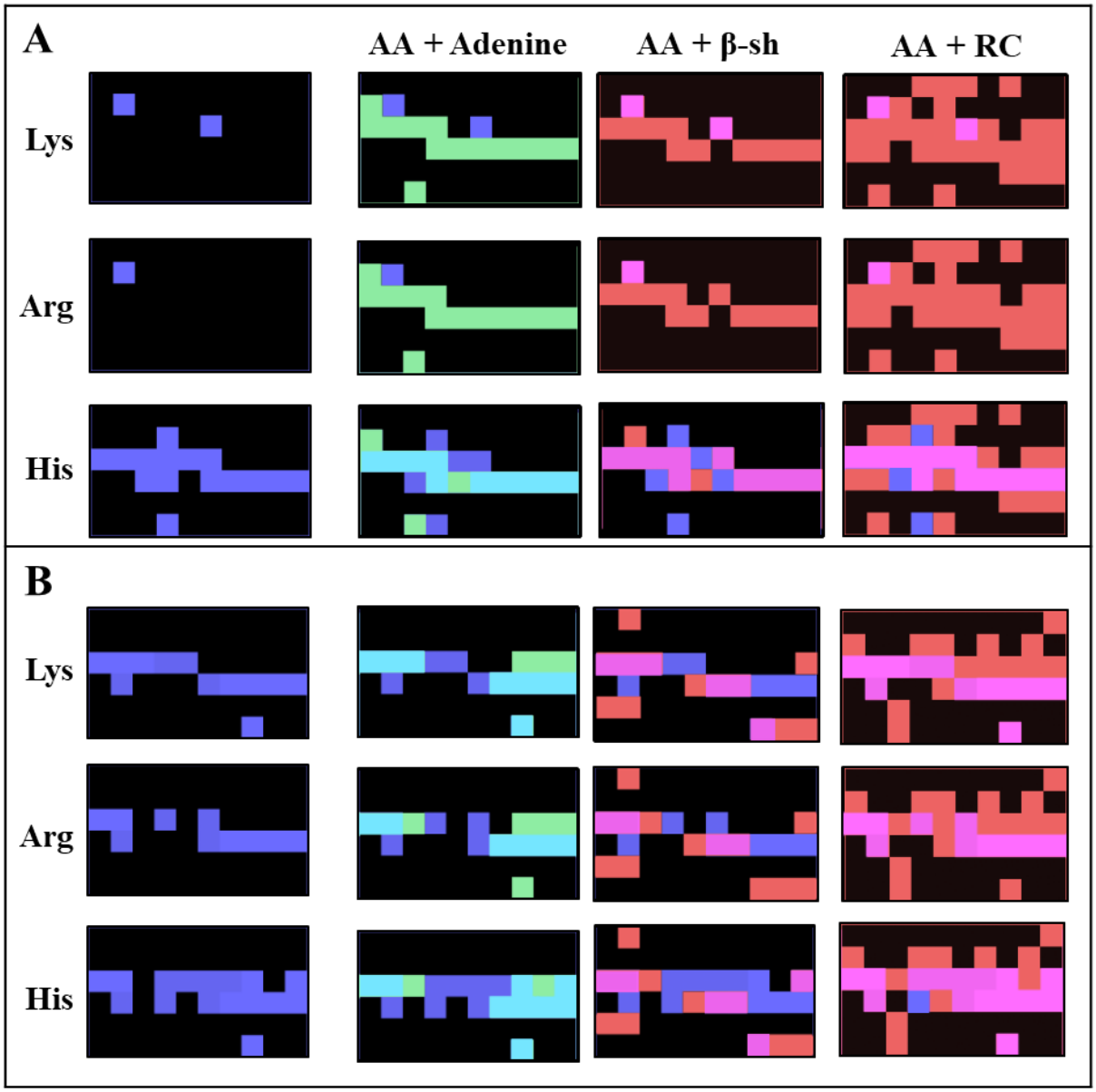

Figure 3.18. *Binary maps of two distinct fibrils reflecting the presence of lysine, arginine, and histidine (blue). Combination of these amino acids with adenine (green) and either β-sheets or random coiled secondary structures (red). The overlays of adenine with amino acids and secondary structures are represented in cyan and magenta, respectively. Incident laser: 561 nm.*

3.3.5. Statistics of TERS spectra

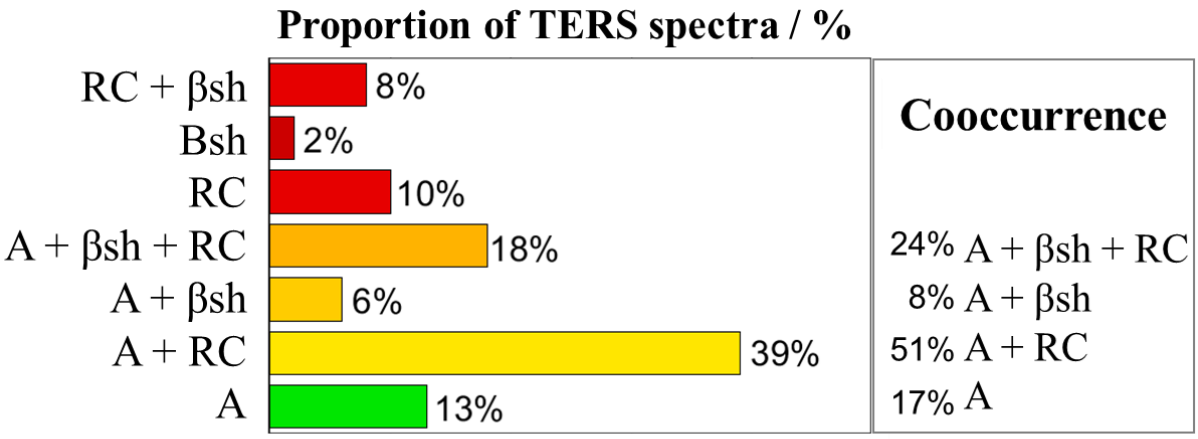

Figure 3.19. *300 TERS spectra across 10 TERS maps visualised as proportions that exhibit spectral fingerprints of the ring breathing mode of adenine (A) and amide I bands of core β-sheets (βsh) and random coils (RC). The proportional occurrence of adenine with Tau secondary structures in summarised on the right.*

To try and better describe the general observations of adenine and amide I cooccurrence in Tau-polyA fibrils, a dataset of 300 TERS spectra was extracted from the 10 TERS maps and the proportional occurrence of adenine (A), β-sheets (βsh), and random coils (RC) was visualised (see **Figure 3.19**). The use of 6 different silver-coated TERS probes to acquire this dataset is sufficiently large to reliably determine the secondary structure of single Tau-polyA fibrils with good statistical relevance. The intensity threshold used for data binarization (see **Chapter 3.3.4.2**) was implemented when discerning the presence or absence of the aforementioned moieties. Despite having interpretable TERS intensity, 4 % of all spectra (12 spectra) contained no discernible contribution from adenine, β-sheets, nor random coils. It is theorised that this observation could be in part due to amide I band suppression which has already been reported with TERS of proteins using silver-coated probes. This phenomenon would additionally explain the proportional occurrence of adenine without either random coils or β-sheets (13 %). Depending on the direct contact of the amide group and the TERS probe, the amide I bands often appear weak in intensity, or can be absent altogether. This is provided that no peptide backbone cleavage also occurs due to this interaction.[20,33,34] It is noteworthy that the ultracentrifugation step in the fibril preparation, in addition to the washing steps implemented after fibril deposition ensures that free unbound polyA is not present in the measured samples.

In contrast to the 4 % of spectra that do not contain neither amide I nor adenine bands, it was found that 20 % of spectra lacked a contribution from adenine. There are several possible origins to this lack of adenine signal seen within fibril regions that contain random coils (10 %), β-sheets (2 %), or both random coils and β-sheets (8 %). First, the lack of adenine signal could arise from the absence of polyA within the given fibril portion. Second, the pyrimidine ring of adenine could have a sub-optimal molecular orientation with respect to the TERS tip axis resulting in a weak enhancement. Third, the polyA molecule could be buried in the fibrillar core at a depth inaccessible to be probed by the TERS tip. This latter prospect is certainly possible given the restricted TERS probe depth of a few nm, in conjunction with the typical diameter of 8 – 13 nm for the studied Tau-polyA fibrils (**Figure 3.9**).

The typical composition of Tau-RNA fibrils as seen in bulk Raman consists of 70 % random coils, and 30 % β-sheets. Here, it is observed that TERS spectra contain 75 % random coils and 34 % β-sheets. The discrepancy in this otherwise good agreement is likely due to the influence of cofactor incorporation on fibril structure (here polyA). It is found that polyA is colocalised with β-sheets 32 % of the time, while being colocalised with random coils 75 % of the time. This would initially suggest that polyA is mostly present in the "fuzzy coat". However, polyA is observed either alone with random coils (39 %), or also accompanied by core β-sheet structures (18 %). These observations indicate that polyA is not buried deep within the cross β-sheet network of the fibril, but rather is associated superficially to the core structure. The "fuzzy coat" is inherently disordered and its fluid nature results in shielding of the fibril core to the TERS probe. Therefore, only regions of certain coat thickness enable probing of the β-sheet structures with the TERS tip. The helical nature of Tau fibrils (**Figure 3.9**) additionally contributes to the effective probing of the fibril core, where polyA is observed in flat regions. This topographical profile explains the high concurrence of polyA with random coils, and it is reasoned that all three structures (A + βsh + RC) are simultaneously detected only at points of relative thinness of the "fuzzy coat". It has already been shown that RNA cofactors are accessible to digestive enzymes such as RNAse, which leads to spontaneous depolymerisation and the release of protein monomers.[11] This fact supports our findings that polyA is bound superficially to the fibril core.

3.3.6. Comparison to Tau-fibrils formed *ex-vivo*

Tau fibrils formed in vivo are believed to be stabilised by a wide variety of cofactors and post-translational modifications, and have been shown to be different from recombinant Tau-heparin and Tau-RNA fibrils.[8,9,11] In addition, different anionic cofactor may stabilise different fibril polymorphs through distinct binding sites. Until recently, it was believed that the negatively charged phosphate backbone of RNA promoted Tau aggregation in a similar fashion to heparin, through the interaction with the positively charged β-sheet core formed in the MBD. However, recent cryo-EM structures have cast doubt on this proposal by suggesting a 36-residue core that is localised in the C-terminal (**Figure 3.1D**).[8] This region has previously been thought to be part of the disordered "fuzzy coat", and this finding suggests the existence of unique cofactor binding sites for different polymorphs of Tau. In this proposed C-terminal core, RNA runs parallel to the fibril axis and is bound via H-bonding of the nucleobases to amino acids such as Arg, Asp, and His.

In our study of Tau-polyA fibrils, it is not possible to discern individual amino acid molecules using TERS. Nevertheless, the demonstrated presence of His, Arg, and adenine in core β-sheet regions supports the hypothesis of a C-terminal core. The parallel in-register alignment of polyA and Tau is also supported by our observations of weak or strong adenine signal along the fibril axis caused by the helical twist of Tau-polyA fibrils, with the TERS signal being dependent on the tip distance to the bound polyA.

Conclusion

In summary, Tau-heparin and Tau-polyA fibrils were structurally and chemically investigated with Raman, SERS, and TERS. Specifically, TIR-TERS was shown to be a promising advancement in instrumentation for the study of biomolecules. The TIR geometry features a large irradiated sample area with a low laser density leading to weak far field signals when performing TERS measurements. The low laser fluence allows for the investigation of light-sensitive biological molecules and limits sample damage. Compared to side- and top-illumination geometries, TIR-TERS facilitates tip-laser alignment and has been shown to have an increased TERS enhancement with respect to linearly and radially polarised bottom-illumination excitation. Tau-heparin amyloid fibrils were used to demonstrate the TIR-TERS system's performance on biological molecules, achieving a 1 – 4 nm axial and 5 – 10 nm lateral SOR. Nanoscale characterisation of fibril portions using TERS identified aromatic and non-

aromatic amino acid residues, disulphide bonds, and amide I bands of random coils and core β-sheet secondary structures.

Tau-polyA fibrils were investigated as prototypical RNA-induced amyloid fibrils to study cofactor incorporation within the mature fibril. Using the ring-breathing mode of adenine as a spectral marker, both β-sheet and random coil secondary structures were found to be colocalised with the anionic cofactor. It was concluded that the anionic cofactor is localised superficial to the β-sheet core but nevertheless enveloped within the protein fuzzy coat. This observation is supported by the literature of cofactor release using RNAse, and consequently, gives credit to the hypothesis that RNA acts as a templating molecule for amyloid fibrilization. Specific amino acid and cofactor interactions implicated in C-terminal core binding were identified by TERS chemical imaging. Adenine was found to be colocalised with positively charged arginine and histidine moieties specifically. When compared to Tau-heparin fibrils, TERS mapping has confirmed the superficial binding of polyA to a unique β-sheet fibril core to that of observed with other negatively charged cofactors.

References

1. Bonhommeau, S., Talaga, D., Hunel, J., Cullin, C., Lecomte, S., Tip-Enhanced Raman Spectroscopy to Distinguish Toxic Oligomers from Aβ 1 – 42 Fibrils at the Nanometer Scale. Angew. Chem. Int. Ed., 129, 1797–1800 (2017).
2. Berthelot, K., Cullin, C., Lecomte, S., What does make an amyloid toxic: Morphology, structure or interaction with membrane?, Biochimie, 95, 12–19 (2013).
3. Henry, S., Vignaud, H., Bobo, C., Decossas, M., Lambert, O., Harte, E., Alves, I., Cullin, C., Lecomte, S., Interaction of Aβ1-42 Amyloids with Lipids Promotes 'Off-Pathway' Oligomerization and Membrane Damage, Biomacromolecules, 16, 944–950 (2015).
4. Zikic, B., Bremner, A., Talaga, D., Lecomte, S. Bonhommeau, S., Tip-enhanced Raman spectroscopy of Aβ (1-42) fibrils, Chem. Phys. Lett. 768, (2021).
5. Fitzpatrick, A. W. P., Falcon, B., He, S., Murzin, A. G., Murshudov, G., Garringer, H. J., Crowther, R. A., Ghetti, B., Goedert, M., Scheres, S. H. W., Cryo-EM structures of tau filaments from Alzheimer's disease, Nature, 547, 185–190 (2017).
6. Talaga, D., Cooney, G. S., Ury-Thiery, V., Fichou, Y., Huang, Y., Lecomte, S., Bonhommeau, S., Total Internal Reflection Tip-Enhanced Raman Spectroscopy of Tau Fibrils, J. Phys. Chem. B, 126, 5024–5032 (2022).
7. Abskharon, R., Sawaya, M. R., Boyer, D. R., Cao, Q. Nguyen, B. A., Cascio, D., Eisenberg, D. S., Han, S., Hong, M., Cryo-EM structure of RNA-induced tau fibrils reveals a small C-terminal core that may nucleate fibril formation, PNAS, 119, (2022).
8. Zhang, W., Falcon, B., Murzin, A. G., Fan, J., Anthony Crowther, R., Goedert, M., Scheres, S. H. W., Heparin-induced tau filaments are polymorphic and differ from those in Alzheimer's and Pick's diseases. eLife, (2019)
9. Ginsberg, S. D., Crino, P. B., Lee, V. M. Y., Eberwine, J. H. Trojanowski, J. Q., Sequestration of RNA in Alzheimer's disease neurofibrillary tangles and senile plaques, Ann. Neurol., 41, 200–209 (1997).
10. Fichou, Y., Lin, Y., Rauch, J. N., Vigers, M., Zeng, Z., Srivastava, M., Keller, T. J., Freed, J. H., Kosik, K. S., Han, S., Cofactors are essential constituents of stable and seeding-active tau fibrils, Proc. Natl. Acad. Sci. USA, 115, 13234–13239 (2018).
11. Zwierzchowski-Zarate, A. N., Mendoza-Oliva, A., Kashmer, O. M., Collazo-Lopez, J. E., White, C. L., Diamond, M. I., RNA induces unique tau strains and stabilizes Alzheimer's disease seeds, J. Biol. Chem., 298, (2022).

12. Fichou, Y., Oberholtzer, Z. R., Ngo, H., Cheng, C. Y., Keller, T. J., Eschmann, N. A., Han, S., Tau-Cofactor Complexes as Building Blocks of Tau Fibrils, Front. Neurosci., 13, (2019).
13. Yeo, B.-S., Stadler, J., Schmid, T., Zenobi, R., Zhang, W., Tip-enhanced Raman Spectroscopy – Its status, challenges and future directions, Chem. Phys. Lett., 472, 1–13 (2009).
14. Levine, H., Thioflavin T interaction with synthetic Alzheimer's disease β-amyloid peptides: Detection of amyloid aggregation in solution, Protein Science, 2, 404–410 (1993).
15. Bartolomeo, G. L., Zhang, Y., Kumar, N., Zenobi, R., Molecular Perturbation Effects in AFM-Based Tip-Enhanced Raman Spectroscopy: Contact versus Tapping Mode, Anal. Chem., 93, 15358–15364 (2021).
16. Talaga, D., Bremner, A., Buffeteau, T., Vallée, R. A. L., Lecomte, S., Bonhommeau, S., Total Internal Reflection Tip-Enhanced Raman Spectroscopy of Cytochrome c, J. Phys. Chem. Lett., 11, 3835–3840 (2020).
17. Bonhommeau, S., Talaga, D., Hunel, J., Cullin, C., Lecomte, S., Tip-Enhanced Raman Spectroscopy to Distinguish Toxic Oligomers from Aβ 1 - 42 Fibrils at the Nanometer Scale, Angew. Chemie Int. Ed., 129, 1797–1800 (2017).
18. Talaga, D., Smeralda, W., Lescos, L., Hunel, J., Lepejova-Caudy, N., Cullin, C., Bonhommeau, S., Lecomte, S., PIP 2 Phospholipid-Induced Aggregation of Tau Filaments Probed by Tip-Enhanced Raman Spectroscopy, Angew. Chem. Int. Ed., 130, 15964–15968 (2018).
19. Bonhommeau, S., Cooney, G. S., Huang, Y., Nanoscale chemical characterization of biomolecules using tip-enhanced Raman spectroscopy., Chem. Soc. Rev., 51 2416–2430 (2022).
20. Bonhommeau, S., Lecomte, S., Tip-Enhanced Raman Spectroscopy: A Tool for Nanoscale Chemical and Structural Characterization of Biomolecules, Chem. Phys. Chem., 19 8–18 (2018).
21. Kurouski, D., Deckert-Gaudig, T., Deckert, V., Lednev, I. K., Structure and composition of insulin fibril surfaces probed by TERS, J. Am. Chem. Soc., 134, 13323–13329 (2012).
22. Kurouski, D., Deckert-Gaudig, T., Deckert, V., Lednev, I. K., Surface characterization of insulin protofilaments and fibril polymorphs using tip-enhanced Raman spectroscopy (TERS), Biophys. J., 106, 263–271 (2014).

23. VandenAkker, C. C., Deckert-Gaudig, T., Schleeger, M., Velikov, K. P., Deckert, V., Bonn, M., Koenderink, G. H., Nanoscale Heterogeneity of the Molecular Structure of Individual hIAPP Amyloid Fibrils Revealed with Tip-Enhanced Raman Spectroscopy, Small, 11, 4131–4139 (2015).
24. Deckert-Gaudig, T., Kurouski, D., Hedegaard, M. A. B., Singh, P., Lednev, I. K., Deckert, V., Spatially resolved spectroscopic differentiation of hydrophilic and hydrophobic domains on individual insulin amyloid fibrils, Sci. Rep., 6, (2016).
25. Heilman, A. L., Gordon, M. J., Tip-enhanced near-field optical microscope with side-on and ATR-mode sample excitation for super-resolution Raman imaging of surfaces, J. Appl. Phys. 119, (2016).
26. Trautmann, S., Aizpurua, J., Götz, I., Undisz, A., Dellith, J., Schneidewind, H., Rettenmayr, M., Deckert, V., A classical description of subnanometer resolution by atomic features in metallic structures, Nanoscale, 9, 391–401 (2017).
27. Lipiec, E., Perez-Guaita, D., Kaderli, J., Wood, B. R., Zenobi, R., Direct Nanospectroscopic Verification of the Amyloid Aggregation Pathway. Angew. Chemie Int. Ed., 130, 8655–8660 (2018).
28. Furukawa, Y., Kaneko, K., Nukina, N., Tau protein assembles into isoform- and disulfide-dependent polymorphic fibrils with distinct structural properties, J. Biol. Chem., 286, 27236–27246 (2011).
29. Prifti, E., Tsakiri, E. N., Vourkou, E., Stamatakis, G., Samiotaki, M., Papanikolopoulou, K., The two cysteines of tau protein are functionally distinct and contribute differentially to its pathogenicity in vivo, J. Neuro., 41, 797–810 (2021).
30. Lipiec, E., Kaderli, J., Kobierski, J., Riek, R., Skirlinska-Nosek, K., Sofinska, K., Szymonski, M., Zenobi, R., Nanoscale Hyperspectral Imaging of Amyloid Secondary Structures in Liquid, Angew. Chem. Int. Ed., 60, 4545 –4550 (2021).
31. D'Andrea, C., Foti, A., Cottat, M., Banchelli, M., Capitini, C., Barreca, F., Canale, C., de Angelis, M., Relini, A., Maragò, O. M., Pini, R., Chiti, F., Gucciardi, P. G., Matteini, P., Nanoscale Discrimination between Toxic and Nontoxic Protein Misfolded Oligomers with Tip-Enhanced Raman Spectroscopy, Small, 14, (2018).
32. Szczerbiński, J., Metternich, J. B., Goubert, G., Zenobi, R., How Peptides Dissociate in Plasmonic Hot Spots, Small, 16, (2020).
33. Kurouski, D., Postiglione, T., Deckert-Gaudig, T., Deckert, V., Lednev, I. K., Amide I vibrational mode suppression in surface (SERS) and tip (TERS) enhanced Raman spectra of protein specimens, Analyst, 138, 1665–1673 (2013).

34. Li, Y., Yan, J., Zhang, X., Huang, K., Disulfide bonds in amyloidogenesis diseases related proteins. Proteins: Structure, Function and Bioinformatics, 81, 1862–1873 (2013).
35. Pavlova, A., Cheng, C. Y., Kinnebrew, M., Lew, J., Dahlquist, F. W., Han, S., Protein structural and surface water rearrangement constitute major events in the earliest aggregation stages of tau., Proc. Natl. Acad. Sci. USA, 113, 127–136 (2016).
36. Goedert, M., Jakes, R., Spillantini, M. G., Hasegawa, M., Smith, M. J., Crowther, R. A., Assembly of microtubule-associated protein tau into Alzheimer-like filaments induced by sulphated glycosaminoglycans, Proc. Natl. Acad. Sci. USA, 15, 15125–15129 (1996).
37. Hasegawa, M., Crowther, R. A., Jakes, R., Goedert, M., Alzheimer-like changes in microtubule-associated protein tau induced by sulfated glycosaminoglycans. Inhibition of microtubule binding stimulation of phosphorylation filament assembly depend on the degree of sulfation, J. Biol. Chem., 272, 33118–33124 (1997).
38. Garcia-Rico, E., Alvarez-Puebla, R. A., Guerrini, L., Direct surface-enhanced Raman scattering (SERS) spectroscopy of nucleic acids: From fundamental studies to real-life applications, Chem. Soc. Rev., 47 4909–4923 (2018).
39. Safar, W., Tatar, A. S., Leray, A., Potara, M., Liu, Q., Edely, M., Djaker, N., Spadavecchia, J., Fu, W., Derouich, S. G., Felidj, N., Astilean, S., Finot, E., Lamy De La Chapelle, M., New insight into the aptamer conformation and aptamer/protein interaction by surface-enhanced Raman scattering and multivariate statistical analysis, Nanoscale, 13, 12443–12453 (2021).
40. Schlücker, S. Surface-enhanced Raman spectroscopy: Concepts and chemical applications, Angew. Chem. Int. Ed., 53, 4756–4795 (2014).
41. Morton, S. M., Silverstein, D. W., Jensen, L., Theoretical studies of plasmonics using electronic structure methods, Chem. Rev., 111, 3962–3994 (2011).
42. Huang, R., Yang, H. T., Cui, L., Wu, D. Y., Ren, B., Tian, Z. Q., Structural and charge sensitivity of surface-enhanced Raman spectroscopy of adenine on silver surface: A quantum chemical study, J. Phys. Chem. C, 117, 23730–23737 (2013).
43. Devitt, G., Crisford, A., Rice, W., Weismiller, H. A., Fan, Z., Commins, C., Hyman, B. T., Margittai, M., Mahajan, S., Mudher, A., Conformational fingerprinting of tau variants and strains by Raman spectroscopy, RSC Adv., 11, 8899–8915 (2021).

Chapter 4

Chemometric investigation of TERS data of Tau fibrils

Introduction

Chemometrics is the use of mathematical or statistical methods in chemistry to optimise experimental procedures and conditions, and to analyse chemical data in the attempt to extract maximal chemical information. This encompasses a wide range of mathematical methods, from basic handling of individual spectroscopic data, manipulating chemical databases, to artificial intelligence and deep learning methods. Back in the 1970's, mainframe computers were used by analytical groups to apply statistical and mathematical methods.[1] Nowadays, there are various software packages available that are tailored to specific types of datasets which enable the processing of data and application of statistical models. Spectroscopic data can often be treated without the use of complex chemometric methods, given the relatively small number of variables (intensity as a function of wavenumber/wavelength). However, this is further complicated in chemical mapping/imaging methods, where the inherently multivariate data cube requires the use of multivariate tools to efficiently extract information from the xyλ-space.

Apart from of the technical implementation of TERS and TERS imaging, the complicated spectral profiles of biological samples combined with the plethora of spectra obtained from TERS maps renders traditional data processing methods as tedious, laborious tasks. While traditional peak-picking and referencing literature values for TERS spectral interpretation is not obsolete, chemometric methods could help alleviate time-consuming processing procedures.[2] The interpretation of TERS data is also hindered by the identification of parasitic spectra which arise from tip contamination by the fabrication procedure, the environment, or the sample.[3] This limitation is further complicated when considering fragile and/or heterogenous biological samples that are prone to photo- and mechanical degradation. Factors such as molecular orientation and the metal nanostructure at the TERS tip apex induces a high degree of variability in TERS band intensities, which is usually the main variable investigated using more traditional chemometric methods such as Principal Component Analysis (PCA), Multivariate Curve Resolution (MCR), Hierarchical Clustering Analysis (HCA), and partial least-squares or linear discriminant analyses (PLS-DA, LDA), to name a

few. As not all chemometric methods are suitable for every data set, therefore distinct methods have been selected when biomolecules and biomaterials are of interest.[2]

4.1. Pre-processing

In a spectroscopic measurement, variance in the data that is not caused by the properties of the sample directly need to be reduced or eliminated to allow for meaningful analyses to be performed. Instrumental noise and physical properties of the sample lead to observed spectral variation between measured samples and between acquisitions of the same sample. It is therefore necessary to remove these unwanted contributions in order to recover a purer sample spectrum.[4] There are numerous methods to pre-process spectroscopic data, all having different applications and a list of pros and cons to accompany them. The determination of the best method or combination of methods is performed via an iterative process, where care is taken not to introduce distortion or spectral artefacts due to the applied pre-processing methods.

The main pre-processing steps are quality control including spike removal, calibration, and baseline correction. Normalisation is required when comparing datasets, while smoothing and spectral truncation are non-essential but commonly applied additional methods. Quality control is the preliminary step in spectral pre-processing, as outliers can be quickly identified and removed from further analysis. Examples of such outliers include spectral bands originating from sample contamination, device artefacts, or spectra with significantly higher noise. However, spectra cannot be deemed as outliers just in order to improve results.

Very narrow and extremely intense bands can often appear at random wavenumbers in Raman spectra. These “spikes” can be due to high-energy cosmic particles that generate electrons on the detector. They are easily identified in repeat measurements as spikes rarely coincide together. If repeat measurements are not possible (i.e. sample evolution over time), then the average spectrum of neighbouring data points can be used to identify spikes as anomalous intensity changes in the individual spectra. Simple linear interpolation between the two boundary points of the spike effectively removes them.

Calibration of wavenumber and spectral intensity is important in order to produce Raman spectra that are independent from the individual set-up and measurement conditions. In order to make measurements comparable to one another, external standards such as the 520.5 cm^{-1} line of a silicon wafer are useful for wavenumber calibration. One method for calibrating spectral intensity is calculating the ratio of the measured intensity by the intensity response

function of the instrument. The intensity response function is derived by taking the theoretical intensity over a given wavenumber range and dividing into the measured intensity.[5]

When performing baseline correction, two contributions need to be addressed: spectral features arising from the substrate, and fluorescence of the sample. A simple method to assess the former is acquiring a spectrum of the pure substrate as a reference and subtracting this from the substrate with sample spectrum. In the case of heterogenous substrate contributions, multivariate curve resolution (MCR) has been demonstrated as a solution.[6] For the latter, mathematical manipulations such as polynomial fitting, calculation of derivative spectra, standard normal variate (SNV), and multiplicative scattering correction (MSC) to name a few, are used to deal with fluorescent baseline contributions. In the context of a TERS experiment, additional contributions from the response of the TERS tip can also appear in the baseline.

Depending on the type of data and the further analysis that is to be performed, spectral smoothing or spatial filtering can optionally be performed. Noise can be reduced using a low-pass filter that replaces an intensity with a computed value based on the mean, median, or polynomial function fit. The Savitzky-Golay filter[7] is a simple moving-window spectral filter based on the method of least squares. While this is a popular method for smoothing data, care is needed when performing subsequent multivariate analysis as correlations can be introduced into the noise structure.[8] Spatial filtering on the contrary, is exclusively used in imaging data, as the low-pass filter is applied in the spatial domain. However, in hyperspectral datasets if a high spatial resolution is desired over spectral resolution, then spectral filtering is preferred.

4.2. Unsupervised Learning Methods

If objects in a dataset are to be grouped together without prior knowledge of membership to a particular class, then unsupervised classification methods can be used. The two main classes of unsupervised methods are data projection of high-dimensional data onto a lower dimensional space and clustering methods. Using a given measure of “similarity”, clustering methods aim to split data into similar trait groups and assign the groups into clusters. Clustering can be further sub-divided into hard-clustering or soft-clustering, which depends on whether a given data point is definitely assigned or not assigned to a given cluster, or whether a probability of cluster assignment is implemented. Two of the most popular clustering algorithms are hierarchical cluster analysis (HCA), and k-means clustering. The former technique works by first assigning all data points to an individual cluster before merging clusters nearest to each other in a

hierarchical fashion. The latter technique finds the local maxima of clustering centroids in an iterative fashion until no further improvement is attained.

Data projection is often referred to as factorial methods and are often used in multivariate data analysis for feature transformation and/or selection. The principal of data projection is to reduce data dimensionality by projecting the high dimensional dataset onto a line, plane, or three-dimensional coordinate system which can then reveal groupings in the optimal projection. Commonly used dimension reduction methods in chemometrics are single value decomposition (SVD), factor analysis (FA), and principal component analysis (PCA).[9]

4.2.1. Principal Component Analysis

A multidimensional data matrix X, is defined to consist of p columns or features and n rows or objects. This matrix X can be projected down to a d-dimensional subspace via the projection matrix L^T to give the new object coordinates in the plane T. The plane T is called the scores matrix and has n rows and d columns, where d is the number of principal components (PC). Similarly, L is called the loading matrix and has d columns and p rows, where p is termed the loading vectors and d is termed the score vectors. Both the loading and score vectors are orthogonal, where $t_i^T t_j = 0$ and $p_i^T p_j = 0$ for $i \neq j$. The result of the reconstruction of the data gives new variables which are uncorrelated. A criterion of maximum variance is used to determine the PCs, which results in the majority of the data variance to be described within the first PC, followed by the second PC, and so forth. It is self-explanatory that a large proportion of the data variance can be described by only a handful of PCs. Therefore, the percentage cumulative variance is used to determine the number of PCs to use (e.g., 90 %). The data obtained from this analysis is often visualised by plotting the PC scores against one another in two-dimensional space (scores plot).[9]

In terms of pre-processing, PCA is generally applied to data that has been mean-centred. Mean-centring translates the axes of the coordinate system to the centroid of the data, which is important when interpreting a PCA scores plot for example, as deviation from the origin may or may not be a useful description of variation within the system. Variance scaling such as autoscaling (which scales the data to unit variance along with mean centring) is useful for putting all variables on an equal basis in the analysis. Generally, for spectroscopy, variables with a high variance are more important than those with little variation as they contain more information about the system under observation. This holds true for TERS data, but

interpretation can be complicated by the underlying selection rules which influence the number of peaks discerned in a TERS spectrum.

4.2.2. Hierarchical Clustering Analysis

Hierarchical Clustering Analysis (HCA) is an unsupervised clustering method that uses agglomerative clustering to group data based on similarity. Regarding spectroscopic data, each spectrum begins as its own cluster and combining (agglomerating) clusters using a distance metric such as the Euclidean distance. This combining of clusters based on a distance metric is termed the linkage rule. The nearest neighbour linkage rule joins the two nearest clusters with a minimum pair-wise distance. Ward's method is a popular linkage rule, in which clusters are joined such that the resulting within-cluster variance (with respect to the centroids) is minimised. The process of clustering is visualised using a dendrogram, which is a tree-like diagram where the height of the individual branches represents the distance (i.e. dissimilarity) between clusters. This visual representation of the clustering aids the interpretability of HCA and the relationships between clusters. Additionally, the number of clusters does not need to be specified prior to its implementation and can be chosen based on the dendrogram and the scientific question asked.

4.3. Chemometric investigation of TERS datasets of Tau fibrils

Data processing of TERS spectra has traditionally been based on "peak picking", where marker bands of interest are selected by using the integrated area under the curve. The wavelengths are then compared with reference data in the literature (when available) of Raman and SERS in order to ease interpretation. However, this traditional peak-picking methodology for TERS spectral processing is inappropriate (but not obsolete) for TERS imaging of complex biological systems. This is due to the TERS spectra of such systems containing an abundance of bands, which makes peak-picking a very time-consuming process. This is especially true for spectral assignments of overlapping bands, often requiring multi-band assignment. The peak-picking process also suffers from information omission, where the selection of only specific vibrational modes from a data set has not utilised the full informational potential.[2]

Chemometric methods that are tailored to TERS spectra could enable ease the processing of the numerous spectra of TERS maps, allowing for spatial mapping of characteristic chemical groups and improving interpretation. Nevertheless, such multivariate analysis of TERS spectra

is quite challenging. This is mainly in part due to the high intensity variation of TERS bands which depends on the molecular orientation with respect to the tip axis, in addition to depending on the plasmonic properties of the metal nanostructure at the tip apex. The use of chemometric methods in TERS is further complicated by the experimental conditions, as sample degradation due to the plasmonic hotspot or contaminations can greatly affect the quality of the processed dataset. Common unsupervised learning methods were tested on TERS data of Tau-heparin and Tau-polyA fibrils, where analysis results were compared with the traditional peak-picking methods. Supervised learning was deemed inappropriate for the investigated TERS datasets, as such methods require a training dataset of labelled input data that is currently unavailable. As shown in **Chapter 3**, the analysis of selected marker bands can provide many information on biological samples, but exploiting the full richness of TERS spectra may provide additional chemical and structural data. This was the main motivation to pursue the investigation of Tau fibrils.

4.3.1. PCA of TERS data

Principal component analysis (PCA) is arguably the most widely used method in multivariate data analysis, and has been widely applied to various types of spectroscopic datasets. In TERS of biological molecules, PCA has been used for the study of $A\beta_{1-42}$ fibrils to reduce data dimensionality and as a comparison with HCA.[10] In a TERS study of a single cell, PCA was used to reduce data dimensionality and find the minimum number of endmembers to be considered in the vertex component analysis (VCA)-like analysis that followed.[11] PCA was used to generate chemical maps of *Bacillus subtilis* spores.[12] While studying DNA double-strand breaks, PCA was used to assess the inter- and intra-sample variability, and it was found that different TERS tips gave distinct spectral profiles, but where nonetheless clustered compared to a control.[13] PCA was also used to explore spectral differences between TERS spectra from DNA samples prepared with Mg^{2+} and those prepared with APTES.[14] In the study of membrane receptor-ligand specificity, PCA of SERS and TERS spectra of integrin-binding peptide ligands was used to show intra-cluster variance heterogeneity in binding.[15] To investigate the potential benefits of PCA versus traditional peak-picking methods, PCA was applied to the Tau fibril datasets of **Chapter 3.2** and **Chapter 3.3**.

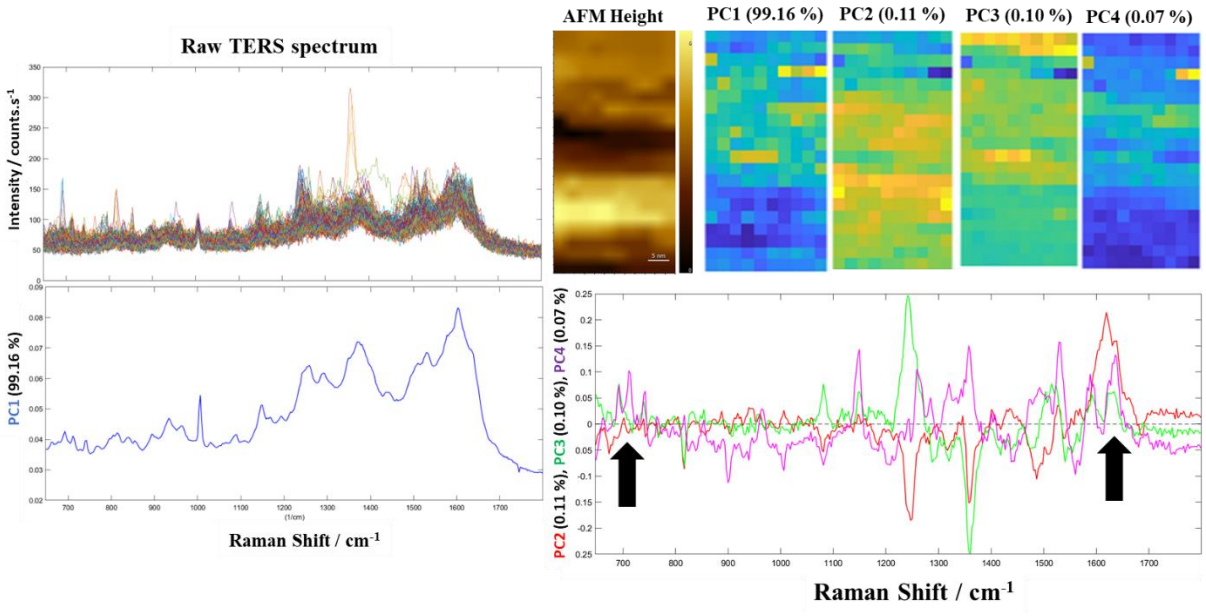

Figure 4.1. *PCA of raw TERS data of Tau-polyA fibrils. PC1 (99.16 %) of the untreated data contains the majority of variance in the data and holds the unwanted contributions of the tip and background also. PC2 (0.11 %), PC3 (0.10 %), and PC4 (0.07 %) contain useful spectral features corresponding to the cofactor polyA and the secondary structure highlighted by the black arrows.*

Figure 4.1 demonstrates a simple PCA performed on a TERS map of Tau-polyA fibrils. The raw TERS spectra are displayed to showcase the shape of the data prior to pre-processing. As is common in all TERS spectra, there are notable contributions to the spectral baseline which originate from the instrument, TERS tip, and the sample itself. Carbonaceous contamination is observed as the broad bands at ~1350 cm^{-1} and ~1590 cm^{-1}. As the tip was TERS-active, this contamination was probably located on its SERS-active sides, without detectable impact on the TERS efficiency at the apex. This is captured in the PC1 (blue, 99.16%) loadings plot, which follows the broad bands observed in the raw spectra. The tip response variation as the map was measured is also captured in PC1, which is notable in the PC1 scores map as generally the spectral variation increases with scanning direction (bottom to top). If anything, the PC1 map is negatively correlated with fibril region at the bottom of the AFM height image. This is a visual representation that PC1 here is not a descriptor of the sample fibril. PC1 also captures a significantly larger amount of the data variance compared to the succeeding PCs, which could indicate a common source of variation throughout the data. This could be the background and tip response throughout the data (not related to the sample), or as this dataset was not mean-centred, this could be the data mean manifesting itself. This shows the importance of pre-processing methods such as scaling and normalisation when using PCA.

PC2 (red, 0.11%), PC3 (green, 0.10%), and PC4 (magenta, 0.07%) have an explained variance an order of magnitude lower than that of PC1 (blue, 99.16%), signifying the large dependence of the variables on the underlying signal. The desirable information of the sample to be extracted is likely contained in these latter principal components. PC2 – 4 show typical positive and negative correlations with the variables (wavenumbers) in the loadings plots, whilst PC1 only contains positive correlations. The only positive correlations could be interpreted as every variable is important to the given PC score, which of course is not meaningful when the goal of the analysis is to find patterns and differences within the data. The meaningful fibril information is hinted at by the positive correlation to the adenine ring breathing mode in PC4 (~720 cm^{-1}) and amide I bands (~1635 cm^{-1}), both noted with a black arrow in the loadings plot of **Figure 4.1**.

This example demonstrates some of the basic interpretation difficulties encountered when using PCA on TERS datasets of biomolecules. The TERS tip response may give rise to a notable background signal that must be carefully reduced or removed without distorting the data. This is made more difficult by the tip response often changing over the course of an imaging experiment, potentially leaving residual background contribution within the data even after standard baseline subtraction. Standardisation of the data through autoscaling or mean-centring is therefore a must. TERS vibrational bands can vary in intensity and slightly in wavenumber position (especially considering the ca. 3 cm^{-1} spectral resolution) in a manner unrelated to the analyte concentration. Methods such as PCA that use the variation in intensity at a given wavenumber as their metric put a greater value on more intense peaks. While this might identify high-Raman cross-section species such as aromatic amino acids, weaker signals are neglected. Normalisation of the data can help bring equal value to each variable, but care is needed as improper processing can distort results.

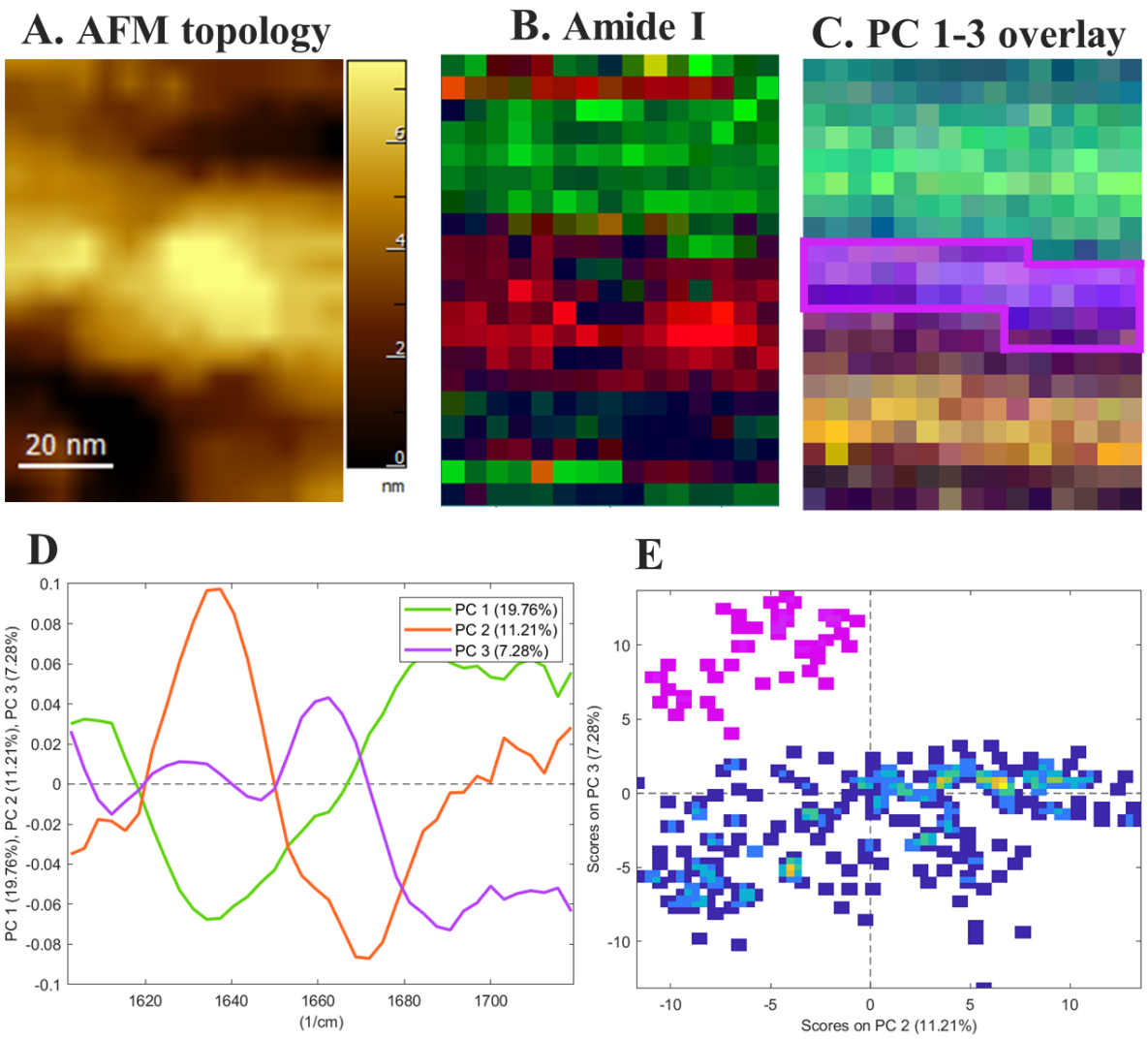

Figure 4.2. *PCA analysis performed on a section of Tau-heparin fibril.* ***[A]*** *AFM height image of the fibril section.* ***[B]*** *Peak integration of core β-sheet amide I band (1660-1682 cm^{-1}, red).* ***[C]*** *Overlay of PC1 (green, 19.76 %), PC2 (orange, 11.21 %), and PC3 (purple, 7.28 %).* ***[D]*** *Loadings plots of PC1 – 3 of the amide I region (1600 – 1720 cm^{-1}).* ***[E]*** *Scores plot of PC2 versus PC3 shows clustering of pixels marked in purple, which are located inside the purple outline in C.*

PCA can be useful in TERS for exploratory data analysis such as outlier, contaminant, and background identification. Additionally, PCA can be useful for localization of region of interest for further analysis. **Figure 4.2A** features a section of Tau-heparin fibril that was analyzed using TERS. Comparing this height image with the integrated area of the amide I region (**Figure 4.2B**), there seems to be some correlation of the core β-sheet amide I band (1660 – 1682 cm^{-1}, red) with the fibril topology. PCA was applied to the same dataset after mean-centering and the overlayed result of the first 3 PCs is shown in **Figure 4.2C**. PC1 (green,

19.76%), PC2 (orange, 11.21%), and PC3 (7.28%) account for only 38.25% of the variance in the data. This is in stark contrast to the data showcased in **Figure 4.1** (PC1 > 99%) and solidifies the importance of spectral pre-processing. Despite the low overall representation of the data variance with just 3 PCs, some information can nevertheless be extracted. The loadings of PC1 – 3 in the amide I region is shown in **Figure 4.2D**. PC2 (orange) is positively correlated with amide I random coils (1630 – 1655 cm^{-1}) and negatively correlated with amide I core β-sheets (1660 – 1680 cm^{-1}). In contrast, PC3 (purple) is positively correlated with amide I core β-sheets. PC1 (green) is negatively correlated with both random coils and β-sheets and is likely not a descriptor of the fibril (especially given the localisation of the PC contribution at the top of the image in a region void of sample). The PC2 versus PC3 scores plot (**Figure 4.2E**) shows a separation of a cluster of data along the PC3 axis. This data cluster is highlighted in purple, and correlates to the purple area denoted in **Figure 4.2C**. This region not only is positively correlated with the amide I band of β-sheets, but is well aligned with the expected placement of the fibril core as per the AFM height image, **Figure 4.2A**.

This dataset shows a potential use of PCA to identify regions of interest within TERS images, given appropriate pre-processing. Given the low percentage of variation explained per PC, PCA as a method for dimensionality reduction of complex biological TERS data is not convincing (at least for Tau fibrils investigated here). Care is needed when interpreting the abstract results of multivariate analysis techniques, as misrepresentation of the data may lead to incorrect conclusions about the studied sample. The highly complex spectra of biological samples have the most to gain from implementation of such analyses, but the numerous peaks of various molecular vibrations that often overlap make resolving individual components challenging.

4.3.2. HCA of TERS data

The same dataset as used in **Figure 4.2** was also subjected to HCA analysis as shown in **Figure 4.3** The region of interest identified in the previous PCA was the focus of the HCA analysis (red box, **Figure 4.3A**). The HCA clustered image **Figure 4.3B**, shows five distinct clusters which were arbitrarily determined after analysis based on the dendrogram **Figure 4.3C**. Based on this dendrogram, cluster C1 (red) is most closely related to cluster C5 (magenta), which next related to C4 (cyan), and then C2 (green) and C3 (blue). C3 could even be considered a subset of C2 given their proximity. With this general relationship of the clusters discerned, the average spectrum of each cluster can be further scrutinised. **Figure 4.3D** shows the spectral region from

950 – 1100 cm^{-1} with the average cluster spectra overlaid. The characteristic peak of the Phe ring breathing mode (1005 cm^{-1}) is evident in all clusters. Even though C3 (blue) is very closely related to C2 (green), the spectral profiles here (and in the full spectra in **Figure 4.3E** and **F**) are distinct. This could be due to a bias of fewer spectra contained in C3 compared to C2, but it is nevertheless interesting to note the significant contribution of the band centred at 1020 cm^{-1} in C3 that is absent in C2. This could arise from the Phe CH ring deformation mode (1018 – 1056 cm^{-1})[16]. The blue bars in **Figure 4.3D** indicate the expected regions for the vibrational bands N-SO_3 (1035 – 1050 cm^{-1}), and 6-OSO_3/3-OSO_3 (1050 – 1065 cm^{-1}) associated with the cofactor heparin. There is minimal contribution of these bands in the averaged cluster spectra, and therefore interpretation of the localisation of the cofactor is ambiguous, as already noted in **Chapter 3.2**.

Figure 4.3E shows the full spectra of each cluster, this time with the amide III (random coils, 1251 – 1273 cm^{-1}; β-sheets, 1218 – 1250 cm^{-1}) and amide I bands (random coils, 1630 – 1655 cm^{-1}; β-sheets, 1660 – 1682 cm^{-1}) indicated. Based on the appearance or lack-of these bands, it can be tentatively concluded that C1 and C5 contain mostly random coils, C2 contains mostly core β-sheets, while both are observed in C3 and C5. This assignment makes sense with the expected structure of fibrils, which have a core of β-sheets that is enveloped in a disorganised fuzzy coat. This showcases the use of clustering methods to group regions of such fibrils based on similar secondary structure. **Figure 4.3F** highlights vibrational modes associated with the amino acid residues lysine (purple, NH_3^+ deformation, 1070 – 1080 cm^{-1} and 1136 – 1155 cm^{-1}) and histidine (cyan, NCN stretching, NH deformation, 1150 – 1194 cm^{-1}; C-N stretching, 1327 – 1337 cm^{-1}; NH deformation, C=C asymmetric stretching, 1482 – 1517 cm^{-1}). The three marker bands allowing for a solid identification of histidine are discerned in C1, C2 and C5. The two marker bands necessary for safe lysine identification are observed in C2, C4 and C5. **Figure 4.3** thus suggests that lysine and histidine are present indifferently in disordered and β-sheet-rich fibril regions. As heparin should be able to bind to these positively charges amino acids, this indicates that the heparin cofactor should be quite homogeneously distributed on Tau-heparin fibrils. However, the analysis of many more Tau-heparin fibrils would be needed to confirm this preliminary conclusion.

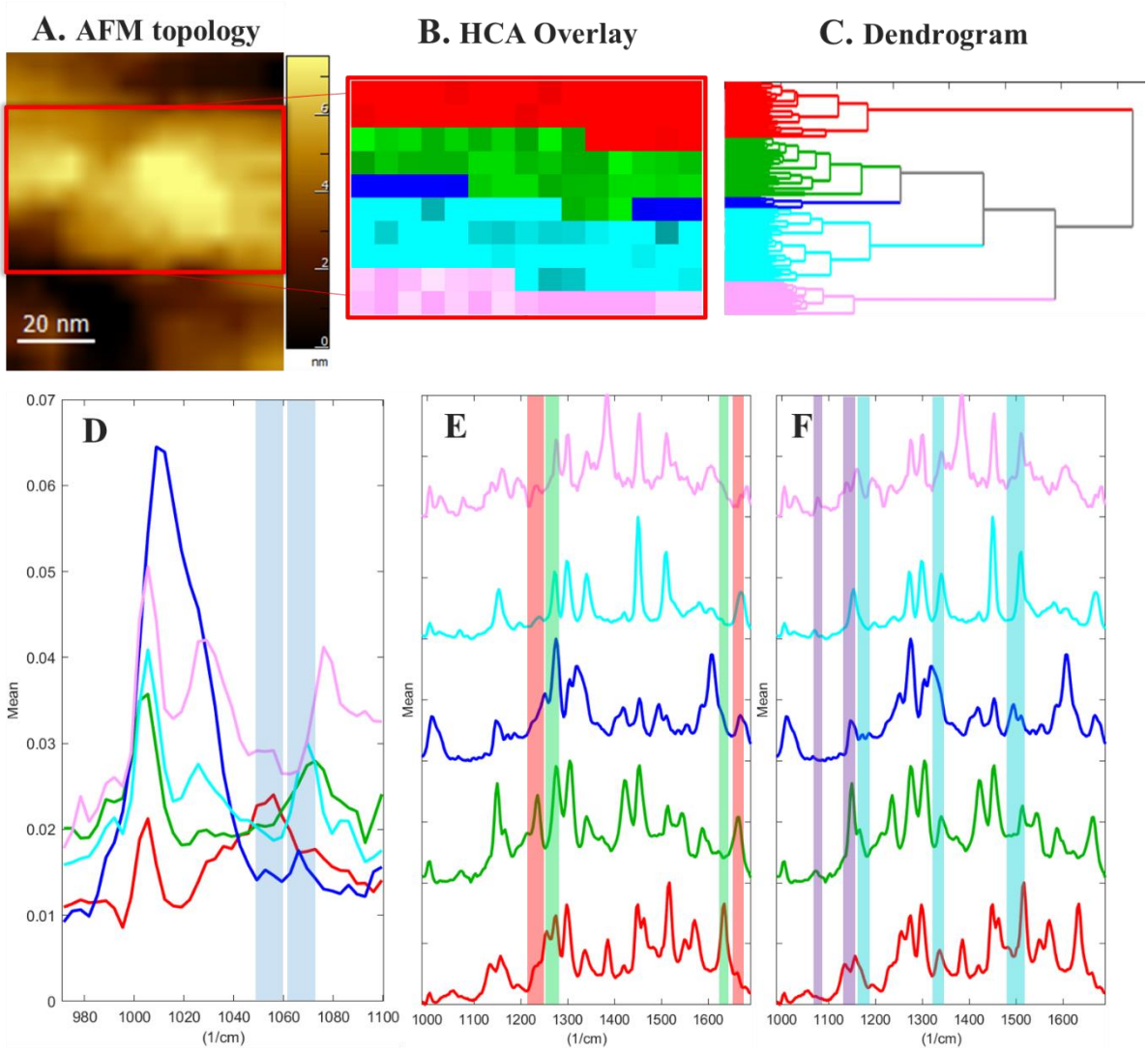

Figure 4.3. *HCA analysis performed on the section of heparin-induced Tau fibril as Figure 4.2.* ***[A]*** *AFM height image of the fibril section.* ***[B]*** *HCA cluster image of the red section outlined in A where C1 = red, C2 = green, C3 = blue, C4 = cyan, and C5 = magenta.* ***[C]*** *HCA dendrogram showing the relationship between the five HCA clusters based on their variance-weighted distance.* ***[D]*** *Mean spectra of HCA clusters in the 950 – 1100 cm^{-1} spectral region. Blue bands correspond to the expected wavenumber of heparin sulphate groups (N-SO_3, 1035 – 1050 cm^{-1}; 6-OSO_3, 3-OSO_3, 1050 – 1065 cm^{-1}).* ***[E]*** *Mean spectra of HCA clusters with amide III and amide I regions of core β-sheets (red) and random coils (green).* ***[F]*** *Mean spectra of HCA clusters with bands associated with histidine (cyan) and lysine (purple).*

Conclusion

This chapter explored the significance of chemometric methods for the analysis of TERS data, specifically complex biological samples. While chemometric methods have the potential to significantly enhance the efficiency of spectral interpretation in TERS imaging, substantial work is still required to develop TERS-specific spectral processing methods. The first hurdle is the application of appropriate pre-processing methods as this step is essential for the integrity of subsequent multivariate analyses. Advancements in pre-processing methods that account for the phenomena encountered in TERS will improve data accuracy, facilitate better comparisons, and the drawing of meaningful conclusions from processed TERS data.

The successful application of chemometric methods to TERS datasets is largely limited by the high degree of variability in band intensity, which arises from molecular orientation and plasmonic properties at the tip apex. The quality of obtained TERS spectra is also subject to contamination and degradation which further complicates analyses. TERS spectra of Tau-heparin and Tau-polyA fibrils were used as a test dataset for initial tests using common unsupervised learning methods, such as PCA and HCA. While these techniques hold potential, experimental conditions and data variability accentuate the need to develop more sophisticated and tailored approaches for TERS.

PCA was proven to be useful as an exploratory tool, especially for identifying outliers, contaminants, and background signals within TERS spectra. However, it is noted that a significant amount of variation was not sufficiently explained by the use of the first few PCs. The inherent complexity of biological molecules is likely the underlying cause of this variation, which compounds with the complex phenomena observed in TERS experiments. For HCA, fibril regions with similar characteristics were clustered together, and fibril core regions could be distinguished from outer disordered regions. In a similar fashion to PCA components, the number of clusters in HCA influences the interpretation, especially for arbitrarily chosen clusters. With proper pre-processing (and potentially in conjunction with PCA), HCA can be useful for exploratory analysis that can reveal compositional relationships within the dataset.

Nevertheless, the biggest influence on determining the utility of multivariate analysis for TERS datasets is the pairing of appropriate (or tailored) chemometric methods with the appropriate research question. The capabilities and limitations of each method should be considered prior to their implementation and interpretation of TERS data. To this end, traditional peak-picking methods still hold a place in the analysis workflow, and should be

complimented with relevant chemometric methods. The lack of available libraries of TERS data hinders the implementation of supervised learning methods, whose importance and usefulness are yet to be realised. To fully exploit the potential of chemometric methods for TERS, sophisticated and tailored processing techniques are required.

References

1. Otto, M. What is Chemometrics?, Chapter 1, 1–13 (2016).
2. Bonhommeau, S., Cooney, G. S., Huang, Y., Nanoscale chemical characterization of biomolecules using tip-enhanced Raman spectroscopy., Chem. Soc. Rev., 51, 2416–2430, (2022).
3. Schmid, T., Opilik, L., Blum, C., Zenobi, R., Nanoscale chemical imaging using tip-enhanced Raman spectroscopy: A critical review, Angew. Chem. Int. Ed., 52 5940–5954 (2013).
4. Guo, S., Popp, J., Bocklitz, T., Chemometric analysis in Raman spectroscopy from experimental design to machine learning–based modelling, Nat. Protoc., 16, 5426–5459 (2021).
5. Ryabchykov, O., Guo, S., Bocklitz, T., Analyzing Raman spectroscopic data, J. Phys. Sci. Rev., 4, (2019).
6. McLaughlin, G., Fikiet, M. A., Ando, M., Hamaguchi, H. O., Lednev, I. K., Universal detection of body fluid traces in situ with Raman hyperspectroscopy for forensic purposes: Evaluation of a new detection algorithm (HAMAND) using semen samples, J.Raman Spec., 50, 1147–1153 (2019).
7. Savitzky, A., E, M. J., Smoothing and Differentiation of Data by Simplified Least Squares Procedures., Physiol. Chem., 40 (1964).
8. Brown, C. D., Wentzell, P. D., Hazards of digital smoothing filters as a preprocessing tool in multivariate calibration, J. Chemom., 13, 133–152 (1999).
9. Varmuza, K., Filzmoser, P., Introduction to Multivariate Statistical Analysis in Chemometrics, (2016).
10. Lipiec, E., Perez-Guaita, D., Kaderli, J., Wood, B. R., Zenobi, R, Direct Nanospectroscopic Verification of the Amyloid Aggregation Pathway, Angew. Chemie, 130, 8655–8660 (2018).
11. Richter, M., Hedegaard, M., Deckert-Gaudig, T., Lampen, P. & Deckert, V., Laterally resolved and direct spectroscopic evidence of nanometer-sized lipid and protein domains on a single cell, Small, 7, 209–214 (2011).
12. Rusciano, G., Zito, G., Isticato, R., Sirec, T., Ricca, E., Bailo, E., Sasso, A., Nanoscale chemical imaging of bacillus subtilis spores by combining tip-enhanced Raman scattering and advanced statistical tools, ACS Nano, 8, 12300–12309 (2014).

13. Lipiec, E., Sekine, R., Bielecki, J., Kwiatek, W. M., Wood, B. R., Molecular Characterization of DNA Double Strand Breaks with Tip-Enhanced Raman Scattering, Angew. Chemie Int. Ed., 126, 173–176 (2014).
14. Lipiec, E., Japaridze, A., Szczerbiński, J., Dietler, G. Zenobi, R., Preparation of Well-Defined DNA Samples for Reproducible Nanospectroscopic Measurements, Small, 12, 4821–4829 (2016).
15. Xiao, L., Bailey, K. A., Wang, H. Schultz, Z. D., Probing Membrane Receptor-Ligand Specificity with Surface- and Tip- Enhanced Raman Scattering, Anal. Chem. 89, 9091–9099 (2017).
16. Bonhommeau, S., Lecomte, S., Tip-Enhanced Raman Spectroscopy: A Tool for Nanoscale Chemical and Structural Characterization of Biomolecules, Chem. Phys. Chem., 19, 8–18 (2018).

Chapter 5

Liquid TERS of supported lipid bilayers

Introduction

Lipid membranes are primarily composed of phospholipids that can form bilayers which act as a barrier between the cellular internal and external environments. Phospholipids consist of a hydrophilic phosphate head and a hydrophobic aliphatic chain or tail. The amphipathic nature of these molecules results in a preferential orientation of the head groups to face outwards and the tail to face inwards creating the bilayer. Lipid membranes have a degree of fluidity depending on the types of lipids present (saturated or unsaturated tails), the temperature, and the presence of cholesterol within the bilayer. Supported lipid bilayers (SLBs) are model systems useful in studying the structure-property relationships of biological cells.[1] One such phenomenon is the formation of lipid rafts, which determine membrane fluidity and sorting of cell membrane proteins.[2] These rafts come about via lipid phase segregation, which is the self-sorting of lipids into regions of tightly packed (liquid-ordered phase) and loosely packed lipids (liquid-disordered phase). In general, saturated lipids are more rigid and aligned compared to unsaturated lipids in which the kinks in the tail prevent tight lipid packing.

TERS has been used primarily to characterise dry phospholipid mixtures to date. The CH stretching (2850 – 3100 cm^{-1}) and bending vibrations have been the most frequently reported,[3–5] but phosphate (1050 – 1250 cm^{-1}) and C=O ester stretching bands (1720 – 1760 cm^{-1}) have also been used as reliable markers for lipids.[5–7] The correlation between topography maps and TERS has been demonstrated using dipalmitoyl-phosphatidylcholine (DPPC) monolayers on Au by Pandey *et al.* in 2021 (see **Figure 5.1**). A 20 nm SOR detected nanoscale holes in the lipid monolayer, with disruption of the packing order around the holes being identified by using the ratio of the 2850 and 2930 cm^{-1} TERS bands assigned to aliphatic saturated CH stretching vibrations.[4] The same authors have continued this work with their 2024 paper focusing on deuterated DPPC ($DPPC_{d62}$) and dioleoyl-phosphocholine (DOPC, **Figure 5.1**). TERS successfully differentiated between $DPPC_{d62}$-rich and DOPC-rich domains and

even revealed the presence of nanometre-sized phase-separated domains.[8] Nevertheless, the biggest criticisms of these works are the use of lipid monolayers rather than bilayers, performance under dry conditions, and the use of Au as a substrate. The same group did publish a TERS study on DPPC bilayers in which only the CH_3 choline head group vibrations were selectively enhanced, but a glass substrate and a different geometry system were used.[9] Even though these works showcase the potential of TERS to characterise lipid bilayers at the nanoscale, the substrate choice (albeit limited to the given STM technique) influences the formation and structure of such systems. It has been determined that micron-scale domains identical to those seen in free-floating giant unilamellar vesicles are only observed when using muscovite mica due to its atomic flatness. The nanoscale roughness and physicochemical properties of glass and quartz substrates was shown to reduce these lipid domains,[10] which questions the TERS results of lipid structure obtained using these substrate materials. Biocompatible TERS substrates based on mica flakes mechanically exfoliated on a supporting substrate have been suggested[11] but have not yet been implemented in the study of lipid bilayers.

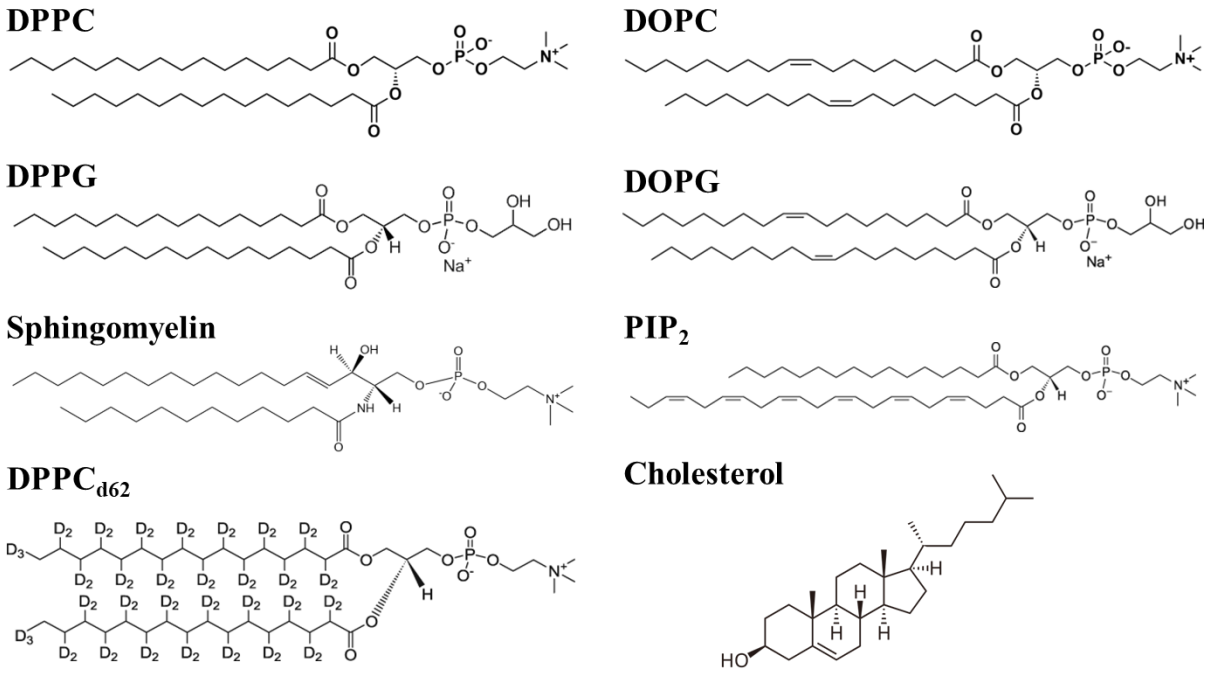

Figure 5.1. Chemical structures of phospholipid molecules and cholesterol.

SLBs are also useful model systems to study lipid interactions with other biomolecules such as proteins. Within the scope of this thesis, one such interesting family of proteins is

amyloids in their disease state. Amyloids such as Aβ and Tau are known to form amyloid plaques and neurofibrillary tangles respectively, which are implied in neurodegenerative diseases such as Alzheimer's. Neuronal cell death is the result of a still unknown mechanism. By modelling the neuronal cell lipid composition, TERS has the potential to give invaluable insights at the nanoscale into the processes and interactions of neurodegeneration. Our group has already demonstrated the ability of TERS to identify phospholipids acting as cofactors for the formation of amyloid fibrils.[7] This work could be expanded to incorporate model membranes to investigate the interaction of lipid bilayers with amyloids as a potential mechanism of neurodegeneration. Complex lipid mixtures of DPPC, DOPC, cholesterol, and sphingomyelin (a sphingolipid abundant in the myelin sheath surrounding neuronal axons) could form the basis of a model neuronal membrane to be investigated using TERS.

Prior to such works, TERS of biomolecules in liquid media needs to evolve into routine analysis and certain challenges need to be overcome. These challenges include the optimisation of the photon excitation and collection of the TERS system in liquid, the fabrication of robust TERS tips for liquid applications, production of biocompatible substrates, and characterisation of simpler systems. The following sections detail optimisations made to the TIR-TERS system previously described in **Chapter 2** and advancements in liquid AFM-TERS experiments of lipid bilayers.

5.1. Description and chemical structure of investigated molecules

As previously described, biocompatible substrates are essential for investigating biomolecules in liquid. This is especially true for SLBs, whose architecture is extremely sensitive to the both the physicochemical properties of the surface and the nanoscale roughness of the surface. Muscovite mica is a commonly used AFM substrate for hosting biological samples due to its desirable physical properties. The shiny plate-like structure has perfect basal cleavage in one direction which produces thin, transparent sheets with atomic smoothness (**Figure 5.2**). A crystal of mica consists of tetrahedral-octahedral-tetrahedral-cation (TOT-c) structure. The outer tetrahedral sheets of silicon-oxygen sandwich the middle octahedral Al cations which are surrounded by six oxygen atoms or hydroxide anions. The relatively weak bonding of the potassium cations to the tetrahedral sheets gives rise to its perfect basal cleavage. The resulting exposed silicate plane carries a net negative charge which is useful for immobilisation of positively-charged biomolecules, which can alternatively have its surface charge modulated

using various salts. A sharp scalpel blade can be used to cleave sheets of a few monolayers thick, with scotch-tape being capable of exfoliating individual monolayers.

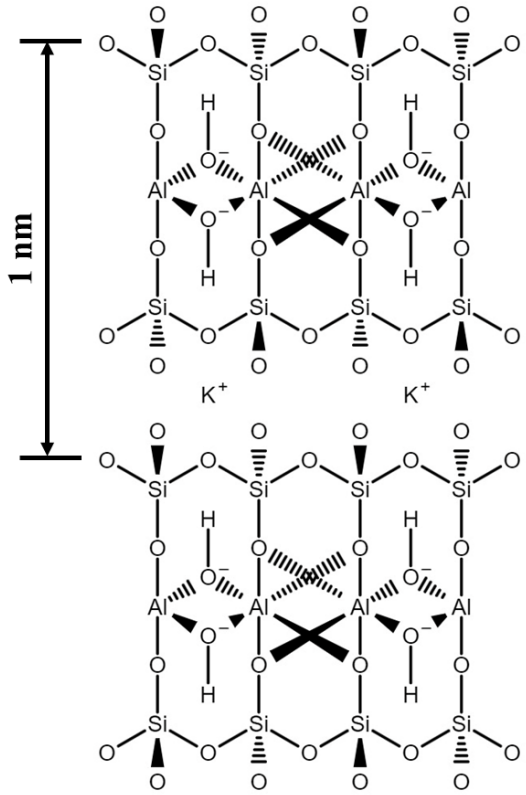

Figure 5.2. TOT-c lattice structure of muscovite mica, $KAl_2(AlSi_3O_{10})(OH)_2$. Small amounts of other elements often substitute into the structure, with Na^+ commonly replacing K^+ and F^- replacing HO^-.

As previously discussed, phospholipids in general contain both a hydrophilic head and a hydrophobic tail. The properties of phospholipids depend largely on their chemical composition of these two parts. The tail group usually features a long aliphatic chain, in which lipid packing properties and fluidity are modulated by the chain length and degree of saturation. As seen in **Figure 5.1**, DPPC contains two saturated aliphatic chains, compared to DOPC which contains an unsaturated bond in both chains. With chain length and head group remaining the same, this difference in chain unsaturation results in DPPC having a transition temperature of 41.3 °C (from gel-phase to liquid crystalline-phase) compared to -16.5 °C of DOPC.[12] Modification of a phospholipid head group often changes the membrane surface charge and structural integrity, and therefore its interactions with the environment and exogenous molecules. DPPC and DOPC both contain the choline head group, a quaternary ammonium salt that results in a neutral zwitterionic lipid. Dipalmitoyl-phosphoglycerol (DPPG) and dioleoyl-

phosphoglycerol (DOPG) on the other hand contain a glycerol headgroup that results in a negatively charged membrane lipid. Deuteration of the acyl tail enables the separation of vibrational bands associated with tail and head groups, as is the case for $DPPC_{d62}$ (**Figure 5.1**). This deuteration additionally enables the discrimination of lipid phases spectroscopically when one fully non-deuterated lipid (DOPC) is used in conjunction with the deuterated $DPPC_{d62}$.

Sphingomyelin is one of the most common sphingolipids in mammalian cells. Sphingolipids are characterised by the sphingosine backbone, which differs from the previously mentioned phospholipids DPPC, DOPC, DPPG, and DOPG.[13] Phosphatidylinositol-bisphosphate (PIP_2) is an inner cytoplasmic membrane component that plays a critical role in cellular signalling and binding of intracellular proteins.[7] Cholesterol along with the phospholipid components are essential for normal cell function. Cholesterol is important in membrane organisation, being implicated in the functional modulation of integral membrane proteins and cholesterol-rich lipid rafts.[14] Through the interaction with phospholipid acyl chains, the fluidity of the cell membrane is controlled.

5.2. TIR-TERS of lipid bilayers in aqueous media

5.2.1. Experimental Procedures

5.2.1.1. Lipid purification and preparation

Small unilamellar vesicles (SUVs) of DPPC, $DPPC_{d62}$, DOPC, DPPG, DOPG and their binary mixtures were prepared by PhD candidate Vicky Ury-Thiery at CBMN using a previously established protocol.[15] In brief, stock ampules (25 mg) of pure lipid in chloroform were purchased from Avanti Polar Lipids Inc. and stored at -20 °C. When ready for preparation, 20 µL of lipid solution was transferred into a glass vial and the chloroform evaporated using inert gas and stored in a vacuum chamber for 8h. Phosphate buffered saline (PBS) buffer (1mL, 10 mM, pH 7.4) was added and sonicated using a sonication probe until the solution became clear. Solution transparency indicates the successful formation of SUVs. As seen in **Figure 5.3A**, multilayer vesicles (MLVs), which consist of several non-concentric vesicles within one another, need to be sonicated to produce the more desirable unilamellar vesicles. SUVs are preferred for the homogenous coverage of a substrate and they limit the formation of lipid multilayers. The SUV lipid solution was stored at 4 °C until required.

5.2.1.2. Deposition of SUVs for TERS measurements

The stored SUV lipid solution was pre-heated in a sonication bath to 60 °C to ensure all lipids were past their transition temperature and in the liquid-crystalline phase. Meanwhile, the freshly-prepared substrate (either glass or mica-glass substrate) was heated to approximately 60 °C in a petri dish using a hot plate. 100 µL of the SUV solution was deposited onto the substrate and incubated in a humid environment. This was achieved by soaking some paper in water, placing it within the petri dish next to the substrate and covering the dish with the lid. A 20 mM PBS pH 7 buffer with 100 mM NaCl was used to every ca. 10 – 15 mins to top-up the incubating lipid sample and thus avoiding the sample drying-out. Incubation times were optimised based on the lipid composition having an average incubation period of 1h before measurement to ensure complete deposition of lipid. The SLB formation follows the mechanism outlined in **Figure 5.3B**. The deposited SUVs settle to the surface and spontaneously rupture before fusing to the substrate. An elevated surface temperature aids in the rupture and fusion of the vesicles, and enables rearrangement of lipid domains as more SUVs fuse with the surface. After the incubation period, the heating source is turned off to allow for the slow cooling of the newly formed SLB. After approximately 10 mins, the SLB is carefully rinsed with buffer solution to remove any remaining free SUVs. This is achieved by pipetting the buffer onto one side of the sample and removing the excess from the opposite side, ensuring the sample does not dry out.

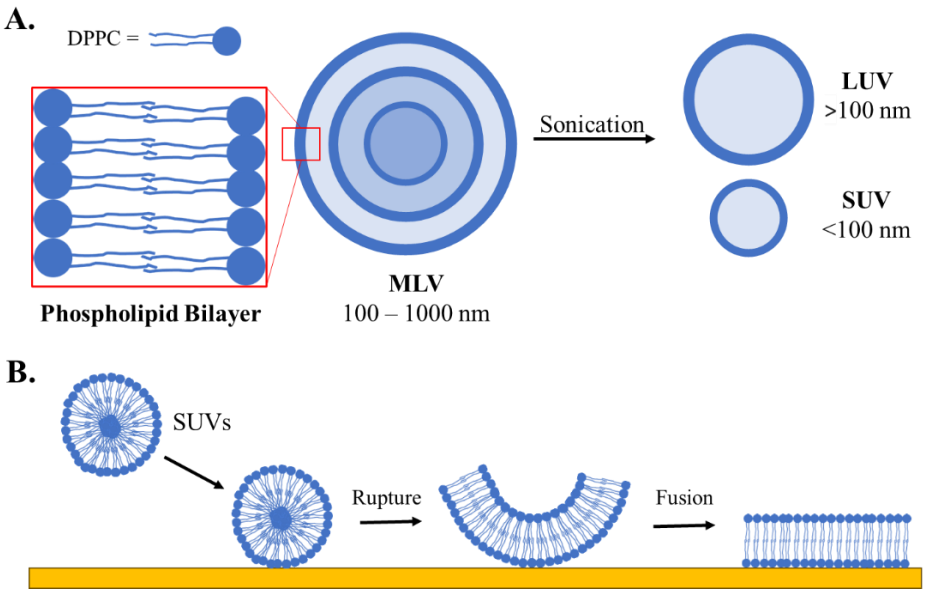

Figure 5.3. [A] *Phospholipids can form bilayers as vesicles when suspended in solution. Multilamellar vesicles (MLVs) are vesicle-in-vesicle systems that can be sonicated to form the more desirable large unilamellar vesicles (LUVs) and small unilamellar vesicles (SUVs).* ***[B]*** *To form supported lipid bilayers, SUVs deposited must first rupture on the surface and fuse before reorganising into domains (depending on the lipid composition).*

5.2.2. AFM-TERS in liquid considerations and optimisations

In order to successfully perform TERS in liquid, there are several issues that need to be addressed regarding the AFM system and performance, and the TERS coupling and optimisation. The former has increased complexity compared to operation in air, as additional components such as specialised tips and liquid cells are needed. **Figure 5.4** presents one of the first issues encountered when performing AFM in liquid. The AFM IR diode laser light (λ = 1300 nm, in our case) is significantly absorbed in aqueous media with the standard n-doped silicon or silicon nitride composition of AFM cantilevers being insufficiently reflective. Therefore, a more reflective metal coating is required to increase the cantilever reflectivity for a good AFM readout. Commercial AFM tips designed for applications in liquid environments typically come with a reflective backside coating of Au or Al. Without having to buy specialist tips, the standard ACCESS-FM can be sufficiently coated in an Au layer via sputter coating, with a deposited thickness larger than 50 nm usually being sufficient for achieving a homogenously reflective backside coating.

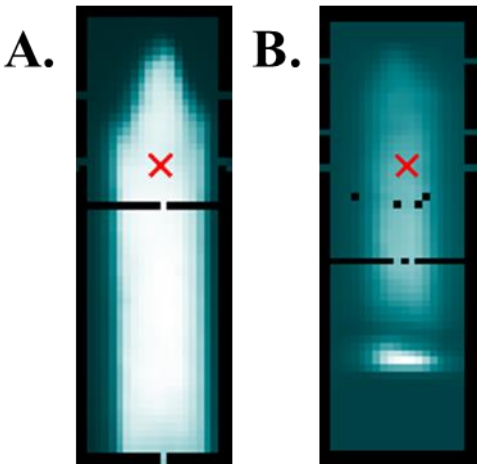

Figure 5.4. *AFM laser reflection image of backside of cantilevers in liquid.* ***[A]*** *ACCESS-FM cantilever backside covered by a 60 nm Au sputter coating shows a high reflectivity and easy laser diode alignment.* ***[B]*** *ACCESS-FM cantilever backside stock silicon is not reflective enough for reliable AFM measurement in liquid.*

A useful function within the AIST-NT AFM system is the “Moto Scan” mode. This mode allows the user to obtain different distribution maps across the reflective surface of the AFM cantilever. This mode is particularly useful for evaluating the quality of the backside

reflective coating and allows for accurate positioning of the IR laser. **Figure 5.5** shows the Moto Scan maps obtained for ACCESS-FM cantilever with 60 nm Au shown above in **Figure 5.4A** for both air and in liquid. Stepper motors mounted on the cantilever holder and on the AFM photodiode allow for the accurate scanning of the cantilever surface. The magnitude signal corresponds to the probe oscillation amplitude across the reflective surface of the cantilever. The nominal force (Nf) is the measured vertical deflection of the cantilever i.e. the nominally designed direction of an AFM cantilever is the up/down deflection with respect to the surface plane. The lateral force (Lf) is the force applied to the tip parallel to the surface plane. This is the measured torsion deflection of the cantilever.

The first point to note about **Figure 5.5** is the apparent difference in cantilever size between the air and liquid scans. This is likely due to the physical differences in the AFM holders for air and liquid, in which the liquid AFM holder contains a compensating lens for the air and liquid refraction indices. This lens may produce a slight magnifying effect of the cantilever. The next general observation between the air and liquid tip scans is the slight decrease in magnitude and force when the tip is in liquid. This is an expected result of the hydrodynamic forces in liquid such as viscous damping which increases the probe's effective mass, thus reducing its resonance frequency. This resonance frequency has been observed to be typically 2 – 3 times less in liquid than in air.

Both the magnitude and lateral force of the tip are comparable in air and in liquid. A notable difference is observed in the nominal force scans, which is exemplified in the line profiles Nf air and Nf liquid below. These profiles demonstrate a gradient in the Nf signal from the tip-end of the cantilever to the cantilever base. The Nf air profile contains mostly negative values, while the Nf liquid initially contains positive values which become negative along the tip length. This signifies the greater repulsive forces acting on the tip end in liquid that lead to a greater difference between the tip-end and the cantilever base.

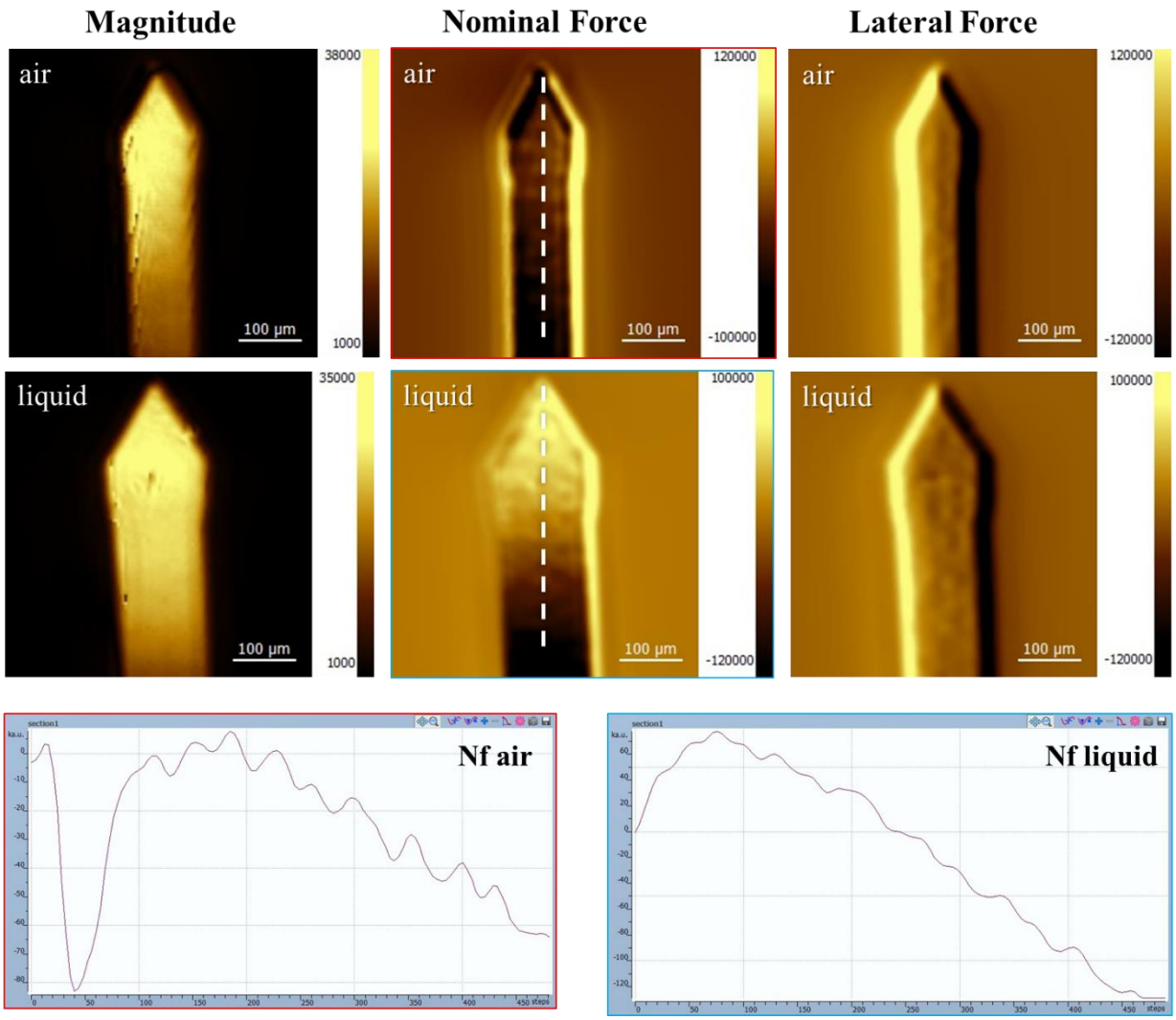

Figure 5.5. *MotoScan mode used on ACCESS-FM tip with a 60 nm Au sputter coating. Comparison of cantilever magnitude signal, vertical cantilever deflection or nominal force (Nf), and the torsion cantilever deflection signal or lateral force (Lf) that the tip is subjected to in both air (top row) and water (bottom row). Two line profiles along the white dashed line of the Nf signal shows a difference in gradient from the cantilever base to the tip, and for in air and in liquid*

Another difference between measurement in air versus in liquid is the influence of the TIR-objective on the stability of the AFM system. When operating in air, the engagement of the TIR-objective to perform TERS measurements did not introduce a significant amount of noise to the AFM system. The same cannot be said for operation in liquid as demonstrated in **Figure 5.6**. This figure shows liquid-AFM height and magnitude images of a mixture of DPPC/DOPG lipids deposited onto glass and measured using a 60 nm Au-sputter coated ACCESS-FM tip. The left-most set of images are taken without the TIR-objective being engaged, and show a relatively disordered SLB of DPPC domains (ca. 200 nm diameter)

amongst a field DOPG. While the height image contains scarring in the direction of scanning (left-to-right), the stability of the tip while scanning is confirmed in the near-perfect magnitude scan. The middle set of images takes the same scan area and parameters (scan rate: 1 Hz, set-point: 80 %) but introduces the TIR-objective which is focused onto the sample surface. Under the same conditions, the quality of the AFM imaging has significantly decreased. The height image features significant scarring and general feature blurring, with a greater range of heights measured (-10 – 15 nm vs. -2 – 13 nm). The tip instability is confirmed in the corresponding magnitude image that is less sharp, but also contains notable noise that is consistent throughout the image. Like with the height measurement, the range of magnitude values recorded (-15000 – 6000 vs. -9000 – 4000). The right-most set of images is a repeat measurement of the same sample area but this time with a reduced scanning rate of 0.5 Hz. Both the height and the magnitude images improve in quality with this reduced scanning rate, and the range of height values measured returns to comparable values to that of the height image without the objective engaged (-5 – 9 nm). While the magnitude image has improved with reducing the scanning rate, the consistent noise is still observable throughout the image. Therefore, a lower scanning rate partially alleviates the observable noise and provides a more stable scanning of the tip. As is with scanning in air, there is a trade-off between higher image quality and scan rate with very low scan rates (e.g. 0.1 Hz) being nearly unfeasible due to their slow image generation.

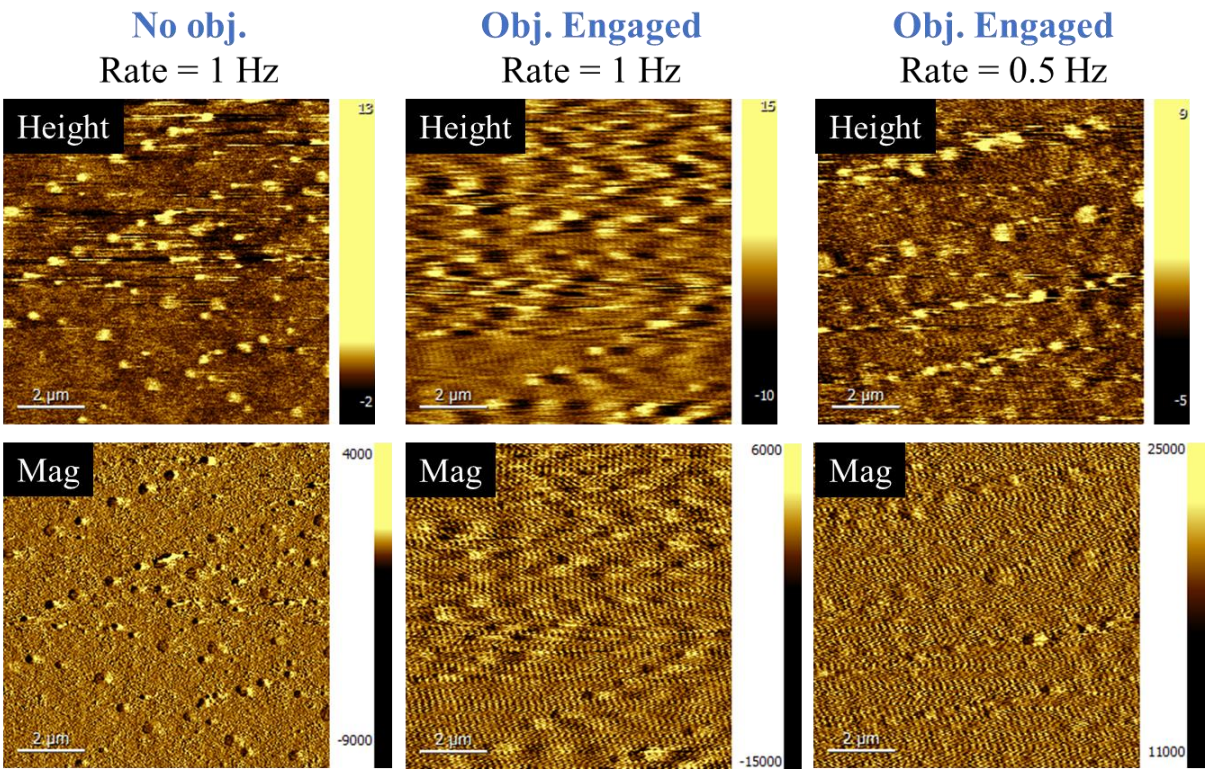

Figure 5.6. *Liquid AFM height and corresponding magnitude images of DPPC/DOPG lipids on glass with and without the TIR objective engaged. Engaging the objective induces noise in the AFM image, which can be partially alleviated by using slower scan rates.*

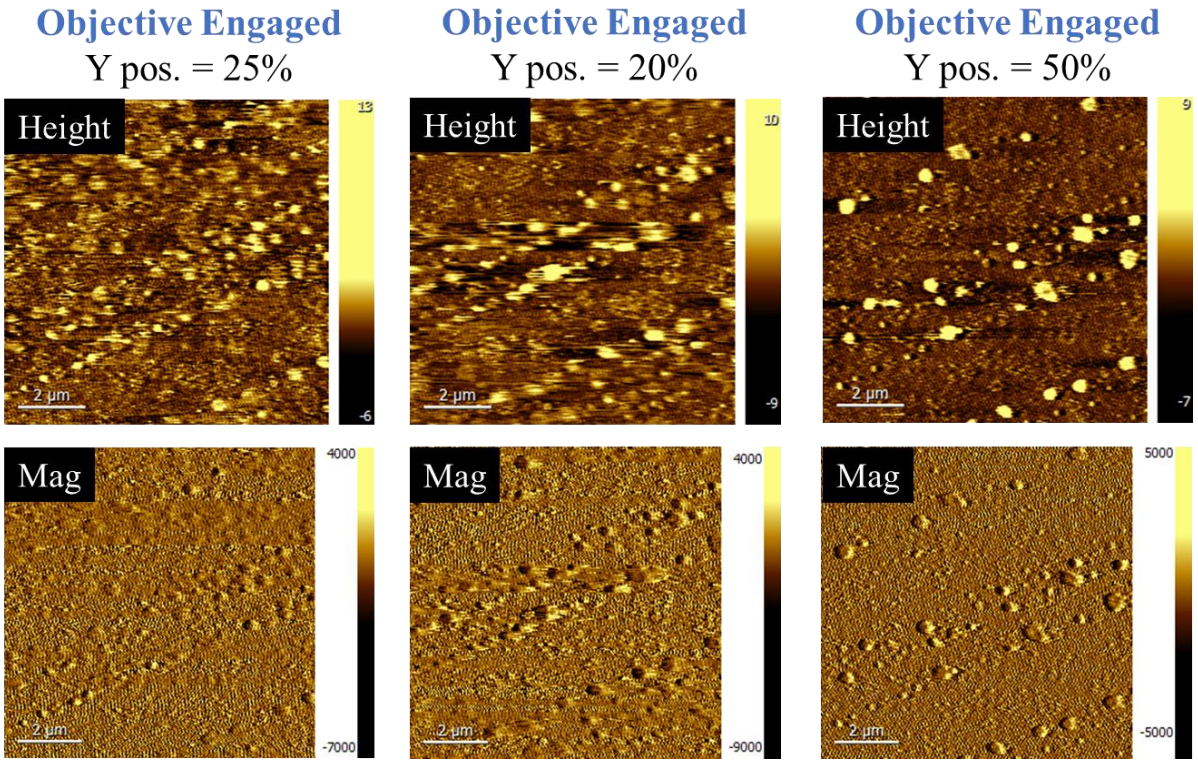

Figure 5.7. *Liquid AFM height and corresponding magnitude images of DPPC/DOPG lipids on glass with the TIR objective engaged. Adjustment of the AFM laser position on the backside of the cantilever (% of total length from the tip end) improves noise.*

The next parameter to verify when operating liquid-AFM with the TIR-objective engaged is the influence of the AFM laser position on the cantilever backside. **Figure 5.7** depicts 3 liquid-AFM scans of DPPC/DOPG lipids on glass with the TIR-objective engaged. Following the experimental procedure outlined in **Chapter 2**, the AFM diode laser spot position was set to 25 % of the total cantilever length before setting the resonance frequency, and performing the landing procedure and scanning. The tip was retracted and the AFM diode laser spot position set to 20 % and 50 % subsequently with the landing and scanning procedure performed each time. This resulted in slightly different scanning areas as seen in the above images. The left-most set of images in **Figure 5.7** use the default automatic positioning of the AFM laser spot. With a similar scan speed and set point of that optimised in **Figure 5.6**, these images are comparable for their amount of scarring and noise in both sets of images. The central set of images in **Figure 5.7** were taken using an AFM laser spot position at 20 % of the cantilever length, which shows a certain improvement in clarity in areas of the height and magnitude images. The cantilever has a greater degree of deflection towards the tip-end which gives a higher magnitude read-out. While this increased read-out makes setting the tip resonance frequency easier, laser spot positions of below 20 % may result in over-deflection in which the cantilever passes out of the AFM laser beam path. This leads to over-compensation of the tip modulation piezo and gives inaccurate deflection read-outs. The right-most set of images in **Figure 5.7** show a notable improvement to the image quality while using a 50 % AFM laser positioning. The degree of scarring observed in the height image is comparable to the **Figure 5.6** image without the TIR-objective engaged. However, careful inspection of the magnitude image in **Figure 5.7** still shows background persistent noise, albeit to a lesser degree. This suggests that while using a higher % positioning of the AFM laser on the cantilever backside results in a more stable tip operation in liquid, external noise transmitted through the engaged TIR-objective is nevertheless present. In contrast to a < 20 % laser spot position, an AFM laser spot position of 50 % has a decreased magnitude read-out which can make setting the tip resonance frequency more challenging – especially for cantilevers with poor quality, less-reflective backside coatings. This laser positioning of 50 % correlates with the crossover point of the Nf liquid plot of **Figure 5.5**, i.e. the point on the cantilever where the vertical cantilever deflection signal (Nf) is equal to zero. Similarly, the default laser position value of 25 % that is used in air correlates to plot values of **Figure 5.5** Nf air that are close to zero. The ACCESS-FM doped silicon probes feature a 245 µm-long driving-board cantilever with and elephant trunk shaped tip. The tip shape in particular is very compatible with the approach angle of our AFM-TERS systems to be conveniently visualised for laser-tip alignment. However,

shorter triangular-shaped silicon nitride cantilevers are often preferred for their applications in biology due to the lower spring constant and higher mechanical stability.[16]

5.2.3. Mica-glass substrates for TIR-TERS

The technical limitations of TIR-TERS of SLBs are similar to those reported in total-internal reflection fluorescence microscopy (TIRFM) or confocal microscopy. Due to the transparency of glass, it is the preferred surface for TIRFM imaging. However, the atomic flatness of freshly cleaved mica is ideal for observing sub-nanometre differences in SLBs using AFM. Mica is uncommon in optical microscopy due to issues in preparation, with thin exfoliations being fragile and thicker mica sheets being non-uniform and wavy. This makes working with high numerical aperture, short working distance objectives challenging. Taking inspiration from the developments in TIRFM field, a substrate that has both the mechanical strength and transparency of a glass slide along with the desirable biocompatibility of muscovite mica was prepared based on a previously reported protocol.[17]

The preparation protocol of the mica-glass (MG)-substrates is visually depicted in **Figure 5.8A**. A base support glass microscope slide is initially cleaned with ethanol before a freshly cleaved piece of mica (ca. 10 x 10 mm) is glued onto the glass slide. A low viscosity optical adhesive (NOA60, Norland Products) is used here to help spread the glue under the mica. **Figure 5.8B** displays two glass slides with 3 mica sheets each that have been glued to the surface. The red arrows indicate areas of excessive and lack of adhesive respectively. The former can be removed using an ethanol-soaked cloth prior to curing or a blade after curing. The latter case is best resolved by removing the mica sheet and reapplying sufficient glue. A curing time of at least 10 min under a UV lamp (8W, 254 nm, VL-4C, Fischer Bioblock Scientific) was used to ensure sufficient curing before proceeding to the next steps. **Figure 5.8C** demonstrates the next step of exfoliating the exposed mica surface using scotch tape until a uniform sheet of mica is obtained on the tape. Next, a high viscosity optical adhesive (NOA30, Norland Products) is applied to the mica and a clean 0.13 mm glass coverslip is placed on top. Initially, this sandwich structure was cured without clamps but variations in finished substrate thickness lead to issues in focusing of the TIR-objective. Hence, simple paper binder clips were later used to secure the glass coverslip during curing which gave consistent substrate thicknesses. A cure time of 10 mins was sufficient for stability but longer times up to 60 mins ruled out any potential problems of lack of curing. These substrate sandwiches could be stored for weeks at a time until required for SLB preparation. When desired, an exacto knife was used

to separate the MG-substrate from the supporting glass microscope slide by carefully lifting the glass coverslip which should retain a few layers of mica.

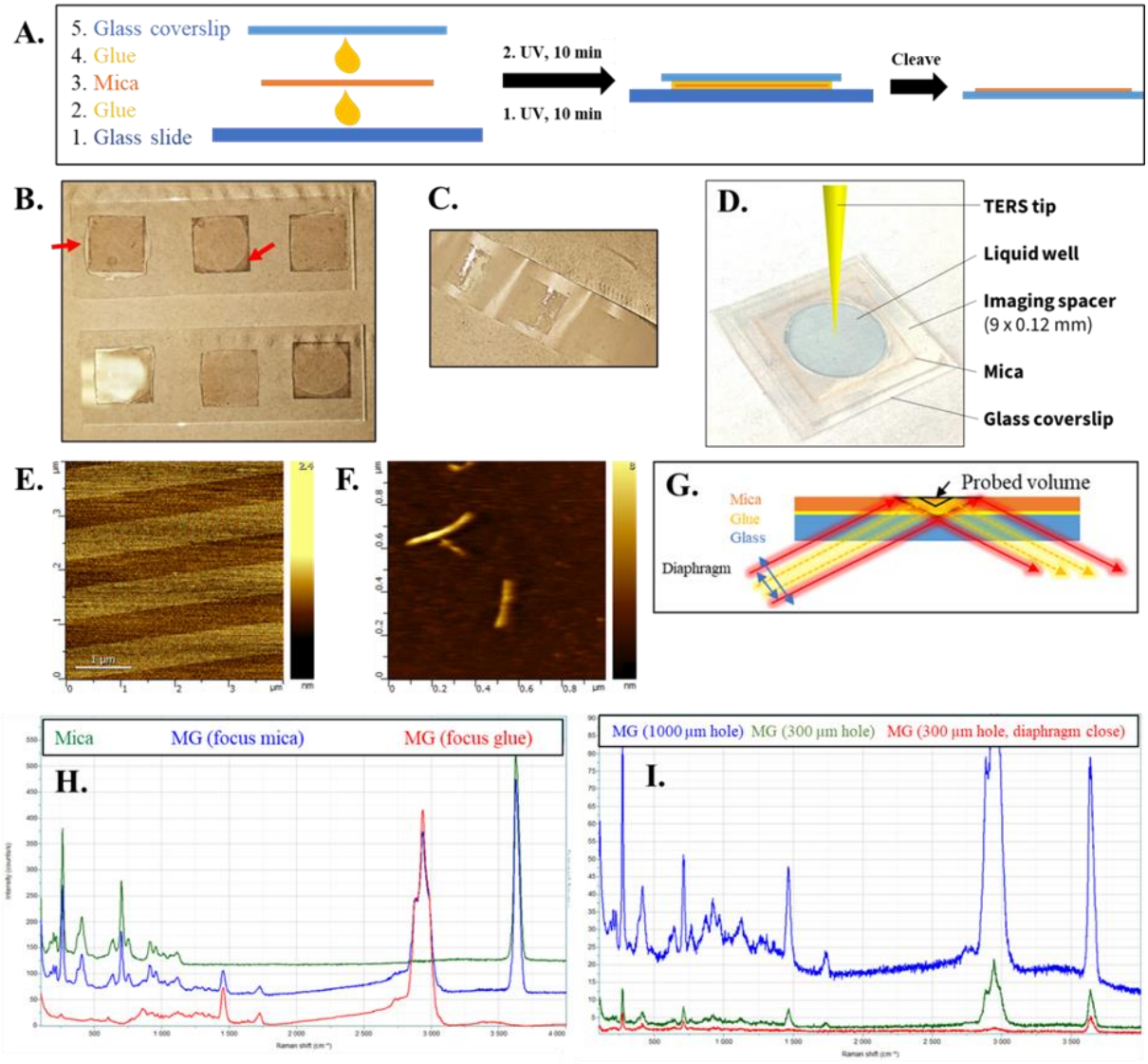

Figure 5.8. *[A] Fabrication of mica-glass substrates via cleavage of glass coverslip-mica-glass slide sandwich sustained by optical adhesive glue.* ***[B]*** *Mica sheets glued onto glass microscope slides. Red arrows indicate excessive and insufficient coverage of optical glue which could lead to issues when cleaving.* ***[C]*** *Thin layers of exfoliated mica on scotch tape.* ***[D]*** *Schematic of liquid cell made from MG substrate and imaging spacer.* ***[E]*** *AFM height image shows instrumental noise of atomically flat MG substrate surface.* ***[F]*** *Tau fibrils on MG substrate.* ***[G]*** *Illustration of TIR-geometry beam and resulting probed substrate volume from adjustment of optical diaphragm.* ***[H]*** *TIR-Raman spectra of pure mica versus MG substrate with focus on mica surface or inside glue.* ***[I]*** *TIR-Raman spectra of MG substrate with the effect of probed volume as illustrated in G.*

Prior to deposition of lipids, a 9 × 0.12 mm imaging spacer (SecureSeal, Grace Bio-Labs) was secured to the MG-substrate using the self-contained adhesive (**Figure 5.8D**). This gives a relatively exposed imaging well that can hold approximately 200 µL of liquid. The prepared MG-substrates have atomic flatness which is confirmed by AFM in **Figure 5.8E**, as only the instrumental noise is visible on the bare surface. **Figure 5.8F** of Tau fibrils on the MG-substrate corroborates this observation, which demonstrate a height of 8 nm in an otherwise uniform and flat surface.

When performing the initial characterisation of the first MG-substrates, it was realised that the substrate gave a Raman response when exposed to medium-high intensity laser light. It was therefore theorised that due to the TIR configuration and the relative thinness of the upper mica layer, that a certain volume within the substrate is probed as visualised in **Figure 5.8G**. Unlike glass or quartz substrates that have spectroscopically void Raman spectra, mica has various bands associated with the silica, metal-oxygen, and hydroxy vibrational modes. Additionally, despite being designed for optical use the optical adhesive used to glue the mica sheet to the glass coverslip support also contains spectroscopic features from the mercapto ester (trade secret) and triallyl isocyanurate compounds. These are demonstrated in their respective measured Raman spectra in **Figure 5.8H**, where a pure mica sheet is shown in green, the MG-substrate with TIR focalisation onto the mica surface (blue), and the MG-substrate with TIR focalisation inside the mica-glass interface (red). The contribution of mica in the MG-substrate Raman spectrum is confirmed by the intense OH stretching vibration mode at ca. 3650 cm^{-1}. A potentially problematic contribution of the optical adhesive is the broad CH stretching bands ca. 2900 cm^{-1}. Efforts were made to reduce the contribution of the substrate, notably by reducing the optical hole and diaphragm. **Figure 5.8I** displays the Raman response of the MG-substrate with a hole size of 1000 µm (blue), the reduced response when the hole size is also reduced to 300 µm (green), and the optimised response with a hole size of 300 µm and a closed diaphragm. This latter set-up was used in all further TERS measurements to minimise the substrate far-field contribution to the acquired TERS signal.

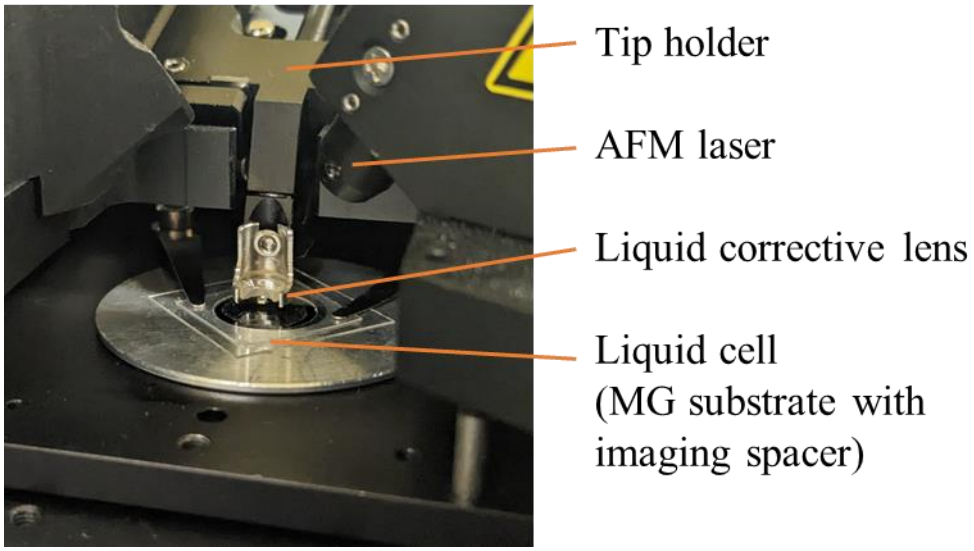

Figure 5.9. *Liquid cell positioned on the Combiscope AFM system. Two metal clamps secure the MG-substrate over the TIR objective. The tip holder features a corrective lens for the AFM deflection laser which accounts for the difference in refractive index between water and air.*

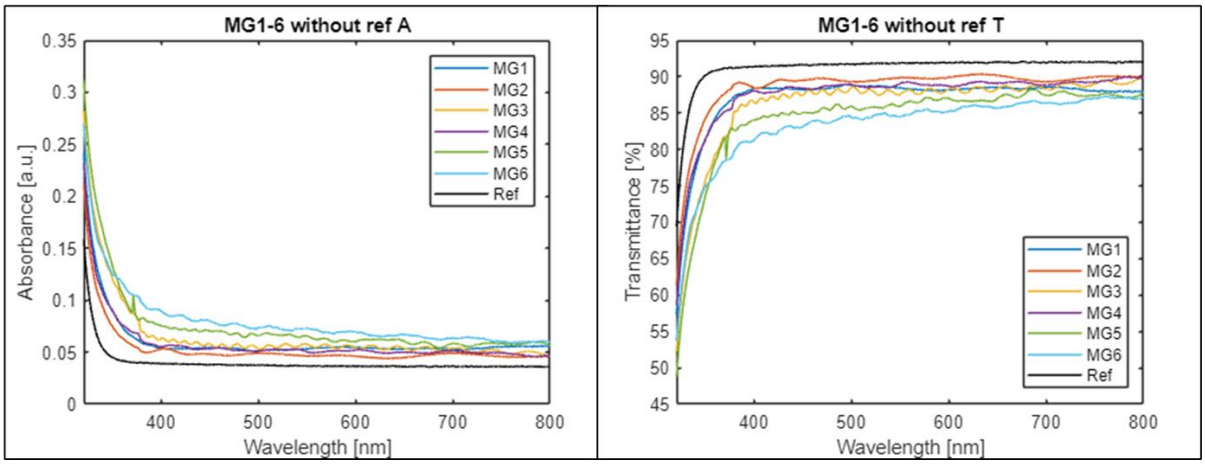

Figure 5.10. *Absorbance and transmittance spectra of mica-glass substrates (MG1 – 6) and bare glass slide (Ref, black).*

Figure 5.9 demonstrates a MG-substrate loaded on the AFM stage. The MG-substrate is centred and sits above the oil objective hole. It is secured with two clamps to ensure no lateral movement during scanning. The AFM tip holder features a corrective lens that compensates for the difference in refractive indexes between air and liquid. This allows for the accurate AFM tip deflection read-out using the AFM IR laser. Stepper motors in the tip holder enable the scanning and localisation of the tip when performing the AFM laser adjustment and the Moto Scan mode as described in **Figure 5.5**. Stepper motors attached to the AFM stage enable coarse

positioning of the objective relative to the sample surface, while piezo motors allow for the precise scanning when performing AFM.

The MG-substrates are estimated to be between 0.15 – 0.19 µm in thickness with the largest variation in thickness being the mica and glue layers. It was postulated that the optical properties of the mica and glue, and/or the added thickness could influence the excitation of the TERS tip. The absorbance/transmittance of several MG-substrates was therefore measured using a Lambda 650 UV/Vis spectrometer (Perkin Elmer) to determine if laser excitation is decreased due to the substrate. When using a gold tip immersed in aqueous media the LSPR of the tip is likely to fall in the red region and therefore an excitation laser of choice is a 660 nm laser source. In **Figure 5.10** the transmittance of glass at 660 nm is found to be 92 %. For the MG-substrates, a transmittance of 86 – 90 % at 660 nm was obtained. It is concluded that absorbance of the substrates should not significantly influence the TERS tip excitation and collection.

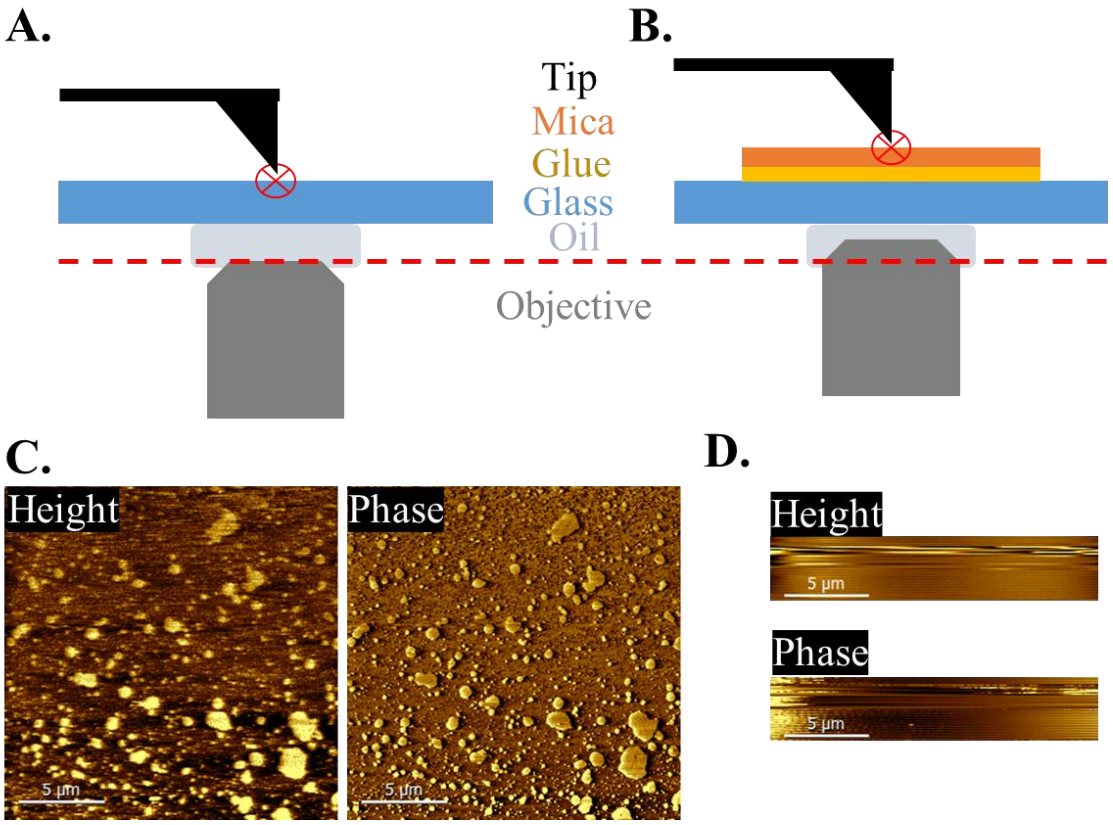

Figure 5.11. *Schematic of TIR objective engaged with a* ***[A]*** *glass substrate and* ***[B]*** *MG-substrate.* ***[C]*** *Liquid AFM height and phase images of DPPC/DOPG lipids on MG substrate before engaging the TIR objective.* ***[D]*** *Liquid AFM height and phase images after engaging the TIR objective. The MG substrate has a greater thickness than the bare glass coverslip extending the required focal depth of the TIR objective. This gives rise to more instrumental noise and less stable AFM operation.*

An unexpected complication of performing AFM-TERS measurements on the fabricated MG-substrates is the detrimental destabilisation of the tip when the oil-immersion objective was focused onto the sample surface. As visualised in **Figure 5.11A** and **B**, the focal point of the TIR objective is set to the surface of the glass or mica surface depending on the substrate used. However, due to the thicker size of MG-substrates the oil immersion objective is forced closer to the supporting glass coverslip which results in an upward pressure on the substrate. In the extreme case, focalisation of the TIR spot on the mica surface is not possible and TERS cannot be performed. The more common issue experienced is the loss of imaging capability as demonstrated in the comparison of **Figure 5.11C** and **D**. The DPPC/DOPG lipid mixture on the MG-substrate is clearly visible when the TIR objective is retracted (**Figure 5.11C**), but AFM tip operation becomes unstable upon engaging the tip (**Figure 5.11D**). The preparation of the MG-substrates was modified in order to combat these operational issues. First, the glass coverslip thickness was reduced to 0.13 µm (from 0.17 – 0.19 µm). These coverslips are more fragile and less rigid than their thicker counterparts, but proved sufficient when handled appropriately. Secondly, the clamping of the mica and coverslip during the curing step of fabrication insured less variance in the overall combined thickness of the glue and mica layers. These adjustments in the substrate preparation resulted in more consistent and compatible MG-substrates for the subsequent experiments.

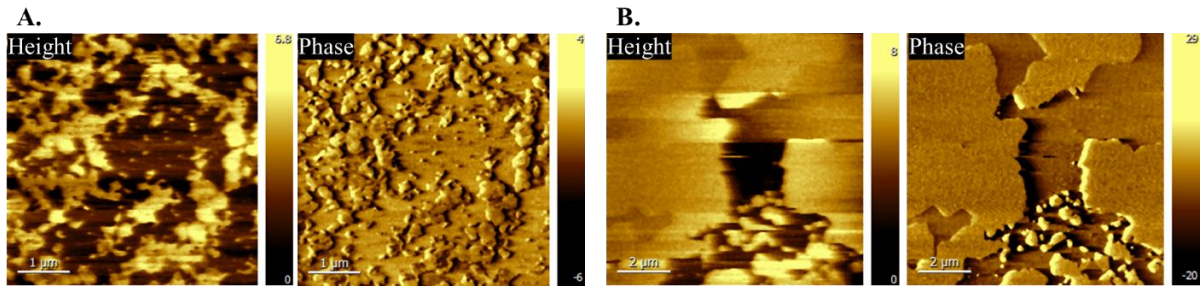

Figure 5.12. *Effect of buffer on bilayer formation.* ***[A]*** *$DPPC_{d62}$/DOPC in 100 mM NaCl solution on MG-substrate.* **[B]** $DPPC_{d62}$/DOPC in 100 mM PBS/NaCl on MG-substrate. The bilayer in A has smaller lipid domains compared to in B.

Initially, SLBs were prepared using ultra-pure MilliQ water only, in an effort to obtain pure TERS signatures of the lipid mixtures without any potential influence of the buffer. Despite the use of mica and sufficient incubation times and conditions, as seen in **Figure 5.12A** the domains of the gel-phase $DPPC_{d62}$ lipids remained small (< 1 µm). Phosphate buffered saline (PBS) was chosen as the desired buffer due to its general lack of Raman spectroscopic features in the region of interest for studying lipids (both the fingerprint and the CH regions).

The improvement in membrane formation of $DPPC_{d62}$/DOPC lipids is shown in **Figure 5.12B**, which has large (> 1 µm) domains of $DPPC_{d62}$ that contrast against the DOPC. Buffered salt solutions are essential for the formation of SLBs as both pH and ionic strength are regulated which promotes lipid vesicle adhesion, rupture, and fusion.[18]

Drastic changes to the pH or salt concentration of SLBs can disrupt lipid structures leading to the formation of defects or even total collapse. Even in controlled PBS buffer solutions formed SLBs nevertheless have an expiry date. As measured over a 4-day period, the $DPPC_{d62}$/DOPC SLBs deteriorate to a significant degree even after just 1 day (**Figure 5.13**). For preliminary TERS experiments of acquiring interpretable TERS spectra, SLBs up to two days old could be sufficient for measurement. However, future investigations outside of the scope of this thesis of more complex lipid systems will require diligence in measuring freshly prepared SLBs.

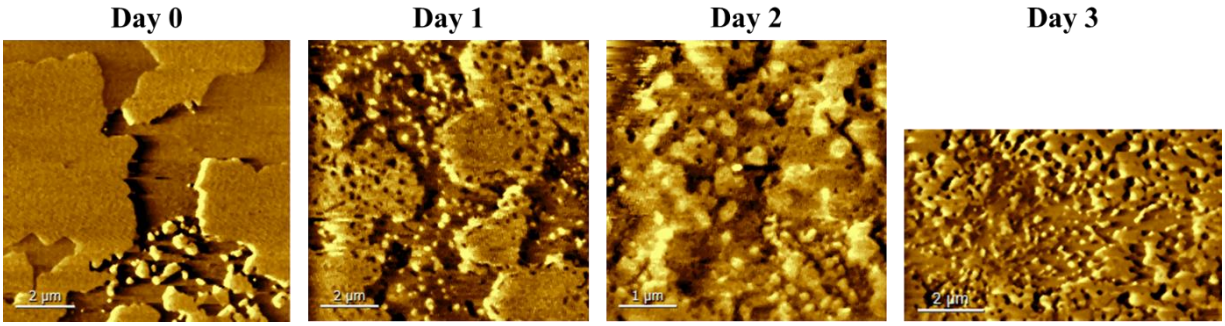

Figure 5.13. *Deterioration of $DPPC_{d62}$/DOPC lipid bilayer over time. Phase images show that even after 1 day after preparation there is significant membrane disorganisation and detachment from the mica surface.*

5.3. Raman and SERS of lipids

Similar to what has already been discussed in **Chapter 3**, the TERS signatures of biomolecules can differ considerably in intensity from their Raman counterparts.[19] SERS band intensities can often resemble those observed in TERS due to both techniques using the phenomenon of the resonant optical excitation of plasmonic metal nanoparticles. Differences between TERS and SERS spectra are nevertheless evident,[20] mainly due to TERS being more sensitive to molecular orientation and even single molecule detection. In a similar fashion to **Chapter 3.3.3**, first obtaining Raman and SERS spectra of samples of interest significantly aids in the interpretation of TERS spectra subsequently acquired. These reference Raman and SERS spectra serve as a

benchmark and give an insight into the prevalent and selectively enhanced modes of the investigated lipid molecules.

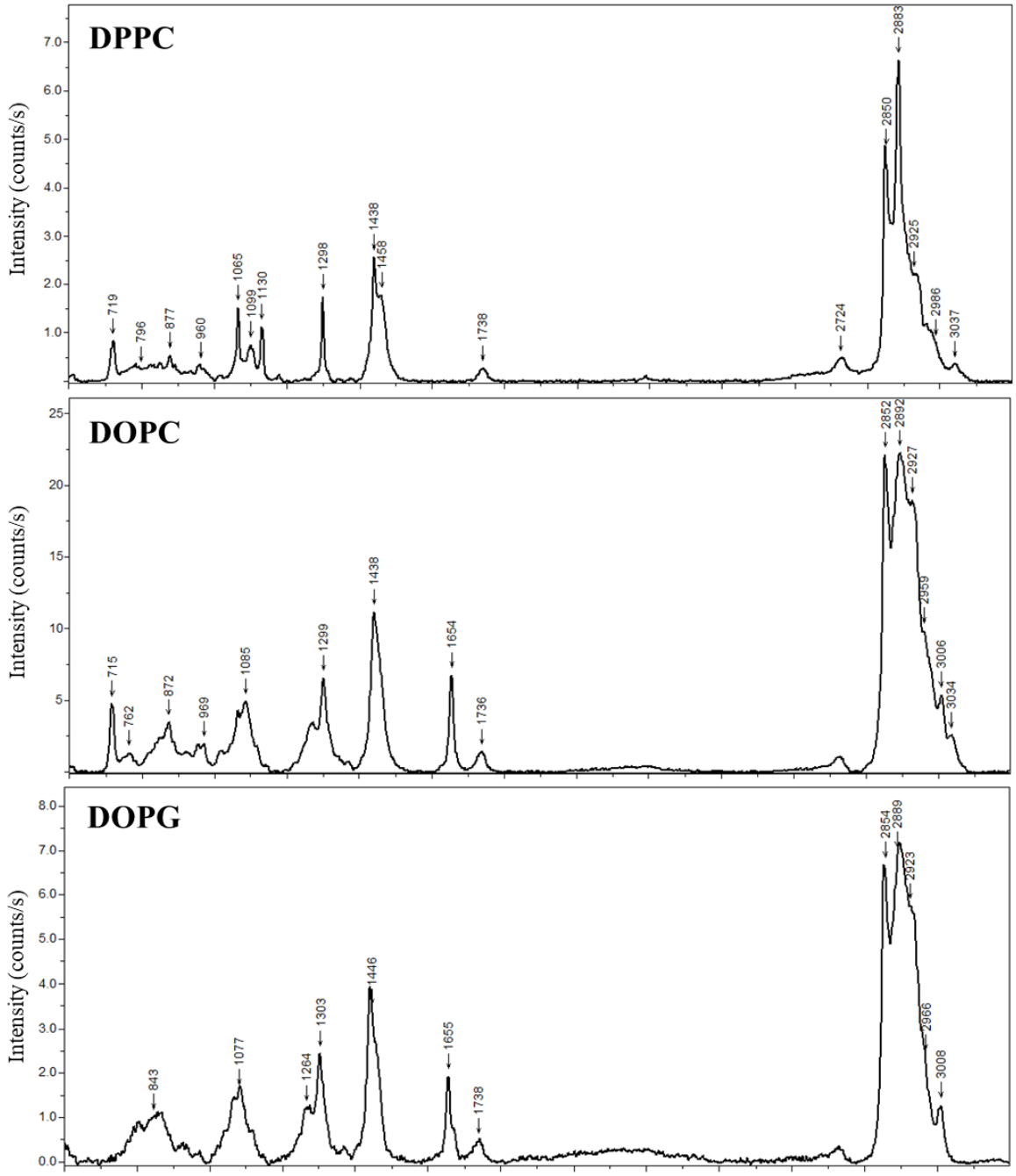

Figure 5.14. *(Top to bottom) Raman spectra of lipids DPPC, DOPC, DOPG, Spectra were obtained using 20 µL of 10 mg mL^{-1} lipid solutions, a LabRAM UV spectrometer, 633 nm laser, 100X objective, 600 grooves per mm grating, 100µm hole, acquisition time: 120s, accumulations: 4.*

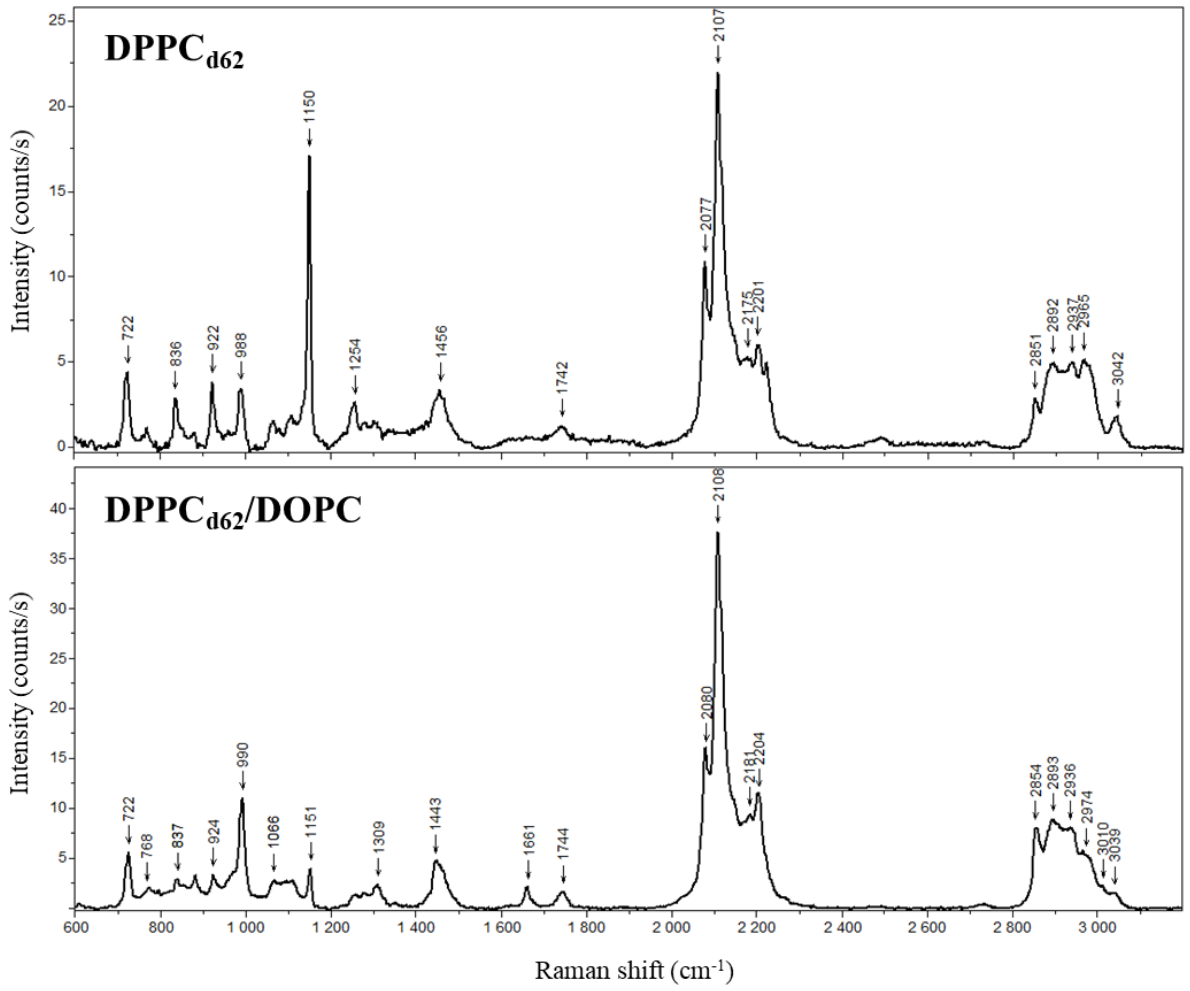

Figure 5.14. *(Continued, top to bottom) Raman spectra of lipids DPPC$_{d62}$ and the 50:50 lipid mixture DPPC$_{d62}$/DOPC. Spectra were obtained using 20 µL of 10 mg mL^{-1} lipid solutions, a LabRAM UV spectrometer, 633 nm laser, 100X objective, 600 grooves per mm grating, 100µm hole, acquisition time: 120s, accumulations: 4.*

The Raman spectra of DPPC, DOPC, DOPG, DPPC$_{d62}$, and DPPC$_{d62}$/DOPC using a 633 nm excitation laser are shown in **Figure 5.14**. The full band assignments of the Raman spectra presented in **Figure 5.14** are contained within **Table 5.1**.

In selecting an interesting SLB system to investigate with TERS, several lipids were considered. A binary mixture of lipids with saturated and unsaturated tails (such as DPPC and DOPC, respectively) results in a bilayer similar to that visualised in **Figure 5.13**, which can be differentiated based on their measured AFM height image. Spectroscopically however, these two molecules have quite similar Raman spectra with the C=C str mode (ca. 1655 cm^{-1}) of the unsaturated DOPC chain being the largest differentiator between the two. Both the fingerprint and CH region of the DPPC and DOPC spectra have several contributions which require

deconvolution to accurately assign. The C=C-H stretching mode (3010 cm^{-1}) occurs in tandem with the C=C stretching mode in the Raman spectra presented in **Figure 5.14** and could be argued to be another marker of the presence of DOPC lipids. Unfortunately, as demonstrated in **Figure 5.15**, the CH stretching region is found to be weakly enhanced in our TERS set-up. The typical LSPR of our Au-coated tips has a maximum ca. 700 nm. When a 660 nm laser source is matched to this plasmon band, it is noted that the intensity of the LSPR response decreases significantly with increasing wavenumber. This results in a lower TERS intensity at high wavenumbers compared to the fingerprint region. For this reason, the C=C-H band is often not resolved, and is not considered in further analysis.

When a mixture of DPPC and DOPC species is used, the resulting Raman spectrum is therefore further complicated. For investigation using TERS, the C=C stretching mode is unlikely to be a reliable band for the differentiation of the two lipid species, as theoretical calculations of DPPC bilayers suggest that only the choline head group is probed by the plasmonic tip.[9] Therefore, by modifying the lipid head group differences may become observable. The choline head group has some characteristic bands that are associated with the CH_3 asymmetric stretching (ca. 3040 cm^{-1}), the CH_2 scissoring (ca. 1456 cm^{-1}), and the CN stretching (ca. 720 cm^{-1}) modes. By changing the head group to glycerol (i.e. DOPG), these bands are now absent. This is an imperfect solution however, as the CH_3 and CH_2 modes due t to the head group are shared with all the other CH moieties throughout the lipids, complicating the interpretation of mixtures of these lipids.

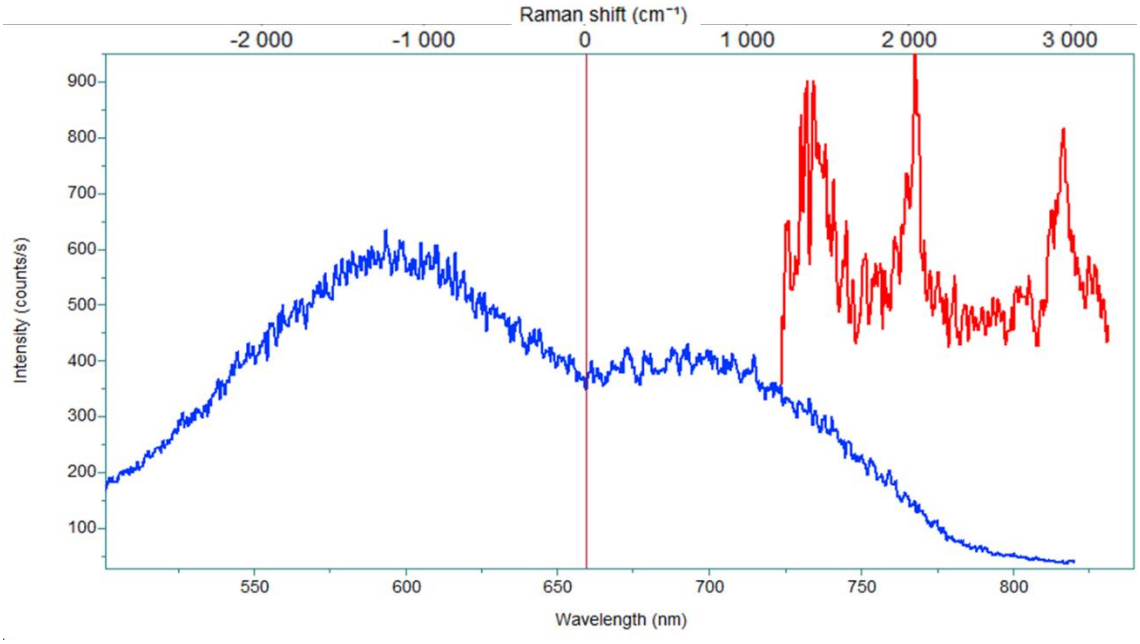

Figure 5.15. *LSPR (p-polarisation) of Au-coated TERS tip using DFSM (blue, bottom axis: wavelength), and TERS point spectrum of DPPC$_{d62}$/DOPC lipids (red, top axis: Raman shift). Red line corresponds to 660 nm excitation laser source.*

An alternative method for differentiating the Raman signals of the two types of lipids in a mixture is to use deuteration. As seen in **Figure 5.14**, the Raman spectrum of DPPC$_{d62}$ has a new set of peaks in the distinct region around 2000 – 2300 cm^{-1} corresponding to the CD_3 and CD_2 stretching modes. As depicted in **Figure 5.1**, DPPC$_{d62}$ contains deuterated aliphatic chains but retains the non-deuterated phosphate-head group. This partial deuteration is why contributions in the CH region are still clearly visible. The final Raman spectrum of **Figure 5.14** shows the 50:50 mixture of DPPC$_{d62}$/DOPC. This spectrum is directly comparable to the pure DPPC$_{d62}$ and pure DOPC spectra, being a visual combination of the two. Another interesting insight of using deuterated lipids is that the presence or absence of the CD_x bands could be used to infer the penetration depth of the TERS probe. In regions of highly ordered DPPC$_{d62}$ lipid, the presence of the deuteration signal could imply a probe depth greater than the mere head group size, unlike previous reports.[9] In disordered regions the measurement of the CD_x bands would signify exposure of the lipid tails and could be used as a qualitative determinant of lipid structure and ordering.

Table 5.1. Raman band assignments for DPPC, DOPC, DOPG, $DPPC_{d62}$, and $DPPC_{d62}$/DOPC lipids from *Figure 5.14. Asym str = asymmetric stretching, sym str = symmetric stretching, sci = scissoring, tw = twist, rk = rocking.*

Band Assignment	**DPPC**	**DOPC**	**DOPG**	**$DPPC_{d62}$**	**$DPPC_{d62}$/DOPC**
CH_3 asym str (choline)	3037	3034	-	3042	3039
C=C-H str	-	3004	3008	-	3010
CH_3 asym str	2986	2959	-	2965	2974
CH_3 sym str	2925	2927	2923	2937	2936
CH_2 asym str	2883	2892	2889	2892	2893
CH_2 sym str	2850	2852	2854	2851	2854
CD_3 asym str	-	-	-	2201	2204
CD_3 sym str	-	-	-	2175	2181
CD_2 asym str	-	-	-	2107	2108
CD_2 sym str	-	-	-	2077	2080
C=O str	1738	1736	1738	1742	1744
C=C str	-	1654	1655	-	1661
CH_2 sci (choline)	1458	1456	-	1456	1450
CH_2 sci	1438	1438	1446	1453	1443
CH_2 tw	1298	1299	1303	1254	1309
CD_2 sci	-	-	-	1150	1151
CC all-trans	1130	-	-	-	-
CC gauche	1099	-	-	-	-
PO_2 sym str	-	1085	1077	-	1066
CC trans	1065	-	-	-	-
CC-all trans (deuterated)	-	-	-	988	990
CN asym str	960	969	-	-	-
CD_2 tw	-	-	-	922	924
PO asym str	877	872	843	-	-
CC trans (deuterated)	-	-	-	836	837
CH_2 rk	796	762	805	-	768
CN str (choline)	719	715	-	722	722

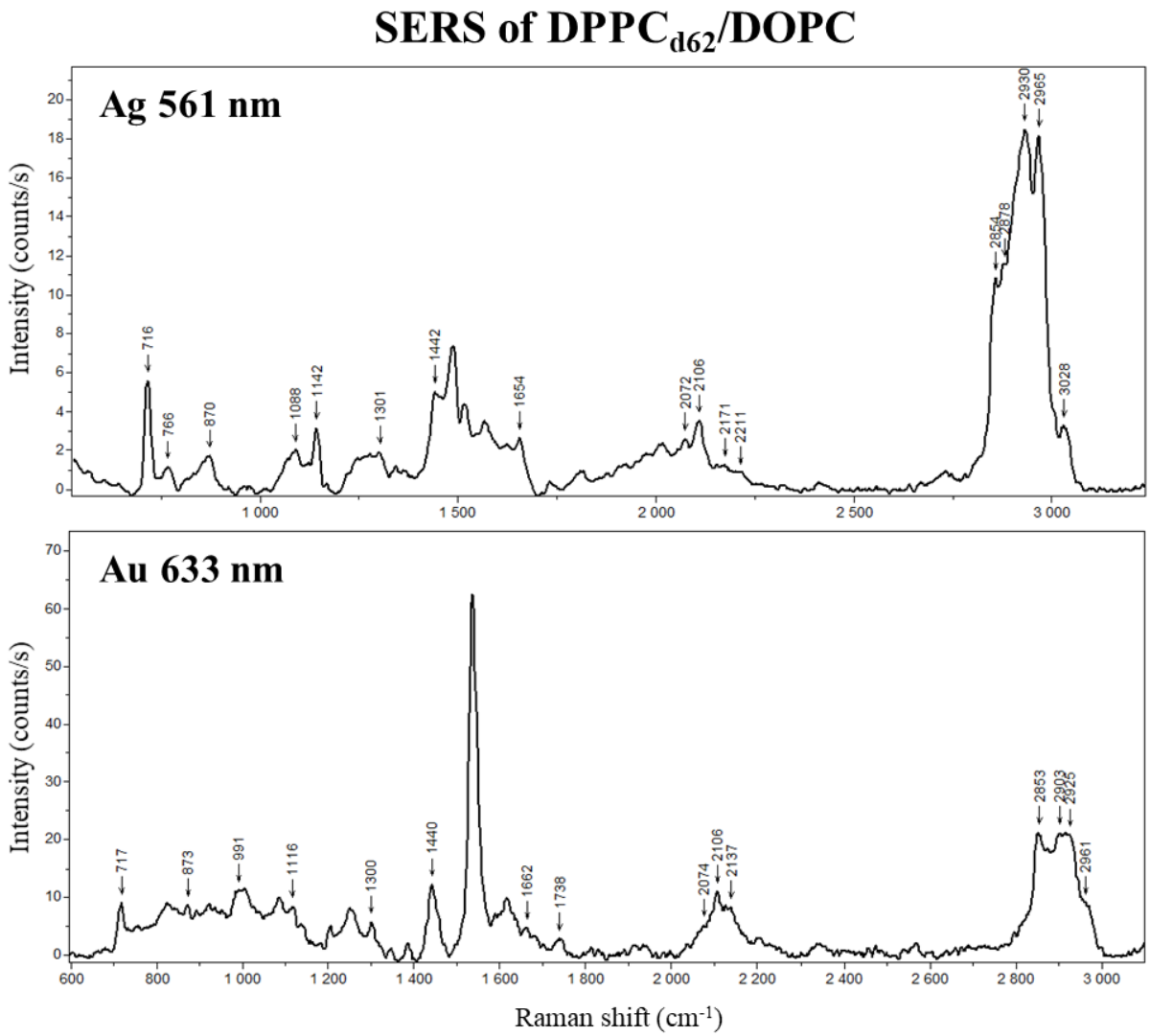

Figure 5.16. *SERS spectra of DPPC$_{d62}$/DOPC lipid deposited on (top) a 10 nm Ag-coated quartz coverslip at 561 nm excitation and (bottom) a 10 nm Au-coated quartz coverslip at 633 nm excitation. The peaks around 1500 – 1600 cm^{-1} are believed to be due to contamination arising from the sputtering process*

As already mentioned, SERS can be a useful assignment tool for TERS spectra due to their similarity in Raman enhancement mechanisms involving the LSPR of metal nanoparticles. The biggest difference is that SERS spectra correspond to a larger probed sample area which includes many hotspots that lead to an averaged signal.[19] The SERS spectra of the DPPC$_{d62}$/DOPC lipid mixture on 10 nm Ag-coated quartz and 10 nm Au-coated quartz are presented in **Figure 5.16**. An excitation laser of 561 nm was used for the SERS measurement using Ag nanoparticles, while a 633 nm laser was used for SERS of Au nanoparticles. The two SERS measurements were performed for various reasons. Firstly, the low imaginary part of the dielectric function of Ag nanoparticles often gives an increased SERS response when compared

to Au nanoparticles. This is in conjunction with our groups personal experience with the SERS substrates fabricated using Ag or Au sputtering, where SERS substrates made of Au nanoparticles tend to have a lower plasmonic response. However, as the desired TERS measurements of the intact SLBs are performed in aqueous environments an Au-coated TERS tip is used. TERS with Ag-coated tips is more difficult in liquid due to the reactivity of Ag with respect to Au. Specifically, the ability of Ag to form bonds with N atoms of the sample (thus creating chemical enhancement of bonds that are not native bonds of the sample), in addition to bonds forming with any potential contaminant in the liquid. Therefore, the SERS spectrum that uses Au nanoparticles is likely to better represent the TERS spectrum acquired using such Au-coated tips.

It is evident from **Figure 5.16** that there are several notable differences between the two SERS substrates, in addition to the differences from the Raman spectra previously presented. **Table 5.2** presents the full assignment of the SERS spectra of **Figure 5.16**. Between the two SERS spectra, both contain the characteristic 717 cm^{-1} peak of the choline head group CN stretching mode. The other choline modes are not resolved for the CH_2 scissoring (ca. 1450 cm^{-1}), and partially resolved for the CH_3 asymmetric stretching (3028 cm^{-1} for Ag SERS). The characteristic C=C stretching of DOPC appears at 1654 and 1662 cm^{-1} for the Ag and Au SERS, respectively. This is very comparable to the measured Raman value of 1661 cm^{-1}.

An interesting observation in the SERS spectra is the low intensity of the CD_x peaks in the 2000 – 2300 cm^{-1} range. The deuterated peaks are broad and not well defined which complicates their interpretation. Nevertheless, the ratio of the CD_2 to CD_3 bands is similar to that seen in **Figure 5.14**. For example, the 2106 cm^{-1} peak corresponds to the CD_2 asymmetric stretching mode which is seen to be the most prevalent across the measured Raman and SERS spectra. This is followed by the CD_2 asymmetric stretching mode (2074 cm^{-1}), then the CD_3 symmetric and asymmetric stretching modes (2181 and 2204 cm^{-1} respectively). Initially, this low intensity observed is unexpected. When the lipids are deposited onto the rough SERS substrate, they are presumed to take a random orientation as the SERS sample is not prepared like a SLB. The roughness of the nanoparticulate surface is expected to hinder the formation of ordered domains and the fusion of lipids at the substrate surface. Under this condition, it could be presumed that both tail and head groups of the lipids have equal opportunity of enhancement from the plasmonic nanoparticles. This presumption breaks-down with the observation that the CH stretching bands (ca. 2900 cm^{-1}) are significantly enhanced compared to the CD stretching bands. An explanation to this observation is that despite the rough surface the lipids do form

some form of preferential orientation. Given the negative surface charge of the Ag or Au nanoparticles, it is likely that the positively charged choline head groups of both $DPPC_{d62}$ and DOPC lipids associate preferentially with the nanoparticle surface, rather than the aliphatic tails. This suggests that the largest contributor to the CH stretching region in the SERS spectra is that of the phospho-choline head group. This conclusion is corroborated by the observable 717 cm^{-1} CN stretching vibration bands.

It is noted that the SERS spectra contain additional peaks not present in the Raman spectrum counterpart. The bands that are present within the 1500 – 1600 cm^{-1} spectral region are unexpected, as it is clearly visible in **Figure 5.14** that this is a spectral region normally void of peaks. It was previously discussed in **Chapter 3** that the use of the sputtering machine can introduce carbonaceous contamination that is observable in the SERS and TERS spectra. However, this carbonaceous contamination in general doesn't lead to such a narrow peak, and is more often seen as a very broad band. Therefore, this SERS experiment merits repeating, as to establish if some other molecular contribution or contamination is observed. Thankfully, this band occurs in a region typically void of peaks **Figure 5.14**, and its presence doesn't influence interpretation of other peaks.

Table 5.2. *SERS band assignments for $DPPC_{d62}$/DOPC 50:50 lipid mixture obtained using 10 nm Ag-coated quartz coverslip at 561 nm and 10 nm Au-coated quartz coverslip at 633 nm laser excitation. Asym str = asymmetric stretching, sym str = symmetric stretching, sci = scissoring, tw = twist, rk = rocking.*

Band Assignment	$DPPC_{d62}$/DOPC		
	Raman (Figure 14)	**SERS Ag 561 nm**	**SERS Au 663 nm**
CH_3 asym str (choline)	3039	3028	-
C=C-H str	3010	-	-
CH_3 asym str	2974	2965	2961
CH_3 sym str	2936	2930	2925
CH_2 asym str	2893	2878	2903
CH_2 sym str	2854	2854	2853
CD_3 asym str	2204	2211	-
CD_3 sym str	2181	2171	2137
CD_2 asym str	2108	2106	2106
CD_2 sym str	2080	2072	2074
C=O str	1744	-	1738
C=C str	1661	1654	1662
CH_2 sci (choline)	1450	-	-
CH_2 sci	1443	1442	1440
CH_2 tw	1309	1301	1300
CD_2 sci	1151	1142	1116
CC all-trans	-	-	-
CC gauche	-	-	-
PO_2 sym str	1066	1088	-
CC trans	-	-	-
CC-all trans (deuterated)	990	-	991
CN asym str	-	-	-
CD_2 tw	924	-	-
PO asym str	-	870	873
CC trans (deuterated)	837	-	-
CH_2 rk	768	766	-
CN str (choline)	722	716	717

5.4. TERS of SLBs in aqueous media

To successfully perform TIR-TERS in liquid, several factors must be considered. While standard AFM tips can be used for both air and liquid measurements, extra care is needed for setting the correct resonance frequency of the tip in liquid. It has been observed for a tip with a given resonance frequency of 60 – 70 kHz in air, the correct resonance frequency is often found to be around 20 – 40 kHz in liquid. The pure silicon AFM tips have a lower reflectivity for the 1300 nm AFM laser in liquid also, and require a backside coating of Au (40 – 60 nm) for effective tip alignment and magnitude read-out. As Ag-coated tips are easily oxidised in aqueous media, our group's initial efforts have focused on Au-coated sputtered TERS tips and the development of electrochemical deposition methods.[21,22] TERS tips fabricated based on potentiostatic electrodeposition and bipolar electrodeposition methods have achieved success in their chemical stability and robustness. These tips show little-to-no degradation after TERS measurements, being stable for 7 hours at least, with a lateral spatial resolution below 20 nm.[21] These TERS tips have highly reflective cantilever backsides, have stable operation in liquid, and good enhancement, making them the tips of choice for liquid TERS measurements.

5.4.1. Liquid-TERS of DPPC/DOPC SLBs

The first two-phase lipid mixture studied using electrochemically fabricated tips and MG-substrates was a 50:50 mixture of DPPC/DOPC. Ideally, these two lipids should form a homogeneous SLB with two distinct phases of the gel-phase DPPC molecules, and the liquid-crystalline phase of DOPC molecules. These two phases can be told apart by the difference in their measured AFM height profiles ca. (1 – 3 nm) which is possible when using the ultra-flat mica surface. **Figure 5.17** displays the AFM height and phase images of DPPC/DOPC lipids on an MG-substrate. While the SLB could be considered defective not having a continuous bilayer, a perfectly formed bilayer sometimes brings about a doubt in the different phases. In this early case, when both the MG-substrate fabrication and the SLB formation were still being optimised, the deposited DPPC/DOPC formed islands of lipids 1 – 2 µm in diameter. The mica layer is confirmed by the visible scratches on the surface (which could be partially the reason for incomplete SLB formation). Phase imaging can show differences in the viscoelasticity of a sample,[23] which is helpful here as the more rigid DPPC domains contrast against the fluid DOPC. With varied performance of the AFM height image read-out, the phase image helps with the discrimination of DPPC and DOPC domains.

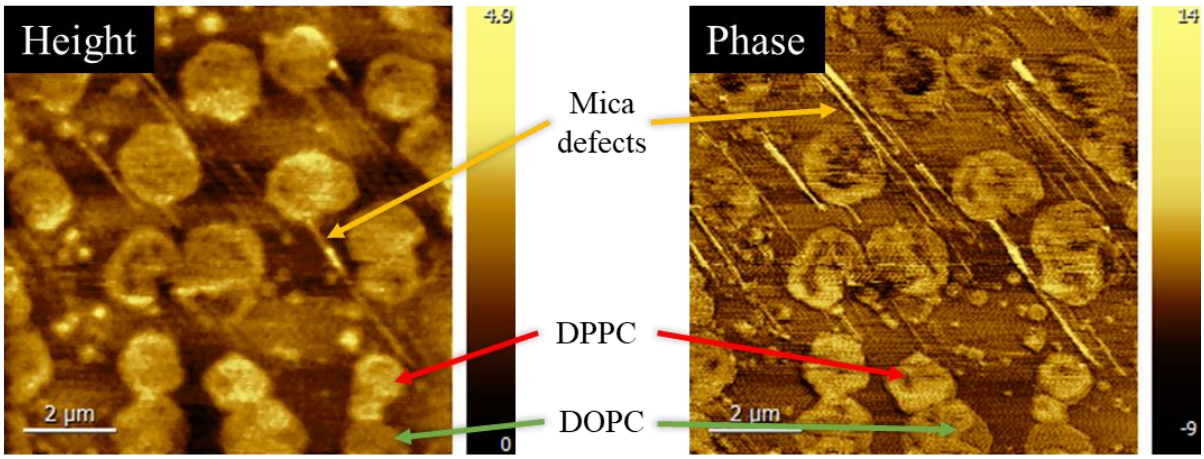

Figure 5.17. *AFM height and phase images of DPPC/DOPC lipids on MG substrate. The bilayer is not uniform and defects in the underlying mica are visible. The phase separation of DPPC and DOPC is visible in the lipid clusters close to the bottom of the image.*

Prior to the deposition of future SUVs, a routine was implemented to check the quality of the mica surface for defects. Using the TIR-objective, this step also enabled the determination of MG-substrate thickness which is essential for performing TERS measurements. The substrate temperature and incubation times were also optimised for the SUV deposition, with the DPPC/DOPC layer having full coverage of the MG-substrate as depicted in **Figure 5.18A**. This SLB, while not featuring large (> 1 µm diameter) DPPC domains, still demonstrates a clear distinction between the gel-phase and liquid-crystalline phase lipids that cover the surface. A TERS map of a 10 x 6 pixel area (step size: 10 nm) was taken from the red box marked in **Figure 5.18A**. Peak integrations of different vibrational modes are presented in **Figure 5.18B**. These correspond to the C=C stretching (red, 1650 – 1686 cm^{-1}), CH_2 scissoring (green, 1427 – 1462 cm^{-1}), CH_2 twisting (blue, 1290 – 1312 cm^{-1}), and the CC all-trans (purple, 1121 – 1142 cm^{-1}) modes. **Figure 5.18C** is the overlay of the aforementioned C=C stretching and CH_2 scissoring TERS maps. The TERS spectra corresponding to points 1 – 5 are shown in **Figure 5.18D**. The spectra also contain the integration regions corresponding to the TERS maps generated in **Figure 5.18B**.

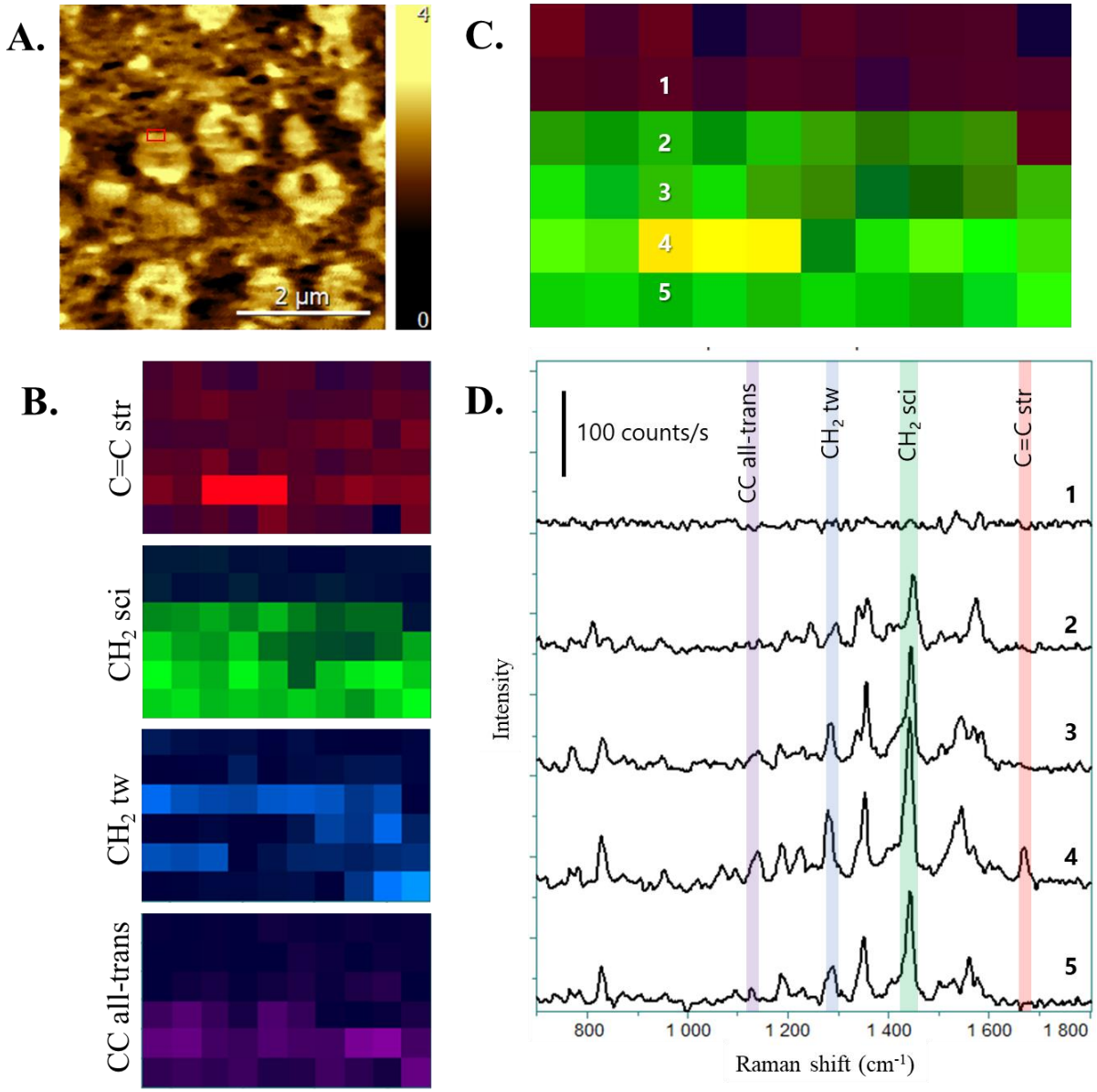

Figure 5.18. [A] *Liquid AFM height image of DPPC/DOPC lipid bilayer.* ***[B]*** *TERS intensity maps of lipid bands C=C str (1655 – 1680 cm^{-1}), CH_2 sci (1427 – 1462 cm^{-1}), CH_2 tw (1219 – 1312 cm^{-1}), CC all-trans (1121 – 1142 cm^{-1}) taken from red rectangular box in A. Step size: 10 nm.* ***[C]*** *Overlay of C=C str and CH_2 sci TERS maps with pixel numbering corresponding to TERS spectra presented in D.* ***[D]*** *Five TERS spectra along a DPPC/DOPC mixed domain. The presence of DOPC is confirmed in pixel 4 from the occurrence of the C=C str band. Laser: 633 nm, Acquisition time: 5 s.*

The first point to note about the TERS maps is the delineation of a line corresponding to the lipids, in which TERS spectra are measured, and outside on the bare mica substrate which show no spectral contribution. This area outside the lipid sample is roughly the two lines of pixels at the top of the TERS images, which is corroborated by the featureless spectrum of pixel 1 (**Figure 5.18C** and **D**). The CH_2 scissoring mode (green TERS map) is a non-specific

vibration related to either DPPC or DOPC. While both CH_2 scissoring and CH_2 twisting evolve following a similar trend, there is subtle difference in their intensities. This change in TERS intensity is likely due to the orientation of the normal vibrational mode with respect to the TERS tip axis. This could in turn be a result of the molecular packing of the lipids in the bilayer. The C=C stretching mode (red TERS map) is characteristic of the unsaturated chain of DOPC, which definitely confirms its presence in this region of interest (pixel 4, **Figure 5.18D**). This mode also occurs close to an area of intense CH_2 twisting. This infers that this region has loose molecular packing that likely a direct result of the presence of DOPC.

The CC all-trans mode (1130 cm^{-1}) is most prevalent in DPPC due to the preferable tight packing of trans alkyl chains compared to gauche configurations. This mode is therefore directly related to the packing order of the lipid bilayer. As seen in the purple TERS map of **Figure 5.18B**, the CC all-trans mode occurs at the bottom of the image, is often less intense in regions containing CH_2 twisting and C=C stretching modes, and absent in pixels close to the outer border of the lipid bilayer (pixel 2, **Figure 5.18D**). Therefore, it is demonstrated that our TERS system can delineate nanoscale regions (SOR of at least 10 nm) of more ordered DPPC lipids and less ordered DOPC lipids.

Nevertheless, it is difficult to conclude the absolute assignment of DPPC and DOPC on the nanoscale when using vibrational modes in the fingerprint region that correspond to the phospholipid tails. As suggested in recent theoretical calculations,[9] the TERS probe depth of DPPC molecules is only 1 – 2 nm which primarily probes the head group moiety. Under this assumption the aforementioned C=C stretching and CC all-trans modes should only be visible in holes in the membrane in which the TERS tip can successfully probe the phospholipid tails. However, this is a contradictory statement as the presence of the CC all-trans mode indicates highly structured DPPC under the TERS tip. This mode is weaker in intensity when compared to the other investigated modes (**Figure 5.18D**), which could be a result of its further distance from the TERS tip. The high efficiency of the electrochemical TERS tip used is likely the main contributing factor to this mode's observation. Therefore, this observation suggests a TERS probe depth beyond the 1 – 2 nm limit.

5.4.2. Liquid-TERS of $DPPC_{d62}$/DOPC SLBs

As already discussed in **Chapter 5.3**, deuteration is useful when studying SLBs as it enhances the ability to probe specific moieties and their structures and interactions. In our case, selective deuteration of the acyl chains enables the spectroscopic differentiation of the gel-phase and liquid-crystalline phase of otherwise very similar DPPC and DOPC lipids. In particular, it is interesting to confirm the available probe depth of TERS for lipid bilayers as this would open further avenues of study in biomechanics and dynamics of membranes. If the probe depth of liquid TIR-TERS is sufficient to observe the acyl deuteration, then this could be used as an additional marker to distinguish different regions of the SLB, specifically the distribution of $DPPC_{d62}$ across the bilayer.

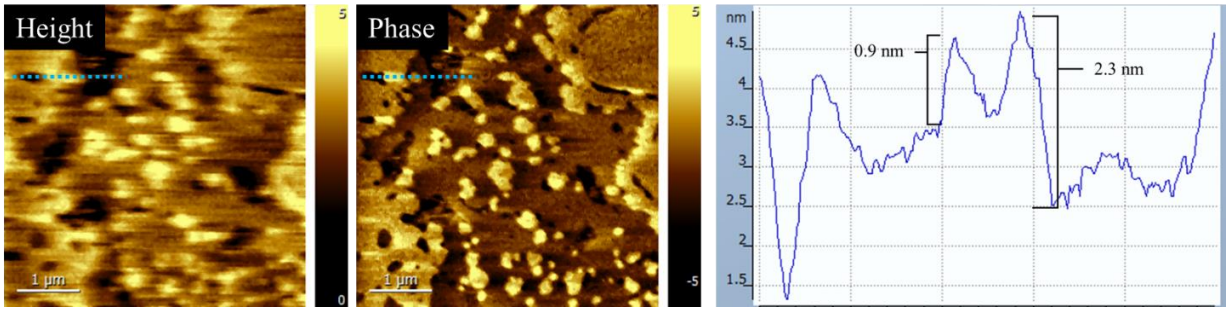

Figure 5.19. *AFM height and phase images of $DPPC_{d62}$/DOPC lipids on MG-substrate. Profile of line section (blue dashed line) distinguishes the lipid-lipid phase boundary and the lipid-mica boundary.*

An example of a 50:50 $DPPC_{d62}$/DOPC SLB formed on a MG-substrate is shown in **Figure 5.19**. The AFM height and phase images show a region of the SLB that features both large domains and smaller islands of $DPPC_{d62}$ which sit next to a layer of DOPC that has some holes down to the mica surface. The AFM operation was unfortunately noisy for the case of the height image, which sees scarring and blurring in the direction of scanning. Fortunately, the phase image gives a very clear image that correlates well with the height image, and clarifies the true boundaries of the lipid domains. The presence of both $DPPC_{d62}$ and DOPC phases is confirmed using a line profile that demonstrates a 0.9 nm height difference between the two phases, and a larger 2.3 nm difference between the SLB and the mica surface. These heights are comparable to those previously reported.[3,12]

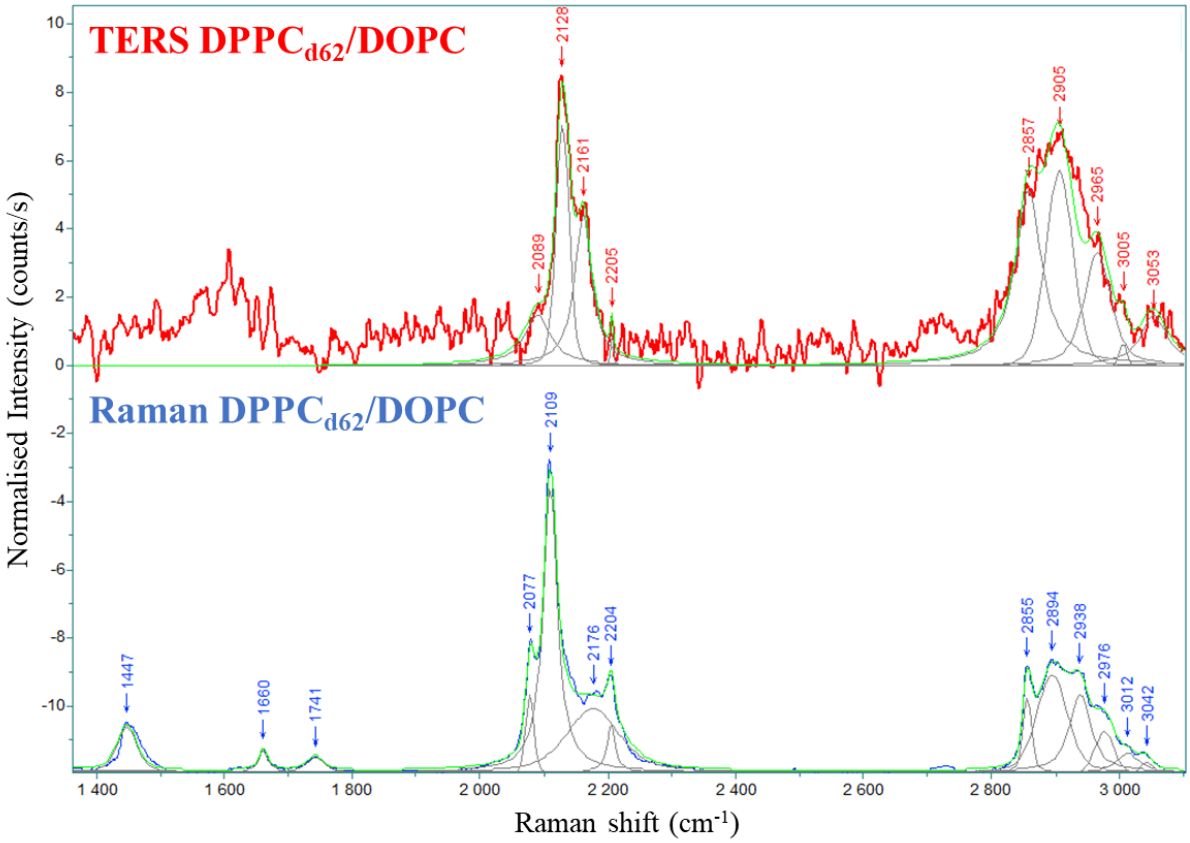

Figure 5.20. *Comparison of TERS point spectrum (red) and Raman spectrum (blue) of DPPC$_{d62}$/DOPC bilayer. Both the CH and CD stretching regions are visible in the TERS spectrum signifying the probing of the hydrocarbon chains.*

The TERS point spectrum of the DPPC$_{d62}$/DOPC bilayer shown in **Figure 5.20** has a very similar enhancement profile as that obtained for the Au-coated SERS substrate of **Figure 5.16**. There is a small broad peak around 1600 cm^{-1} that is characteristic of the TERS tip response, similar to that experienced in the Tau fibril studies of **Chapter 3**. With the signal-to-noise ratio seen in the above TERS point spectrum, it is difficult to confidently assign peaks within the 1400 – 1800 cm^{-1} region, specifically the CH_2 scissoring mode (1447 cm^{-1}), or C=O stretching mode (1741 cm^{-1}).

The Au-coated TERS tip used in the investigation of DPPC$_{d62}$/DOPC bilayers has a lower enhancement compared to that used for the DPPC/DOPC bilayers of **Chapter 5.4.1**. Despite this, both the CD and CH stretching bands are clearly visible in **Figure 5.20**. There are subtle differences between the Raman, SERS, and TERS spectral profiles for these two regions. The most intense deuterated peak is the 2128 cm^{-1} peak that is assigned to the CD_2 asymmetric stretching mode, while the 2161 cm^{-1} peak is assigned to the CD_3 symmetric stretching vibration. These peaks have a relatively large shift compared to their Raman (2109 cm^{-1} and

2176 cm^{-1}) and their SERS (2106 cm^{-1} and 2137 cm^{-1}). This is likely due to chemical and mechanical interactions between the tip and bilayer. For example, compression of the SLB by the tip end can alter bond length and angles leading to higher observed wavenumbers.[24,25] This effect is plausible as despite operating in tapping mode, the ACCESS-FM probes have a relatively high force constant of 2.7 N/m. Silicon nitride-based probes that are more common in the AFM field for studying soft biomolecules typically have force constants lower than 0.1 N/m in comparison. Nevertheless, the presence of the deuterated peaks confirms the ability of the TERS tip to probe the aliphatic chains of the $DPPC_{d62}$ lipids. The CH stretching region is comparable to both the Raman and SERS spectra acquired, albeit the 2857 cm^{-1} CH_2 stretching mode is less prevalent. Notably, the CH_3 asymmetric stretching mode appears at 3053 cm^{-1} in the TERS spectrum, which was absent in the SERS spectrum (**Figure 5.16**). The presence of this peak confirms the successful probing of both the head choline moiety and the deuterated acyl chain of $DPPC_{d62}$.

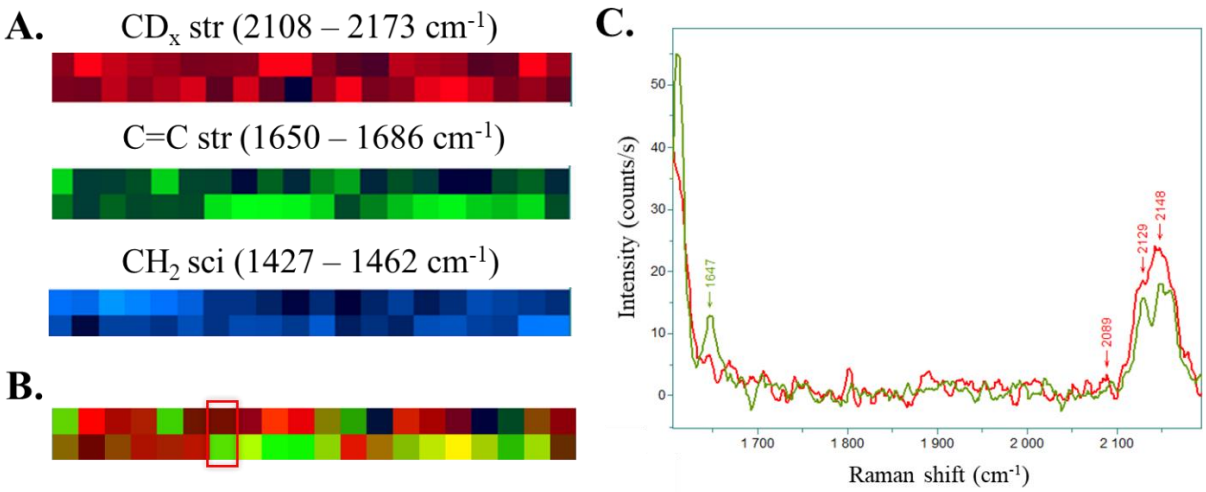

Figure 5.21. [A] *TERS images of a 20 x 2 pixel-area (20 nm step) with integrated spectral regions corresponding to CD_2 and CD_3 str modes (red, 2108 – 2173 cm^{-1}), C=C str (green, 1650 – 1686 cm^{-1}), and CH_2 sci (blue, 1427 – 1462 cm^{-1}).* ***[B]*** *The overlay of red and green maps from A corresponding to CD_x str and C=C str, respectively.* ***[C]*** *TERS spectra of 1600 – 2300 cm^{-1} spectral region corresponding to the two pixels highlighted by the red box in B.*

In a similar fashion to the DPPC/DOPC bilayer of **Figure 5.18**, TIR-TERS mapping of $DPPC_{d62}$/DOPC bilayers was attempted using various electrochemical Au-coated tips which had varying degrees of success. One such successful measurement is summarised in **Figure 5.21**. Two lines were taken across a 400 nm area of the SLB with a step size of 20 nm. From this, several TERS chemical maps were generated in order to localise areas of $DPPC_{d62}$ and

DOPC lipids. **Figure 5.21A** features the distribution of the CD_x bands (red, 2108 – 2173 cm^{-1}) which mainly consist of the contribution of the CD_2 asymmetric stretching and the CD_3 symmetric stretching modes, the C=C stretching (green, 1650 – 1686 cm^{-1}) mode that is specific to DOPC, and the non-specific CH_2 scissoring (blue, 1427 – 1462 cm^{-1}). As anticipated, the deuterated signature of $DPPC_{d62}$ lipids appears in pixels where the C=C stretching signature of DOPC is lower, and vice-versa. This is better visualised in **Figure 5.21B** which shows the overlap of the red and green chemical maps. Pixels that appear more yellow in this image share both the $DPPC_{d62}$ and DOPC signatures, which is likely a result of the 20 nm step-size that images a border region between the two domains. This boundary could potentially be resolved by reducing the imaging step-size, down to 10 nm at least, which was already proven when imaging DPPC/DOPC bilayers in **Figure 5.18**.

An intriguing observation about the distribution of CH_2 scissoring mode (blue map, **Figure 5.21A**) is its relatively-low intensity in regions of high intensity C=C stretching. The occurrence of DOPC lipids would suggest a less structured (more fluid) membrane domain and therefore it could be presumed that the acyl tails are more efficiently probed by the TERS tip. This assumption is supported by the observation of the C=C bond, which is located within this acyl tail. However, the lack of colocalization of these spectral signatures instead suggests the CH_2 scissoring mode is not efficiently enhanced within these DOPC regions. Molecular orientation with respect to the tip axis is likely the culprit, where the CH_2 scissoring mode is perpendicular with respect to the tip axis and is therefore not enhanced. The CH_2 scissoring mode also features contributions from the phospholipid head groups of both $DPPC_{d62}$ and DOPC, which explains its consistent and non-specific observation throughout the bilayer.

Figure 5.21C shows the corresponding TERS spectra of the two pixels highlighted by the red box of **Figure 5.21B**. The spectral region between 1600 – 2300 cm^{-1} is selected as this region contains both the C=C stretching and CD_x stretching vibrational modes. These spectra show the definite observation of the C=C stretching band at 1647 cm^{-1} (green spectrum) which is an absolute indicator of the presence of DOPC lipids. This peak is absent in the neighbouring pixel above (red spectrum), which signifies a SOR of at least 20 nm. For the deuterium spectral region, the main contributing peaks are the CD_2 asymmetric stretching at 2129 cm^{-1} and the CD_3 symmetric stretching at 2148 cm^{-1}. Much like in the point spectrum in **Figure 5.20**, the CD_2 asymmetric stretching mode is particularly shifted from the Raman and SERS counterparts (2109 cm^{-1} and 2106 cm^{-1}, respectively). The deuterium peaks are enhanced to a greater degree in the red spectrum, but are nonetheless observable in both the green and red spectrum. The increased intensity observed in the red spectrum signifies a greater quantity of $DPPC_{d62}$ within

this region while the absence of the C=C stretching band signifies a lack of DOPC. For the green spectrum, it is likely that $DPPC_{d62}$ molecules within the vicinity of the DOPC domain are simultaneously probed, especially considering the relatively large 20 nm step size used.

Conclusion

Using TIR-TERS in a liquid medium, the nanoscale characteristics of SLBs was explored with focus being put on phase segregation and the identification of nanometre-sized lipid domains. The results presented highlight the capability of TERS to distinguish lipid compositions which has further reaching applications in dynamic studies of lipid packing and lipid rafts. These first steps liquid-TERS also has significance within the field of neurodegenerative research. The potential of TERS to identify protein-lipid interactions, such as those between amyloids and phospholipids, is an exciting prospect for the deeper understanding of the molecular mechanisms behind prevalent diseases such as Alzheimer's.

The application of TERS to characterise biomolecules to date has been largely limited to dry conditions, often with experiments being performed on less-representative substrates like glass and gold. The technical challenges of performing TERS in liquid environments, such as substrate choice, tip fabrication, and the optimisation of liquid experimental conditions were addressed. For the former, MG-substrates that are tailored to studying lipid mixtures using the TIR-TERS system were fabricated. These substrates, have atomic smoothness that allow for the formation of SLBs with the negative surface charge facilitating immobilisation of the deposited biomolecules. By careful tuning of the optical path of the TIR laser beam onto the substrate surface, the far-field Raman signature of the mica could be sufficiently supressed to give a clean spectral background for TERS measurements. For the latter technical challenge, AFM specific parameters, such as laser spot positioning on the cantilever and scan rate, were optimised to mitigate noise while scanning.

Raman and SERS measurements of lipids provided a benchmark for later liquid-TERS analyses. Specifically, 50:50 mixtures of DPPC (gel-phase) and DOPC (liquid-crystalline phase) have been examined which form SLBs with distinct phases. With the aid of AFM phase imaging, which highlights viscoelasticity differences within the lipid domains, liquid-TERS could resolve more ordered DPPC from the less ordered DOPC lipids at nanoscale resolution. The probe depth of the TERS tip was also suggested to be greater than previously estimated in the literature, given the observation of vibrational modes associated with the phospholipid tails. Therefore, deuteration of the acyl chain of DPPC ($DPPC_{d62}$) was used to confirm the TERS

probe depth of 50:50 $DPPC_{d62}$/DOPC bilayers. Liquid TERS was shown to distinguish $DPPC_{d62}$-rich domains from DOPC-rich domains, with spectral overlap of signatures potentially indicating the presence of mixed lipid domains. This work has demonstrated the potential of liquid-TERS to provide nanoscale information on lipid membranes, cementing it as a powerful tool for fundamental biophysical and biomedical research applications.

References

1. Bonhommeau, S., Cooney, G. S., Huang, Y., Nanoscale chemical characterization of biomolecules using tip-enhanced Raman spectroscopy, Chem. Soc. Rev., 51, 2416–2430 (2022).

2. Lingwood, D., Simons, K., Lipid rafts as a membrane-organizing principle, Science, 327, 46–50 (2010).

3. Opilik, L., Bauer, T., Schmid, T., Stadler, J., Zenobi, R., Nanoscale chemical imaging of segregated lipid domains using tip-enhanced Raman spectroscopy, Phys. Chem. Chem. Phys., 13, 9978–9981 (2011).

4. Pandey, Y., Kumar, N., Goubert, G., Zenobi, R., Nanoscale Chemical Imaging of Supported Lipid Monolayers using Tip-Enhanced Raman Spectroscopy, Angew. Chem. Int. Ed., 60, 19041–19046 (2021).

5. Böhme, R., Richter, M., Cialla, D., Rösch, P., Deckert, V., Popp, J., Towards a specific characterisation of components on a cell surface - combined TERS-investigations of lipids and human cells, J. Raman Spec., 40, 1452–1457 (2009).

6. VandenAkker, C. C., Deckert-Gaudig, T., Schleeger, M., Velikov, K. P., Deckert, V., Bonn, M., Koenderink, G. H., Nanoscale Heterogeneity of the Molecular Structure of Individual hIAPP Amyloid Fibrils Revealed with Tip-Enhanced Raman Spectroscopy, Small 1, 4131–4139 (2015).

7. Talaga, D., Smeralda, W., Lescos, L., Hunel, J., Lepejova-Caudy, N., Cullin, C., Bonhommeau, S., Lecomte, S., PIP 2 Phospholipid-Induced Aggregation of Tau Filaments Probed by Tip-Enhanced Raman Spectroscopy, Angew. Chem. Int. Ed., 130, 15964–15968 (2018).

8. Pandey, Y., Ingold, A., Kumar, N., Zenobi, R., Nanoscale visualization of phase separation in binary supported lipid monolayer using tip-enhanced Raman spectroscopy, Nanoscale, 16, 10578–10583 (2024).

9. Mrđenović, D., Tang, Z. X., Pandey, Y., Su, W., Zhang, Y., Kumar, N., Zenobi, R., Regioselective Tip-Enhanced Raman Spectroscopy of Lipid Membranes with Sub-Nanometer Axial Resolution, Nano Lett., 23, 3939–3946 (2023).

10. Goodchild, J. A., Walsh, D. L., Connell, S. D., Nanoscale Substrate Roughness Hinders Domain Formation in Supported Lipid Bilayers, Langmuir, 35, 15352–15363 (2019).

11. You, X., Casper, C. B., Lentz, E. E., Erie, D. A., Atkin, J. M., Fabrication of a Biocompatible Mica/Gold Surface for Tip-Enhanced Raman Spectroscopy, ChemPhys Chem, 21, 188–193 (2020).

12. Attwood, S. J., Choi, Y., Leonenko, Z., Preparation of DOPC and DPPC supported planar lipid bilayers for atomic force microscopy and atomic force spectroscopy, Int. J. Mol. Sci., 14, 3514–3539 (2013).

13. Slotte, J. P., Biological functions of sphingomyelins, Prog. Lipid Res., 52, 424–437 (2013).

14. Paukner, K., Lesná, I. K., Poledne, R., Cholesterol in the Cell Membrane—An Emerging Player in Atherogenesis. Int. J. Mol. Sci., 23 (2022).

15. Lv, Z., Banerjee, S., Zagorski, K., Lyubchenko, Y. L., Supported lipid bilayers for atomic force microscopy studies. in Methods in Molecular Biology, 1814, 129–143 (Humana Press Inc., 2018).

16. Füzik, T., Umbrich, P., Rumi, T., Imaging of Biological Samples in Liquid Environment, Application Note 080, NT-MDT Spectrum Instruments, (2017).

17. Matysik, A., Kraut, R. S., Preparation of mica supported lipid bilayers for high resolution optical microscopy imaging, J. Vis. Exp. (2014)

18. Harb, F. F., Tinland, B., Effect of ionic strength on dynamics of supported phosphatidylcholine lipid bilayer revealed by FRAPP and langmuir-blodgett transfer ratios, Langmuir, 29, 5540–5546 (2013).

19. Bonhommeau, S., Lecomte, S., Tip-Enhanced Raman Spectroscopy: A Tool for Nanoscale Chemical and Structural Characterization of Biomolecules, Chem. Phys. Chem., 19, 8–18 (2018).

20. Bonhommeau, S., Talaga, D., Hunel, J., Cullin, C., Lecomte, S., Tip-Enhanced Raman Spectroscopy to Distinguish Toxic Oligomers from Aβ 1 – 42 Fibrils at the Nanometer Scale, Angew. Chem. Int. Ed., 129, 1797–1800 (2017).

21. Huang, Y., Talaga, D., Garrigue, P., Salinas, G., Cooney, G. S., Reculusa, S., Kuhn, A., Bouffier, L., Bonhommeau, S., Nanostructured gold-coated AFM tips generated by potentiostatic electrodeposition for tip-enhanced Raman spectroscopy, Chem. Phys. Lett. 832, (2023).

22. Huang, Y.,Talaga, D., Salinas, G., Garrigue, P., Cooney, G. S., Reculusa, S., Kuhn, A., Bonhommeau, S., Bouffier, L., Contactless manufacturing of TERS-active AFM tips by bipolar electrodeposition, under revision (2024).

23. Nagao, E., Dvorak, J. A., Phase imaging by atomic force microscopy: Analysis of living homoiothermic vertebrate cells, Biophys. J., 76, 3289–3297 (1999).

24. Stadler, J., Schmid, T., Zenobi, R., Nanoscale chemical imaging using top-illumination tip-enhanced Raman spectroscopy, Nano Lett., 10, 4514–4520 (2010).

25. Yano, T. A., Verma, P., Saito, Y., Ichimura, T., Kawata, S., Pressure-assisted tip-enhanced Raman imaging at a resolution of a few nanometres, Nat. Photonics, 3, 473–477 (2009).

General Conclusion

Tip-enhanced Raman spectroscopy has demonstrated significant progress since its conception in the early 2000s. In the study of biomolecules in particular, it has helped advance the understanding of various molecular classes, including DNA and RNA, proteins, and lipids. Its power as an analytical tool is founded in its nanoscale chemical and spatial resolution, which has found application in the study of disordered proteins and amyloid aggregation. Specifically, Alzheimer's-related amyloids Aβ and Tau protein have been characterised using TERS, with part of this thesis addressing a gap in current research and focusing on the relatively unexplored Tau protein.

Despite these achievements, there are several technical challenges to progress the application of TERS in liquid environments. In particular to the TERS technique, tip degradation and enhancement, incident laser focusing and signal collection in liquid media are the main limiting factors. The identified needs for the advancement of liquid TERS are the production of high-quality robust TERS tips and more efficient coupled optical systems. The experiments that have been conducted using SLBs as a model system are preliminary steps towards overcoming the current limitations of liquid TERS. This is in addition to the development and implementation of advanced TERS configurations such as the total-internal reflection system with dark-field microscopy capabilities.

The commercialisation of TERS instrumentation has augmented the accessibility of this specialist technique, and has allowed the broader scientific community to engage in nanoscale research. New users can quickly adopt commercially available systems, such as the side-illumination geometry LabRAM HR-OmegaScope, as described in **Chapter 2**. This is in contrast to commercially sold TERS probes, which often fail to meet expectations particularly for delicate biological samples. Their high cost does not reflect in their performance, and there is a definite need for the development of TERS probes that minimise mechanical damage to the sample. Currently, alternative fabrication methods such as physical vapour deposition and electrodeposition are required by the researcher to produce TERS-active probes at a reasonable cost.

The TIR-TERS system with integrated DFSM described in **Chapter 2** is a key contribution of our group in the instrumental innovation of TERS instruments. This system

enables the characterisation of the LSPR of TERS probes in an efficient manner, that allows the optimal choice of laser light source to be used for a given TERS experiment. Using *p*-polarised light in the TIR configuration has also been demonstrated to be the most effective TERS tip excitation due to the enhanced Z-component. This set-up boasts features such as easy laser-tip alignment, efficient hotspot generation, and reduced sample degradation thanks to the low laser power density at the substrate surface. As proven in **Chapter 3**, these characteristics make TIR-TERS especially suitable for biological applications.

The study of Tau-heparin fibrils using TIR-TERS demonstrates the system's ability to achieve 1 – 4 nm axial and 5 – 10 nm lateral resolution, all the while allowing the identification of aromatic and non-aromatic amino acids, disulphide bonds, and protein secondary structures. The following study using this time Tau-RNA fibrils, has provided insights into the role of anionic cofactors in the fibrillization of amyloids. With the adenine moiety being used as a spectral marker for the polyA cofactor, this work revealed the superficial colocalization of RNA molecules with the core β-sheet structures. TERS mapping confirmed the localisation of the anionic cofactor within the fuzzy coat of the fibril which in turn supports the templating hypothesis of amyloid fibril formation. Additionally, specific interactions between adenine and positively charged amino acids were identified and reasoned to be involved in cofactor incorporation.

Chapter 4 examined the relevance of chemometric methods in the analysis of complex biological TERS data. While these methods have undeniable potential, the need for the development of TERS-specific spectral processing was identified. The application of chemometric methods is further complicated by variance in TERS band intensities, contamination, and sample degradation. Data obtained from Tau-heparin and Tau-polyA fibrils was used to test common unsupervised learning techniques such as PCA and HCA. These methods have some promise, but traditional peak-picking approaches to TERS data analysis still play a substantial role in the data processing workflow. For chemometric methods to reach their full potential, more sophisticated and tailored analyses need to be developed.

TIR-TERS has been adapted to perform experimental measurements in liquid environments, which opens new avenues for the nanoscale characterisation of biomolecules. SLBs were explored using this system in **Chapter 5** with phase segregation of lipids and nanometre sized lipid domains being identified. These studies have proven TERS to be able to differentiate lipid composition with high precision, with wide reaching implications on future investigations of lipid packing dynamics and lipid rafts. Probing biological systems in

physiologically relevant liquid environments is a significant step forward for TERS as a technique and has further implications beyond lipid analysis, such as protein-lipid interactions. This is particularly true for the relationship between amyloids and phospholipids, in which future TERS studies could prove critical for understanding the molecular mechanisms involved in neurodegenerative diseases like Alzheimer's.

Up until very recently, TERS experiments have been primarily conducted under dry conditions and on non-representative substrates such as gold or glass. This work has addressed some of the key technical challenges with liquid TERS, including substrate fabrication, TERS tip production and characterisation, and optimisation of experimental conditions in liquid. For example, custom MG-substrates with the atomic smoothness and negative surface charge of muscovite mica, allowed for the formation and immobilisation of SLBs. Additionally, far-field Raman interferences arising from this substrate could be minimised by carefully tuning the optical path of the TIR laser. Using Raman and SERS measurements as benchmarks, liquid TERS was used to study lipid mixtures of DPPC (gel-phase) and DOPC (liquid-crystalline phase) and the deuterated form $DPPC_{d62}$. Somewhat unexpected observation of vibrational modes associated with phospholipid tails suggests a greater TERS probe depth than previously reported. Chemometric tools were not tested to process liquid TERS spectra which have been reported to be less subject to intensity variations owing to the improved heat dissipation in liquid medium compared to air, but this would constitute a natural extension of future works. All in all, while these results are tentative and merit further conformational studies, the ability of liquid TERS to resolve lipid domains is undoubted.

In conclusion, the immense potential of TERS and liquid TERS for providing nanoscale information of proteins and lipids has been demonstrated in this work. TERS is progressively solidifying itself as a powerful tool for research in biophysics and biomedicine. The nanoscale resolution and chemical sensitivity of TERS, along with its ability to operate in liquid environments, has proven the technique in exploring proteins and lipids, with protein-lipid interactions being the next achievable step. Therefore, the groundwork for future TERS studies aimed at investigating disease mechanisms in native environments has been laid with this thesis.

Annex 1

Tau protein expression, purification, and sample preparation

Heparin-induced Tau protein expression and purification

Full-length Tau 2N4R P301L was expressed and purified by PhD candidate Vicky Ury-Thiery at CBMN in the frame of her PhD work. *Escherichia Coli* BL21 (DE3) was used to express the protein via the transformation with a pET28 plasmid containing the 2N4R tau gene which was tagged with a poly-histidine tag at the N-terminus. The cells were inoculated in 1L of lysogeny broth (LB) with kanamycin before growing at 37 ^{o}C with shaking at 200 rpm. An optical density (OD600) of 0.6 indicated complete cell growth. The addition of 1mM isopropyl β-D-1-thiogalactopyranoside (IPTG, Sigma-Aldrich) and 3-hour incubation at 37°C and 200 rpm induced the expression of the protein. Centrifugation for 20 min at 5000 g at 4 ^{o}C enabled the cells to be harvested before resuspending the pellets in lysis buffer (50 mM Tris-HCl (pH 7.4), 100 mM NaCl, 0.5 mM DTT, 0.1 mM ethylenediaminetetraacetic acid (EDTA)) supplemented with 1 mM phenylmethylsulphonyl fluoride (PMSF), 20 µg mL^{-1} DNase, 10 mM $MgCl_2$, and 1 Piece protease inhibitor tablet (Thermo Fisher). The solution was stored at -20 °C until use. Lysozyme (2 mg mL^{-1}) was added to initiate cell lysis and incubated for 30 min at room temperature in an orbital shaker. Liquid nitrogen was used to break down the cells using three freeze-thaw cycles, before being centrifuged at 10,000 rpm for 10 min at 4 °C to remove cell debris. The remaining supernatant was heated to 90 °C for 12 min and then cooled on ice for 20 min. Precipitated proteins were removed by centrifugation at 10,000 rpm at 4 °C for 10 min. The Tau protein-containing supernatant was run through a 5 mL Ni-NTA agarose column that had been pre-equilibrated with sodium phosphate 20 mM (pH 7.0), NaCl 500 mM, imidazole 10 mM, EDTA 100 µM (buffer A). The column was washed with 10 column volumes (CV) of buffer A, 8 CV of sodium phosphate 20 mM, NaCl 500 mM, imidazole 10 M, EDTA 100 µM (buffer 2), and 2 CV of buffer A, before being eluted with 8 CV of sodium phosphate 20 mM, imidazole 500 mM, dithiothreitol (DTT), and NaCl 100 mM (buffer C). Sodium dodecyl sulphate-polyacrylamide gel electrophoresis (SDS-PAGE) and the absorption at 280 nm was used to monitor the elution. Centrifugal filters (MWCO 10 kDa, Sigma-Aldrich) for gel filtration chromatography were used to concentrate the pooled Tau 2NR4 fractions. A

Superdex 200 pg HiLoad 16-600 was equilibrated using 4-(2-hydroxyethyl)-1-piperazineethanesulfonic acid (HEPES) 20 mM pH 7.0, and NaCl 100 mM. UV-vis absorption at 274 nm with an extinction coefficient of 7.5 $cm^{-1}.mM^{-1}$ was then used to determine the final concentration of the protein solution. The purified P301L Tau was subsequently incubated with heparin sodium (Sigma-Aldrich, H6279, from porcine intestinal mucosa) and suspended in HEPES buffer. To follow fibril formation, a thioflavin T (Tht, Sigma-Aldrich, T3516) fluorescence assay was used. Fibrils were pelleted using an ultracentrifuge and resuspended in Milli-Q water.

Heparin-induced Tau protein sample preparation for AFM-TERS studies

A borosilicate glass coverslip (Electron Microscopy Sciences; 22 x 22 x 0.16 mm) was cleaned via ultrasonication in three successive steps in acetone (5 min), absolute ethanol (5 min), and ultrapure water (Milli-Q; 5 min) before drying under nitrogen flow. A smooth gold 10 nm layer was deposited onto the clean glass coverslip by sputtering (Q300T D, Quorum Technologies) under 5 $x10^{-3}$ mbar argon atmosphere at a rate of 0.04 $nm.s^{-1}$ with 20 mA current.

ThT-free Tau-heparin (3 µL) was spin-coated onto the gold-covered glass substrate to homogenously spread the fibrils to aid identifying individual fibrils for measurement. The sample was then dried under nitrogen flow.

Poly-A-induced Tau protein expression and purification

Full-length Tau 2N4R P301L was expressed and purified by PhD candidate Vicky Ury-Thiery at CBMN under a previously established protocol, similar to protocol above. In brief, *E. coli* BL21 (DE3) was used to express the full-length Tau protein and purified using nickel affinity chromatography. The mutation P301L was added via site-directed mutagenesis.

The purified P301L Tau was subsequently incubated polyadenosine (polyA, Sigma-Aldrich, T3516) and suspended in HEPES buffer. To follow fibril formation, a thioflavin T (Tht, Sigma-Aldrich, T3516) fluorescence assay was used. Fibrils were pelleted using an ultracentrifuge and resuspended in Milli-Q water.

Poly-A-induced Tau protein sample preparation for Raman, SERS, and TERS

A quartz coverslip (Electron Microscopy Sciences, 22 x 22 x 0.16 mm) was cleaned via ultrasonication in three successive steps in acetone (5 min), absolute ethanol (5 min), and finally Milli-Q water (5 min) before drying under nitrogen flow. For Raman measurements, a clean quartz coverslip was coated with 0.5 µL of either i) pure polyA, ii) polyA-induced Tau (Tau-polyA), or iii) heparin-induced Tau (Tau-heparin) samples before washing with Milli-Q water and drying under vacuum. For SERS experiments, a clean quartz coverslip was covered by a 10 nm rough layer of silver via sputtering (Q300T D, Quorum Technologies) at a rate of 0.03 $nm.s^{-1}$ under 1 $x10^{-2}$ mbar Ar atmosphere (99.999% purity) with sputter current of 20 mA. Immediately after sputtering, 2.5 µL of either i) pure polyA, ii) pure heparin, iii) Tau-polyA, or iv) Tau-heparin were drop-cast onto the Ag-covered quartz coverslip. The fibril suspension of Tau-polyA (2.5 µL) was spin-coated onto a clean coverslip for measurement with TERS. TERS samples were washed using Milli-Q water and dried under nitrogen flow prior to measurement. This method allowed for the distribution of fibrils across the substrate and for the visualisation and probing of individual separated fibrils.

List of Publications

Huang, Y., Talaga, D., Salinas, G., Garrigue, P., Cooney, G. S., Reculusa, S., Kuhn, A., Bonhommeau, S., Bouffier, L., (2025) Contactless manufacturing of TERS-active AFM tips by bipolar electrodeposition, Nanoscale, 17, 1411-1416. doi: 10.1039/d4nr03068k

Huang, Y, Cooney, G.S., Talaga, D., Vallée, R. A. L., Quinzi, R., Bouffier, L., Lecomte, S., Bonhommeau, S., (2024) Nanoscale Chemical Imaging of Amyloid Fibrils in Water Using Total-Internal-Reflection Tip-Enhanced Raman Spectroscopy, The Journal of Physical Chemistry Letters, 15, 40, 10190-10197. doi: 10.1021/acs.jpclett.4c02309.

Huang, Y., Talaga, D., Garrigue, P., Salinas, G., Cooney, G. S., Reculusa, S., Kuhn, A., Bouffier, L., Bonhommeau, S. (2023) Nanostructured gold-coated AFM tips generated by potentiostatic electrodeposition for tip-enhanced Raman spectroscopy, Chemical Physics Letters, 832, 140893. doi: 10.1016/j.cplett.2023.140893.

Cooney, G. S., Talaga, D., Ury-Thiery, V., Fichou, Y., Huang, Y., Lecomte, S., Bonhommeau, S., (2023) Chemical Imaging of RNA-Tau Amyloid Fibrils at the Nanoscale Using Tip-Enhanced Raman Spectroscopy, Angewandte Chemie International Edition, 62, e202314369. doi: 10.1002/anie.202314369.

Talaga, D., Cooney, G.S., Ury-Thiery, V., Fichou, Y., Huang, Y., Lecomte, S. Bonhommeau, S., (2022) Total Internal Reflection Tip-Enhanced Raman Spectroscopy of Tau Fibrils, The Journal of Physical Chemistry B, 126, 27, 5024-5032. doi: 10.1021/acs.jpcb.2c02786.

Bonhommeau, S., Cooney, G.S., Huang, Y., (2021) Nanoscale chemical characterisation of biomolecules using tip-enhanced Raman spectroscopy, Chemical Society Reviews, 2022, 51, 2416-2430. doi: 10.1039/D1CS01039E.

Conference Contributions

01st – 2nd Feb 2024 Oral presentation for Journées Grand Sud-Ouest, French Chemical Society, Bordeaux, France.

31st July – 4th Aug 2023 Poster presentation for 14th European Biophysics Congress (EBSA2023), Stockholm, Sweden. Awarded best poster presentation prize (€100).

13th Apr – 13th Apr 2023 Poster presentation for 25th Doctoral School of Chemical Sciences day (JEDSC2023), Bordeaux, Talence. Awarded best poster presentation prize (€1500).

29th Aug – 1st Sept 2022 Flash and Poster presentations for 19th European Conference on the Spectroscopy of Biological Molecules (ECSBM2022), Reims, France. Awarded best flash presentation prize (€500).

Titre: Spectroscopie Raman exaltée de pointe pour la caractérisation de systèmes biologiques : De l'imagerie chimique et structurale nanométrique à l'air à son développement en milieu liquide

Résumé: Cette thèse a pour objectif le développement de la spectroscopie Raman exaltée de pointe (TERS) pour des applications en milieux liquides, et plus particulièrement pour l'étude de membranes lipidiques et de protéines amyloïdes qui sont impliquées dans des maladies neurodégénératives comme la maladie d'Alzheimer. La TERS s'affranchit de la limite de diffraction de la spectroscopie Raman conventionnelle en combinant la haute résolution spatiale de la microscopie à sonde locale et la spécificité chimique de la spectroscopie Raman exaltée de surface (SERS). En utilisant une pointe de microscope à sonde locale métallisée et effilée au niveau nanométrique, la TERS génère une exaltation localisée du signal Raman au sommet de la pointe. Ceci permet l'étude de biomolécules optiquement non-résonnantes à l'échelle nanométrique sans marquage moléculaire et de manière non-destructive. Les défis clés qui sont traités dans ce travail incluent la fabrication de pointes actives en TERS, l'optimisation d'un nouveau système TERS en réflexion totale interne (RTI) pour des utilisations en environnements liquides, et l'exploitation de données complexes obtenues par imagerie TERS hyperspectrale. Des protéines amyloïdes sous forme de fibrilles de protéine Tau ont été étudiées au moyen de notre instrument de RTI-TERS en prenant des fibrilles induites par de l'héparine comme référence pour évaluer la performance du système. Des études TERS de fibrilles Tau induites par de l'ARN ont donné un aperçu des mécanismes de formation sous-jacents des fibrilles amyloïdes. Par ailleurs, ces données ont été utilisées pour explorer le potentiel des méthodes chimiométriques, telles que l'Analyse en Composantes Principales (ACP) et l'Analyse en Cluster Hiérarchique (ACH), pour leur analyse fine. Ces méthodes ont été évaluées dans le contexte des méthodes plus traditionnelles de sélection de pics individuels. Cette thèse détaille aussi le développement d'un système RTI-TERS compatible avec le milieu liquide et son application à l'étude de bicouches lipidiques supportées en milieux aqueux. Cette avancée permet la caractérisation nanométrique de membranes lipidiques dans des milieux biologiquement pertinents et plus réalistes que l'air. Dans la perspective de futurs travaux examinant les interactions protéines-lipides, ces innovations sont cruciales pour comprendre la formation des fibrilles amyloïdes et leurs effets délétères sur les cellules neuronales. Au final, cette thèse a amélioré la TERS en tant qu'outil pour étudier les structures biomoléculaires à l'échelle nanométrique dans le contexte des maladies neurodégénératives, et le système RTI-TERS optimisé fournit une plateforme pour de futures recherches dans des applications biologiques et biomédicales.

Mots clés: Spectroscopies Raman exaltées de pointe et de surface, Imagerie chimique nanométrique, Traitement des données et Chimiométrie, Nanosources optiques, Fibrilles amyloïdes, Bicouches lipidiques

---

Title: Tip-enhanced Raman spectroscopy for the characterization of biological systems: From nanoscale chemical and structural imaging in air to its development in liquid media

Abstract: The aims of this thesis are the development of tip-enhanced Raman spectroscopy (TERS) for applications in liquid media, specifically for the study of lipid membranes and amyloid proteins which are implicated in neurodegenerative diseases like Alzheimer's. TERS overcomes the diffraction limit of conventional Raman spectroscopy by combining the high spatial resolution of scanning probe microscopy with the chemical specificity of surface-enhanced Raman spectroscopy (SERS). By employing a metal-coated nano-tapered scanning probe microscopy probe tip, TERS generates a localised enhancement of the Raman signal at the tip apex. This enables the study of optically non-resonant biomolecules at the nanoscale in a label-free and non-destructive manner. The key challenges that are addressed in this work include the fabrication of TERS-active tips, the optimisation of our novel total-internal reflection (TIR)-TERS system for use in liquid environments, and the handling of the complex data obtained from hyperspectral TERS imaging. Amyloid proteins in the form of Tau fibrils were studied using this TIR-TERS setup with heparin-induced Tau fibrils being a benchmark for evaluating the performance of the system. TERS studies of RNA-induced Tau fibrils provided insight into the underlying formation mechanisms of amyloid fibrils. In addition, these data were used to explore the use of chemometric methods, such as Principal Component Analysis (PCA) and Hierarchical Cluster Analysis (HCA), for their fine analysis. These methods were evaluated in the context of more traditional peak-picking methods. This thesis also details the development of a liquid-compatible TIR-TERS system and its application to the study of supported lipid bilayers in aqueous media. This advancement enables the nanoscale investigation of lipid membranes in biologically relevant media, which is more representative compared to TERS in air. With the outlook of future works investigating protein-lipid interactions, these innovations are crucial for understanding amyloid fibril formation and their deleterious effects on neuronal cells. To conclude, this thesis enhances TERS as a tool for studying biomolecular structures in the context of neurodegenerative diseases at the nanoscale, and the optimised TIR-TERS system provides a platform for future research in biological and biomedical applications.

Keywords: Tip-Enhanced and Surface-Enhanced Raman Spectroscopy, Nanoscale chemical imaging, Data processing and Chemometrics, Optical nanosources, Amyloid fibrils, Supported Lipid Bilayers

---

Unité de recherche

ISM, UMR 5255, F-33400 Talence, France